Catalytic co-valorization of C_1 and N_1 compounds towards nitrile chemicals

PhD thesis

Presented by:

María Elena Martínez Monje

Supervised by:

Dr. Gonzalo Prieto

Instituto de Tecnología Química (ITQ-CSIC)

Valencia, July 2024

ACKNOWLEDGEMENTS (*AGRADECIMIENTOS*)

The journey to become a doctor has taken place over six long years, during which I have known many fascinating individuals, and, more importantly, kind-hearted people who have stood by me through good and not-so-good moments.

The Department of Education, Research, Culture, and Sports (Conselleria d'Educació, Investigació, Cultura I Esport) of the Valencian Region is acknowledged for financial support through the project SEJI/2018/011. I would like to acknowledge the FET Proactive and the European Research Council (ERC) under the Horizon 2020 research and innovation program (ERC-CoG-TANDEnd; grant agreement 864195). Both financial supports have made possible the realization of this thesis. I would also like to thank the Spanish Research Council (CSIC) and, particularly, the Institute of Chemical Technology (ITQ), for providing the infrastructure where I have developed my PhD work. Next, I want to thank the Max-Planck-Insitute für Kohlenforshung (KOFO) for giving me access to their facilities during my short PhD research stay, and to the ALBA synchrotron, especially to the CLÆSS and NOTOS beamlines, for the several beamtimes granted.

I would like to start by acknowledging the people who have made the realization of this thesis possible. First and foremost, I am grateful to Dr. Gonzalo Prieto for providing me with the opportunity to join his small group at that time. Thanks for initiating my interest in engineering chemistry and patiently guiding me through all these new concepts that were beyond my scope as a chemistry/material science person. His patience in improving my English vocabulary and soft skills and teaching me how to deliver effective presentations is truly commendable.

I also want to express my gratitude to Prof. Dra. Claudia Weidenthaler for hosting me in your group at the Max Planck Institute as a visiting student. Thank you for your lessons and your time, which enriched my scientific knowledge and reminded me of old times when I wanted to jump out of bed in the morning with the eagerness to learn.

I would like to extend my gratitude to the people of ALBA; their dedication to the users is outstanding. Dr. Giovanni Agostini taught me so much during my initial encounters with X-ray absorption spectroscopy, making that learning experience a memorable one. Thanks, Giovanni, for helping me during the experiments and giving me force in the academic world. Alongside him, thanks to Dr. Carlo Marini, an example of knowledge in the XAS community, always willing to help and share his expertise. Gracias a Carlos Escudero por tu alegría contagiosa y tu ayuda durante mi experimento crucial, en NOTOS. Gracias también al fantástico grupo que se está formando en NOTOS por toda su ayuda.

Sin duda el comienzo de la tesis en el ITQ fue toda una aventura, volviendo a dar vida a un laboratorio al que daba miedo pasar. Pero que, con más de una reforma y limpieza, reubicación de reactivos y muestras (incluidas las de Dr. Prieto de su tesis) y mucha paciencia, conseguimos que volviera a parecer un laboratorio. Gracias a todo equipo de taller por la ayuda de todas estas transformaciones. Además, agradecerles, la ayuda en los arreglos y desarreglos del reactor, del que

ha llegado a ser una maraña de tuberías y cables. Gracias a toda la gente de administración por toda la ayuda con los tediosos trámites de administración, en especial a Cristina Fandos por ser tan directa, pero a la vez tan graciosa haciendo tu trabajo.

Gracias a todo el equipo de caracterización por recibir siempre con una sonrisa mis muestras. Gracias Dolo y Adelina por vuestra profesionalidad y por vuestro tiempo midiendo mis tediosas muestras sensibles al aire. Gracias Maribel por tu buen hacer y por tus consejos para recuperar mis doloridos brazos. Gracias Dr. Jose Luis Jordá por tu ayuda en mis inicios en difracción de rayos X en inerte.

Durante toda esta transición, es imposible no agradecer a Carla y Eva (de Nanomedicina) por acogernos en su laboratorio, cuando éramos polizones en el ITQ. A Manolo Moliner por tu simpatía. A Agustín Martínez por hacernos sentir como nietos en el mundo académico. Al Dr. Joaquín Martínez (Ximo) y a la Dra. Cristina Martínez, gracias por estar siempre con tanta disposición a ayudar y no solo en el mundo de la cromatografía sino en cualquier otra duda que pudiéramos tener.

I extend my heartfelt thanks to all the group members for teaching me so much during my time at KOFO, specially to Dr. Hilke, Isabella, and Tolga, and additionally to Sebastian and Jan for your assistance in XPS and XRD and your teaching. Over those three months, I am particularly grateful to Tolga, Damla, Ezgi, Alper, Jillian and Leila for your warm friendship in such a short period of time. All of you made my stay in Mulheim truly pleasant.

Volviendo de nuevo al ITQ, agradecer a *becarios seguros*, en el que más de un día ha sido imposible mantener la concentración, por tener las mejores conversaciones y risas, dando siempre tanto apoyo, escuchando cuando lo necesitabas y de los que creo que me he dejado pocos por abrazar. No creo que vuelva a tener unos compañeros de trabajo iguales. A Bea, Lorena, Ferrán, Sofía y Adrián gracias por vuestras conversaciones tan amenas y por vuestras sonrisas que alegran el día. A Jose y Pla que cuando se juntan ofrecen las mejores risas, gracias por alegrarme tanto cada vez que os veía. A Agustín, mi compañero de mesa que esconde un gran carisma y cariño, gracias por ayudarme cada vez que he tenido alguna duda y por todos tus abrazos. A Álvaro, gracias por tu gran optimismo, por tus enseñanzas de escalada y ser un ejemplo de energía y actividad sin duda envidiable.

Más allá del ámbito académico, quiero agradecer sin duda a Andrés, Jordan, Sergio, Javi (Ceuta), Mauri, Jorge, Eva, Julliete, Silvia y Jose, por ser personas tan buenas y con tan buen humor, por regalarme tan buenas conversaciones y buenos momentos en el que más de una vez que me ha dolido de reírme. Dentro y fuera del trabajo, quiero agradecerle a José Miguel, siempre intentando ayudar, pero sobre todo por todas las risas y tu buen humor, convirtiéndose en un gran amigo con el que siempre querer competir en cualquier deporte.

A esas personitas que hacen tanto bien estando cerca. A Anto gracias por todas las risas y unir tanto al grupo. Rubén gracias por tener un carácter tan gracioso y literalmente despegarme los pies del suelo con tus abrazos. A Ana por tus buenas conversaciones. Sandra, gracias por ser un cielo de persona y tan buena compi de bádminton.

Dentro de lo que comenzó siendo el pequeño *Prieto group*, creció llenándose de gente fantástica, que me ha regalado tanto apoyo, amistad, risas y buenos momentos, tanto fuera como dentro del instituto.). A Tania, gracias por tus conversaciones tan agradables. Kai, Jonglack and Bidyut thanks for being always willing to help and teach. A Laura, Fausto y Adriá por vuestra energía y alegría. A Sebas, gracias por tu buen humor y por tus buenas palabras. A Ilaria por tu gran carácter, tu buen hacer y tus buenas conversaciones. A Wilson gracias por tu ayuda en el mundo de XAS y por enseñarme diferentes perspectivas de la vida. A Niloufar por tus sonrisas y tu carácter amable. A Adri por ser tan buena persona y por tu actitud optimista. A Raquel por toda tu ayuda, tus sonrisas y tu apoyo (siempre me reiré del momento de la BPR). A Alberto, gracias por saber escuchar y tu buen humor (y animarme a volver a jugar al bádminton). A Vero por todos los pequeños huecos que has sacado para ayudarme, por tu cariño y buenos abrazos, estoy terriblemente agradecida. A Quique, gracias por ser tan buen compañero, y por regalarme tantas risas con tu humor tan peculiar y divertido.

Entre ellos no puedo evitar agradecer especialmente a mis mosqueteros. Juntos levantamos un *Palomar* irreconocible, pero sobre todo una familia dentro y fuera del instituto. No tengo suficientes palabras ni papel para agradeceros todos estos años. Sin duda, sin vuestros abrazos habría tomado un camino muy diferente. Marcos, gracias por enseñarme a ser un poco más pícara en la vida, tu optimismo, por tus consejos, por unir tanto a la gente y por querer hacerme feliz poniéndome Aitana. Eva, amor, gracias por darme siempre un punto diferente, por enseñarme tanto dentro y fuera del ITQ, por nuestras confidencias y por ser tan buena amiga. Iván, gracias enormemente por estar siempre ahí, da igual el lugar, siempre ayudándome a avanzar. Gracias por ser mi coach, por enseñarme a bailar cuando estaba perdida y por todas las cervecitas y charlas juntos.

Fuera de lo que ha sido la tesis, quiero agradecer a todas esas personas que han sido fuente de revitalización. A Laura, Patri,y mis Alvaritos, gracias por acompañarme en el mundo de la química, vuestro gran apoyo y los consejos tan bonitos que siempre me habéis dado. Sin duda, no podría encontrar mejores recursos químicos, aunque viviera siglos. A mis niñas de la infancia, Lau y Ari, por vuestra amistad infinita, vuestro cariño y por intentar entenderme siempre. A mis *Avengers*, Raquel, Diego, Andrés, Dani, Casares, Rebe, Francesc, Edu y Andrea gracias por aceptarme siempre como una más, por vuestro saber escuchar y por hacerme sentir en familia.

Gracias a mi pequeña pero gran familia. A mis tios, a mi Tata, Pepe, Olaya y Ramón. Gracias por siempre tratar de escuchar. A lo mejores primos, Jaime, Cortes, Miriam, Irene y Alberto. por regalarme tanta desconexión y cariño. Alberto e Irene, gracias por entenderme tanto. A mis abuelos y abuelas, que siempre os llevo conmigo y os hecho tanto de menos. A mi sister, Cris, and mother in “love” por hacerme sentir siempre de la familia. A mis hermanos, Guille y Víctor, por avanzar conmigo en la vida. Y finalmente a mis padres, Manuel y María, por vuestro apoyo y amor incondicional.

Agradecer especialmente a Pablo, mi mejor amigo y compañero de vida, que me ha acompañado desde mi inicio en la química hasta la finalización de la tesis, y sigue. Gracias por toda tu comprensión, por todos los puntos de vista, por tu paz y en definitiva por todo tu apoyo infinito.

María Elena Martínez Monje

La felicidad es un abrazo inesperado

ABSTRACT

The current industrial landscape is facing significant challenges as it transitions towards decarbonization and sustainability, driven by the imperative of achieving net-zero emissions by 2050. An important contribution towards this goal is expected from connecting unconventional and renewable feedstocks, alternative to conventional fossil raw materials such as crude oil, to existing value chains of the chemical industry.

There is currently growing industrial interest in the production of short-chain nitriles such as acid cyanide and acetonitrile, while lower global demand rates are expected in the next years for acrylonitrile. Departing from conventional raw materials for nitrile production, such as C_{2-3} light olefin petrochemicals, the development of selective conversion routes from renewable C_1 building blocks, such as bio/e-*syngas* or its derivative methanol, and renewable N_1 precursors, like green ammonia, provides prospectively lower carbon footprint routes towards nitrile commodity chemicals.

The present thesis develops and studies solid catalysts able to concomitantly steer C-N and C-C coupling reactions for the production of C_{2+} aliphatic nitrile N-chemicals, precisely acetonitrile. Emphasis is placed on unveiling the nature and structure or the true working catalyst, which develops under relevant process conditions. Specifically, the thesis studies promotional effects brought about by the combination of two metals in mixed-metal interstitial compounds, alloys and intermetallic compounds.

First, complementary catalytic and theoretical Density Functional Theory studies on the conversion of mixtures of ammonia (N_1) and syngas (C_1, CO and H_2) to acetonitrile with a monometallic MoO_3 (pre)catalyst show $MoN_{1-x,}$ which develops upon near-surface nitridation, as the actual working catalyst and suggest O-assisted dissociative activation of HCN as a kinetically controlling step towards acetonitrile and higher nitriles.

Next, promotional effects by first-row divalent transition metals on molybdenum-based catalysts are studied, using a set of structurally analogous

crystalline ammonium mixed-metal molybdate compounds as catalyst precursors. Doping with Mn (Mn:Mo ~1) affords a particularly selective and stable catalyst for acetonitrile synthesis from NH_3/syngas mixtures, achieving an acetonitrile formation rate of $50 \cdot 10^{-3}$ mmol g_{cat}^{-1} min^{-1} at 723 K. A battery of bulk and near-surface sensitive methods provide evidence that a defective MnMo mixed-metal oxynitride, with a *Fm-3m* symmetry, best represents the working catalyst. The higher oxophilicity of the mixed-metal MnMo oxynitride, alongside the key role of surface oxygen for HCN dissociative activation, is suggested to underlie the Mn-Mo bimetallic synergistic effect.

Finally, the conversion of vapor mixtures of methanol (C_1) and ammonia (N_1) to N-compounds was studied on SiO_2-supported GaNi bimetallic nanocrystals. Disordered GaNi alloys (Ga/(Ga+Ni)< 20 %) show to be particularly selective towards nitrile synthesis, whereas GaNi intermetallic compounds (Ga/(Ga+Ni)> 40 %) catalyzed primarily methanol amination to methylamines. *In situ* and *operando* X-ray diffraction and X-ray absorption spectroscopy reveal that Ga is a necessary promoter in nickel-based nanocrystals, contributing to the stabilization of expanded *fcc* Ni(C, N) and Ni_3C phases at catalysis relevant temperatures (673-773 K), whose development on the catalyst surface corresponds to the onset of C_{2+} nitrile production by integration of C-N and C-C coupling reactions.

RESUMEN

El panorama industrial actual se enfrenta a desafíos significativos mientras transita hacia la descarbonización y la sostenibilidad, impulsado por el imperativo de lograr emisiones netas cero para 2050. Se espera una importante contribución hacia este objetivo al conectar materias primas no convencionales y renovables, alternativas a los materiales fósiles convencionales como el petróleo, a las cadenas de valor existentes de la industria química.

Actualmente, existe un creciente interés industrial en la producción de nitrilos de cadena corta como HCN y acetonitrilo, mientras que se espera que las tasas de demanda global disminuyan en los próximos años en el caso del acrilonitrilo. Como reemplazo para materias primas convencionales para la producción de nitrilos, como las olefinas ligeras C_{2-3} de origen fósil, el desarrollo de rutas de conversión selectivas a partir de bloques de construcción C_1 renovables, como el bio/*e-syngas* o su derivado metanol, y precursores N_1 renovables, como el amoníaco verde, proporciona rutas hacia los productos químicos nitrilos, prospectivamente con una huella de carbono más baja.

La presente tesis desarrolla y estudia catalizadores sólidos capaces de dirigir simultáneamente reacciones de acoplamiento C-N y C-C para la producción de nitrilos alifáticos C_{2+}, particularmente acetonitrilo. Se hace hincapié en desvelar la naturaleza y estructura del verdadero catalizador activo, que se desarrolla bajo las condiciones del proceso. Específicamente, la tesis estudia efectos promocionales provocados por la combinación de dos metales en compuestos intersticiales mixtos de metales, aleaciones y compuestos intermetálicos.

En primer lugar, se realizan estudios catalíticos y teóricos complementarios de Teoría del Funcional de la Densidad (DFT) sobre la conversión de mezclas de amoníaco (N_1) y gas de síntesis (C_1, CO + H_2) a acetonitrilo con un (pre)catalizador monometálico MoO_3. Estos estudios demuestran que catalizador activo real se desarrolla mediante nitridación superficial, formando MoN_{1-x} y sugieren que la activación disociativa de HCN,

asistida por oxígeno, es el paso controlante de la cinética de formación de acetonitrilo.

A continuación, se estudian efectos promocionales de metales de transición divalentes de primera fila en catalizadores basados en molibdeno, utilizando un conjunto de compuestos de molibdato mixto cristalino, estructuralmente análogos, como precursores de catalizador. El dopado con Mn (Mn:Mo ~1) proporciona un catalizador particularmente selectivo y estable para la síntesis de acetonitrilo a partir de mezclas de NH_3/gas de síntesis, logrando una tasa de formación de acetonitrilo de $50 \cdot 10^{-3}$ mmol g_{cat}^{-1} min^{-1} a 723 K. Un conjunto de métodos con sensibilidad *bulk* y superficial, proporcionan evidencias de que un oxinitruro mixto MnM, con una simetría *Fm-3m*, y rico en defectos estructurales, representa el catalizador activo. Se sugiere que la mayor oxofilia del oxinitruro mixto MnMo, junto con el papel clave del oxígeno superficial para la activación disociativa de HCN, subyacen al efecto sinérgico de ambos metales.

Finalmente, se estudió la conversión de mezclas en fase vapor de metanol (C_1) y amoníaco (N_1) a compuestos nitrogenados sobre nanocristales bimetálicos GaNi soportados en SiO_2. Las aleaciones desordenadas de GaNi (Ga/(Ga+Ni)< 20 %) son particularmente selectivas hacia la síntesis de nitrilos, mientras que los compuestos intermetálicos GaNi (Ga/(Ga+Ni)> 40 %) catalizan principalmente la aminación de metanol a metilaminas. La difracción de rayos X y espectroscopía de absorción de rayos X, *in situ* y *operando*, revelan que el galio es un promotor necesario, el cual contribuye a la estabilización de fases expandidas de *fcc* Ni(C, N) así como Ni_3C, a temperaturas relevantes para la catálisis (673-773 K), cuyo desarrollo en la superficie del catalizador corresponde al inicio de la producción de nitrilos C_{2+} mediante la integración de reacciones de acoplamiento C-N y C-C.

RESUM

El panorama industrial actual s'enfronta a desafiaments significatius mentres transita cap a la descarbonització i la sostenibilitat, impulsat per l'imperatiu d'aconseguir emissions netes zero per a 2050. S'espera una important contribució cap a este objectiu en connectar matèries primeres no convencionals i renovables, alternatives als materials fòssils convencionals com el petroli, a les cadenes de valor existents de la indústria química.

Actualment, existix un creixent interés industrial en la producció de nitrils de cadena curta com HCN i acetonitril, mentres que s'espera que les taxes de demanda global disminuïsquen en els pròxims anys en el cas del acrilonitrilo. Com a reemplaçament per a matèries primeres convencionals per a la producció de nitrils, com les olefines lleugeres C_{2-3} d'origen fòssil, el desenvolupament de rutes de conversió selectives a partir de blocs de construcció C_1 renovables, com el bio/*e-syngas* o el seu derivat metanol, i precursors N_1 renovables, com l'amoníac verd, proporciona rutes cap als productes químics nitrils, prospectivament amb una petjada de carboni més baixa.

La present tesi desenvolupa i estudia catalitzadors sòlids capaços de dirigir simultàniament reaccions d'acoblament C-N i C-C per a la producció de nitrils alifàtics C_{2+}, particularment acetonitril. Es posa l'accent a revelar la naturalesa i estructura del verdader catalitzador actiu, que es desenvolupa sota les condicions del procés. Específicament, la tesi estudia efectes promocionals provocats per la combinació de dos metalls en compostos intersticials mixtos de metalls, aliatges i compostos intermetàl·lics.

En primer lloc, es realitzen estudis catalítics i teòrics complementaris de Teoria del Funcional de la Densitat (DFT) sobre la conversió de mescles d'amoníac (N_1) i gas de síntesi (C_1, CO + H_2) a acetonitril amb un (pre)catalitzador monometálico MoO_3. Estos estudis demostren que MoN_{1-x}, que es desenvolupa mitjançant nitridació superficial, és el catalitzador actiu real i suggerixen que l'activació dissociativa de HCN, assistida per oxigen, és el pas controlante de la cinètica de formació d'acetonitril.

A continuació, s'estudien efectes promocionals de metalls de transició divalentes de primera fila en catalitzadors basats en molibdé, utilitzant un conjunt de compostos de molibdat mixt cristal·lí, estructuralment anàlegs, com a precursors de catalitzador. El dopat amb Mn (Mn:Mo ~1) proporciona un catalitzador particularment selectiu i estable per a la síntesi d'acetonitril a partir de mescles de NH_3/gas de síntesi, aconseguint una taxa de formació d'acetonitril de $50 \cdot 10^{-3}$ mmol g_{cat}^{-1} min^{-1} a 723 K. Un conjunt de mètodes *in situ* i *operant* amb sensibilitat *bulk* i superficial, proporcionen evidències que un oxinitrur mixt MnM, amb una simetria *Fm-3m*, i ric en defectes estructurals, representa el catalitzador actiu. Se suggerix que la major oxofilia del oxinitrur mixt MnMo, juntament amb el paper clau de l'oxigen superficial per a l'activació dissociativa de HCN, subjauen a este efecte sinèrgic de tots dos metalls.

Finalment, es va estudiar la conversió de mescles en fase vapor de metanol (C_1) i amoníac (N_1) a compostos nitrogenats sobre nanocristalls bimetàl·lics GaNi suportats en SiO_2. Els aliatges desordenats de GaNi (Ga/(Ga+Ni)< 20 %) són particularment selectives cap a la síntesi de nitrils, mentres que els compostos intermetàl·lics GaNi (Ga/(Ga+Ni)> 40 %) catalitzen principalment l'aminació de metanol a metilamines. La difracció de raigs X i *espectroscòpia* d'absorció de raigs X, *in situ* i *operant*, revelen que el gal·li és un promotor necessari, el qual contribuïx a l'estabilització de fases expandides de *fcc* Ni(C, N) així com Ni_3C, a temperatures rellevants per a la catàlisi (673-773 K), el desenvolupament de la qual en la superfície del catalitzador correspon a l'inici de la producció de nitrils C_{2+} mitjançant la integració de reaccions d'acoblament C-N i C-C.

INDEX

CHAPTER 1. INTRODUCTION..... 1

1.1 NITROGENATED COMPOUNDS: SYNTHESIS, APPLICATIONS, AND INDUSTRIAL SIGNIFICANCE..... 3

1.2 RENEWABLE C_1 RESOURCES..... 7

1.3 RENEWABLE N_1 RESOURCES..... 15

1.4 SYNTHESIS OF N-COMPOUNDS THROUGH CATALYTIC C-N COUPLING..... 23

1.4.1 Conversion of methane and ammonia..... 24

1.4.2 Reactions of carbon oxides (CO_2 and CO) and ammonia ... 28

1.4.2.1 Reactions of carbon dioxide and ammonia 29

1.4.2.2 Reactions of carbon monoxide and ammonia 31

1.4.3 Reactions of methanol and ammonia 38

1.5 BI- AND MULTIMETALLIC MATERIALS IN CATALYSIS.... 43

1.5.1 Solid catalysts: concept, surface and bulk interactions and *in situ/operando* development of active phases..... 43

1.5.2 Bimetallic effects in heterogeneous catalysis 48

1.5.3 Solid solutions 49

1.5.3.1 Substitutional solutions..... 49

1.5.3.2 Interstitial solid solutions 52

1.5.3.2.1 Lattice defects in solid solutions..... 54

1.5.3.2.2 Interstitial alloys in catalysis 57

1.5.4 Intermetallic compounds 60

1.6 REFERENCES 63

CHAPTER 2. OBJECTIVES 83

CHAPTER 3. METHODS 89

3.1 CATALYST SYNTHESIS 91

3.1.1 Co-precipitation method 91

3.1.2 Thermal treatment under NH_3/syngas mixture 92

3.1.3 Reduction-nitridation treatment 92

3.1.4 Impregnation method 93

3.1.5 Reduction treatment 94

3.2 CATALYST CHARACTERIZATION 94

3.2.1 Inductively coupled plasma optical-emission spectrometry (ICP-OES) 94

3.2.2 Elemental (C, N, H, S) analysis 94

3.2.3 N_2-physisorption 95

3.2.4 Temperature programmed reduction (H_2-TPR) 96

3.2.5 Raman spectroscopy 96

3.2.6 X-Ray Diffraction 96

3.2.6.1 *Ex situ* powder X-ray diffraction (XRPD) 97

3.2.6.2 *In situ* temperature-resolved X-ray powder diffraction 100

3.2.7 X-ray photoelectron spectroscopy (XPS) 102
3.2.8 Synchrotron radiation techniques 105
3.2.8.1 Total X-ray scattering analysis 105
3.2.8.2 Synchrotron-radiation X-ray photoelectron spectroscopy (SR-XPS) 106
3.2.8.3 X-ray absorption spectroscopy (XAS) 107
3.2.8.4 *In situ/operando* High-resolution X-ray powder diffraction and X-ray adsorption spectroscopy 111
3.2.9 Electron microscopy techniques 114
3.2.9.1 Scanning electron microscopy (SEM) 115
3.2.9.2 High-resolution transmission electron microscopy (HR-TEM) and high-angle annular dark-field scanning-transmission electron microscopy (HAADF-STEM) 116
3.3 COMPUTATIONAL METHODS 119
3.3.1 Mechanistic studies on NH_3/syngas conversion reaction on Mo_2N(100) 119
3.3.2 First principles thermochemistry of (Mn-doped) Mo oxynitride catalysts 120
3.4 CATALYST TESTING 123
3.4.1 Microactivity XS15 reactor 123
3.4.1.1 Reactor configuration for conversion tests with syngas and ammonia gas feeds 124

3.4.1.2 Reactor configuration for conversion tests with methanol and ammonia gas feeds 124

3.4.2 Analytics 126

3.4.2.1 Gas Chromatography 126

3.4.2.2 Calculation of catalytic performance parameters 131

3.4.2.3 Mass spectrometry 132

3.5 REFERENCES 133

CHAPTER 4. 137NITRILE SYNTHESIS BY REACTION OF NH_3/SYNGAS MIXTURES ON MOLYBDENUM NITRIDE: INSIGHTS INTO THE REACTION MECHANISM 137

4.1 INTRODUCTION 139

4.2 RESULTS AND DISCUSSION 140

4.3 THEORETICAL INSIGHTS INTO THE REACTION MECHANISM 148

4.3.1 Reactant activation 150

4.3.2 C-N coupling reactions 155

4.3.3 Acetonitrile formation 156

4.4 CONCLUSION 159

4.5 REFERENCES 160

CHAPTER 5. BIMETALLIC PROMOTIONAL EFFECTS IN MOLYBDENUM-BASED CATALYSTS FOR ACETONITRILE SYNTHESIS FROM SYNGAS AND AMMONIA 163

5.1 INTRODUCTION 165

5.2 BIMETALLIC MOLYBDENUM COMPOUNDS AS CATALYST PRECURSORS 167

5.3 SYNTHESIS OF ACETONITRILE WITH A BIMETALLIC MANGANESE-MOLYBDENUM CATALYST 170

5.4 EVOLUTION OF LONG-RANGE STRUCTURE OF THE BIMETALLIC MANGANESE-MOLYBDENUM CATALYST UNDER REACTION CONDITIONS 175

5.5 FIRST-PRINCIPLES DFT AND THERMOCHEMISTRY INSIGHTS INTO METAL AND MIXED-METAL NITRIDES 181

5.6 EVOLUTION OF SHORT-RANGE STRUCTURE OF THE BIMETALLIC MANGANESE-MOLYBDENUM CATALYST UNDER REACTION CONDITIONS 186

5.7 DEPTH-SENSITIVE NEAR-SURFACE TRACKING OF CATALYST NITRIDATION UNDER PROCESS CONDITIONS . 189

5.8 NANOSTRUCTURE AND METAL NANOSPATIAL DISTRIBUTION 192

5.9 DFT INSIGHTS INTO SURFACE CHEMISTRY AND MIXED METAL PROMOTIONAL EFFECTS 194

5.10 CONCLUSIONS 196

5.11 REFERENCES 198

CHAPTER 6. SYNTHESIS OF N-COMPOUNDS FROM NH_3/METHANOL MIXTURES ON NICKEL-GALLIUM CATALYSTS: ALLOYS VS INTERMETALLIC COMPOUNDS. 201

6.1 INTRODUCTION 203

6.2 RESULTS AND DISCUSSION 205

6.2.1 Bulk properties of Ni-Ga pre-catalyst series 205

6.2.2 Catalytic performance in the conversion of NH_3/methanol mixtures 209

6.2.3 Catalyst nanostructure and near-surface structure prior to and after catalysis 219

6.2.4 *In situ* and *operando* HRXRD and XAS studies 226

6.2.4.1 Structure of the Ni-based catalysts after in situ reduction 226

6.2.4.2 *In situ* and *operando* XRD/XAS studies on Ni/SiO_2 .. 229

6.2.4.3 *In situ* and *operando* XRD/XAS studies on $Ga_{0.05}Ni_{0.95}/SiO_2$ 233

6.2.4.3.1 *Operando* XRD studies on $Ga_{0.05}Ni_{0.95}/SiO_2$ 233

6.2.4.3.2 *In situ* XAS studies on $Ga_{0.05}Ni_{0.95}/SiO_2$ 238

6.2.4.3.3 Structural dynamics of $Ga_{0.05}Ni_{0.95}/SiO_2$ upon selected reactant removal 239

6.2.4.4 *In situ* and *operando* XRD/XAS studies on $Ga_{0.60}Ni_{0.40}/SiO_2$ 242

6.2.4.4.1 *Operando* XRD studies on $Ga_{0.60}Ni_{0.40}/SiO_2$ 242

6.2.4.4.2 *In situ* XAS studies on $Ga_{0.60}Ni_{0.40}/SiO_2$ 245

6.3 CONCLUSIONS 247

6.4 REFERENCES 249

CHAPTER 7. GENERAL CONCLUSIONS 253

APPENDICES 259

Appendix I: List of figures and tables 261

Appendix II: List of symbol and acronyms 277

Appendix III: Supporting information for Chapter 3 281

Appendix IV: Supporting information for Chapter 4 283

Appendix V: Supporting information for Chapter 5 285

Appendix VI: Supporting information for Chapter 6: First-principles DFT and thermochemistry insights into Ni metal and mixed (Ni, Ga)-metal nitride/carbides 299

Appendix VII: ASPEN-HYSYS simulation: Thermodynamic analysis 304

CHAPTER 1.

INTRODUCTION

1.1 NITROGENATED COMPOUNDS: SYNTHESIS, APPLICATIONS, AND INDUSTRIAL SIGNIFICANCE

Organic nitrogenated compounds, hereafter also referred to as N-compounds, are chemicals with a backbone composed of carbon and hydrogen, distinguished for containing at least one nitrogen atom. Synthetic N-compounds are derived from ammonia, a pivotal platform chemical obtained through one of the most crucial synthesis processes globally, the Haber-Bosch reaction. Depending on the nature of the bond between the N heteroatom and the hydrocarbonaceous molecular backbone, N-compounds are often categorized into *nitro-compounds* in the case of those containing R-N=O functional groups, *amides*, those having N-C=O bonds, *amines,* containing the simplest N-C bonds, and *nitriles,* which display the strongest C≡N triple bond. The hybridization of the nitrogen bond and the nature of the substituent (-R) influence solubility, polarity, and Lewis/Brønsted base properties.

C-N bonding is a matter of particular interest in many different scientific and technological areas. As an example, there is keen interest in N-compounds bearing C≡N nitrile bonds in studies around the origins of life, as these types of compounds are considered to have played a critical role in the prebiotic synthesis of RNA and protein precursors.[1] In chemical production, short-chain N-compounds such as hydrogen cyanide, acetonitrile, or methylamines, serve as central raw materials in a number of value chains of the current chemical industry.

Figure 1.1 shows a diagram summarizing the most relevant industrial synthetic routes for methylamines and light (C_{1-3}) nitriles.

The industrial production of the smallest and lightest amines (C_1) has been well-established for over a century. This process entails the vapor-phase reaction of methanol and ammonia in the presence of an equilibrium dehydrogenating catalyst, accompanied by the recycling of the undesired trimethylamine (TMA) side-product. Methylamines, including monomethylamine, dimethylamine, and trimethylamine, are currently produced in quantities exceeding one million

tons a^{-1}, with an anticipated annual growth rate of 3.2 % from 2020 to 2027.[2] The degree of methylation of the N atom determines the specific applications. Monomethylamine (MMA), as the simplest primary amine, serves as a key intermediate for the production of solvents and pharmaceuticals, playing a crucial role as a precursor in the agrochemical sector. Dimethylamine (DMA) holds particular significance in the global methylamines market due to its role as precursor for highly demanded solvents such as N,N-dimethylformamide (DMF) and N,N-dimethylacetamide (DMAC). DMA also finds versatile applications in the production of tensioactive compounds, water treatment, paper and rubber processing, personal care products, dyes and textiles. Meanwhile, trimethylamine (TMA) experiences lower demand compared to other methylamines. TMA serves various purposes, functioning as a basic catalyst for ammonium hydroxides, salts, choline supplements and ion-exchange resins. Additionally, it is applied in the production of dyes.[3,4]

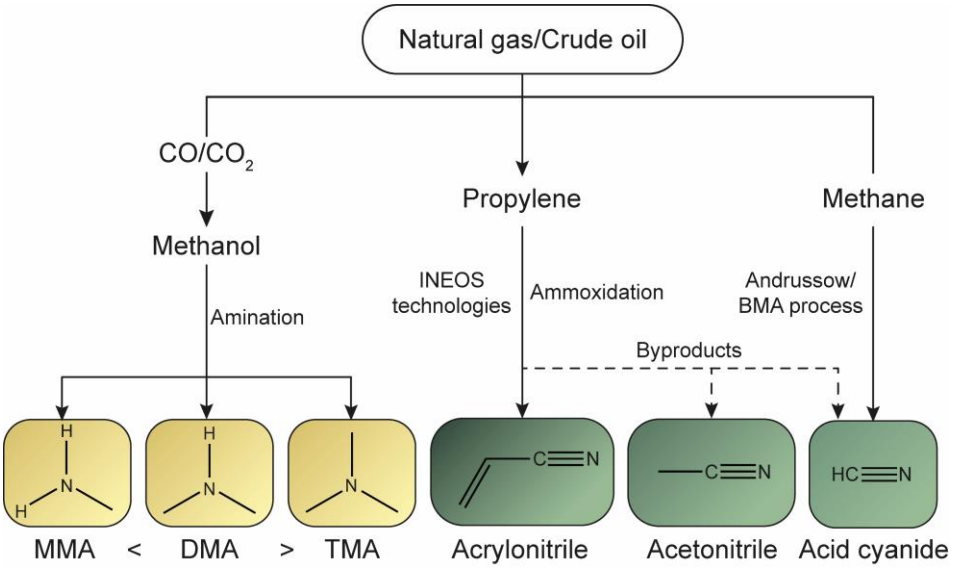

Figure 1.1. *Major industrial routes for the manufacture of methylamines (methylamine, MMA, dimethylamine, DMA, and trimethylamine, TMA) and short-chain (C_{1-3}) nitriles.*

Acid cyanide (HCN), formally the shortest (C_1) nitrile compound, is a versatile chemical that serves as a precursor for the synthesis of specialties in agriculture (insecticide and rodenticide), water treatment and personal care sectors. Many chemicals, including chelating agents, acrylonitrile, adiponitrile, cyanuric chloride, or intermediates for the production of methyl methacrylate, such as acetone cyanohydrin, are derived from acid cyanide.[5] Processes for the production of acid cyanide from C_1 sources are established at full industrial scale. In the so-called BMA process, which receives a name derived from the German terms *Blausäure* (hydrogen cyanide), *Methan* (methane), and *Ammoniak* (ammonia), also known as the Degussa process, hydrogen cyanide is produced by an endothermic reaction of methane and ammonia on a bulk platinum catalyst, typically a Pt-coated tubular reactor, at approximately 1673 K. Alternatively, in the so-called Andrussow process, which currently dominates industrial HCN manufacture, the reaction takes place under oxidative conditions, i.e., in the presence of O_2, and it is markedly exothermic. Also, unsupported Pt-catalysts, e.g. metal gauzes, are applied in this case, with extremely short reactant-catalyst contact times to minimize secondary (over)oxidation side-reactions.[6]

Acrylonitrile (prop-2-enenitrile) is another important industrial nitrile N-compound, with a global demand exceeding 6 million ton a^{-1}. The most established industrial process for acrylonitrile production is based on the ammoxidation of propylene with ammonia in the presence of oxygen, a highly exothermic reaction, see **Equation 1.1**.[5]

$$NH_3 + \mathrm{CH_3CHCH_2} + 3/2\,\mathrm{O_2} \rightarrow \mathrm{CH_2CHCN} + 3\mathrm{H_2O}; \qquad \textbf{\textit{Eq. 1.1}}$$
$$\Delta H^{\circ}_{298K} = -123\ kJ\ mol^{-1}$$

This catalytic process operates in the vapor-phase at temperatures ranging between 673-783 K and at atmospheric pressure or slightly higher (2-3 bar), typically on solid catalysts based on bismuth phosphomolybdate. This process is commonly known as the Standard Oil of Ohio (SOHIO) process, and it is nowadays incorporated into the process portfolio of the global chemical

company INEOS Technologies. This technology is also applied by Asahi Kasei in Japan or by Jiangsu Sailboat in China.[5]

With a global annual market close to 1 billion USD, acetonitrile is another relevant industrial light nitrile N-compound. Acetonitrile finds applications in electronics, construction, agriculture and automotive sectors. Moreover, it serves for pharmaceuticals manufacture, as a solvent in the production of insulin and antibiotics (Crop science), olefin extractive agent and as mobile phase in HPLC analytical applications, among others. Acetonitrile is currently obtained as a side-product of acrylonitrile production through propylene ammoxidation. Unfortunately, only approximately 0.03 kg of acetonitrile per kg of acrylonitrile are produced in this industrial process.[5,7,8]

The anticipated growth rate for global demand in acetonitrile and HCN is expected to reach an annual average of 5-6 %. Notably, the escalating demand for the latter is predominantly linked to its role as a precursor in the production of adiponitrile, a key dinitrile compound, which holds centrality in the synthesis of nylon 66 fibers and resins.[9–11]

The rising demand for HCN and acetonitrile stands in contrast to the present decline in demand for acrylonitrile, a downturn closely tied to prevailing economic conditions and the emergence of low-cost polyester fibers. These conflicting trends create a disparity in the industry's focus on these nitrogen compounds. Furthermore, propylene ammoxidation processes are heavily reliant on conventional crude oil for propylene production, a precursor that accounts for more than 70 % of the overall cost. This reliance creates a direct connection to the fluctuations in market prices, introducing an additional layer of complexity to the economic dynamics of the industry.[5] Alternative routes, substituting propylene with propane, have been proposed as a strategic measure to alleviate final production costs.[12]

The considerations mentioned above emphasize the necessity of establishing independent synthesis routes for important commodity chemicals such as acid cyanide and acetonitrile, disentangled from acrylonitrile production. Moreover, the transition from production concepts reliant on conventional fossil

feedstocks, which are attached to high carbon footprints, to new manufacture routes, based on renewable carbon and nitrogen resources, is considered highly relevant in the quest for a more sustainable chemical industry.

1.2 RENEWABLE C_1 RESOURCES

Global warming poses a formidable challenge to the ongoing industrial and technological transformations aimed at achieving zero net emissions by 2050. The complexity of this endeavor becomes apparent when considering that CO_2 emissions amounted to 36.8 Gt in 2022, representing a threefold increase over the past four decades, as depicted in **Figure 1.2. a**.[13] The sectors of heat and energy production, transportation, and large-scale chemical manufacturing stand out as the primary contributors to CO_2 emissions. These sectors exhibit a discernible upward trend in emissions, as illustrated in **Figure 1.2. b**.[13] Consequently, substantial efforts are imperative to mitigate greenhouse gas (GHG) emissions and counteract the escalating trend in global temperature. Next to CO_2, methane emerges as a second important greenhouse gas, which possesses the ability to absorb energy in the atmosphere at a rate that is ca. 28 times higher than CO_2. Consequently, methane emissions play a substantial role in global warming, contributing to 30 % of the overall temperature rise. The primary origins of methane emissions are linked to agriculture, closely followed by the energy sector encompassing coal, natural gas, biofuels, and oil industries, reaching a total of 135 Mt in 2022, as depicted in **Figure 1.2. c**.[14]

In an ideal industrial landscape, the valorization of small C_1 molecules, as a commodity for conversion into higher-value chemicals is contingent to the establishment of efficient catalytic activation and conversion processes. The essence of what is typically referred to as *C_1 catalysis* is firmly entwined with the valorization of light, monocarbonated compounds such as CH_4, carbon oxides, CO_2 and CO, and other derivatives thereof such as methanol (CH_3OH) and dimethylether (H_3COCH_3, DME), which is formally a C_1 compound too.

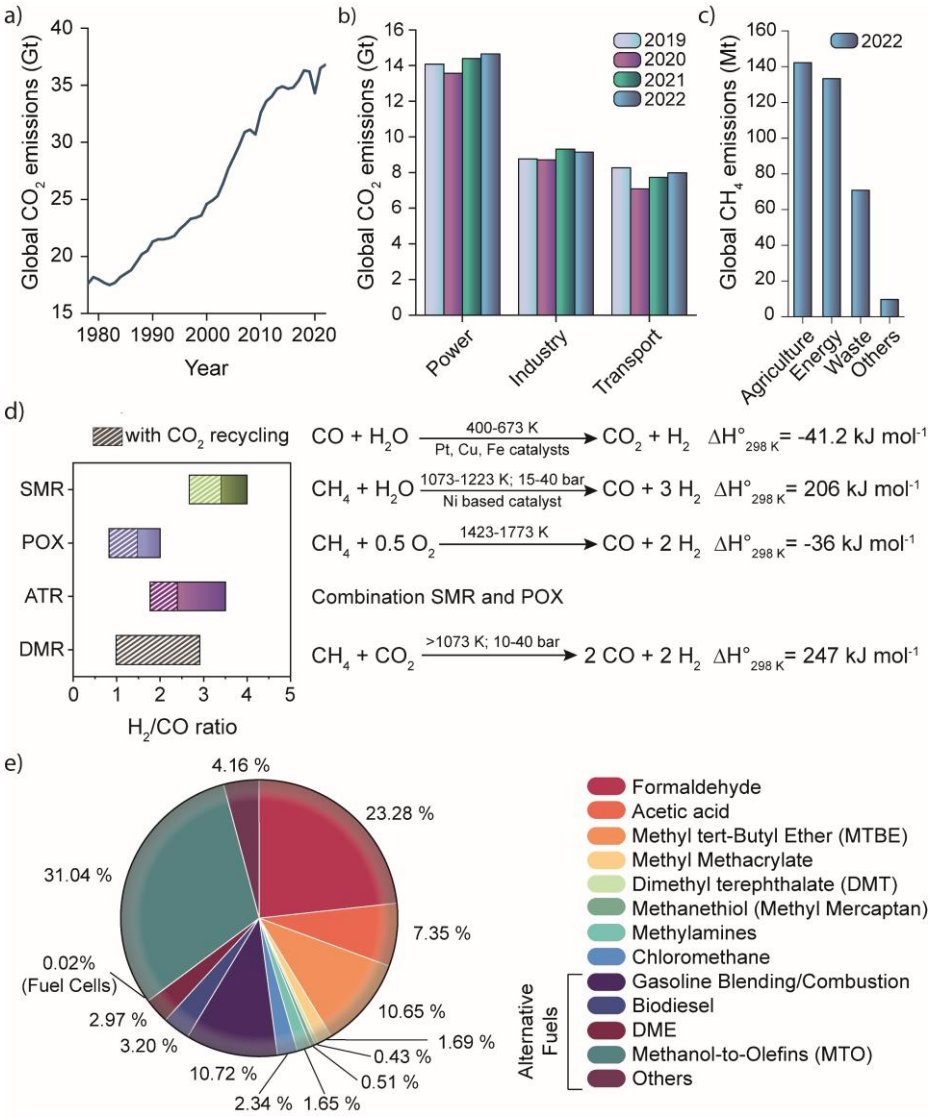

Figure 1.2: *a) Evolution of global CO_2 emissions in the period 1978-2022. b) CO_2 emissions, breakdown per sector, for recent years, adapted from the International Energy Agency (IEA) report.*[13] *c) Global methane emissions by sector, in 2022, adapted from International Energy Agency (IEA) report (2022).*[14] *d) Major reactions and typical H_2/CO ratios in the syngas product mixture for different processes for methane-to-syngas conversion, adapted from ref.*[15–17] *SMR: steam methane reforming, POX: partial methane oxidation, ATR: autothermal reforming, DMR: dry methane reforming. e) Breakdown of major methanol industrial uses (2022), adapted from ref.*[18]

This paradigm underscores the need for efficient and selective catalytic routes, capable of activating C_1 compounds and propagating the C-C chain into added-value products, to unlock the potential value inherent in these unconventional raw materials within the industry.

Synthesis gas (H_2+CO+(CO_2)), often abbreviated as *syngas*, stands out as a versatile feedstock in the context of C_1 catalysis. Its adaptability stems from its capacity to serve as a precursor for an extensive range of valuable chemicals and synthetic fuels. The global demand for syngas reached 240 million $Nm^3\ h^{-1}$ in 2023, and it is projected to experience an annual growth exceeding 6 %.

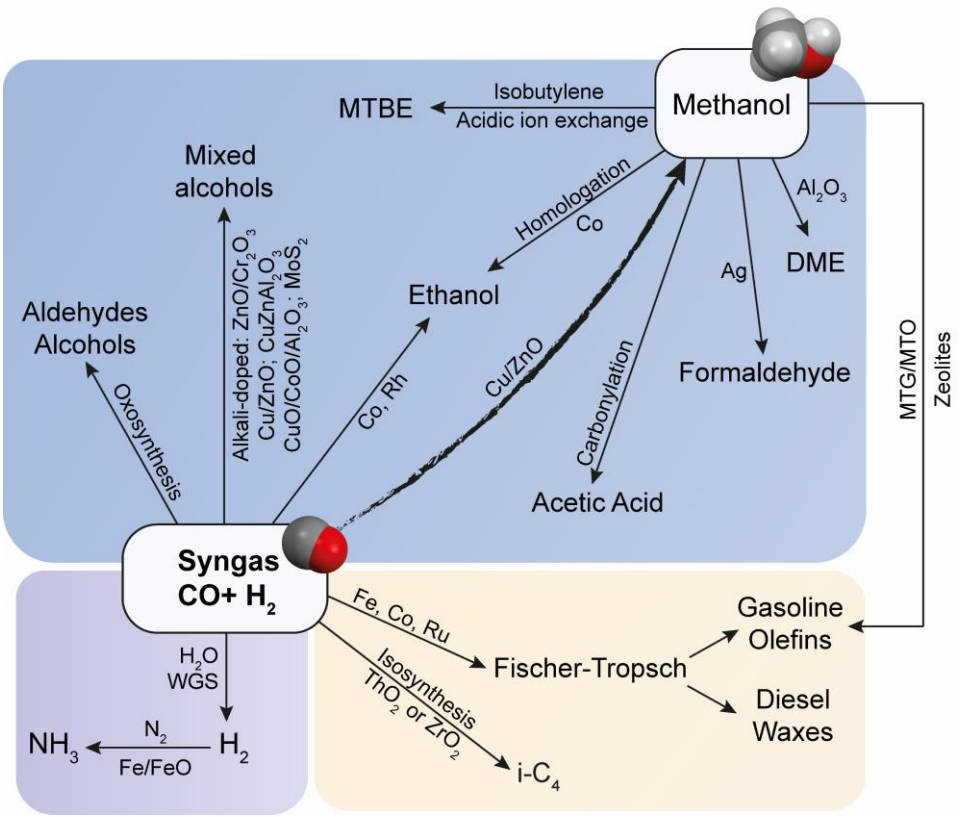

Figure 1.3: *Scheme of some syngas conversion routes into valuable ammonia, O-containing compounds and hydrocarbons/olefins chemicals. Adapted from ref.*[19]

Figure 1.3 summarizes some of the established syngas conversion routes. Syngas serves as a fundamental input for the Fischer-Tropsch synthesis, a nearly 100-year-old process, which has reached full industrial implementation for the production of condensed paraffinic hydrocarbons such as synthetic fuels (diesel, jetfuel) and waxes. Another major syngas conversion path involves the synthesis of methanol, a second C_1 building block which may be further converted into a broad array of oxygenated and hydrocarbon chemicals, such as C_{2-4} light olefins, or applied directly as liquid energy vector in fuel cells and internal combustion engines.

Most of the currently produced syngas originates from fossil resources, chiefly gas, and coal.[20] Particularly, the valorization of methane, via syngas as intermediate, is considered an attractive route to exploit extensive natural and shale gas reserves as well as an alternative to flaring activities in the case of stranded gas reservoirs. Methane is prevalent in geologic formation cavities, oil and natural gas deposits (associated natural gas), as well as the pores of sedimentary rock (shale gas). As illustrated in **Figure 1.2. d,** industrial methane conversion to syngas is implemented through two major processes: steam methane reforming (SMR) and partial oxidation (POX) with O_2 as oxidant. The integration of SMR and POX reactions is known as autothermal reforming (ATR), a process which aims at capitalizing on the respective advantages of reforming and partial oxidation reactions. Albeit not operated in full industrial scale to the best of my knowledge, the replacement of steam or O_2 for CO_2, a mild oxidant, gives rise to a fourth syngas production process known as dry reforming of methane (DRM). Each route results in syngas mixtures with different H_2/CO molar ratios, as also illustrated in **Figure 1.2. d,** and this composition determines its suitability as feed to different downstream syngas conversion processes. Across these processes, the H_2/CO ratio in the final syngas mixture may be adjusted (concentrated in hydrogen) through the water gas shift (WGS) reaction, also included in **Figure 1.2.d,** albeit at the expense of rejecting carbon in the form of CO_2.

While syngas production is currently dominated by raw materials of fossil origin, there is an ever-increasing interest in leveraging the chemical versatility and established conversion schemes of syngas to also connect alternative, lower carbon footprint, ideally renewable carbon resources to existing value chains of the chemical industry.

Renewable biogas (CH_4+CO_2) can be derived from bio-waste through anaerobic digestion (AD) using the combined action of acid-forming bacteria (acetobacter, clostridium), acetogenic bacteria and methanogenic archaea microorganisms. The exact composition of biogas depends conspicuously on the raw material used, but it generally consists of 45 to 70 % CH_4, 30-44 % CO_2, 0.1-13 % N_2 and 0.1-3 % of O_2, traces of H_2S and non-H_2S sulfur, silicon, halogenated and organic compounds.[21,22] Biogenic methane (biomethane) is the result of a selective CO_2 recovery from biogas (biogas upgrade). Biomethane's market represents barely 0.2 % of the global demand at present. However, its production in Europe grew by almost 20 % in 2022 compared to the previous years.[23,24]

Biomass gasification offers a direct route to syngas of biogenic origin, often referred to as biosyngas.[25] Several routes can be employed for biosyngas synthesis, with the most common being gasification and anaerobic digestion. In gasification, biomass feedstocks such as wood chips, agricultural residues, or organic waste are subjected to high temperatures (>973 K) in the presence of a controlled amount of O_2 (typically <20 %(v)) or steam, resulting in the partial oxidation of the biomass. Biomass gasification processes typically yield biosyngas with a variable H_2/CO ratio, influenced by factors such as the type of biomass feedstock, gasification temperature, and the amount of oxygen or steam applied in the gasifying agent. In general, gasification can produce biosyngas with H_2/CO ratios ranging from approximately 0.5 to 1.8, depending on process conditions. The latter may be further adjusted with additional process steps based on high- or and/or low-temperature WGSR.

Additionally, waste CO_2, either captured from stationary point sources or, in the future, from direct air capture (DAC), provides another environmentally friendly source for syngas. Presently, commercial practice for CO_2 capture

primarily relies on acid-base chemical reaction with organic amines in amine scrubbers.[26] Alternative technologies based on membrane separations are also gaining momentum at high pace.

CO_2 has been long established as a feedstock in the chemical industry, primarily as precursor in the synthesis of urea.[13] More than 1.3 million tonnes capacity for CO_2-based products already exist and are expected to at least quadruple by 2030. The expected increasing availability of renewable electrons (power) and hydrogen, as green reducing agents, at competitive prices, currently drives the interest in CO_2 reductive conversion to electrical or *e-syngas* in the context of Power-to-X (PtX) technologies. Harnessing CO_2 via electrified reduction to e-syngas presents an opportunity to abate greenhouse emissions while providing a feedstock for further e-syngas transformations in the emerging area of carbon capture and utilization (CCU).[27]

There are two major methods to produce e-syngas which comprise a direct synthesis or a two-step route. The direct CO_2 conversion implies the co-electrolysis of water and carbon dioxide, while the junction of water electrolysis for green H_2 production, followed by the reverse water splitting reaction (r-WGSR) offers a two-step pathway for e-syngas production, resulting in a hybrid thermo-electrochemical process.[28] The heart of these electrified processes is the electrolytic cells. The fuel cells that have gained more attention are alkaline electrolysis cells (AECs), polymer electrolyte membrane electrolysis cells (PEMECs) and solid oxide electrolysis cells (SOECs). Among them, SOECs are emerging as a potential technology for reaching net-zero emissions in the electrochemical reduction of CO and water electrolysis. SOE cells can be classified depending on the type of electrolyte used. H-SOE cells use (H^+)-conducting ceramic electrolytes while O-SOEC cells are based on (O^{2-})-conducting electrolytes.[29]

The co-electrolysis of water and CO_2 in O-SOEC cells is a promising system at which the CO_2 is reduced at the cathode and O^{2-} anions are oxidized to O_2 at the anode. Cathodes composed of Ni, Co, Fe and their exsolved alloys nanoparticles from perovskite bulk materials have shown the ability to avoid

carbon coking and agglomeration while maintaining reasonable electrocatalytic activity compared to conventional Ni-based cermets.[30–32] H-SOEC cells face similar challenges as their electrodes still are based on Ni-based cermets.[33]

In the two-step e-syngas production, the electrochemically produced H_2 is subsequently used for the thermochemical hydrogenation of CO_2 through the reverse water gas shift reaction. For the latter process, Topsoe has recently introduced the so-called eREACT™, an electrified version based on the ohmic heating of a structured reactor coated with a film of the solid RWGS catalyst.[33]

Methanol, a direct derivative of syngas, is another versatile platform compound in the context of C_1 catalysis. Methanol synthesis from syngas is an overall exothermic reaction characterized by volume reduction and constrained by equilibrium limitations to yield.[34] **Equations 1.2** to **1.4** summarized the three formal reactions that are considered at play in methanol synthesis.

$$CO_{2(g)} + 3H_{2(g)} \rightarrow CH_3OH_{(g)} + H_2O_{(g)}\,;\, \Delta H^{\circ}_{298K} = -49.5\ kJ\ mol^{-1} \qquad \textbf{Eq. 1.2}$$

$$CO_{(g)} + 2H_{2(g)} \rightarrow CH_3OH_{(g)}\,;\, \Delta H^{\circ}_{298K} = -90.6\ kJ\ mol^{-1} \qquad \textbf{Eq. 1.3}$$

$$CO_{(g)} + H_2O_{(g)} \rightleftarrows CO_{2(g)} + H_{2(g)}\,;\, \Delta H^{\circ}_{298K} = -41\ kJ\ mol^{-1} \qquad \textbf{Eq. 1.4}$$

The inception of industrial catalytic methanol synthesis from syngas is attributed to Mittasch and Pier's endeavors at BASF (Germany) in the 1920s of the last century.[35] Even though several bi- and multimetallic solid catalysts were outlined in the original patent, the optimal balance between efficiency and resistance to sulfur poisoning led to the selection of the ZnO/Cr_2O_3 system. While, its application necessitated harsh operational conditions, with pressures in the range of 250-350 bar and temperatures of 593-723 K, these operation conditions were already within reach owing to the earlier groundwork laid by Carl Bosch and the BASF team on high-pressure ammonia synthesis. Consequently, processes utilizing the ZnO/Cr_2O_3 catalyst became the established technology for over four

decades. This changed when in the 1960s, ICI (UK) introduced a new process based on a $Cu/ZnO/Al_2O_3$ catalyst, which delivered higher selectivity and yield to methanol at notably milder operation conditions (T=473-523 K, P=20-50 bar). The industrial deployment of the latter process was delayed several decades, until advances in syngas purification technologies, which reduced sulfur and chlorine concentrations in the synthesis gas feed to <100 ppb, served to attain industrially relevant lifetimes from the more poison-susceptible Cu-based catalysts. This catalyst system, still today, dominates industrial methanol synthesis practice.

Next to the industrially established methanol synthesis from syngas, the direct conversion of mixtures of CO_2 and (green) hydrogen, as stoichiometrically indicated in **Equation 1.2** above, attracts currently substantial interest as a CCU process concept. Classical methanol synthesis copper-based catalysts, and modifications thereof to withstand the higher water partial pressures pertaining to the direct conversion of CO_2/H_2 feeds, remain the most popular catalysts due to their reliable activity, stability and competitive price.[36] However, alternative catalysts, e.g., based on ZrO_2-In_2O_3 mixed oxides, have been developed *ad hoc* for methanol synthesis from CO_2 and are currently being evaluated for industrial practice.[37,38]

Methanol finds a wide range of applications in industry, primarily as a precursor for commodity chemicals, including formaldehyde, acetic acid, methyl methacrylate, methylamines synthesis and light olefins, among others, see **Figure 1.2. e**.[18] While partial oxidation to formaldehyde has traditionally represented the major use of methanol, in recent years, the methanol-to-olefins (MTO) process has been increasingly installed, particularly in Asian countries, as an on-purpose source for highly demanded ethylene and particularly propylene olefins.[39,40]

1.3 RENEWABLE N_1 RESOURCES

Nitrogen gas (N_2) stands out as a renewable resource with remarkable potential for sustainable chemical production. Unlike most other chemical feedstocks, nitrogen is abundantly available in the Earth's atmosphere, comprising approximately 78 % of the air. Its renewable nature is rooted in the continuous and virtually limitless cycling of nitrogen through the biosphere. Nitrogen-fixing bacteria play a crucial role in converting atmospheric nitrogen into biologically accessible forms, fostering a constant supply for ecosystems. Synthetic fixation of nitrogen into chemicals has been traditionally dominated by the Haber-Bosch catalytic process of ammonia (NH_3) synthesis from its elements (N_2 and H_2). This is arguably one of the most crucial catalytic processes ever devised, given its paramount role in sustaining the global population (growth) through the supply of synthetic, ammonia-derived nitrate-based fertilizers. The first patent application on the process was filed in 1908, and the profound impact of this process in the chemical industry and society is underscored by the Noble Prizes awarded to Fritz Haber in 1918 for the synthesis of ammonia from the elements and subsequently to Carl Bosch, along with Friedrich Bergius, in 1931 for their contributions to the discovery and development of chemical high-pressure processes, with ammonia synthesis serving as a prominent illustration.

The Haber-Bosh process is rooted in the direct conversion of N_2 and H_2 to NH_3 according to the reaction depicted in **Equation 1.5.** The process operates at temperatures in the range of 573-773 K which are required to activate the stable N≡N bond (bond energy of 945 kJ mol^{-1}), and high total pressures, typically exceeding 100 bar, to shift the equilibrium towards ammonia production by Le Chatelier´s principle.

$$3\,H_{2(g)} + N_{2(g)} \rightleftarrows 2\,NH_{3(g)};\ \Delta H^{\circ}_{298K} = -91.8\,kJ\,mol^{-1} \qquad \textbf{\textit{Eq. 1.5}}$$

Typically, technical unsupported (bulk-type) iron oxide catalysts are employed. The yield to ammonia is typically around 25 vol % per reactor pass.

Under *in situ* activation and reaction conditions, the iron-based catalyst undergoes reduction to α-iron from wüstite ($Fe_{1-x}O$), hematite (Fe_2O_3) or the most commonly used, magnetite (Fe_3O_4) precursors, which typically contain also small amounts of Ca, K and Al, Mg and Si and rare earth elements as promoters.[41–45] Mechanistic studies over neat Fe (100) monocrystals have shown that N_2 dissociative adsorption is the rate-determining step.[46,47] Moreover, oxygenate compounds, such as CO_2, O_2 and water, have been shown to act as strong poisons on iron-based ammonia synthesis catalysts. Hence, the stringent purity specifications for the gas feed impose high energy costs associated with gas purification.[45]

Other transition metals, traditionally ruthenium but also nickel and cobalt, supported on metal oxides or graphite-based carriers, have proven to be competitive alternatives to Fe-based catalysts, particularly aiming at milder operation conditions and greater tolerance for oxygenated poisons.[45] The latter two operational aspects are deemed to contribute significantly to mitigating the high-energy demand and thus associated carbon footprint of the process. Additionally, considerable research efforts have been dedicated, over the last two decades, to devise alternative catalyst materials. The list encompasses ruthenium clusters supported on strongly electrondonating electride materials,[48,49] to iron supported on metal hydrides[50] and oxynitrides-hydrides perovskite,[51] and nitrides,[52] which may act as solid donors of activated nitrogen. As an example, a Ce-doped Co_3Mo_3N nitride has been consistently shown to exhibit superior performance compared to a conventional iron-based catalyst at 673 K and 50 bar.[53]

At present, about 70 % of the ammonia produced is used for the manufacture of nitrogen-based fertilisers.[54] As a result, approximately 40 % of the nitrogen fixated into synthetic ammonia finds its way into our daily dietary intake. The remainder is used to satisfy the demand in various other industrial sectors, which consume ammonia as precursor in the production of polymers, fibers and explosives. Currently, we live an important and swift diversification of ammonia applications, including its role as a renewable synthetic carrier for hydrogen storage and a carbonless fuel in fuel cell and direct ICE applications, e.g., for hard-

to-abate mobility sectors like marine transport. As a result, anticipated projections indicate that by 2030, the global ammonia demand is poised to surge from the current ca. 190 to over 280 million tons a^{-1}. This technology currently accounts for a remarkable 1.3 % of the global CO_2 emissions.

Ammonia synthesis is the chemical process with the greatest demand for hydrogen, with more than twice as high demand compared to the entire oil refining sector. Depending on the overall carbon footprint associated with its production, hydrogen has been given different "color shades", as visually summarized for major hydrogen production routes in **Figure 1.4**. Conventional ammonia synthesis relies on so-called *gray hydrogen*, which is derived from steam methane reforming (SMR). Given that SMR processes are responsible for over 230 Mt a^{-1} of CO_2 globally, with an intrinsic GHG footprint of about 80 $g_{CO2,eq}\,MJ^{-1}$ (or ca. 12 $kg_{CO2,eq}\,kg_{H2}^{-1}$) hydrogen production itself is a major contributor to the overall carbon footprint associated to the chemical fixation of N_2 into NH_3. Indeed, should the expected near-future surge in ammonia global demand be satisfied by conventional ammonia synthesis processes, relying on *gray hydrogen* as feed.[55]

The above concerns about the carbon footprint of ammonia production acts as a driver for the development of greener routes to produce ammonia. One solution is through CO_2 capture, and utilization or storage (CCUS) at the point of hydrogen production by SMR, i.e., to produce *blue hydrogen*, which shows a notably lower GHG footprint of about 20 $g_{CO2,eq}\,MJ^{-1}$ (or ca. 8 $kg_{CO2,eq}\,kg_{H2}^{-1}$).[56]

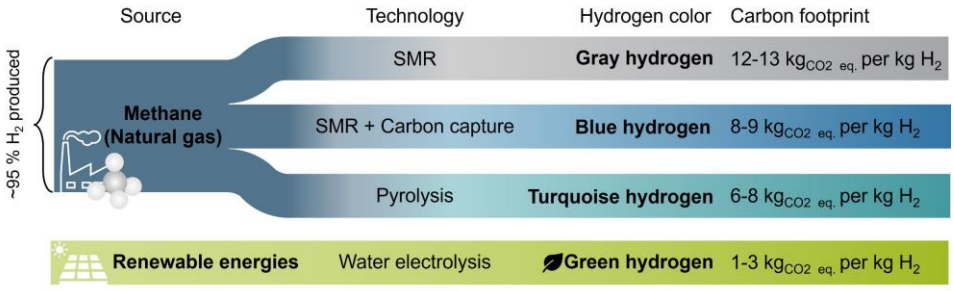

Figure 1.4: *Different color shades associated to industrial hydrogen depending on the source and carbon footprint attached to the production technologies.*[58–60]

Ongoing development efforts focus on CO_2 ab- and adsorbents that operate at moderate pressures, are easily regenerable and economically feasible.[57] However, it is important to note that CCUS alone cannot mitigate all those CO_2 emissions associated to the process.

Alternative hydrogen production technologies with lower net CO_2 emissions include biomass gasification and methane pyrolysis/cracking into its elements (**Equation 1.6**), both of which entail high operation temperatures, above 973 K.

$$CH_{4_{(g)}} \rightarrow 2H_{2_{(g)}} + C_{(s)}\,;\, \Delta H^{\circ}_{298K} = 74.6\ kJ\ mol^{-1} \qquad \textit{Eq. 1.6}$$

Biomass gasification can achieve different H_2 yields depending on the raw biomass feed composition. This technology is still immature, and factors such as biomass availability, cost reduction, and logistics development are crucial for its implementation.[61] Methane pyrolysis/cracking, in turn, leads to the production of so-called *turquoise hydrogen,* and inherently sequestrates carbon in the form of elemental carbon allotropes. Even though specific techno-economic analyses have suggested that the process may show significant economic prospects,[62] e.g., as compared to biomass gasification, specific technical challenges remain, including the need to accommodate markets of sufficient demand for the valorization of the carbon side-products, the development of methane cracking catalysts with sufficiently long operation lifetimes at temperatures significantly slower than those required for non-catalytic methane pyrolysis, or improvements in the overall energy efficiency of the process.[63,64]

Electrocatalytic water-splitting to its elements (as shown in **Equation 1.7**) emerges as an ultimate technology for hydrogen production. The LCA carbon footprint associated to hydrogen derived from water electrolysis varies significantly by electricity source, but it can reach down to <20 $g_{CO2\text{-}eq}\ MJ^{-1}$ (<3 $kg_{CO2\text{-}eq}\ kg_{H2}^{-1}$) for so-called *green hydrogen*, i.e., when exclusively renewable

power, e.g., solar energy, wind energy, or a mix thereof, is used as the sole energy input.

$$H_2O_{(l)} \rightarrow H_{2_{(g)}} + 1/2\, O_{2_{(g)}};\ \Delta H^{\circ}_{298K} = 285.8\ kJ\ mol^{-1} \qquad \textbf{Eq. 1.7}$$

Two main parameters play a crucial role in water-splitting reactions. The first is the temperature factor, which influences the thermodynamic voltage change in accordance with the decreasing trend of the Gibbs free energy change with temperature. Therefore, these technologies can be divided into low-temperature (<423 K), medium-temperature (473 K< T< 873 K) and high-temperature (<873 K). The second parameter is the electrolyte pH, as different current ion species (H^+, O^{2-}, OH^-) are responsible for the current, depending on the acid-base media of the cell.[65]

The prominent water electrolysis technologies include alkaline water electrolysis (AWE), proton exchange membrane (PEM), alkaline anion exchange membrane (AEM) water electrolysis and solid oxide electrolyzers (SOE). Alkaline water electrolysis (AWE) uses a corrosive liquid electrolyte based on KOH/NaOH aqueous solution. This technology operates at low temperatures (303-353 K) and pressures (2-10 bar) and in the presence of anode and cathodes based on Ni materials.[66] PEM electrolyzers are based on solid polysulfonated or polyfluorinated membranes that operate at high pressures (15-30 bar) and low temperatures (323-363 K) using electrodes based typically in precious metals (Pt, Ir, Ru, Pt) dispersed, at high loadings (>20 wt%), on conductive carbon carriers, that increase the cost of the technology.[67] Alkaline anion exchange membrane (AEM) electrolysis merges aspects of both AWE and PEM technologies by combining low-concentration KOH/NaOH aqueous solution with solid electrolyte membranes composed of polymers. This electrolyzer operates at pressures up to 35 bar and temperatures ranging from 323 to 340 K. The materials for the cathodes and anode are based on Nickel (foams) and Ni, Ni-Fe and $NiFe_2O_4$, respectively. Finally, SOE technologies operate at high temperatures ranging from 1073-1273 K with a solid ceramic as electrolyte, commonly based on ZrO_2 doped

with yttrium and/or scandium cations. PEM, AEM and AWE are mature and commercially available technologies, while SOE is still in an early commercial stage. At present, AWE and PEM technologies have reached the highest commercial scale, with capacities reaching the gigawatt range.

Figure 1.5 showcases different ways to integrate renewable power into chemical N_2 fixation, as a means to attain greener ammonia synthesis. Direct utilization of green H_2 via the Haber-Bosh process is expected to contribute to lowering the overall GHG footprint of ammonia production significantely.[55,67,68] Alternatively, renewable energies can be applied directly to steer the electrochemical reduction of nitrogen, to attain the direct production of ammonia under ambient conditions. In recent years, this reaction has emerged as a green alternative to the classical Haber-Bosh process.

$$N_{2(g)} + 3H_2O_{(l)} \rightarrow 2NH_{3(g)} + 3/2\, O_{2(g)}\,;\, \Delta H^{\circ}_{298K} = 471.12\ kJ\ mol^{-1} \quad \textbf{Eq. 1.8}$$

Direct ammonia electrosynthesis deploys electrochemical cells, fed with N_2 and water, respectively. **Equation 1.8** shows the overall redox reaction. Mechanistic investigations indicate that the rate-limiting step is an initial hydrogenation of N_2, an elementary reaction step which is believed to involve proton-coupled electron transfer (PCET).[69,70] Both hydrogen evolution reaction (HER) and nitrogen reduction reactions (NRR) share similar standard potentials. Therefore, a key challenge arises from the fact that the HER exhibits faster reaction kinetics than the NRR, leading to lower Faradaic efficiencies for NH_3 production.

Hence, the thoughtful selection and synergistic pairing of an aqueous electrolyte with an effective electro-catalyst are pivotal for enhancing selectivity in the NRR. The choice of electrolyte is intricately linked to the availability of protons in the aqueous medium. It has been observed that achieving higher Faradaic efficiencies is more feasible at close to neutral pH. On the one hand, neutral media

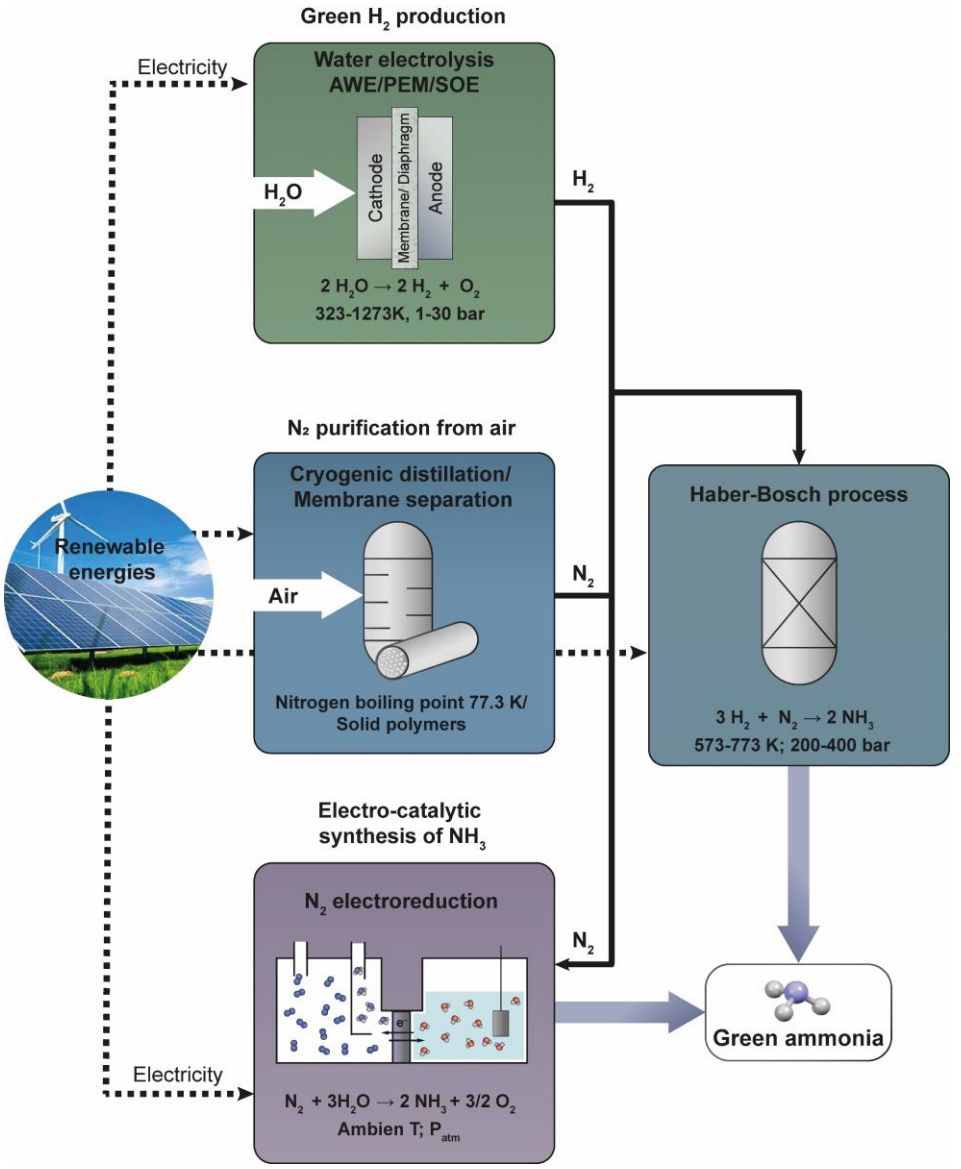

Figure. 1.5: *Illustration depicting the integration of renewable energy sources into a sustainable process for ammonia synthesis. The scheme outlines the sequential stages involving electricity application from renewables, encompassing nitrogen purification from air, nitrogen electroreduction, and the Haber-Bosch process. The hydrogen reactant for the latter is generated through water electrolysis with renewable power (green hydrogen).*

may lead to comparatively higher hydrogen coverages on the metal catalyst, hindering nitrogen adsorption and activation. On the other hand, acidic media may facilitate Proton-Coupled Electron Transfer (PCET) transitions with metals that are less inclined towards hydrogen adsorption, thus preserving nitrogen adsorption sites and consequently enhancing both the selectivity and activity of the process.

Electrocatalyst materials that have been studied cover a wide array of materials from supported precious metals, and non-noble metals,[71] to transition metal nitrides[72,73] oxides,[74] atomically dispersed “single-atom” catalysts,[75] N-doped carbon,[76,77], among other candidates. Research in this area seeks to develop active catalysts able to catalyze the NRR while inhibiting the hydrogen availability on the surface as a means to suppress, or at least inhibit the competitive HER.[78,79] The nanoscale structure of the preferred active sites, e.g., isolated metal atoms, defect sites on metal nanocrystals, e.g., at step-edges, corners, etc, remains heavily debated in the scientific literature. Even the contribution of nitrogen impurities and their electrocatalysis derivatives to the macroscopically determined NH_3 production rates remains a controversial matter.[80] Therefore, further investigations are needed to overcome the comparatively low efficiencies and pave the way towards a viable ammonia electrosynthesis technology.[78]

An additional pathway for ammonia electrosynthesis is referred to as lithium-mediated nitrogen reduction (LiNR). This technology operates effectively at ambient temperature, as lithium is the only metal capable of cleaving the triple bond in molecular N_2 under such mild conditions. Chorkendorff and coworkers developed a $LiBF_4$-based solid-electrolyte interphase (SEI) layer on a porous Cu electrode, using ethanol as a proton carrier. This system delivered a promising behavior under 20 bar N_2, with ammonia production rates of 2.5 μmol s^{-1} cm^{-2} and faradaic efficiencies of 71 %.[81]

The decarbonization of the aforementioned technologies is crucial for achieving the goal of zero carbon emissions by 2050. Given the significant global impact of ammonia synthesis, it stands as a priority sector for decarbonization efforts.

1.4 SYNTHESIS OF N-COMPOUNDS THROUGH CATALYTIC C-N COUPLING

The concomitant valorization of C_1 resources, such as carbon oxides, methane or methanol, and N_1 resources, such as ammonia, through catalytic processes involving C-N coupling reactions, represents an appealing approach towards the synthesis of N-compounds such as nitriles, amines and urea, among others. This is schematically illustrated in **Figure 1.6**. With the above-discussed prospects for a future-proof availability of renewable C_1 and N_1 raw materials, this strategy holds potential to contribute towards the sustainability of chemical production.

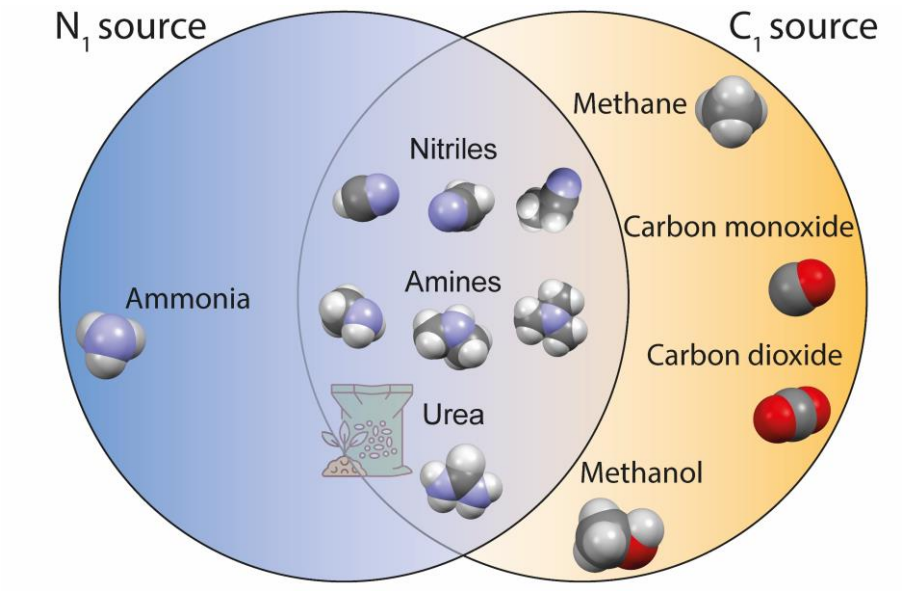

Figure 1.6: *Illustration of the integration of C_1 and N_1 sources, via catalytic C-N coupling, for the synthesis of N-compound commodity chemicals.*

In the following sections, different C-N coupling reactions from C_1 and N_1, of significance for the production of platform chemicals, are succinctly introduced.

1.4.1 Conversion of methane and ammonia

The synthesis of hydrogen cyanide (HCN) is a central process in the current chemical industry, which has been operated since the 1930s. HCN is primarily manufactured from methane as the carbon source and ammonia as the nitrogen source through two major processes, both of which require high operating temperatures to activate the stable C-H bond in CH_4.

The well-known Andrussow process was developed in 1935 by L. Andrussow, and proceeds under oxidative conditions, **Equation 1.9**. Molecular O_2 is fed as an oxidant, alongside methane and NH_3. The reaction proceeds typically at temperatures in the range of 1123-1373 K on bulk-type (unsupported) noble metal catalyst, such as Pt-Rh or Pt-Ir alloy gauzes. The process runs at very low gas-catalyst contact times in order to minimize secondary oxidation side-reactions, leading to CO_x.

$$NH_3 + CH_4 + 3/2\, O_2 \rightarrow HCN + 3H_2O;\ \Delta H^{\circ}_{298K} = -483\ kJ\ mol^{-1} \qquad \textbf{Eq. 1.9}$$

The mechanism of the reaction has been a matter of research for decades. In his seminal article, Andrussow postulated that the reaction proceeds via a hydronitroxyl (HNO^*) intermediate.[82] In the 1980s D. Hasenberg and L. D. Schmidt proposed that the HCN synthesis may occur via the coupling of NH^* and C^* adspecies on polycrystalline Rh and Pt surfaces. Besides, the catalyst was shown to undergo significant nitrogen uptake and coke buildup under working conditions. The latter was hypothesized to play a catalytic role. On the one hand, methane cleavage was posited to occur more easily on a carbon-covered metal surface than on a neat metal surface. On the other hand, carbon deposits were proposed to block sites that are otherwise active for ammonia decomposition into nitrogen.[83–85]

Studies conducted by V.A. Kondratenko et al. using pulsed transient isotopic experiments over Pt–Rh gauzes confirmed that oxygen species assist methane and ammonia activation into NH_x (x=0-2) and CH_y (y=0-3) adspecies.

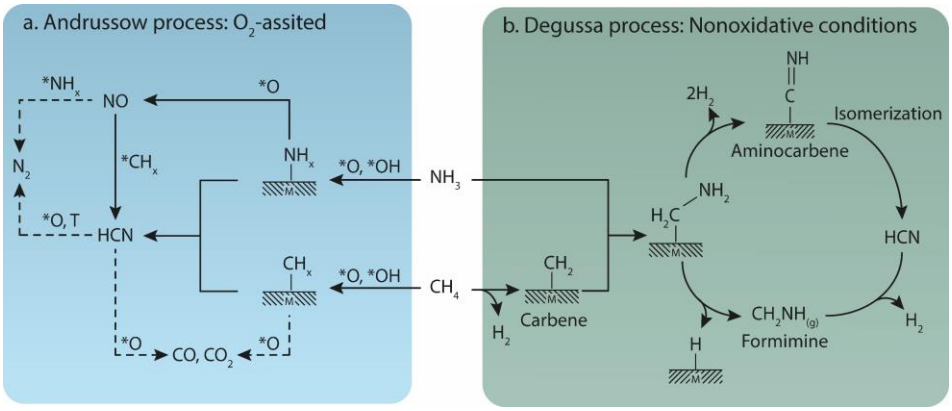

Figure 1.7: *a) Scheme for HCN formation via either direct coupling of NH_3 and CH_4 or the participation of NO as reaction intermediate, as postulated for the oxidative synthesis of HCN in the Andressow process (* marks adsorbed species). Secondary reactions that may be undesirably exacerbated be enhanced by an imbalanced availability of activated oxygen species are denoted with dashed lines (Adapted from ref.*[87]*). b) Scheme for HCN formation over metal catalyst under the non-oxidative conditions of the Degussa process, based on mechanistic proposals put forth in the scientific literature.*

It was observed that high oxygen coverage facilitates the formation of NO, which can then undergo coupling with methane derivatives to HCN, consistently with previous mechanistic proposals.[86] It was concluded that, whilst acid cyanide can form via direct coupling of ammonia and methane, the contribution of this reaction pathway in the presence of molecular oxygen is limited due to the faster formation of nitrogen monoxide by ammonia oxidation (see reaction scheme in **Figure 1.7. a**. Consequently, NO is proposed to be a key reaction intermediate that further reacts with methane. According to this mechanistic theory, selectivity to acid cyanide becomes primarily determined by the NO formation rate and the catalyst's ability to offer a balance in terms of affinity for oxygen adspecies.[87]

Alternatively, the BMA ("Blausäure aus Methan and Ammoniak") process, a method pioneered by Degussa AG, proceeds under non-oxidative conditions, hence formally, it entails an ammonia-assisted CH_4 reforming into HCN and it is markedly endothermic (**Equation 1.10**).

$$NH_3 + CH_4 \rightarrow HCN + 3H_2;\ \Delta H^{\circ}_{298K} = 251\ kJ\ mol^{-1} \qquad \textbf{Eq. 1.10}$$

In the absence of an oxidant, the BMA process necessitates even higher temperatures compared to the Andrussow process, typically in the range of 1473-1673 K. Platinum-based catalysts are also commonly deployed. While yields to HCN up to 90 % are feasible, in contrast to a maximum 60-70 % yield under oxidative conditions, the high energy demand contributes to diminishing the industrial significance of the BMA process compared to the most widely spread Andrussow route.[6]

Several studies have addressed the reaction of HCN synthesis under the nonoxidative conditions, which pertain to the Degussa process. H. Schwarz and coworkers have considered gas-phase Pt^+ cations generated under Fourier transform ion cyclotron resonance (FTICR) mass spectrometry conditions, as model active centers, and combined their experimental observation with theoretical calculations.[88] Their experiments suggested two parallel pathways implying a single metal carbide intermediate, which reacts with ammonia gas or with dehydrogenated NH_x species to form a C-N bond. The first pathway implies the formation of formimine, followed by its dehydrogenation to acid cyanide. The second path leads to a metal-bound aminocarbene, which decomposes into acid cyanide at high temperatures, as depicted in the mechanism pathways included in **Figure 1.7. b.** These mechanisms were further supported by molecular beam mass spectrometry studies performed by R. Horn et al.[89] More recently, periodic Density Functional Theory studies over a Pt(111) surface slab revealed high stabilities for H_xC (x= 0, 1) and NH_2 intermediates under nonoxidative (O_2 free) conditions. Conversely, these intermediates were destabilized in the presence of O^* or OH^* adspecies, with HC/C and N species been favored instead.[90] Additional DFT calculations for C-N coupling in the form of CH_xNH_y intermediates have been carried out on monometallic Ag, Cu, Pt, and Rh, as well as IrAg and IrAu alloy surfaces to rationalize the mechanism for HCN and methylamine formation.[91,92] It was highlighted that Pt carbenes, particularly those formed on bimetallic MPt

clusters of Pt with coinage metals (M= Cu, Ag and Au), can act as N-C coupling catalysts.

Yet a third, non-catalytic reaction, the so-called Shawiningan HCN process (1960), is known for the manufacture of HCN from ammonia and light hydrocarbons, methane in the most traditional version of the process, but preferably propane. In this case, the absence of catalyst results in ultrahigh temperatures, ranging from 1580 K to 1920 K, being required to operate the conversion at ambient pressure. For these reasons, this process is preferably employed in places where electricity has low cost and natural gas is not available.[93]

The realization that NO is likely to be a central intermediate in the classical Andrussow process, led recently the group of Takagaki et al. to investigate the direct conversion of CH_4 and NO to HCN under milder operational conditions. Studying a series of supported catalysts based on Pt dispersed on different oxide carriers, the authors identified Al_2O_3 as a particularly suitable support. Among the different Al_2O_3 allotropes investigated, the lack of surface acid sites in α-Al_2O_3 was concluded to be particularly desirable to prevent secondary hydrolysis side-reactions of HCN to ammonia.[94] In another study with Pt/γ-Al_2O_3, measurable HCN production rates were achieved even at 573 K, indicating that C–H bond cleavage, NO dissociation, and simultaneous C–N coupling occurred at this remarkably milder reaction temperature. The HCN yield reached 3.2 %, with a selectivity of 49 %, at 698 K, a performance which notably surpassed the yield obtained from the reaction when NH_3 was fed as the N_1 reactant. In a follow up study by the same group, Pt particle size effects were assessed. Platinum nanoparticles larger than 4 nm were found to be more efficient than smaller nanoparticles, proposedly as a result to the latter becoming surface poisoned by a higher coverage of $^*CN$ adsorbates under operation conditions.[95,96] Cold plasma reactant pre-activation has also been explored to lower the temperature at which the reaction proceeds, nonoxidatively, on the surface of metal catalysts. The combination of plasma conditions with Cu/silicalite-1 or Pt-supported on Ti silicalite-1 zeolite reached HCN formation at temperatures around 673 K.[97,98] A combinatorial catalyst

discovery study revealed the superior performance of Pt supported on Si_3N_4 or SiC carriers, and additionally incorporating Ir, Re or Au as promoters.[99]

As delineated above, numerous studies have concentrated on the synthesis of hydrogen cyanide from methane and ammonia, both in industrial settings and academic research. Despite the significant attention, the formidable temperatures necessary for these reactions pose a persistent challenge. The high temperatures required make the process energy-intensive, calling for the development of new catalysts and conversion concepts, e.g. plasma assistance, to realize HCN synthesis under milder conditions.

1.4.2 Reactions of carbon oxides (CO_2 and CO) and ammonia

Nowadays, the conversion of carbon oxides into synthetic fuels and high added-value commodities represents a well-established and continuously evolving field, actively pursued by both industrial and academic sectors.

A prominent example is the direct conversion of synthesis gas ($CO+H_2+(CO_2)$) into synthetic paraffinic fuels through the Fischer-Tropsch (FT) reaction, a landmark reaction, which is about to celebrate its 100-anniversary next year. Alongside the Fischer-Tropsch reaction, another syngas conversion process, which has reached full industrial scale since the earlier 1920s, is the methanol synthesis, and more recently its modified version for the direct synthesis of DME by tandem integration of methanol synthesis and dehydration reactions. The latter processes are currently gaining significant momentum, steered by the consideration of both methanol and DME as promising renewable energy carriers.

Beyond direct hydrogenation, the concomitant conversion of C_1 alternative carbon sources with ammonia, as a N_1 source, provides an alternative strategy to connect these alternative, potentially renewable raw materials with value chains of the current chemical industry. The following subsections summarize the state of the art for different transformations, which involve the reaction of CO_x carbon oxides with ammonia.

1.4.2.1 Reactions of carbon dioxide and ammonia

Coupling CO_2 valorization with nitrogen management represents a promising strategy towards a sustainable cycle. This approach was proposed for consideration within the European Innovation Council in 2022.[100] At present, industrial carbon dioxide is typically valorized to urea, the most common precursor for fertilizers globally. As a matter of fact, the synthesis of urea consumes approximately 50 % of the ammonia produced in the Haber-Bosh process.[54,101] Urea production is intricately linked to industrial ammonia plants and occurs at moderate temperatures (440-493 K) and elevated pressures (120-250 bar). In this process, carbon dioxide undergoes conversion with ammonia to form ammonium carbamate, subsequently undergoing further transformation into urea, **equation 1.11**.[102–105] The latter step is considered to be rate-determining for the overall transformation, and it requires the participation of a Lewis acid/base catalyst to overcome those kinetic barriers associated to the cleavage of a C-O bond and the formation of a C-N bond.

$$2NH_3 + CO_2 \leftrightarrows NH_2\mathrm{COO}NH_4 \leftrightarrows (NH_2)_2CO + H_2O\,; \qquad \Delta H^{\circ}_{298K} = 8.2\ kJ\ mol^{-1} \qquad \textit{Eq. 1.11}$$

Methylamines may also be synthesized by the reaction of carbon dioxide, and ammonia in the presence of hydrogen and metal catalysts. In the late 1990s, Gredig and coworkers[106–108] studied methylamine synthesis on different supported metal catalysts, covering metals Cu, Pd, Fe, Co, Ni, Pt, or Ag. Conversion tests were performed in a packed-bed reactor at temperatures ranging from 473 to 573 K and a total pressure of 6 bar. Among the tested catalysts, supported Ag catalyst exhibited a unique behavior, offering no activity towards amines. Instead, byproducts such as CO and HCN were detected, hinting at the potential of this metal for nitrile production. Interestingly, high-metal-loading Cu catalysts emerged as the most active materials for the synthesis of methylamines, albeit with the generation of HCN as a side-product.[109] Catalysts based on Co and Fe exhibited a catalytic performance, which was conspicuously dependent on the metal

loading, and prospectively on the degree of metal reduction, ranging from essentially no activity towards methylamine formation to selectivities >98 % to monomethylamine (MMA). Moreover, the investigation of diverse catalyst supports, such as SiO_2, ZnO, MgO, Cr_2O_3, ZrO_2, and Al_2O_3, highlighted that the latter three oxides, i.e., those exhibiting the higher surface Lewis acidity, showed the highest activity for methylamine synthesis, underscoring the likelihood of the participation of Lewis acid sites in the reaction mechanism. Compared to process conditions for the direct hydrogenation of CO_2, the addition of ammonia as an additional reactant had a marked inhibition effect on methanol synthesis rates, leading to methylamine production rates, which surpassed those for methanol formation. These observations suggested that the reaction may proceed via methanol, or derivatives thereof, as intermediates.

Following these earlier studies, there was a noticeable absence of significant investigations into heterogeneous gas-phase synthesis of methylamines involving the reaction of CO_2 and ammonia until 2017. K. Shimizu and coworkers reported the use of a solid Pt catalyst for the selective synthesis of trimethylamine (TMA), reigniting the interest in this reaction.[110] Unfortunately, this technology is not widely implemented in the industry, despite its potential application for the synthesis of methylamines, an important chemical commodity, and CO_2 recycling. Possible reasons could stem from the establishment of competing routes, such as methanol synthesis followed by alcohol amination, or technical challenges related to issues like solid ammonium carbonate or urea precipitation under process conditions.

In more recent years, electrochemical routes have also been explored for the formation of C-N bonds using nitrogen (N_2), ammonia (NH_3), or nitric oxide/nitrates coupled with carbon oxide electroreduction. Among the array of N-compounds observed as products of these direct electrosynthesis routes are urea, methylamines, and acetamide. This emerging field holds significant potential, as it is aligned with the contemporary landscape of process electrification.[111–117] However, such electrocatalytic reduction approach is still in its infancy and future

improvements in efficiency as well in product recovery would be required to progress towards a technical implementation.

1.4.2.2 Reactions of carbon monoxide and ammonia

The interest in the catalytic co-conversion of CO and NH_3 into N-compounds dates to the 1920s. **Figure 1.8**. provides a chronological overview of the evolution of this field, which has showcased the synthesis of different amine, amide, and nitrile compounds.

In 1950, the synthesis of a wide array of primary C_1-C_{12} aliphatic amines was realized through the modification of the Fischer-Tropsch (FT) process by co-feeding ammonia.[118] Conventional FT catalysts such as bulk-type iron (carbides) and promoted supported cobalt catalysts were tested, alongside Ni-based catalysts too. The resulting distribution of aliphatic amine products followed the (Anderson-) Schulz-Flory statistical distribution, which is reminiscent for the surface polymerization mechanism of the FT synthesis. Moreover, ammonium carbonate and urea were already noted as a side-products, which requires particular consideration due to its solid nature and decomposition temperature (309 K and 463 K, respectively, at atmospheric pressure).[119] Two decades later, G. Herici-Olivé and S. Olive proposed a mechanism for amine formation based on the direct amination of the alkyl-metal bond at surface-bound growing hydrocarbon chains, a step which could compete with further chain propagation by CO insertion, see **Figure 1.9. a**.[120]

In the early 1970s, a patent was issued for the synthesis of methylamine and dimethylamine from mixtures of syngas and nitrogen, instead of ammonia as the N-source compound.[121] The process required temperatures ranging from 573-673 K and high pressures, from 50 to 600 bar. This document identified catalysts based on hafnium and zirconium alloyed with Cu, Ag, Au, Ni, Co or group VIII noble metal, which are further converted into a hydride, nitride or carbide form under reaction conditions.

Nitrile synthesis has also been a matter of research. The direct conversion of CO and NH_3 to HCN, formally the simplest nitrile, is known since the 1920s. A

series of patents by Bredig et al. disclosed such a process, operating at high temperatures of 673-1073 K, and on different catalysts such as group IVA and IVB carbide compounds, early transition metal oxides, and rare earth oxides.[122–124] Other intellectual property documents disclosed to the use of alkaline charcoal[125] or carbide compounds of iron, either in neat form or combined with molybdenum and tungsten.[126] Even the suitability of molecular N_2 as a direct N-source was documented when co-feeding O_2 and in the presence of uranium carbide catalysts.[127] Research in this area ramped down with the establishment of alternative processes for HCN synthesis from CH_4 and ammonia, as described in **section 1.4.1** (*vide supra*).

In the later 1970s and 1980s, several patent applications were filed for the synthesis of nitrile chemicals from CO and NH_3 feeds. The Standard Oil company, responsible for the global SOHIO process for the synthesis of acrylonitrile, also introduced a process in 1982 for the production of acid cyanide from mixtures of CO and ammonia using carbon-supported Fe, Ni, Co or Ru transition metals. The inventors claimed that the new carbon-supported catalysts improved the reaction yield and catalyst lifetime compared to earlier processes developed in the 1920s, by unlocking lower operation temperatures, typically 723 K.[128] One year later, Monsanto protected an alternative process applying alumina silicate or zeolite catalysts, e.g. ZSM-5, with Brønsted acid properties.[129] These metal-free catalysts require more severe reaction temperatures from 823 to 1023 K, and pressures ranging from 14 to 42 bar. Nevertheless, HCN selectivities greater than 85 % could be attained, preferably under reaction conditions featuring an excess of NH_3 in the feed stream and high gas space velocities (GHVS=5000-9000 h^{-1}) to maintain CO conversion at moderate values (7-13 %), while preventing excessive CO_2 formation.[130]

Coinciding with the above developments in HCN production, Monsanto reported, for the first time, a route for synthesizing C_{2+} nitriles, thereby entailing not only C-N but additionally C-C coupling reaction, from mixtures of syngas and NH_3. G. Olivé and S. Olivé showcased acetonitrile production at temperatures ranging from 623 to 823 K and pressures up to 200 bar. The most effective metals

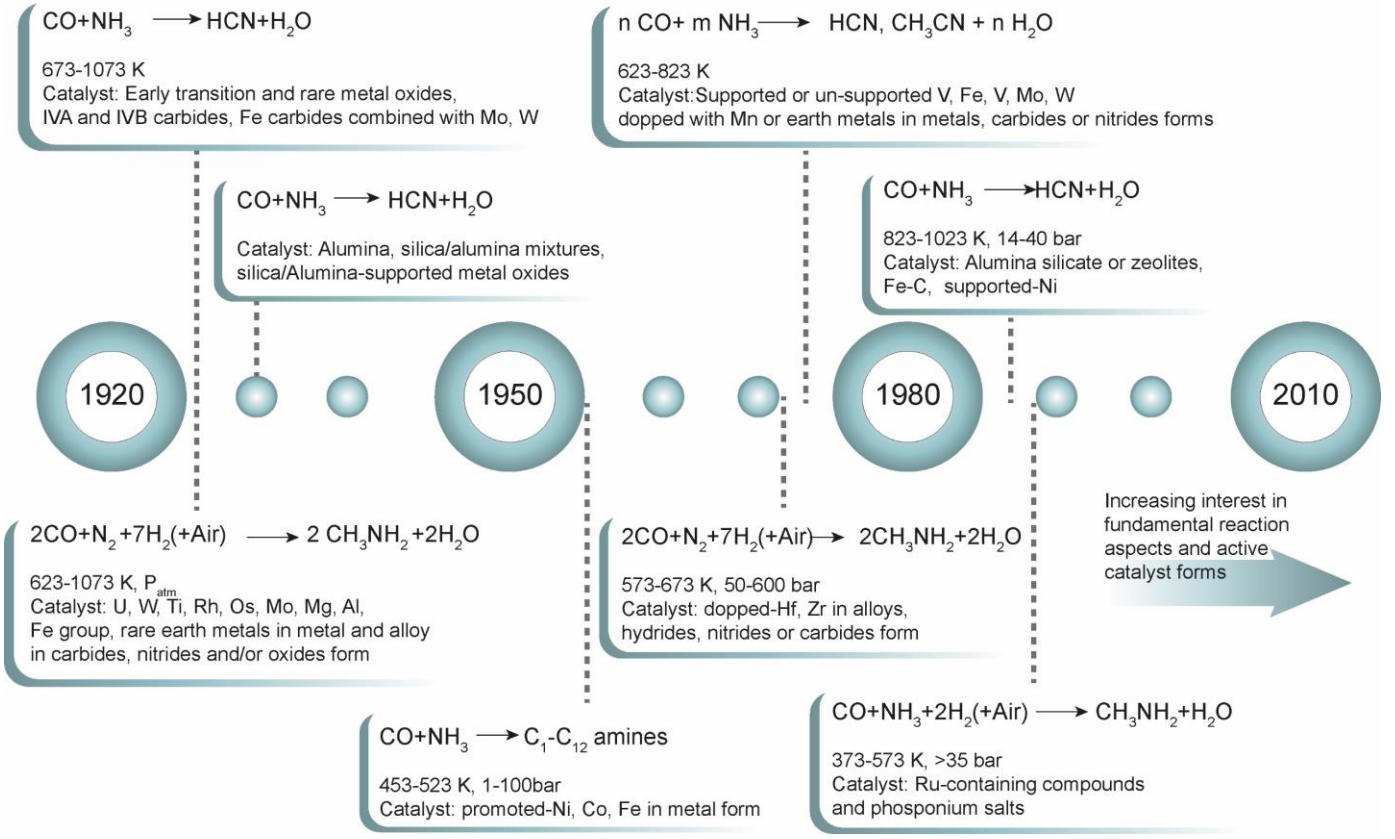

Figure 1.8: *Timeline and selected milestones for investigations on catalytic reactions between carbon monoxide and ammonia from 1920 to date, showcasing the varying product distributions —amines, amides, and nitriles—reported as a function of the catalyst and reaction conditions applied.*

were shown to be V, Fe, Mo and W, whether in unsupported form or dispersed on oxide carriers. Already in these early reports, the partial conversion of the active metal to interstitial metal compounds, i.e., metal carbides or nitrides, was indicated under process conditions atmospheres.[131]

Follow-up patent applications and scientific articles reported beneficial effects on nitrile selectivity brought about by the deliberate addition of CO_2 to the reactant mixtures (CO_2:CO molar ratios in the range of 1:5). The increase in the carbon dioxide partial pressure was suggested to shift the thermodynamic equilibrium composition for the (reverse) WGSR towards the formation of carbon monoxide, following the Le Chatelier´s principle.[132] Additionally, the incorporation of promoters, such as Mg, Sr and/or Mn, onto the formulation of SiO_2 and Al_2O_3-supported molybdenum-based catalysts, was shown to result in an increase of the acetonitrile selectivity, albeit at the expense of lower CO conversion rates.[133]

While this series of patents set the earliest evidence for the direct conversion of CO_x into C_{2+} nitrile N-compounds, a limited degree of understanding of the structure of the actual working catalysts was attained at that time, primarily due to the limited availability of physicochemical diagnostic methods which could be applied *operando*, i.e., while the catalyst is exposed to relevant reaction conditions.

Later, in the 1980s, the synthesis of N-compounds was extended to amides. In this case, mixtures of syngas and N-sourcing compounds such as NH_3 o NO_x were applied as feedstocks. The process involved the application of a Rh-Mn bimetallic catalyst at temperatures ranging from 523 to 623 K and pressures of approximately 20 to 350 bar.[134]

In the 1990s, several scientific studies focused on addressing fundamental aspects relative to the catalytically active species and reaction mechanism behind the integration of C-C coupling and C-N coupling functions to convert C_1 and N_1 reactants into C_{2+} N-compounds, such as nitriles. Based on work with silica-supported molybdenum catalysts, T. Tatsumi et al. suggested HCN as an intermediate for acetonitrile production.[135] M. Lane and coworkers studied a similar silica-supported molybdenum catalyst in the direct conversion of

syngas and NH_3 to nitriles, observing deviations with respect to the theoretical Schulz-Flory carbon chain-length distribution compared to earlier studies.[136] This led these authors to postulate a reaction mechanism mediated by CO insertion into the M-N bond in surface -NH_2. Along the proposed mechanism, subsequent reaction steps involved either the formation of acid cyanide by hydrogenative desorption or the formation of acetonitrile via coupling of CN adspecies with surface alkyl groups (-CH_x). The latter were considered to form by CO insertion into a metal hydride, on the catalyst surface, followed by OH elimination and the consecutive hydrogenation into -CH_x species, see **Figure 1.9. b**. Independent infrared studies, conducted by Collin H. Rochester and coworkers, identified FTIR bands for NH_x and isocyanate (NCO) adsorbates, which could act as reaction intermediates.[137]

W.N. Delgass and coworkers proposed, using Mössbauer spectroscopy, iron carbide, and most particularly the superparamagnetic ε´-carbide phase, as the active state of iron-based catalysts under process conditions for the synthesis of acetonitrile. They asserted that an optimal catalyst performance was attained when small catalyst particle sizes could be stabilized while avoiding excessive iron reduction beyond Fe^{2+}. The latter effects were jointly considered to minimize the contribution from alternative θ- and χ-iron carbide phases. Besides, specific activation pre-treatments of the iron catalyst with ammonia, to form iron nitride as an intermediate catalyst precursor, resulted in higher initial catalyst activity. However, deactivation was also accelerated, and it proceeded more severely over just a few minutes, reportedly by catalyst particle growth during the development of the iron carbide phase under the reactive syngas/NH_3 atmosphere. Nonetheless, these transient observations provided evidence that iron nitride could also act as a catalytically active species.[138–141]

In the past decade, research has primarily concentrated on modifying the product pattern of the Fisher-Tropsch synthesis by introducing moderate percentages of ammonia, as an additional N-sourcing co-reactant, to the syngas feed stream, at temperatures akin to those employed in the unmodified FT reaction. T. Sango et al.[143] explored this modification using a stirred slurry reactor

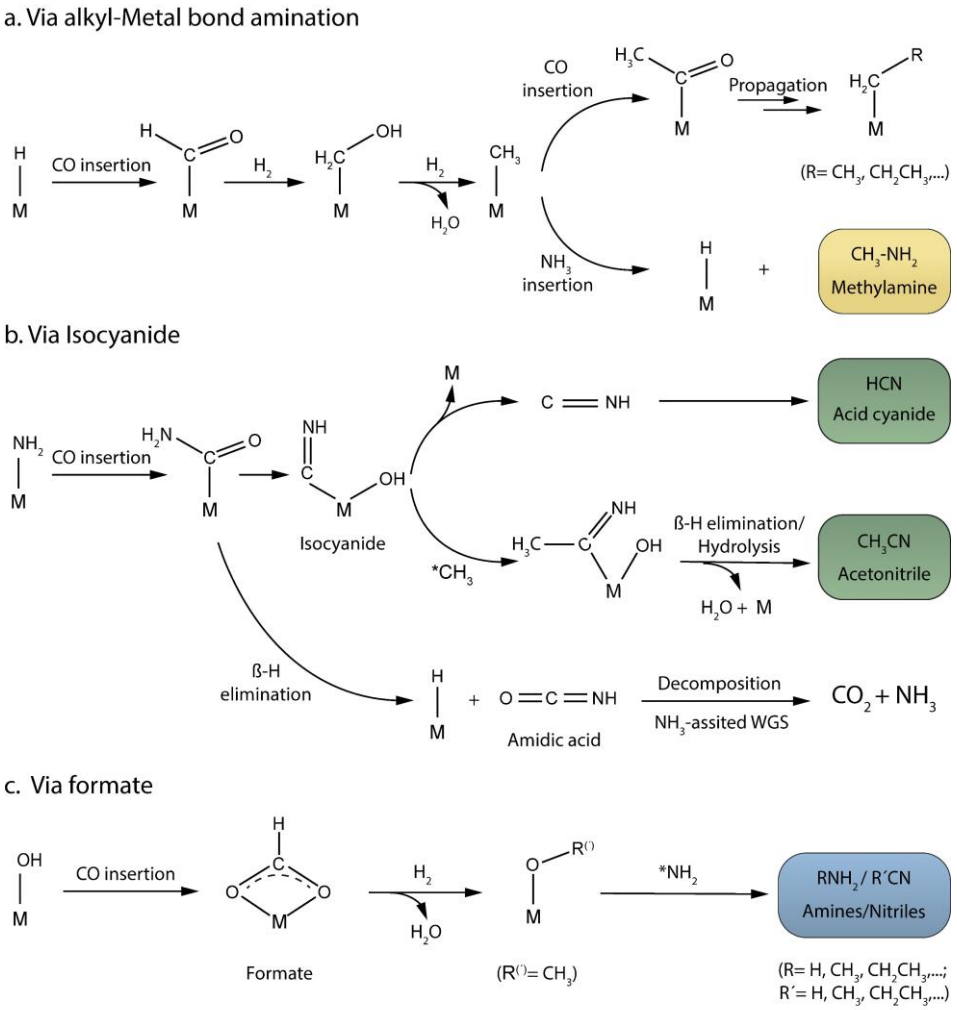

Figure 1.9: *Summary of different mechanistic proposals put forth in the earlier scientific literature for the synthesis of N-compounds from mixtures containing carbon monoxide and ammonia. a) Via alkyl-metal bond amination to produce amines (adapted from ref.*[120]*). b) Via an isocyanide intermediate for the synthesis of acid cyanide and acetonitrile (adapted from ref.*[136]*). c) Via a formate intermediate for the synthesis of amines and nitriles (Adapted from ref.*[142]*). Species marked with * are meant to be adsorbed on the catalyst's surface.*

at 523 K and 5 bar, and an unsupported iron FT catalyst promoted with potassium. Their findings revealed the suppression of alcohols, aldehydes, and carboxylic acid oxygenate products, which are otherwise observed in the absence of NH_3. Instead, they reported the emergence of mid-chain amine, nitrile, and amide N-products, in order to decrease selectivity. Additionally, a solid side-product was identified as ammonium bicarbonate. A subsequent study by the same group investigated the performance of a supported FeRh alloy catalyst in a gas-solid conversion process using a packed-bed reactor.[144] In line with the earlier study with an iron carbide FT catalyst, the secondary conversion of alcohols was suggested to be responsible for the N-compounds formation (mainly acetonitrile with a selectivity of 37.7 %).[143,144] Comparatively similar conclusions were drawn in studies performed by H. Karroum et al. using $X_{0.1}Co_4Mn_1$ bimetallic catalysts promoted with alkaline metals (X=Li, Na, K, Cs) at high pressures between 10-17 bar and temperatures of 533 K.[142] Through in-situ diffuse reflection infrared Fourier transform spectroscopy (DRIFTS) under $H_2/CO/NH_3$ and FT (H_2/CO) reaction conditions, these authors proposed a reaction mechanism proceeding via formate species, as schematically depicted in **Figure 1.9. c**. This mechanism involves the CO insertion into an adsorbed hydroxyl, which is further transformed into an alkoxy group by dehydration. This adsorbed alkoxy group is proposed to react with NH_x adspecies to form amines, as well as nitriles. Additionally, they also suggested that inhibition of oxygenates formed in FT conditions could occur via the formation of NH_x adsorbed species when ammonia is fed into the reactor blocking the active sites.

All considered, the concomitant conversion of CO and NH_3 into a wide range of N-compounds is already known for about a century, which simultaneously underscores the versatility as well as the complexity of the reaction networks and their underlying mechanisms. Despite compelling experimental examples with various types of catalysts, further studies are imperative to delve deeper into the actual form of the functioning catalysts as well as the fundamental reasons behind the commonly observed positive effects of catalyst's bi- and multimetallicity on performance.

1.4.3 Reactions of methanol and ammonia

Methanol serves as another versatile C_1 building block, which can participate in reactions with NH_3 to achieve the formation of C-N bonds. As detailed in **section 1.2** above, methanol can be efficiently produced from CO_x and hydrogen with high yield and selectivity through methanol synthesis processes that have been long established at full industrial scale.

The simplest C-N bond-forming process from methanol and ammonia entails the transformation of the former into methylamines (MMA, DMA, TMA). With a global production capacity exceeding 800 ktonnes a^{-1}, methylamines are central platforms in various industries. Dimethylamine (DMA), the most highly sought-after industrial methylamine, acts as a key intermediary in solvents (dimethylformamide, dimethylacetamide), agricultural chemicals, water treatment compounds (acrylates, Mannich polymers, etc.) and surfactants such as fatty amine oxides. Monomethylamine (MMA) is valuable for solvent production (N-methylpyrrolidone), the synthesis of carbamate insecticides (via methylisocyanate), and surfactants. Meanwhile, trimethylamine (TMA) finds a narrower niche of applications in animal feed supplements (choline chloride), and ion exchange resins, among others.[3] Historically, the production of methylamines relied on the vapor-phase amination of methanol with ammonia using several variations of the so-called Leonard process,[145] which typically deploys amorphous silica-alumina catalysts at temperatures around 653 K in adiabatic packed-bed reactors. However, thermodynamic equilibrium for the set of stepwise amination reactions included in **Equations 1.12** to **1.14**, dictates a methylamine product distribution with 17MMA/ 21DMA/ 62TMA molar ratio under representative reaction conditions (673 K and NH_3/CH_3OH molar ratio ~1 in the feed stream).[146]

$$CH_3OH_{(g)} + NH_{3(g)} \leftrightarrows CH_3NH_{2(g)} + H_2O_{(g)}; \qquad \textbf{Eq. 1.12}$$
$$\Delta H^{\circ}_{298K} = -16.6\ kJ\ mol^{-1}$$

$$CH_3NH_{2(g)} + CH_3OH_{(g)} \leftrightarrows (CH_3)_2NH_{(g)} + H_2O_{(g)}; \quad \Delta H^{\circ}_{298K} = -37.2 kJ\ mol^{-1}$$ **Eq. 1.13**

$$(CH_3)_2NH_{(g)} + CH_3OH_{(g)} \leftrightarrows (CH_3)_3N_{(g)} + H_2O_{(g)}; \quad \Delta H^{\circ}_{298K} = -50.1\ kJ\ mol^{-1}$$ **Eq. 1.14**

This is obviously suboptimal in view of the different demands from the different methylamine products and served as a driver for the development of modern methanol amination processes, which aimed at improving the selectivity, particularly to DMA. One such process is the one introduced by Nitto Chemical (Japan), later part of now Mitsubishi Rayon (Japan), that can produce a non-equilibrium product mix having a high dimethylamine content.[147] This process operates typically at reaction temperatures and pressures ranging between 623-773 K and 15-30 bar and in the presence of a solid acid catalyst. The process relies on the known shape-selectivity exerted by the molecular-size channels and cavities of acidic zeolites to steer selectivity to DMA. Zeolites with MOR, CHA, or LTA topologies have been recursively reported in different academic and patent documents to be suitable and, therefore, are most likely part of commercial catalyst formulations.[148–151] Next to confinement within their microporous topology, aluminosilicate zeolites show significant acidity. This acidity may be associated to framework sites, which in the case of aluminosilicate forms correspond to the occurrence of isomorphic lattice substitution of tetrahedral Si^{4+} in the silicate structure by trivalent Al^{3+}. This lattice substitution introduces a negative charge in the lattice which must be compensated by cations at nearby ion exchangeable position. In the H-form of zeolites, these cations are H^{+}, leading to Brønsted acid sites.[152] Additionally, aluminosilicate zeolites may exhibit Lewis acidity, typically associated to extra-framework Al species. Both types of acidity show variable degrees of tunability, in terms of acid site density as well as strength.[153] Particularly in the case of the Nitto process for methanol amination, it has been observed that a moderate acid strength is essential to enhance selectivity to primary and secondary methylamines, and various ion exchange procedures, e.g.

with lanthanides or alkaline ions, have been proposed therefor.[146,154] Moreover, to exacerbate micropore confinement effects and minimize contributions from unconfined acid centers on the outer surface of the zeolite crystals, surface passivation treatments[146] have been disclosed which enhance the selectivity to DMA. Proprietary process configurations reaching selectivities to DMA up to 86 % have been reported.

The reaction mechanism behind the macroscopically observed shape selectivity offered by zeolites in methanol amination has been the matter of various studies. Within the framework of the markedly acidic zeolite, ammonia with a prominent Lewis base character, binds stronger to acid sites. Therefore, some mechanistic proposals posited, particularly in wide-pore zeolites like MOR, the reaction of free methanol with adsorbed ammonia, i.e., through a mechanism of the Eley-Rideal type. Conversely, Langmuir-Hinshelwood type mechanisms, which consider the reaction of adspecies derived from methanol and ammonia, activated adsorption, have been proposed when the reaction proceeds in the more confined spaced of small-pore zeolites, prototypically CHA. In the latter case, steric restrictions to develop bulky reaction transition states, i.e., the so-called “transition state selectivity” have been argued to drive shape selectivity, preventing the formation of TMA.[155]. In addition to the considerations above, which do not necessarily entail assumptions as to the surface coverage on the zeolite catalysts, Lercher, and coworkers proposed that a higher concentration of alkylammonium ions in the zeolite pores and higher substitution of sorbed molecules suppress the formation of trimethylamine.[156]

Next to amination, methanol ammoxidation represents another relevant process for C_1 and N_1 catalytic coupling. Ammoxidation involves the reaction of CH_3OH and NH_3 in the presence of oxygen (O_2) to produce hydrogen cyanide (HCN), with water as a side-product of O-scavenging. The process applies solid catalysts based on redox-active bismuth-promoted molybdates, antimonates, tungstates, bimetallic FeMo oxide or M_aPO_X phosphates (M= Mn, Fe, Co, Ni, Zn, B, U), in bulk form or supported on silica, zirconia, alumina, titania or silicon carbide carriers, typically. [157–160]

More recently, few examples of the direct conversion of mixtures of methanol and ammonia to C_{2+} N-products have been reported. Topsoe introduced a process for the synthesis of acid cyanide, but also acetonitrile, on supported metal catalysts at near-ambient pressure and temperatures ranging from 673 to 973 K. Preferred catalysts were based on combinations of transition metal elements such as Ni, Fe, Ru or Co with late- and post-transition metals such as Zn, Sn or Ge. The development of alloys and ternary carbide compounds was signified after activation in the presence of methanol and ammonia. The latter species have been tentatively proposed as active species, enabling first the amination of methanol (**Equation 1.12)** followed by subsequent dehydrogenation of monomethylamine to hydrogen cyanide (**Equation 1.15)**, which can further react with another methanol molecule for the formation of acetonitrile (**Equation 1.16**).[161,162]

$$CH_3NH_{2(g)} \longrightarrow HCN_{(g)} + 2H_{2(g)};\ \Delta H^{\circ}_{298K} = 150.1\ kJ\ mol^{-1} \qquad \textbf{\textit{Eq. 1.15}}$$

$$CH_3OH_{(g)} + HCN_{(g)} \longrightarrow CH_3CN_{(g)} + H_2O_{(g)};\quad \Delta H^{\circ}_{298K} = -96.1\ kJ\ mol^{-1} \qquad \textbf{\textit{Eq. 1.16}}$$

Separately, studies by D. C. Kang. et al., using alternative $ZnAl_2O_4$ spinel catalysts, emphasized the relevance of the cooperation of both acid and weak base sites on the catalyst surface for the selective formation of acetonitrile.[163] These recent works have laid the groundwork for the development of this process of co-valorization of methanol and ammonia into C_{2+} N-compounds. Yet, many open questions remain as to the nature of bimetallic promotional effects and the actual catalyst molecular-scale structure responsible for steering the reaction to acetonitrile production, i.e., by harmonizing the rates for C-C and C-N coupling elementary reactions.

Finally, although more marginally relevant for the present thesis, other methanol catalytic N-functionalization routes have been reported in the liquid phase. For instance, alcohols can serve as precursors for the *in situ* generation of

carbonyl compounds, e.g., through dehydrogenation in a hydrogen-borrowing mechanism in combination with a separate hydrogen acceptor. Typical hydrogen-borrowing catalysts are based on molecular complexes of Ru and Ir or solid supported metals catalysts based on transition 3d (Cu, Fe, Co, Ni, Cr) or precious metals (Pd, Ru, Au, Pt and Ag). The resulting carbonyl compounds are well known to show a rich reductive amination chemistry in the presence of ammonia and amines amination agents, favoring conversion routes through imine intermediates at mild conditions. These catalysts are more extensively used in the N-alkylation of amines with alcohols, whilst the use of ammonia as amination agent is rather restricted.[164–167]. Moreover, the reductive amination of formaldehyde, the simplest aldehyde, and the derivative of methanol dehydrogenation, is a technically complex transformation, owing to the propensity of formaldehyde to undergo self-polymerization side-reactions. This reaction is typically carried out in aqueous solutions using acids or bases in homogeneous catalysis processes leading to the formation of hexamethylenetetramine.[168] Recently, studies have pointed to the viability of a direct formamide electrosynthesis from ammonia and methanol at ambient conditions, opening routes to additional N-compounds.[169]

1.5 BI- AND MULTIMETALLIC MATERIALS IN CATALYSIS

1.5.1 Solid catalysts: concept, surface and bulk interactions and *in situ/operando* development of active phases

Solid catalysts stand out as the preferred option for industrial deployment, compared to their molecular or enzymatic counterparts, for several compelling reasons. Firstly, solid catalysts often exhibit greater stability under harsh industrial conditions, ensuring prolonged catalyst lifespan and sustained activity. Their robust nature makes them resistant to variations in temperature, pressure, and other operational parameters. Secondly, solid catalysts facilitate easy separation from reaction mixtures, simplifying downstream processing and enhancing the efficiency of product isolation. Additionally, the solid nature allows for straightforward handling and recycling of catalysts, contributing to cost-effectiveness and reduced environmental impact. These advantages collectively position solid catalysts as the preferred choice for achieving efficiency, sustainability, and economic viability in industrial catalysis.

As delineated in the preceding sections in this introductory chapter, metal-based catalysts are central to the (co)valorization of C_1 and N_1 resources into added-value energy carriers and platform chemicals. Metal catalysts can take the form of bulk materials, when utilized in an unsupported state, e.g. as metal grids, foams, gauzes, etc. Alternatively, metal catalysts may be supported, i.e., when the active metal is dispersed over a support material. This metal dispersion aims at the creation of stable metal nanoparticles, sub-nm nanoclusters or in the limit atomically dispersed (single-atom) catalysts with enhanced surface-to-volume ratios and adjustable surface topology and electronic properties. The support material itself is often porous, and it may offer different degrees of spatial confinement to the supported metal species, as well as different properties of intrapore molecular transport depending on whether it consists primarily of macro-, meso- or micro-pores, with diameters >50 nm, 50-2 nm or <2 nm, respectively.[170] Depending on the specific reaction being examined, physical and chemical factors such as chemical composition, redox properties, metal-support interaction,[171]

acid-base properties,[172,173] confinement/geometric structure effects (shape, lattice, defects),[174] can influence the catalyst performance.[175]

The adsorption of reactants and intermediates is an essential step in any catalytic process proceeding on the surface of a solid catalyst. Adsorption energies on metal surfaces are often considered to be governed by the d-band theory postulated by Hammer and Nørskov,[176] which establishes correlations between the d-band character of the solid, i.e., the involvement of d orbitals from metal atoms in the formation of chemical bonds with adsorbates, the corresponding chemisorption energies, and the activation energy barriers for elementary steps in the reaction mechanism. According to this model, adsorption energies are influenced by the occupancy of antibonding sites resulting from the overlap between the adsorbate and the metal d-orbitals. When bonding orbitals are filled and antibonding orbitals remain empty, attractive hybridization effects are expected, resulting in the formation of short and strong metal-absorbate bonds. Conversely, an increase of electron occupancy (Fermi level) within antibonding orbitals does not contribute to gain hybridization energy, leading to the elongation or breaking of the adsorbate-metal bond. Bi- and multimetallic effects can influence the energy level for the bonding and antibonding orbitals (d-band center), while also generating charge transfer effects between metals exhibiting different electron donating/withdrawing character. This latter effect influences the electron density of the active metal, a factor often considered to play a pivotal role in the catalytic reaction.

These concepts are intimately intertwined to the Sabatier´s principle,[177] a well-established concept in the field. Sabatier's principle states that the adsorption of a species on a catalytic surface should strike a balance, i.e., neither too weak nor too strong, to attain the maximum conversion rate. The former results in no or too slow reactant activation, while the latter drives surface site *poisoning*. This concept gives rise to the volcano appearance for plots of the conversion rate or the *turnover frequency* (TOF) when normalized per unit active site, against the binding energy or bond strength, as depicted in **Figure 1.10. a**.[178,179]

The chemical affinity of a solid catalyst for specific reactants can exert profound transformations on its surface, as described by the Sabatier's principle, but additionally through the occurrence of adsorbate-driven surface reconstructions.[180] Moreover, reactant-induced structural transformations may extend beyond the solid's surface, into sub-surface lattice and interstitial positions. As summarized in **Figure 1.10 b**, Montemore and coworkers investigated, using DFT modeling, the relations between surface adsorption energies for oxygen- and carbon-based adsorbates on metals and the experimental bulk formation energies for the corresponding metal oxide, carbide, nitride and sulfide *bulk* compounds. Their findings suggest that these properties tend to correlate when similar species are considered on the surface and in the bulk of the solid, e.g., the adsorption energy for carbon-based adspecies exhibited a low correlation with bulk metal compound formation energies except for carbides.[181] Unfortunately, this study did not consider nitrogen- and sulfide-based adsorbate species, which would have provided a more comprehensive insight into general trends for oxophilic,[183] azophilic, carbophilic[181] and/or thiophilic[184] characters of metal catalysts.

The formation of stable bonds between hydrogen (H), nitrogen (N), oxygen (O), carbon (C), and sulfur (S), with metals plays a central role in surface and sub-surface transformations, which specific metals or their compounds may undergo, from an initial (pre-catalyst) state into the actual working catalyst, when exposed to reaction conditions. Dynamic transformations can give rise to new, truly active species as it can be the cases of metal, hydrides, nitrides, oxides, carbides, and combinations thereof, e.g., oxycarbides, oxynitrides, etc., or even amorphous materials lacking long-range atomic order.[185] The consideration of bulk formation energies for oxide, carbide, nitride, and sulfide metal compounds becomes crucial in understanding and predicting such *in situ* catalyst development.[176]

Moreover, the recognition of solid catalysts as dynamic entities, which may undergo profound surface and bulk structural rearrangements as a result of their exposure to reactive atmospheres and the activation of specific reactants, emphasizes the need for *in situ* and *operando* characterization methods to unequivocally reveal the nature of the actual catalytically active solid.

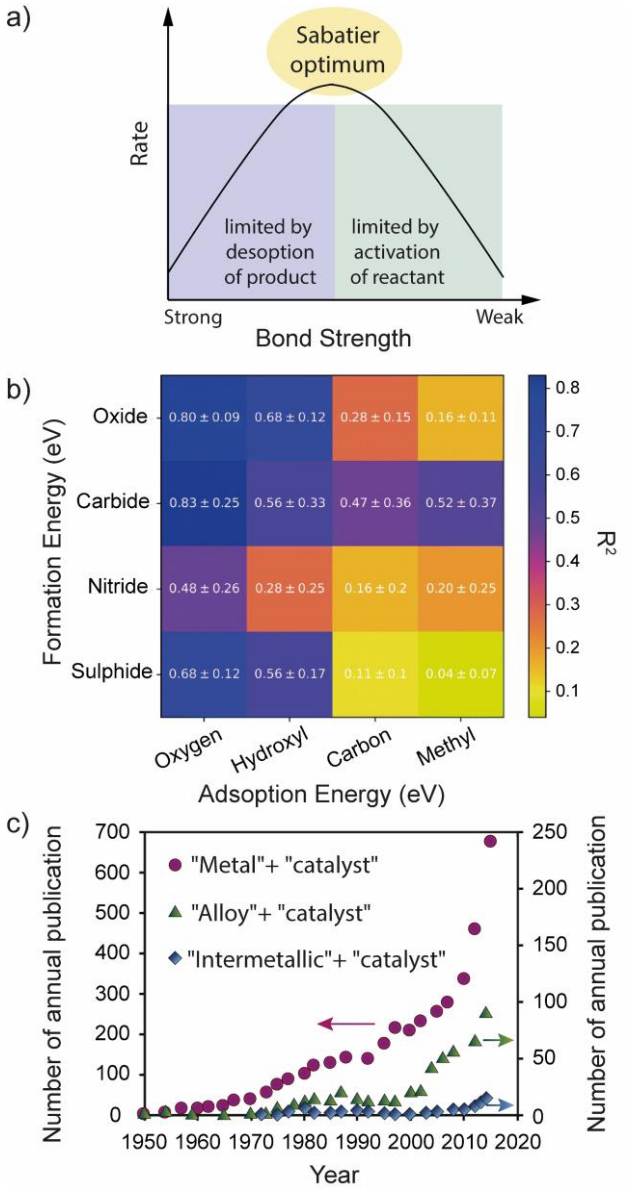

Figure 1.10: *a) Qualitative representation of the Sabatier principle in catalysis, adapted from ref.*[178] *b) Correlation of DFT-calculated surface adsorption energy for oxygen- and carbon-based adspecies and experimental bulk formation energy for different metal compounds, adapted from ref.*[181] c*) Evolution of the annual number of scientific publications with a title containing the words metal, alloy or intermetallic in combination with the word catalyst in the period from 1950 to 2020. Adapted from ref.*[182]

In situ characterization refers to the investigation of catalysts in a controlled environment, while exposed to conditions (composition, temperature, pressure, fluid-solid dynamics, etc), which emulate those applied for activation or catalytic action. Similarly, the term *operando,* coined by Bañares, Weckhuysen, Mestl and Gaigneaux in the early 2000s, refers specifically to studies performed on catalyst materials during their exposure to catalysis relevant conditions and it additionally requires a simultaneous monitoring of catalytic performance.

Operando characterization methods have evolved to encompass a diverse range of spectroscopic, imaging, and diffraction techniques that provide insights into the structures of the actual working solid catalysts. These methods include X-ray absorption (XAS), infrared, Raman, UV-vis and a wider range of spectroscopies, among other methods, which are able to probe catalyst materials without interrupting their action.

Strongly connected to *operando* characterization of solid catalysts, synchrotron radiation has emerged as a powerful tool, revolutionizing scientists' ability to unravel the complex and dynamic structural modifications undergone by solid catalysts while at work. Synchrotron radiation offers a unique set of attributes that make it particularly suitable for *operando* studies.

Firstly, a central strength of synchrotron radiation lies in its broad spectral coverage, spanning ultraviolet to X-ray wavelengths. This expansive range enables researchers to employ a variety of spectroscopic techniques including, but not limited to, X-ray absorption spectroscopy (XAS), X-ray diffraction (XRD), and X-ray photoelectron spectroscopy (XPS). The ability to tailor the energy of the incoming radiation with high precision allows the selective excitation of specific elements in XAS, or to precisely adjust analysis depths in XPS.

Secondly, the high flux of photons available at synchrotron facilities enables the use of fast detectors with short integration times, offering higher time resolution than laboratory-based techniques, e.g., in methods such as XRD, which is valuable for capturing dynamic catalyst transformations.

1.5.2 Bimetallic effects in heterogeneous catalysis

Since prehistoric times, there have existed examples of the exploitation of bimetallic effects in materials across decorative arts, weaponry, and currency. Ancient civilizations employed synthetic bimetallic materials and alloys for a variety of purposes beyond metallurgy. Techniques like *cloisonné* adorned metal objects with vibrant enamel, while *mokume-gane* in Japan created intricate patterns in swords and jewelry through layered metal forging. Besides, bi-metallic coins, issued by civilizations like the Romans and Byzantines, facilitated trade with distinct values denoted by the combination of metals, all adorned with intricate designs reflecting the issuing authority.

At present the metal alloys market scales to around 291 billion (2021).[186] In the catalysis field the benefits of combining two metals are exploited in a wide range of technically relevant reactions such as hydrogen evolution (HER),[187] CO_2 reduction,[188] CO oxidation,[183] and ammonia synthesis,[179] among others. For the latter case, which as discussed earlier in this introduction chapter, is an industrial process of utmost significance, Co-Mo alloys have shown intermediate nitrogen binding, delivering ammonia synthesis performances which approach those of catalysts based on Ru precious metal. Bimetallic promotion effects have also been proven critical for the optimized performance of technical Fe-based ammonia synthesis catalysts.[189–191]

Multi-metallic compounds can be present in different forms, such as mixed-metal compounds, mixed-metal interstitial alloys, and metallic solid solutions. Over the last two decades, these materials have garnered increasing attention in the field of catalysis, see **Figure 1.10. c**.

1.5.3 Solid solutions

A solid solution refers to a homogeneous mixture of two or more substances in a solid state, where the components are uniformly distributed at the atomic or molecular level. In a solid solution, the individual atoms, ions, or molecules of the different components are integrated into the crystal lattice or structure of the solid material. Solid solutions can be categorized into two main subsets of families: *substitutional* and *interstitial* solutions.

1.5.3.1 Substitutional solutions

Substitutional solutions are formed by the replacement of atoms of one element by atoms of a second, alien element, in the lattice positions of a specific crystalline structure. The substitution degree is generally expressed as the atomic ratio of the less abundant element in the solid solution range. A complete solid solution, i.e., with substitution degrees spanning the entire range from 0 to 50 %, is attainable only when the individual elements share the same valence and crystal structure.

This class of solid solutions includes common substitutional alloys (**Figure 1.11. a**), top-left), characterized by their metallic bonding character. Within these metal alloys, metal elements are randomly distributed within the lattice positions of body-centered cubic (*bcc*), face-centered cubic (*fcc*), or hexagonal closed-packed (*hcp*) crystal structures, which are characteristic for metals.

Single-atom alloys (SAAs) and high-entropy alloys (HEA) can be additionally included as subsets within the substitutional solutions. Single-atom alloys are simply substitutional alloys in the limit of dilution of one metal within a matrix of the second metal, so the former appears as isolated metal atoms lacking direct self-coordination. Meanwhile, high-entropy alloys are substitutional alloys characterized by a random set of more than four metal elements, wherein each of the elements is present in a similar atomic proportion.[192]

In substitutional alloys, the atomic size of the *substitutional* element should ideally not differ more than 15 % from that of the *host* element. Moreover, additional constrictions, such as similar electronegativity and valence may apply

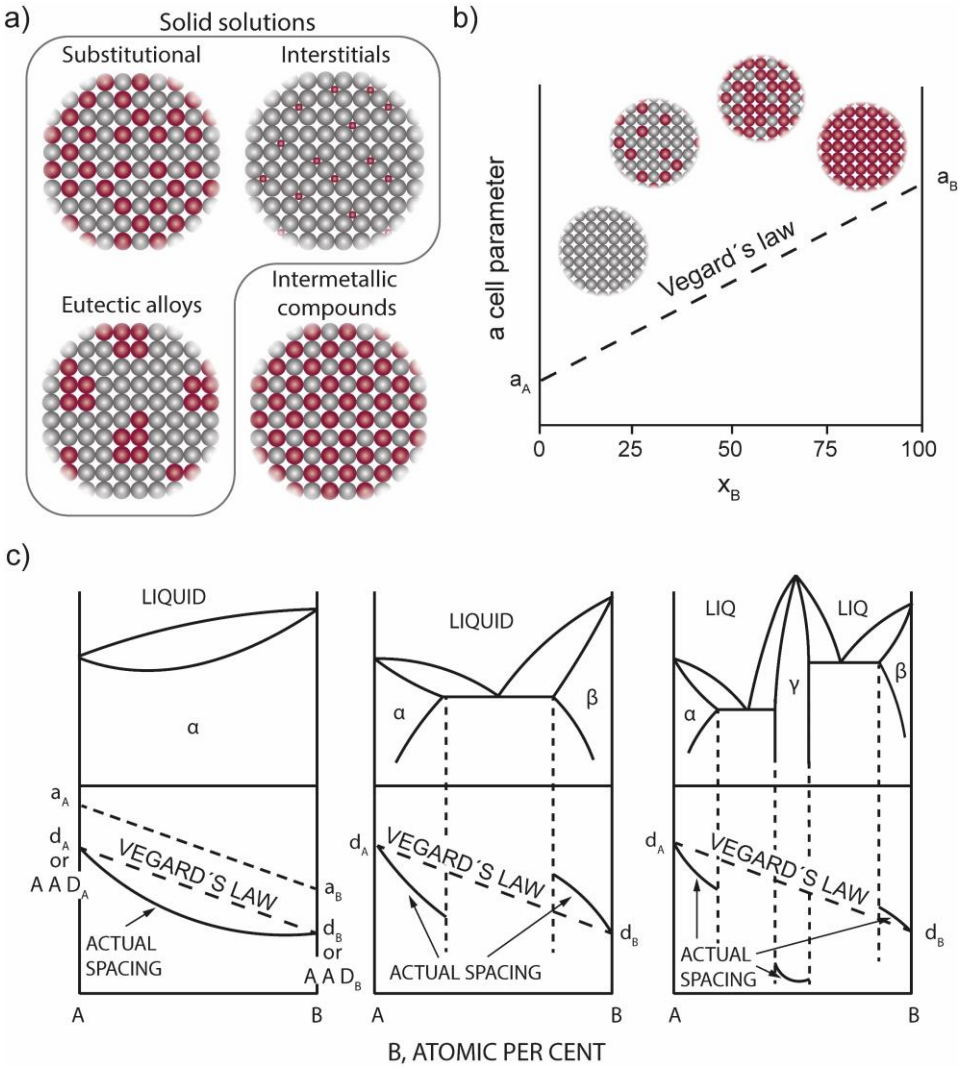

Figure 1.11: *a) Schematic representation of substitutional solid solutions (top-left), interstitial compounds (top-right) eutectic alloys (bottom-left) and intermetallic compounds (bottom-right). b) Schematic representation of the evolution of the lattice parameter with the fractional composition in a substitutional solid solution with complete solubility of pure compounds. c) Compositional-lattice parameter curves and phase diagrams of conventional binary alloys with complete solubility (left), partial solubility (e.g., A possesses higher valence than B, middle) and with high electrochemical A-B interaction leading to a different and more stable phase (right). Adapted from ref.*[194]

as described in the Hume-Rothery rules.[193] The lattice parameter for an alloy of A and B elements, denoted as a_{AB}, may typically be estimated by the known Vegard´s law, which uses the average of the lattice parameters of the individual metals, pondered by the alloy composition (**Equation 1.17)**. This is visually sketched in **Figure 1.11. b**.

$$a_{AB} = X_A a_A + (1 - X_A) a_B \qquad \textit{Eq. 1.17}$$

As illustrated in **Figure 1.11. c**, deviations of the linear Vegard's law occur frequently, due to differences in bonding strength between the two metals. In instances where self-association of elements or their immiscible properties prevail, these materials can form isolated clusters or undergo phase segregation, known as eutectic alloys, illustrated **Figure 1.11. a**, bottom-left. Moreover, yet a different phase diagram can emerge in cases where a thermodynamically more stable mixed metal phase emerges at an intermediate composition, as portrayed in **Figure 1.11. c**, right.

Introducing alien metal elements in an alloy material may disrupt the surface's geometrical arrangement, consequently decreasing the coordination number of each metal and the degree of the "ensemble effect". This disturbance in the surface structure can inherently alter adsorption modes, which has the potential to significantly modify the material's electronic properties, through both "ligand" and "strain" effects. The *ligand effect* involves changes in the d-band center and local atomic charge, while *strain effects* arise from lattice compression or expansion, creating distortions in the local coordination environment of the metals. Such modifications can impede reactions that rely on multipoint bonding for reactant activation. Additionally, alloyed materials may exhibit ordering and steric effects, potentially enhancing the regio- or stereo-selectivity of reactions.[195] While alloy formation is primarily driven by enthalpy, the formation of multinary or high-entropy alloys by multimetallization can create metal synergisms and

multifunctional properties that enable the stabilization of the catalyst by entropy and low diffusion effects.

1.5.3.2 Interstitial solid solutions

Interstitial solid solutions emerge through the diffusion of comparatively small atoms, of elements such as e.g. lithium, boron, hydrogen, nitrogen, or carbon within the interstitial voids of the crystal lattice of a metal. This diffusion process gives rise to structures that show a blend of covalent, ionic, and metallic bond characters. In **Figure 1.12. a**, the distinctive metal, covalence, and ionic bond characteristics are illustrated in various ternary nitride compounds. In systems where a dominant metal character prevails, N-poor compounds are generated, while the coexistence of ionic/covalent bond character results in N-rich compounds.

This interplay is further influenced by the electronegativity difference between the metal and the light element. Late transition metals typically exhibit lower ionic character compared to N, O, and C, while early transition metals manifest higher ionic characters.[196]

Hägg's rules dictate the feasibility of forming an interstitial solid solution, grounded in a geometric principle. This principle posits that the atomic radii of the solute element must be compact enough to facilitate diffusion through the interstitial voids within the host lattice. Empirically determined by Hägg, the ionic radius ratio r_x/r_M (where *x* represents the solid solute element and M the host metal element) must be ≤0.59 to fulfill the criteria for interstitial solid solution formation.[201] If this condition is not met, energetically unfavorable interstitials are generated, resulting in the formation of more intricate structures rather than the typical cubic and hexagonal arrangements.

Anthony, Miller, and Turnbull expanded Hagg's rule by incorporating additional conditions for the dilute interstitial system.[202] According to these criteria, the host metal must exhibit a significant electropositive nature or be a polyvalent metal, while the foreign ion must be sufficiently small and possess a low valence. The theoretical estimation of void sizes or interstitial sites can be achieved through

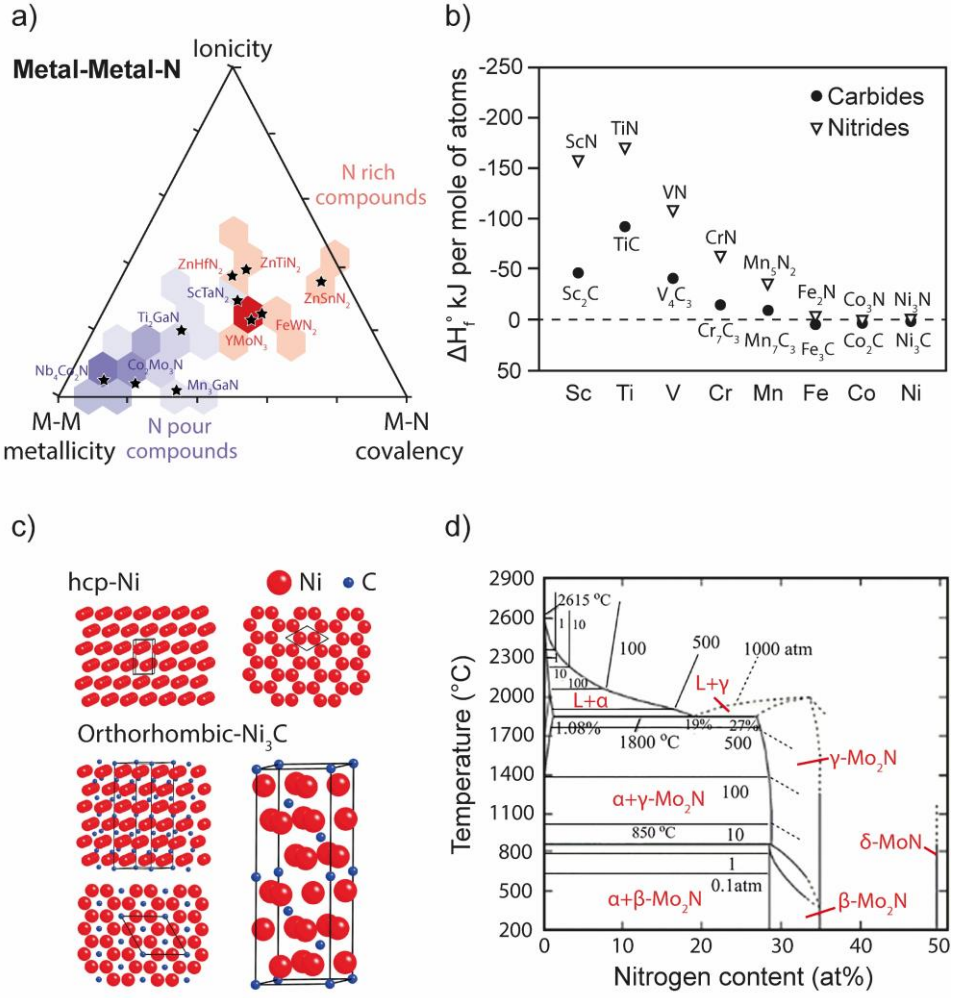

Figure 1.12: *a) Van Arkel triangles of N-poor and N-rich ternary nitrides showing the dependency with the metallic, ionic and covalent bond character. The hexagons are represented when more than two data points are available. Adapted from ref.*[197] *b) Formation enthalpy for carbides and nitrides of first raw transition metals, adapted from ref.*[198] *c) Comparison of the crystal structures for the hexagonal hcp-Ni (top) and the rhombohedral Ni_3C carbide interstitial solid solution forming a superlattice.*[199] *d) Phase diagram for molybdenum nitrides determined by H. Jehn. et al.*[200]*. Adapted from ref.*[199]

geometry, following Pauling's rule, where elements are treated as spheres. As an illustration, **Table 1.1** presents the calculated r_x/r_M ratio for tetrahedral and octahedral interstitial sites in a face-centered cubic (*fcc*) crystal structure, based on these considerations.

Table 1.1: *Interstitial site position in a face-centered cubic (fcc) crystal system with tetrahedra and octahedra coordination and the geometrically calculated r_i/r_M ratio.*

Coord. number	Geometry	Interstitial positions in a FCC	r_x/r_M ratio
4 (*Th*)	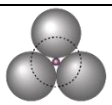	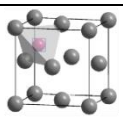	0.225
6 (*Oh*)	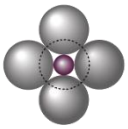	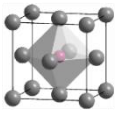	0.414

1.5.3.2.1 Lattice defects in solid solutions

Defects are intrinsic to solid materials and confer characteristic chemical and physical properties, including electronic, optical, bulk, and thermoelectric properties. These defects can be categorized based on dimensionality into point defects (zero-dimensional), dislocation defects (one-dimensional), external or internal surfaces (two-dimensional), and bulk defects (clusters of point defects, precipitation, and voids in the crystal lattice).[203]

Among these, point defects emerge as the most relevant in the present thesis. They do not extend throughout the lattice and are thus considered zero-dimensional. These defects exist in thermodynamically stable equilibrium and are not easily eliminated. They result in a strained rearrangement of nearby atoms, leading to distortions in the planes and surface microstructures, which in turn

create geometric and electronic structure differences compared to the pure compound. Additionally, under the influence of external chemical or electric driving forces such as radiation, temperature, or chemical potential, kinetic processes can occur, leading to chemical and physical diffusion, electrical conduction, and reactions, thus generating induced defects. These concepts are further elucidated and schematically represented in **Figure 1.13**.

Vacancy defects are characterized by the absence of an atom that regularly occupies a site within the crystal lattice, producing defective materials with nonstoichiometric composition. These vacancy defects are usually referred to as V_a where *a* is the missing atom. Materials with ionic character can present anion or cation vacancies, depending on the leaving atom. These materials must maintain a zero net charge, necessitating the achievement of compensation charge. This process results in the creation of additional point defects to balance the charge.

Related to vacancies are *Frenkel defects*, named after Yakov Frenkel, which occur when an atom from the lattice occupies a void position, forming an interstitial defect denoted with a subscript *i*, A_i. This rearrangement results in an equal number of interstitial defects (A_i) and vacancies (V_a), as illustrated in **Figure 1.13**. Frenkel defects do not create an imbalance in the structure's charge since the atoms or ions are merely shifted internally within the lattice. *Schottky defects*, named after Walter H. Schottky, occur when an equal number of cation and anion vacancies are created within the crystal lattice, ensuring the material´s overall charge neutrality. In some cases, Schottky defects are also classified based on the distance between the paired vacancies. For example, "NN1" may refer to vacancies that are the closest neighboring pair (or divacancy), "NN3" indicates the third nearest neighboring pair, and so on.

When an atom within a lattice is replaced by another element from the material, which originally occupied a different lattice position, this defect is known as an *antisite*. This type of defect is commonly observed in materials with weak ionic or covalent bonding, as strong electrostatic repulsion between ions of the same charge would typically prevent such substitution in ionic compounds.

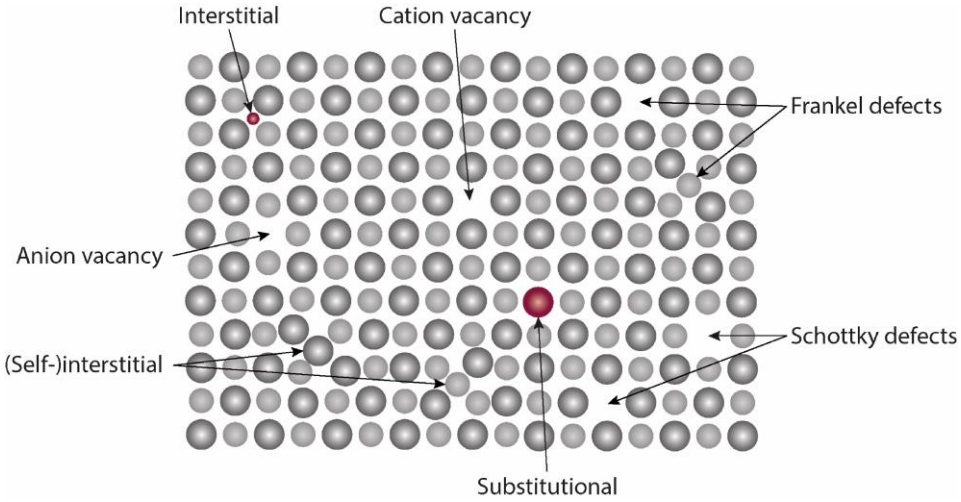

Figure 1.13: *Illustrative AB crystal lattice with major point defects discussed in this section, including anion and cation vacancies, substitutional, Schottky, Frenkel and (self-) interstitials defects.*

Antisite defects are prevalent in materials exhibiting metallic or semiconductor characteristics, where electronic charge is delocalized throughout the solid structure. This is the case of some substitutional alloys, like metal carbides, nitrides, etc. The formation of an antisite can often be offset by the creation of an opposite antisite defect, preserving the stoichiometry of the balanced material. Antisites may arise as a result of Frenkel defects, as suggested by **Equations 1.18-1.21**.

$$A_A \longrightarrow A_i + V_A \qquad \textbf{Eq. 1.18}$$

$$A_i + B_B \longrightarrow A_B + B_i \qquad \textbf{Eq. 1.19}$$

$$B_i + V_A \longrightarrow B_A \qquad \textbf{Eq. 1.20}$$

$$A_A + B_B \longrightarrow A_B + B_A \qquad \textbf{Eq. 1.21}$$

The replacement of a lattice atom by a foreign element, rather than an internal element atom, is referred to as *substitutional defects* and denoted as M_N, where M is the atom occupying the position of N. Typically, the substituted atoms are cation ions or metallic elements. However, substitution of anions or covalent atoms by other elements is also considered as substitutional defect, altering the electronic and structural properties (distortion) of the material. For example, substituting oxygen in metal oxides or carbon atoms in graphene with nitrogen creates nitrogen substitutional defects, resulting in the formation of oxynitrides[204] and N-doped graphene, respectively.

Small foreign atoms, such as C, N, H, and B, among others, can occupy the interstitial spaces within the lattice, leading to the formation of carbides, nitrides, hydrides, and borides, respectively. These defects are referred to as *interstitials*. When these defects occur unintentionally, they are categorized as impurities, however, when deliberately introduced into the structure, they are termed dopant atoms. Small interstitial atoms often produce high distortion in the surrounding lattice atoms, resulting in a lattice expansion. This is typically observed for metal carbides and nitrides.

Conditions for the formation of substitutional and interstitial defects align with those of substitutional and interstitial solid solutions, where a high concentration of these specific defects is prevalent within the material, as detailed in **section 1.5.3.1** and **section 1.5.3.2**, respectively.

1.5.3.2.2 Interstitial alloys in catalysis

Interstitial alloys constitute a specific category within interstitial solid solutions. Traditional interstitial alloys encompass hydrides, borides, nitrides, or carbides. In the context of this thesis, special attention will be devoted to nitrides and carbides, given their particular significance in catalysis.

Metal nitrides and carbides are usually synthesized at high temperatures from their respective main element in metal form, as a metal oxide, or in the form of clusters. In the synthesis process, nitrogen or carbon diffuse through the host lattice and reject oxygen in the form of water, nitrogen oxides or carbon oxides,

respectively, usually leading to pseudomorphic and non-stochiometric final interstitial structures.[205] **Figure 1.12. b** illustrates the formation enthalpies of the first-row (3d) transition metal carbides and nitrides. The two types of interstitial compounds exhibit similar trends, owing to the similar properties of N and C as interstitial elements. Discrepancies in the formation enthalpy are noted between nitrides and carbides for 3d transition metals from Sc to Mn. However, Fe, Co, and Ni carbides and nitrides exhibit comparable values close to zero, suggesting the presence of metastable phases. Interstitials may be randomly distributed but still maintain order, occasionally forming superlattices. For instance, nickel adopts a hexagonal close-packed (*hcp*) structure where carbon is dissolved in the octahedral positions, forming a superlattice, as depicted in **Figure 1.12. c**.[206] An illustrative example is found in one of the most extensively studied transition metal nitrides (MTNs), molybdenum nitride. This compound exhibits a cubic γ-Mo_2N structure at elevated temperatures, characterized by a diverse range of randomly distributed nitrogen atomic percentages, consequently giving rise to the formation of nitrogen vacancies.[199] Controlled nitridation allows for the achievement of stoichiometric cubic structures, from γ-Mo_2N to B1-MoN phase (not shown). However, this phase is inherently unstable and tends to transform into a more thermodynamically stable hexagonal δ-MoN phase. Therefore, B1-MoN is not depicted in the stability phase diagram included in **Figure 1.12. d**.[199]

Transition metal carbides and nitrides have traditionally attracted a significant deal of attention as solid catalysts. In 1973, Levy and Boudart made a significant observation that tungsten carbide demonstrates surface and catalytic properties reminiscent of noble platinum metals. This phenomenon is attributed to the incorporation of carbon into the W structure, leading to a modification of electronic properties through the hybridization of the metallic d band with the C s-p bands.[207] As discussed earlier, these electronic effects can influence the adsorption strength of adsorbents. There exists a general trend wherein carbides exhibit different reactivities compared to their respective metals. The formation of interstitial carbides results in the passivation of the intrinsic reactivity of the neat metal and the stabilization of different intermediates, consequently steering the catalytic conversions to a different set of products.[196] As an example, Teschner et

al. demonstrated that the incorporation of interstitial carbon not only reduces hydrogen diffusion through the Pd structure, but it additionally destabilizes adsorbed H^* species, resulting in lower hydrogen surface coverage, under specific hydrogenation conditions, compared to the neat metal. This modification provides greater control over the selectivity in reactions such as the hydrogenation of alkynes.[208]

Next to adjustment of electronic properties, the formation of metal carbides or nitrides may lead to changes in the crystal structure and morphology, and these may also strongly influence the mechanism of reactions proceeding on the surface of the interstitial compounds.[196] Distinct catalyst reactivities may be observed depending on whether carbon or nitrogen interstitials are introduced. As an example, R. Kojima and K. Aika demonstrated that molybdenum carbide catalysts exhibited superior performance for ammonia synthesis from its elements compared to the corresponding metal nitride.[209] Additionally, the employment of different catalyst precursors, as well as the conditions applied to develop the interstitial compounds, commonly affect the final carbide/ nitride composition, i.e., through different crystal structures, various types and densities of point defects, resulting in differences in reactivity.[210,211]

In recent decades, transition metal carbides and nitrides have proven to be suitable as solid catalysts, alternative to their (noble) metallic counterparts, for a wide range of relevant reactions. This includes the Fischer-Tropsch (FT)[212–215] synthesis of synthetic hydrocarbons, ammonia synthesis[190,209,216] and decomposition,[217] CO_2 reduction,[218,219] and the water gas shift reaction,[220] among others.[221] Besides, oxynitrides and oxycarbides can be formed in the presence of oxygen ions at interstitial positions, along with nitrogen or carbon, respectively. For example, Nb-Al, Mn–Nb, Mo-W and Mo oxynitrides were synthesized by partial ammonolysis of the corresponding metal oxide precursors.[222–226] These compounds present Brønsted acid, metallic and (C, N)-vacant surface sites that induce bifunctional properties and serve, in certain instances, to decrease reaction barriers. These properties make them interesting for reactions such as

hydrodenitrogenation,[227] dehydrogenation and isomerization reactions,[228] oxygen evolution reaction (OER),[229] water gas shift reactions,[220] among others.[221]

1.5.4 Intermetallic compounds

Intermetallic compounds (such as AB, AB_2, AB_3, A_2B_3) consist of two or more metal components homogeneously arranged in a long-range ordered structure with well-defined site occupancies. These compounds are less commonly referred to as ordered alloys**.**[230] An illustration of an intermetallic compound can be observed in **Figure 1.11.a**. These compounds exhibit well-defined crystal and electronic structures that differ from their respective alloys (with random lattice distributions of the conforming elements) and/or the respective pure metals. Intermetallics with a strictly fixed stoichiometric composition are known as Daltonide-type, while those with compositions ranging beyond stoichiometry are termed Bertholide and Kurnakov-type intermetallics**.** The former has a narrow range of composition, while the latter allows for a more permissive and wide range of composition ratios. Particularly, Kurnakov-type intermetallics are composed of metal elements with similar characteristics, typically vicinal in the periodic table.

As illustrated in the periodic table included in **Figure 1.14**, intermetallic compounds typically feature a first element, which is often a late transition metal, such as Fe, Co, Ni, Ru, Rh, Pd, Pt, and Au. These elements are paired with a second element, which is typically a post-transition metal, i.e., with greater electronegativity than the first element. Early transition metals are less commonly found in intermetallic compounds due to challenges associated with reducing their precursors to their metallic state.[182]

Intermetallic compounds have started to be developed and applied as catalysts only relatively recently, as it can inferred in **Figure 1.10. c**. Therefore, the catalysis scientific community foresees still a large potential for further developments with this specific class of materials.[182]

Due to their relatively recent emergence in catalysis, the synthesis of catalysts based on intermetallic compounds is not extensively documented in the

literature. The dispersion of intermetallic nanoparticles on specific supports is typically achieved through impregnation methods. These methods involve the incorporation of the respective metal precursors from metal solutions, prepared to reflect the stoichiometry metal contents in the desired intermetallic compound, followed by controlled precursor decomposition and metal reduction thermal treatments. Additionally, factors such as heating and cooling rates, temperatures (typically ranging between 673-1073 K) and dwell times during the thermal treatments, are determinant for the extent of formation and nanocrystallite features of the supported intermetallic compound.[182,230] The synthesis of metals in supported or unsupported forms, including colloidal synthesis, can also be achieved using liquid-phase reduction agents. Strong reducing agents, such as alkaline metal borohydrides ($NaBH_4$, $LiBH_4$, among others), are commonly employed in this process. Additionally, various synthesis methods, including chemical vapor deposition (CVD), the Czochralski method, or metallurgical alloying, offer alternative approaches to produce intermetallic compounds. These

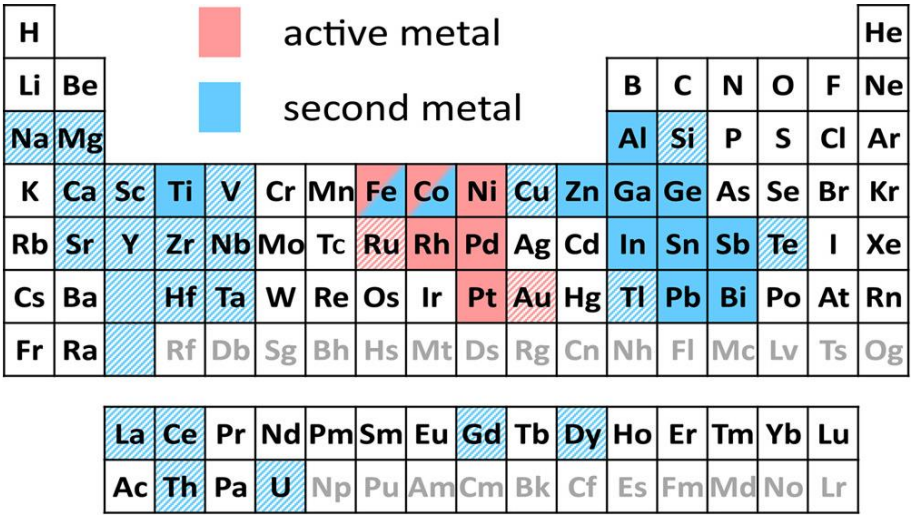

Figure 1.14: *Periodic table highlighting the common active metals (red) and the second metal (blue) providing electronic, structural, steric, and order effects in intermetallic compounds. Blue and red dashed means metals that are less commonly utilized. Adapted from ref.*[182]

diverse synthesis techniques provide flexibility in tailoring the properties and structures of intermetallic materials based on the desired application and performance characteristics.

Intermetallic compounds hold particular potential to manipulate and exploit so-called *ensembled effects* in catalysis. Ensemble effects arise as a result of the influence exerted by ensembles of vicinal surface metal atoms on the reaction mechanism. These effects involve both electronic and geometric aspects. Cooperative electronic interactions determine the adsorption properties, while specific spatial arrangements of surface atoms may generate bifunctional sites or contribute to isolate/dilute specific active centers.

Electronic and geometric effects are not specific characteristics of intermetallics, as they also manifest in other (disordered) alloy materials. However, there exist specific steric effects which are associated to the highly regular spatial arrangement of the two (or more) component metals across specific surface facets in intermetallic compounds. In this case, a common interpretation of ensemble effects goes as the atoms of a non-active element acting as spacers for (surface) atoms of an active metal. Such site isolation effects can profoundly modify the binding and catalytic properties of the latter with respect to the case of uninterrupted extended surfaces of the active metal.[230] In a particularly revealing study, K. Mayrhofer and coworkers studied the structural ordering effect in Pt-Cu bimetallic catalysts for the oxygen evolution electrocatalytic reaction (OER). A $Pt_{0.25}Cu_{0.75}$ disordered alloy catalyst (*Pm-3m*) was compared to a compositionally equivalent intermetallic $PtCu_3$ catalyst (*Fm-3m*). The latter attained 20-30 % higher OER activity, an effect which the authors attributed to higher stability and retention of Cu on the structure alongside structural ordering effects.[231]

The aforementioned effects, associated to the high structural and surface regularity of intermetallic compounds, jointly provide a particularly precise engineering tool for metal catalysts. Therefore, it is not surprising that intermetallics have been explored to attain advanced selectivities in a wide array of reactions, including the hydrogenation of aldehydes,[232] alkenes, the reduction

of carbon oxides (CO and CO_2) to methane [233] or methanol,[234] and alcohol aminations,[235] among other transformations.[230]

1.6 REFERENCES

(1) Rivilla, V. M.; Jiménez-Serra, I.; Martín-Pintado, J.; Colzi, L.; Tercero, B.; de Vicente, P.; Zeng, S.; Martín, S.; García de la Concepción, J.; Bizzocchi, L.; Melosso, M.; Rico-Villas, F.; Requena-Torres, M. A. Molecular Precursors of the RNA-World in Space: New Nitriles in the G+0.693−0.027 Molecular Cloud. *Frontiers in Astronomy and Space Sciences* **2022**, *9*. https://doi.org/10.3389/fspas.2022.876870.

(2) MarketResearch.com. *Global Methylamines (Monomethylamine, Dimethylamine, Trimethylamine) Market Research Report* ***2021***.

(3) Hayes, K. S. Industrial Processes for Manufacturing Amines. *Appl. Catal. A Gen* **2001**, *221* (1–2), 187–195. https://doi.org/10.1016/S0926-860X(01)00813-4.

(4) Roose, P. Methylamines. In *Ullmann's Encyclopedia of Industrial Chemistry*; Wiley-VCH Verlag GmbH & Co. KGaA: Weinheim, Germany, **2015**; 1–10. https://doi.org/10.1002/14356007.a16_535.pub4.

(5) Brazdil, J. F. Acrylonitrile. In *Ullmann's Encyclopedia of Industrial Chemistry*; Wiley-VCH Verlag GmbH & Co. KGaA: Weinheim, Germany, **2012**. https://doi.org/10.1002/14356007.a01_177.pub3.

(6) Gail, E.; Gos, S.; Kulzer, R.; Lorösch, J.; Rubo, A.; Sauer, M.; Kellens, R.; Reddy, J.; Steier, N.; Hasenpusch, W. Cyano Compounds, Inorganic. In *Ullmann's Encyclopedia of Industrial Chemistry*; Wiley, **2011**. https://doi.org/10.1002/14356007.a08_159.pub3.

(7) James D. Idol. Process for the Manufacture of Acrylonitrile. US 2,904,580, **1959**.

(8) C. Dimian, A.; Sorin Bildea, C. Acrylonitrile by Propene Ammoxidation. In *Chemical Process Design*; Wiley, **2008**; 313–338. https://doi.org/10.1002/9783527621583.ch11.

(9) *Hydrogen Cyanide*. Chemical Economics Handbook, **2020**.

(10) *Acetonitrile*. Chemical Economics Handbook, **2020**.

(11) *Acrylonitrile*. Chemical Economics Handbook, **2021**.

(12) Cespi, D.; Passarini, F.; Neri, E.; Vassura, I.; Ciacci, L.; Cavani, F. Life Cycle Assessment Comparison of Two Ways for Acrylonitrile Production: The SOHIO Process and an Alternative Route Using Propane. *J. Clean. Prod.* **2014**, *69*, 17–25. https://doi.org/10.1016/j.jclepro.2014.01.057.

(13) *CO_2 Emissions in 2022*. IEA (2023), CO_2 Emissions in 2022, IEA, Paris.

(14) *Understanding methane emissions*. IEA (2023), Global Methane Tracker.

(15) Vita, A.; Italiano, C. Fuel and Hydrogen Related Problems for Conventional Steam Reforming of Natural Gas. In *Current Trends and Future Developments on (Bio-) Membranes*; Elsevier, 2020; pp 71–89. https://doi.org/10.1016/B978-0-12-816778-6.00004-7.

(16) Wittich, K.; Krämer, M.; Bottke, N.; Schunk, S. A. Catalytic Dry Reforming of Methane: Insights from Model Systems. *ChemCatChem.* **2020**, *12* (8), 2130–2147. https://doi.org/10.1002/cctc.201902142.

(17) González-Castaño, M.; Dorneanu, B.; Arellano-García, H. The Reverse Water Gas Shift Reaction: A Process Systems Engineering Perspective. *React Chem Eng* **2021**, *6* (6), 954–976. https://doi.org/10.1039/D0RE00478B.

(18) Methanol Institute. *Methanol price and supply/demand*. https://www.methanol.org/methanol-price-supply-demand/.

(19) Spath, P. L.; Dayton, D. C. *Preliminary Screening -- Technical and Economic Assessment of Synthesis Gas to Fuels and Chemicals with Emphasis on the Potential for Biomass-Derived Syngas*; Golden, CO (United States), **2003**. https://doi.org/10.2172/15006100.

(20) Bachmann, M.; Völker, S.; Kleinekorte, J.; Bardow, A. Syngas from What? Comparative Life-Cycle Assessment for Syngas Production from Biomass, CO_2, and Steel Mill Off-Gases. *ACS Sustain. Chem. Eng.* **2023**, *11* (14), 5356–5366. https://doi.org/10.1021/acssuschemeng.2c05390.

(21) Calbry-Muzyka, A.; Madi, H.; Rüsch-Pfund, F.; Gandiglio, M.; Biollaz, S. Biogas Composition from Agricultural Sources and Organic Fraction of Municipal Solid Waste. *Renew Energy* **2022**, *181*, 1000–1007. https://doi.org/10.1016/j.renene.2021.09.100.

(22) Ullah Khan, I.; Hafiz Dzarfan Othman, M.; Hashim, H.; Matsuura, T.; Ismail, A. F.; Rezaei-DashtArzhandi, M.; Wan Azelee, I. Biogas as a Renewable Energy Fuel – A Review of Biogas Upgrading, Utilisation and Storage. *Energy Convers. Manag.* **2017**, *150*, 277–294. https://doi.org/10.1016/j.enconman.2017.08.035.

(23) Surendra, K. C.; Takara, D.; Hashimoto, A. G.; Khanal, S. K. Biogas as a Sustainable Energy Source for Developing Countries: Opportunities and Challenges. *Renewable and Sustainable Energy Reviews* **2014**, *31*, 846–859. https://doi.org/10.1016/j.rser.2013.12.015.

(24) *20% increase in biomethane production in Europe, shows biogases industry report released today*. European Biogas Association (EBA).

(25) Sikarwar, V. S.; Zhao, M.; Clough, P.; Yao, J.; Zhong, X.; Memon, M. Z.; Shah, N.; Anthony, E. J.; Fennell, P. S. An Overview of Advances in Biomass Gasification. *Energy Environ. Sci.* **2016**, *9* (10), 2939–2977. https://doi.org/10.1039/C6EE00935B.

(26) Keith, D. W.; Holmes, G.; St. Angelo, D.; Heidel, K. A Process for Capturing CO_2 from the Atmosphere. *Joule* **2018**, *2* (8), 1573–1594. https://doi.org/10.1016/j.joule.2018.05.006.

(27) Zhu, Q. Developments on CO_2-Utilization Technologies. *Clean Energy* **2019**, *3* (2), 85–100. https://doi.org/10.1093/ce/zkz008.

(28) Kibria Nabil, S.; McCoy, S.; Kibria, M. G. Comparative Life Cycle Assessment of Electrochemical Upgrading of CO_2 to Fuels and Feedstocks. *Green Chemistry* **2021**, *23* (2), 867–880. https://doi.org/10.1039/D0GC02831B.

(29) Hauch, A.; Küngas, R.; Blennow, P.; Hansen, A. B.; Hansen, J. B.; Mathiesen, B. V.; Mogensen, M. B. Recent Advances in Solid Oxide Cell Technology for Electrolysis. *Science (1979)* **2020**, *370* (6513). https://doi.org/10.1126/science.aba6118.

(30) Wang, W.; Gan, L.; Lemmon, J. P.; Chen, F.; Irvine, J. T. S.; Xie, K. Enhanced Carbon Dioxide Electrolysis at Redox Manipulated Interfaces. *Nat. Commun.* **2019**, *10* (1), 1550. https://doi.org/10.1038/s41467-019-09568-1.

(31) Bai, L.; Li, H.; Yan, Z.; Hao, X.; Ke, M.; Xie, K.; Li, B. New Insight into the Doped Strontium Titanate Cathode with In Situ Exsolved Nickel Nanoparticles for Electrolysis of Carbon Dioxide. *Adv. Mater. Interfaces* **2021**, *8* (3). https://doi.org/10.1002/admi.202001598.

(32) Wang, W.; Gan, L.; Lemmon, J. P.; Chen, F.; Irvine, J. T. S.; Xie, K. Enhanced Carbon Dioxide Electrolysis at Redox Manipulated Interfaces. *Nat. Commun.* **2019**, *10* (1), 1550. https://doi.org/10.1038/s41467-019-09568-1.

(33) Tian, Y.; Manzotti, A.; Wang, Y.; Song, Y.; Fu, X.-Z.; Chi, B.; Ciucci, F. Achieving Net-Zero Emissions with Solid Oxide Electrolysis Cells: The Power-to-X Approach. *J. Phys. Chem. Lett.* **2023**, *14* (20), 4688–4695. https://doi.org/10.1021/acs.jpclett.3c00140.

(34) Liu, G.; Hagelin-Weaver, H.; Welt, B. A Concise Review of Catalytic Synthesis of Methanol from Synthesis Gas. *Waste* **2023**, *1* (1), 228–248. https://doi.org/10.3390/waste1010015.

(35) Prieto, G.; Schüth, F. The Yin and Yang in the Development of Catalytic Processes: Catalysis Research and Reaction Engineering. *Angewandte Chemie International Edition* **2015**, *54* (11), 3222–3239. https://doi.org/10.1002/anie.201409885.

(36) Álvarez, A.; Bansode, A.; Urakawa, A.; Bavykina, A. V.; Wezendonk, T. A.; Makkee, M.; Gascon, J.; Kapteijn, F. Challenges in the Greener Production of Formates/Formic Acid, Methanol, and DME by Heterogeneously Catalyzed CO_2 Hydrogenation Processes. *Chem Rev* **2017**, *117* (14), 9804–9838. https://doi.org/10.1021/acs.chemrev.6b00816.

(37) Frei, M. S.; Mondelli, C.; Cesarini, A.; Krumeich, F.; Hauert, R.; Stewart, J. A.; Curulla Ferré, D.; Pérez-Ramírez, J. Role of Zirconia in Indium Oxide-Catalyzed CO_2 Hydrogenation to Methanol. *ACS Catal.* **2020**, *10* (2), 1133–1145. https://doi.org/10.1021/acscatal.9b03305.

(38) Martin, O.; Martín, A. J.; Mondelli, C.; Mitchell, S.; Segawa, T. F.; Hauert, R.; Drouilly, C.; Curulla-Ferré, D.; Pérez-Ramírez, J. Indium Oxide as a Superior

Catalyst for Methanol Synthesis by CO_2 Hydrogenation. *Angewandte Chemie* **2016**, *128* (21), 6369–6373. https://doi.org/10.1002/ange.201600943.

(39) Yang, M.; Fan, D.; Wei, Y.; Tian, P.; Liu, Z. Recent Progress in Methanol-to-Olefins (MTO) Catalysts. *Advanced Materials* **2019**, *31* (50). https://doi.org/10.1002/adma.201902181.

(40) Tian, P.; Wei, Y.; Ye, M.; Liu, Z. Methanol to Olefins (MTO): From Fundamentals to Commercialization. *ACS Catal* **2015**, *5* (3), 1922–1938. https://doi.org/10.1021/acscatal.5b00007.

(41) Nielsen, A. Review of ammonia catalysis. *Catalysis Reviews* **1971**, *4* (1), 1–26. https://doi.org/10.1080/01614947108075483.

(42) Nielsen, A. Ammonia Synthesis: Exploratory and Applied Research. *Catalysis Reviews* **1981**, *23* (1–2), 17–51. https://doi.org/10.1080/03602458108068067.

(43) Rouwenhorst, K. H. R.; Elishav, O.; Mosevitzky Lis, B.; Grader, G. S.; Mounaïm-Rousselle, C.; Roldan, A.; Valera-Medina, A. Future Trends. In *Techno-Economic Challenges of Green Ammonia as an Energy Vector*; Elsevier, **2021**, 303–319. https://doi.org/10.1016/B978-0-12-820560-0.00013-8.

(44) Yu, X.; Lin, B.; Lin, J.; Wang, R.; Wei, K. A Novel Fused Iron Catalyst for Ammonia Synthesis Promoted with Rare Earth Gangue. *Journal of Rare Earths* **2008**, *26* (5), 711–716. https://doi.org/10.1016/S1002-0721(08)60168-4.

(45) Humphreys, J.; Lan, R.; Tao, S. Development and Recent Progress on Ammonia Synthesis Catalysts for Haber–Bosch Process. *Advanced Energy and Sustainability Research* **2021**, *2* (1), 2000043. https://doi.org/10.1002/aesr.202000043.

(46) Ertl, G. Elementary Steps in Heterogeneous Catalysis. *Angewandte Chemie International Edition in English* **1990**, *29* (11), 1219–1227. https://doi.org/10.1002/anie.199012191.

(47) Ertl, G. Reactions at Surfaces: From Atoms to Complexity (Nobel Lecture). *Angewandte Chemie International Edition* **2008**, *47* (19), 3524–3535. https://doi.org/10.1002/anie.200800480.

(48) Inoue, Y.; Kitano, M.; Kim, S.-W.; Yokoyama, T.; Hara, M.; Hosono, H. Highly Dispersed Ru on Electride $[Ca_{24}Al_{28}O_{64}]^{4+}(e^-)_4$ as a Catalyst for Ammonia Synthesis. *ACS Catal.* **2014**, *4* (2), 674–680. https://doi.org/10.1021/cs401044a.

(49) Kitano, M.; Inoue, Y.; Yamazaki, Y.; Hayashi, F.; Kanbara, S.; Matsuishi, S.; Yokoyama, T.; Kim, S.-W.; Hara, M.; Hosono, H. Ammonia Synthesis Using a Stable Electride as an Electron Donor and Reversible Hydrogen Store. *Nat. Chem.* **2012**, *4* (11), 934–940. https://doi.org/10.1038/nchem.1476.

(50) Ravi, M.; Makepeace, J. W. Lithium–Nitrogen–Hydrogen Systems for Ammonia Synthesis: Exploring a More Efficient Pathway Using Lithium Nitride–Hydride. *Chemical Communications* **2022**, *58* (41), 6076–6079. https://doi.org/10.1039/D2CC01345B.

(51) Kitano, M.; Kujirai, J.; Ogasawara, K.; Matsuishi, S.; Tada, T.; Abe, H.; Niwa, Y.; Hosono, H. Low-Temperature Synthesis of Perovskite Oxynitride-Hydrides as Ammonia Synthesis Catalysts. *J. Am. Chem. Soc.* **2019**, *141* (51), 20344–20353. https://doi.org/10.1021/jacs.9b10726.

(52) Jacobsen, C. J. H. Novel Class of Ammonia Synthesis Catalysts. *Chemical Communications* **2000**, No. 12, 1057–1058. https://doi.org/10.1039/b002930k.

(53) Jacobsen, C. J. H. Novel Class of Ammonia Synthesis Catalysts. *Chemical Communications* **2000**, No. 12, 1057–1058. https://doi.org/10.1039/b002930k.

(54) International Energy Agency (IEA). *Ammonia Technology Roadmap*; **2021**.

(55) Lee, B.; Winter, L. R.; Lee, H.; Lim, D.; Lim, H.; Elimelech, M. Pathways to a Green Ammonia Future. *ACS Energy Lett* **2022**, *7* (9), 3032–3038. https://doi.org/10.1021/acsenergylett.2c01615.

(56) Patel, G. H.; Havukainen, J.; Horttanainen, M.; Soukka, R.; Tuomaala, M. Climate Change Performance of Hydrogen Production Based on Life Cycle Assessment. *Green Chemistry* **2024**, *26* (2), 992–1006. https://doi.org/10.1039/D3GC02410E.

(57) García-Gutiérrez, P.; Jacquemin, J.; McCrellis, C.; Dimitriou, I.; Taylor, S. F. R.; Hardacre, C.; Allen, R. W. K. Techno-Economic Feasibility of Selective CO_2 Capture Processes from Biogas Streams Using Ionic Liquids as Physical Absorbents. *Energy & Fuels* **2016**, *30* (6), 5052–5064. https://doi.org/10.1021/acs.energyfuels.6b00364.

(58) Cao, L.; Yu, I. K. M.; Xiong, X.; Tsang, D. C. W.; Zhang, S.; Clark, J. H.; Hu, C.; Ng, Y. H.; Shang, J.; Ok, Y. S. Biorenewable Hydrogen Production through Biomass Gasification: A Review and Future Prospects. *Environ. Res.* **2020**, *186*, 109547. https://doi.org/10.1016/j.envres.2020.109547.

(59) Forum Agenda. *Grey, blue, green-why are there so many colours of hydrogen*. World Economic Forum.

(60) International Renewable Energy Agency, I. *Green Hydrogen: A Guide to Policy Making*; Abu Dhabi, **2020**.

(61) Valente, A.; Iribarren, D.; Dufour, J. Life Cycle Sustainability Assessment of Hydrogen from Biomass Gasification: A Comparison with Conventional Hydrogen. *Int. J. Hydrogen Energy* **2019**, *44* (38), 21193–21203. https://doi.org/10.1016/j.ijhydene.2019.01.105.

(62) Sánchez-Bastardo, N.; Schlögl, R.; Ruland, H. Methane Pyrolysis for Zero-Emission Hydrogen Production: A Potential Bridge Technology from Fossil Fuels to a Renewable and Sustainable Hydrogen Economy. *Ind Eng Chem Res* **2021**, *60* (32), 11855–11881. https://doi.org/10.1021/acs.iecr.1c01679.

(63) Machhammer, O.; Bode, A.; Hormuth, W. Financial and Ecological Evaluation of Hydrogen Production Processes on Large Scale. *Chem. Eng. Technol.* **2016**, *39* (6), 1185–1193. https://doi.org/10.1002/ceat.201600023.

(64) Sánchez-Bastardo, N.; Schlögl, R.; Ruland, H. Methane Pyrolysis for Zero-Emission Hydrogen Production: A Potential Bridge Technology from Fossil Fuels to a Renewable and Sustainable Hydrogen Economy. *Ind. Eng. Chem. Res.* **2021**, *60* (32), 11855–11881. https://doi.org/10.1021/acs.iecr.1c01679.

(65) Millet, P.; Grigoriev, S. Water Electrolysis Technologies. In *Renewable Hydrogen Technologies*; Elsevier, **2013**; 19–41. https://doi.org/10.1016/B978-0-444-56352-1.00002-7.

(66) Brauns, J.; Turek, T. Alkaline Water Electrolysis Powered by Renewable Energy: A Review. *Processes* **2020**, *8* (2), 248. https://doi.org/10.3390/pr8020248.

(67) Shiva Kumar, S.; Himabindu, V. Hydrogen Production by PEM Water Electrolysis – A Review. *Mater. Sci. Energy Technol.* **2019**, *2* (3), 442–454. https://doi.org/10.1016/j.mset.2019.03.002.

(68) Benghanem, M.; Mellit, A.; Almohamadi, H.; Haddad, S.; Chettibi, N.; Alanazi, A. M.; Dasalla, D.; Alzahrani, A. Hydrogen Production Methods Based on Solar and Wind Energy: A Review. *Energies (Basel)* **2023**, *16* (2), 757. https://doi.org/10.3390/en16020757.

(69) Singh, A. R.; Rohr, B. A.; Schwalbe, J. A.; Cargnello, M.; Chan, K.; Jaramillo, T. F.; Chorkendorff, I.; Nørskov, J. K. Electrochemical Ammonia Synthesis—The Selectivity Challenge. *ACS Catal.* **2017**, *7* (1), 706–709. https://doi.org/10.1021/acscatal.6b03035.

(70) Montoya, J. H.; Tsai, C.; Vojvodic, A.; Nørskov, J. K. The Challenge of Electrochemical Ammonia Synthesis: A New Perspective on the Role of Nitrogen Scaling Relations. *ChemSusChem* **2015**, *8* (13), 2180–2186. https://doi.org/10.1002/cssc.201500322.

(71) Yang, D.; Chen, T.; Wang, Z. Electrochemical Reduction of Aqueous Nitrogen (N_2) at a Low Overpotential on (110)-Oriented Mo Nanofilm. *J. Mater. Chem. A Mater.* **2017**, *5* (36), 18967–18971. https://doi.org/10.1039/C7TA06139K.

(72) Jin, H.; Li, L.; Liu, X.; Tang, C.; Xu, W.; Chen, S.; Song, L.; Zheng, Y.; Qiao, S. Nitrogen Vacancies on 2D Layered W_2N_3: A Stable and Efficient Active Site for Nitrogen Reduction Reaction. *Advanced Materials* **2019**, *31* (32). https://doi.org/10.1002/adma.201902709.

(73) Yang, X.; Nash, J.; Anibal, J.; Dunwell, M.; Kattel, S.; Stavitski, E.; Attenkofer, K.; Chen, J. G.; Yan, Y.; Xu, B. Mechanistic Insights into Electrochemical Nitrogen Reduction Reaction on Vanadium Nitride Nanoparticles. *J. Am. Chem. Soc.* **2018**, *140* (41), 13387–13391. https://doi.org/10.1021/jacs.8b08379.

(74) Lv, C.; Yan, C.; Chen, G.; Ding, Y.; Sun, J.; Zhou, Y.; Yu, G. An Amorphous Noble-Metal-Free Electrocatalyst That Enables Nitrogen Fixation under Ambient Conditions. *Angewandte Chemie International Edition* **2018**, *57* (21), 6073–6076. https://doi.org/10.1002/anie.201801538.

(75) Tao, H.; Choi, C.; Ding, L.-X.; Jiang, Z.; Han, Z.; Jia, M.; Fan, Q.; Gao, Y.; Wang, H.; Robertson, A. W.; Hong, S.; Jung, Y.; Liu, S.; Sun, Z. Nitrogen Fixation by Ru

Single-Atom Electrocatalytic Reduction. *Chem.* **2019**, *5* (1), 204–214. https://doi.org/10.1016/j.chempr.2018.10.007.

(76) Liu, Y.; Su, Y.; Quan, X.; Fan, X.; Chen, S.; Yu, H.; Zhao, H.; Zhang, Y.; Zhao, J. Facile Ammonia Synthesis from Electrocatalytic N_2 Reduction under Ambient Conditions on N-Doped Porous Carbon. *ACS Catal.* **2018**, *8* (2), 1186–1191. https://doi.org/10.1021/acscatal.7b02165.

(77) Chen, S.; Perathoner, S.; Ampelli, C.; Mebrahtu, C.; Su, D.; Centi, G. Electrocatalytic Synthesis of Ammonia at Room Temperature and Atmospheric Pressure from Water and Nitrogen on a Carbon-Nanotube-Based Electrocatalyst. *Angewandte Chemie International Edition* **2017**, *56* (10), 2699–2703. https://doi.org/10.1002/anie.201609533.

(78) Hu, L.; Xing, Z.; Feng, X. Understanding the Electrocatalytic Interface for Ambient Ammonia Synthesis. *ACS Energy Lett.* **2020**, *5* (2), 430–436. https://doi.org/10.1021/acsenergylett.9b02679.

(79) Duan, G.; Chen, Y.; Tang, Y.; Gasem, K. A. M.; Wan, P.; Ding, D.; Fan, M. Advances in Electrocatalytic Ammonia Synthesis under Mild Conditions. *Prog. Energy Combust. Sci.* **2020**, *81*, 100860. https://doi.org/10.1016/j.pecs.2020.100860.

(80) Montoya, J. H.; Tsai, C.; Vojvodic, A.; Nørskov, J. K. The Challenge of Electrochemical Ammonia Synthesis: A New Perspective on the Role of Nitrogen Scaling Relations. *ChemSusChem* **2015**, *8* (13), 2180–2186. https://doi.org/10.1002/cssc.201500322.

(81) Li, S.; Zhou, Y.; Li, K.; Saccoccio, M.; Sažinas, R.; Andersen, S. Z.; Pedersen, J. B.; Fu, X.; Shadravan, V.; Chakraborty, D.; Kibsgaard, J.; Vesborg, P. C. K.; Nørskov, J. K.; Chorkendorff, I. Electrosynthesis of Ammonia with High Selectivity and High Rates via Engineering of the Solid-Electrolyte Interphase. *Joule* **2022**, *6* (9), 2083–2101. https://doi.org/10.1016/j.joule.2022.07.009.

(82) Andrussow, L. Über Die Katalytische Oxydation von Ammoniak-Methan-Gemischen Zu Blausäure. *Angewandte Chemie* **1935**, *48* (37), 593–595. https://doi.org/10.1002/ange.19350483702.

(83) Hasenberg, D.; Schmidt, L. D. HCN Synthesis from CH_4 and NH_3 on Clean Rh. *J. Catal.* **1985**, *91* (1), 116–131. https://doi.org/10.1016/0021-9517(85)90294-5.

(84) Hasenberg, D.; Schmidt, L. D. HCN Synthesis from CH_4 and NH_3 on Platinum. *J. Catal.* **1986**, *97* (1), 156–168. https://doi.org/10.1016/0021-9517(86)90046-1.

(85) Hasenberg, D.; Schmidt, L. D. HCN Synthesis from CH_4, NH_3, and O_2 on Clean Pt. *J. Catal.* **1987**, *104* (2), 441–453. https://doi.org/10.1016/0021-9517(87)90376-9.

(86) Kondratenko, V. A. Mechanistic Aspects of the Andrussow Process over Pt–Rh Gauzes. Pathways of Formation and Consumption of HCN. *Appl. Catal. A Gen* **2010**, *381* (1–2), 74–82. https://doi.org/10.1016/j.apcata.2010.03.012.

(87) Kondratenko, V. A. Mechanistic Analysis of Oxygen-Assisted Coupling of Methane and Ammonia to Hydrogen Cyanide over Polycrystalline Pt and Rh. *Catal. Sci. Technol.* **2015**, *5* (3), 1598–1605. https://doi.org/10.1039/C4CY01305K.

(88) Aschi, M.; Brönstrup, M.; Diefenbach, M.; Harvey, J. N.; Schröder, D.; Schwarz, H. A Gas-Phase Model for the Pt^+-Catalyzed Coupling of Methane and Ammonia. *Angewandte Chemie International Edition* **1998**, *37* (6), 829–832. https://doi.org/10.1002/(SICI)1521-3773(19980403)37:6<829::AID-ANIE829>3.0.CO;2-N.

(89) Horn, R.; Mestl, G.; Thiede, M.; Jentoft, F. C.; Schmidt, P. M.; Bewersdorf, M.; Weber, R.; Schlögl, R. Gas Phase Contributions to the Catalytic Formation of HCN from CH_4 and NH_3 over Pt: An in Situ Study by Molecular Beam Mass Spectrometry with Threshold Ionization. *Phys. Chem. Chem. Phys.* **2004**, *6* (18), 4514–4521. https://doi.org/10.1039/B407897G.

(90) Gómez-Díaz, J.; López, N. Mechanistic Switch between Oxidative (Andrussow) and Nonoxidative (Degussa) Formation of HCN on Pt(111) by Density Functional Theory. *The Journal of Physical Chemistry C* **2011**, *115* (13), 5667–5674. https://doi.org/10.1021/jp1093349.

(91) Hou, X.; Geng, Z.; Wang, Y.; Liu, S. The Small Metal Cluster $IrAu^+$ Mediated C–N Coupling: A Density Functional Theory Study. *Comput. Theor. Chem.* **2012**, *983*, 76–82. https://doi.org/10.1016/j.comptc.2012.01.002.

(92) Grabow, L. C.; Studt, F.; Abild-Pedersen, F.; Petzold, V.; Kleis, J.; Bligaard, T.; Nørskov, J. K. Descriptor-Based Analysis Applied to HCN Synthesis from NH_3 and CH_4. *Angewandte Chemie International Edition* **2011**, *50* (20), 4601–4605. https://doi.org/10.1002/anie.201100353.

(93) New Shawinigan Process Lowers Production Cost of Hydrogen Cyanide. *Chemical & Engineering News Archive* **1961**, *39* (41), 1. https://doi.org/10.1021/cen-v039n041.p001.

(94) Suganuma, N.; Ghampson, I. T.; Miura, H.; Murakami, J.; Bando, K. K.; Kodaira, T.; Yamasaki, T.; Takagaki, A.; Ishihara, T.; Shishido, T. Methane Activation with Nitric Oxide at Low Temperatures on Supported Pt Catalysts: Effects of the Support. *Catal. Sci. Technol.* **2023**, *13* (13), 3927–3939. https://doi.org/10.1039/D3CY00555K.

(95) Yamasaki, T.; Nishida, A.; Suganuma, N.; Song, Y.; Li, X.; Murakami, J.; Kodaira, T.; Bando, K. K.; Ishihara, T.; Shishido, T.; Takagaki, A. Low-Temperature Activation of Methane with Nitric Oxide and Formation of Hydrogen Cyanide over an Alumina-Supported Platinum Catalyst. *ACS Catal.* **2021**, *11* (23), 14660–14668. https://doi.org/10.1021/acscatal.1c04548.

(96) Yamasaki, T.; Takagaki, A.; Shishido, T.; Bando, K. K.; Kodaira, T.; Murakami, J.; Song, J. T.; Niwa, E.; Watanabe, M.; Ishihara, T. Particle Size Effect on Hydrogen Cyanide Synthesis with CH_4 and NO over an Alumina-Supported Platinum Catalyst. *Journal of the Japan Petroleum Institute* **2022**, *65* (5), 184–191. https://doi.org/10.1627/jpi.65.184.

(97) Yi, Y.; Wang, X.; Jafarzadeh, A.; Wang, L.; Liu, P.; He, B.; Yan, J.; Zhang, R.; Zhang, H.; Liu, X.; Guo, H.; Neyts, E. C.; Bogaerts, A. Plasma-Catalytic Ammonia Reforming of Methane over Cu-Based Catalysts for the Production of HCN and H_2 at Reduced Temperature. *ACS Catal.* **2021**, *11* (3), 1765–1773. https://doi.org/10.1021/acscatal.0c04940.

(98) Guo, Z.; Yi, Y.; Wang, L.; Yan, J.; Guo, H. Pt/TS-1 Catalyst Promoted C–N Coupling Reaction in CH_4 –NH_3 Plasma for HCN Synthesis at Low Temperature. *ACS Catal.* **2018**, *8* (11), 10219–10224. https://doi.org/10.1021/acscatal.8b02950.

(99) Moehmel, S.; Steinfeldt, N.; Engelschalt, S.; Holena, M.; Kolf, S.; Baerns, M.; Dingerdissen, U.; Wolf, D.; Weber, R.; Bewersdorf, M. New Catalytic Materials for the High-Temperature Synthesis of Hydrocyanic Acid from Methane and Ammonia by High-Throughput Approach. *Appl. Catal. A Gen* **2008**, *334* (1–2), 73–83. https://doi.org/10.1016/j.apcata.2007.09.035.

(100) *EIC Pathfinder Challenge: Carbon dioxide and nitrogen management and valorisation*. https://eic.ec.europa.eu/eic-funding-opportunities/calls-proposals/eic-pathfinder-challenge-carbon-dioxide-and-nitrogen-management-and-valorisation_en#specific-conditions.

(101) Erisman, J. W.; Sutton, M. A.; Galloway, J.; Klimont, Z.; Winiwarter, W. How a Century of Ammonia Synthesis Changed the World. *Nat. Geosci.* **2008**, *1* (10), 636–639. https://doi.org/10.1038/ngeo325.

(102) Krase, N. W.; Gaddy, V. L. Synthesis of Urea from Ammonia and Carbon Dioxide. *Journal of Industrial & Engineering Chemistry* **1922**, *14* (7), 611–615. https://doi.org/10.1021/ie50151a009.

(103) Pérez-Fortes, M.; Bocin-Dumitriu, A.; Tzimas, E. CO_2 Utilization Pathways: Techno-Economic Assessment and Market Opportunities. *Energy Procedia* **2014**, *63*, 7968–7975. https://doi.org/10.1016/j.egypro.2014.11.834.

(104) Ding, J.; Ye, R.; Fu, Y.; He, Y.; Wu, Y.; Zhang, Y.; Zhong, Q.; Kung, H. H.; Fan, M. Direct Synthesis of Urea from Carbon Dioxide and Ammonia. *Nat. Commun.* **2023**, *14* (1), 4586. https://doi.org/10.1038/s41467-023-40351-5.

(105) Mao, C.; Byun, J.; MacLeod, H. W.; Maravelias, C. T.; Ozin, G. A. Green Urea Production for Sustainable Agriculture. *Joule* **2024**. https://doi.org/10.1016/j.joule.2024.02.021.

(106) Gredig, S. V.; Koeppel, René A.; Baiker, A. Synthesis of Methylamines from CO_2, H_2 and NH_3. Catalytic Behaviour of Various Metal-Alumina Catalysts. *Appl. Catal. A Gen* **1997**, *162* (1–2), 249–260. https://doi.org/10.1016/S0926-860X(97)00107-5.

(107) Gredig, S. V.; Koeppel, RenéA.; Baiker, A. Comparative Study of Synthesis of Methylamines from Carbon Oxides and Ammonia over Cu/Al_2O_3. *Catal. Today* **1996**, *29* (1–4), 339–342. https://doi.org/10.1016/0920-5861(95)00301-0.

(108) Gredig, S. V.; Koeppel, R. A.; Baiker, A. Palladium Catalyzed Synthesis of Methylamines from Carbon Dioxide, Hydrogen and Ammonia. *Catal. Letters* **1997**, *46* (1/2), 49–55. https://doi.org/10.1023/A:1019085511301.

(109) Auer, S. Synthesis of Methylamines from CO_2, H2 and NH_3 over Cu–Mg–Al Mixed Oxides. *J. Mol. Catal. A Chem.* **1999**, *141* (1–3), 193–203. https://doi.org/10.1016/S1381-1169(98)00263-5.

(110) Toyao, T.; Siddiki, S. M. A. H.; Ishihara, K.; Kon, K.; Onodera, W.; Shimizu, K. Heterogeneous Platinum Catalysts for Direct Synthesis of Trimethylamine by *N* -Methylation of Ammonia and Its Surrogates with CO_2 /H_2. *Chem. Lett.* **2017**, *46* (1), 68–70. https://doi.org/10.1246/cl.160875.

(111) Feng, Y.; Yang, H.; Zhang, Y.; Huang, X.; Li, L.; Cheng, T.; Shao, Q. Te-Doped Pd Nanocrystal for Electrochemical Urea Production by Efficiently Coupling Carbon Dioxide Reduction with Nitrite Reduction. *Nano Lett.* **2020**, *20* (11), 8282–8289. https://doi.org/10.1021/acs.nanolett.0c03400.

(112) Li, J.; Kornienko, N. Electrochemically Driven C–N Bond Formation from CO_2 and Ammonia at the Triple-Phase Boundary. *Chem. Sci.* **2022**, *13* (14), 3957–3964. https://doi.org/10.1039/D1SC06590D.

(113) Jouny, M.; Lv, J.-J.; Cheng, T.; Ko, B. H.; Zhu, J.-J.; Goddard, W. A.; Jiao, F. Formation of Carbon–Nitrogen Bonds in Carbon Monoxide Electrolysis. *Nat. Chem.* **2019**, *11* (9), 846–851. https://doi.org/10.1038/s41557-019-0312-z.

(114) Wu, Y.; Jiang, Z.; Lin, Z.; Liang, Y.; Wang, H. Direct Electrosynthesis of Methylamine from Carbon Dioxide and Nitrate. *Nat. Sustain.* **2021**, *4* (8), 725–730. https://doi.org/10.1038/s41893-021-00705-7.

(115) Chen, C.; He, N.; Wang, S. Electrocatalytic C–N Coupling for Urea Synthesis. *Small Science* **2021**, *1* (11), 2100070. https://doi.org/10.1002/smsc.202100070.

(116) Zhu, X.; Zhou, X.; Jing, Y.; Li, Y. Electrochemical Synthesis of Urea on MBenes. *Nat. Commun.* **2021**, *12* (1), 4080. https://doi.org/10.1038/s41467-021-24400-5.

(117) Han, C.; Li, Y.; Li, J.; Qi, M.; Tang, Z.; Xu, Y. Cooperative Syngas Production and C−N Bond Formation in One Photoredox Cycle. *Angewandte Chemie International Edition* **2021**, *60* (14), 7962–7970. https://doi.org/10.1002/anie.202015756.

(118) Clark, A.; Okla, B. Process of Synthesizing Aliphatic Amines. US 2,518,754, 1950.

(119) M. Brown. Patrick; M. Maselli James. Process for Preparing N-Alkylamines. US 3,726,926, **1973**.

(120) Herici-Olivé, G.; Olive, S. Mechanism of the Modified Fischer-Tropsch Synthesis for the Production of Amines. *Journal of Molecular Catalysis* **1978**, *4*, 379–383.

(121) Enders, E.; Flittard, C.; Hillstrung, D. Process for the Production of Methylamine Together with Dimethylamine. US 3,636,153, **1972**.

(122) Bredig, G.; Elöd, E. Process for the Production of Hydrocyanic Acid. US 1,598,707A, **1926**.

(123) Bredig, G.; Elöd, E. Process for the Production of Hydrocyanic Acid. US 1,627,144, **1927**.

(124) Bredig G.; Elöd, E. Process for Production of Hydrocyanic Acid. US 1,634,735, **1927**.

(125) Liebknecht O.. Process for the Manufacture of Hydrocyanic Acid. US 1,626,848A, **1927**.

(126) Lindner, F.; Link, F. Production of Hydrocyanic Acyd. US 1,751,933, **1930**.

(127) Beindl, C. Method of Producing Hydrocyanic Acid. US 1,492,193, **1924**.

(128) J. Velenyi, L.; F. Hardman, H.; A. Pesa, F. Process Hydrocyanic acid from Carbon Monoxide and Ammonia.

(129) W. Gambell, J.; R. Auvie, S. Hydrogen Cyanide Process. US 4,457,904, 1984.

(130) W. Gambell, J.; R. Auvie, S. Hydrogen Cyanide Process, **1984**.

(131) Olive, G.; Olive, S. Process for Preparing Acetonitrile. US 4,179,462, **1979**.

(132) R. Auvil, S.; R. Penquite, C. Process for Preparing Acetonitirle. US 4,272,452, **1981**.

(133) W. Gambell, J.; R. Auvil, S. Acetonitrile Process with Improved Catalysts. US 4,272,451, **1979**.

(134) J. Bartley, W.; L. O'Connor, G. Production of Acetamides with Rhodium-Manganese Catalysts. US 4,244,889, **1981**.

(135) Tatsumi, T.; Kunitomi, S.; Yoshiwara, J.; Muramatsu, A.; Tominaga, H. Synthesis of Acetonitrile and Related Compounds from CO-H_2-NH_3 over Mo/SiO_2. *Catal. Letters* **1989**, *3* (3), 223–226. https://doi.org/10.1007/BF00766397.

(136) N. Kim, K.; M. Lane, A. The Selective Synthesis of Acetonitrile from Carbon Monoxide, Hydrogen, and Ammonia over Mo/SiO_2. *J. Catal.* **1992**, *137* (1), 127–138. https://doi.org/10.1016/0021-9517(92)90144-7.

(137) Johnston, C.; Jorgensen, N.; Rochester, C. H. Infrared Study of Ammonia–Carbon Monoxide Reactions on Silica-Supported Iron Catalysts. *Journal of the Chemical Society, Faraday Transactions 1: Physical Chemistry in Condensed Phases* **1988**, *84* (10), 3605. https://doi.org/10.1039/f19888403605.

(138) Eshelman, L. M.; Delgass, W. N. Acetonitrile Synthesis over Potassium-Promoted, Supported Iron Catalysts. *Catal. Today* **1994**, *21* (1), 229–242. https://doi.org/10.1016/0920-5861(94)80046-4.

(139) Badani, M. V.; Nicholas Delgass, W. The Active Phase of Iron Catalysts for Acetonitrile Synthesis. *J. Catal.* **1999**, *187* (2), 506–517. https://doi.org/10.1006/jcat.1999.2640.

(140) Badani, M. V.; Eshelman, L. M.; Delgass, W. N. Acetonitrile Synthesis from CO, H_2 and NH_3 Over Fe/C and K, Fe/C. Studies in Surface Science and Catalysis **1993**, 175, 1223–1234. https://doi.org/10.1016/S0167-2991(08)64446-8.

(141) Hummel, A. A.; Badani, M. V.; Hummel, K. E.; Delgass, W. N. Acetonitrile Synthesis from CO, H_2, and NH_3 over Iron Catalysts. *J. Catal.* **1993**, *139* (2), 392–405. https://doi.org/10.1006/jcat.1993.1035.

(142) Karroum, H.; Chenakin, S.; Alekseev, S.; Iablokov, V.; Xiang, Y.; Dubois, V.; Kruse, N. Terminal Amines, Nitriles, and Olefins through Catalytic CO Hydrogenation in the Presence of Ammonia. *ACS Catal.* **2021**, *11* (24), 14977–14985. https://doi.org/10.1021/acscatal.1c03645.

(143) Sango, T.; Fischer, N.; Henkel, R.; Roessner, F.; Steen, E. van; Claeys, M. Formation of Nitrogen Containing Compounds from Ammonia Co-Fed to the Fischer–Tropsch Synthesis. *Appl. Catal. A Gen.* **2015**, *502*, 150–156. https://doi.org/10.1016/j.apcata.2015.06.006.

(144) Fischer, N.; Henkel, R.; Kotzé, H.; Fürst, M.; Olivier, J.; Neethling, J.; Claeys, M. Acetonitrile via CO Hydrogenation in the Presence of NH_3. *Catal. Commun.* **2016**, *87*, 14–17. https://doi.org/10.1016/j.catcom.2016.08.019.

(145) J. D. Leonard. Process for the Manufacture of Methylamines. US 3,387,032, 1968.

(146) Corbin, D. R.; Schwarz, S.; Sonnichsen, G. C. Methylamines Synthesis: A Review. *Catal. Today* **1997**, *37* (2), 71–102. https://doi.org/10.1016/S0920-5861(97)00003-5.

(147) S&P Global. *The Nitto Chemical Methylamines Process*; **1991**.

(148) Ashina, Y.; Fujita, T.; Fukatsu, M.; Niwa, K.; Yagi, J. Manufacture of Dimethylamine Using Zeolite Catalyst. Studies in Surface Science and Catalysis, **1986**, 28, 779–786. https://doi.org/10.1016/S0167-2991(09)60947-2.

(149) Segawa, K.; Tachibana, H. Shape-Selective Reactions for Methylamine Synthesis from Methanol and Ammonia. Studies in Surface Science and Catalysis **1993**, 75 1273–1283. https://doi.org/10.1016/S0167-2991(08)64450-X.

(150) Deeba, M.; N. Cochran, R. Highly Active Catalysts for Methanol Amination. US 4,458,092, **1984**.

(151) Deeba, E. M.; J. Ambs, W.; N. Cochran, R. Methanol Amination. US 4,434,300, **1984**.

(152) Verdoliva, V.; Saviano, M.; De Luca, S. Zeolites as Acid/Basic Solid Catalysts: Recent Synthetic Developments. *Catalysts* **2019**, *9* (3), 248. https://doi.org/10.3390/catal9030248.

(153) Corma, A. From Microporous to Mesoporous Molecular Sieve Materials and Their Use in Catalysis. *Chem. Rev.* **1997**, *97* (6), 2373–2420. https://doi.org/10.1021/cr960406n.

(154) Mochida, I. Selective Synthesis of Dimethylamine (DMA) from Methanol and Ammonia over Zeolites. *J. Catal.* **1983**, *82* (2), 313–321. https://doi.org/10.1016/0021-9517(83)90197-5.

(155) Ilao, M. C.; Yamamoto, H.; Segawa, K. Shape-Selective Methylamine Synthesis over Small-Pore Zeolite Catalysts. *J. Catal.* **1996**, *161* (1), 20–30. https://doi.org/10.1006/jcat.1996.0158.

(156) Veefkind, V. A.; Gründling, C.; Lercher, J. A. Steric Aspects in Methylamine and Dimethylether Synthesis over Acidic Mordenites. *J. Mol. Catal. A Chem.* **1998**, *134* (1–3), 111–119. https://doi.org/10.1016/S1381-1169(98)00027-2.

(157) F. Brazdil, J.; G. Attig, T.; K. Grasselli, R. Ammoxidation of Methanol to Produce Hydrogen Cyanide, **1983**.

(158) T. G. Attig; Grasselli, R. K. Ammoxidation of Methanol to Produce Hydrogen Cyanide. 4,511,548, **1985**.

(159) Process for Oxidation and Ammoxidation. EU0121032 A1, **1983**.

(160) Ebner, J. R.; Gleaves, J. T.; Kuechler, T. C.; Li, T. P. Ammoxidation of Methanol to Hydrogen Cyanide. *ACS Symposium Series* **1987**, 328, 189–205. https://doi.org/10.1021/bk-1987-0328.ch013.

(161) Højlund Nielsen, P. E.; Nielsen, M.; Olsen, B. K. Production of Acetonitrile and/or Hydrogen Cyanide from Ammonia and Methanol. US 2020/0095193A1, **2018**.

(162) H. Nielsen, P. E.; Nielsen, R. M.; Olsen, B. K. Production of Acetonitrile and/ or Hydrogen Cyanide from Ammonia and Methanol. WO 2018/141826A1, **2018**.

(163) Kang, D.-C.; Kim, E.-J.; Kim, D.-P.; Shin, C.-H. Amination of Methanol for Selective Production of Acetonitrile over Zn-Al Mixed Oxide Catalysts Synthesized at Different PH. *Appl. Catal. A Gen.* **2022**, *641*, 118688. https://doi.org/10.1016/j.apcata.2022.118688.

(164) Afanasyev, O. I.; Kuchuk, E.; Usanov, D. L.; Chusov, D. Reductive Amination in the Synthesis of Pharmaceuticals. *Chem. Rev.* **2019**, *119* (23), 11857–11911. https://doi.org/10.1021/acs.chemrev.9b00383.

(165) Corma, A.; Navas, J.; Sabater, M. J. Advances in One-Pot Synthesis through Borrowing Hydrogen Catalysis. *Chem. Rev.* **2018**, *118* (4), 1410–1459. https://doi.org/10.1021/acs.chemrev.7b00340.

(166) Komanoya, T.; Kinemura, T.; Kita, Y.; Kamata, K.; Hara, M. Electronic Effect of Ruthenium Nanoparticles on Efficient Reductive Amination of Carbonyl Compounds. *J. Am. Chem. Soc.* **2017**, *139* (33), 11493–11499. https://doi.org/10.1021/jacs.7b04481.

(167) Shimizu, K.; Kanno, S.; Kon, K.; Hakim Siddiki, S. M. A.; Tanaka, H.; Sakata, Y. N-Alkylation of Ammonia and Amines with Alcohols Catalyzed by Ni-Loaded $CaSiO_3$. *Catal. Today* **2014**, *232*, 134–138. https://doi.org/10.1016/j.cattod.2013.09.002.

(168) Ogata, Y.; Kawasaki, A. The Kinetics of the Reaction of Formaldehyde with Ammonia. *Bull Chem. Soc. Jpn.* **1964**, *37* (4), 514–519. https://doi.org/10.1246/bcsj.37.514.

(169) Meng, N.; Shao, J.; Li, H.; Wang, Y.; Fu, X.; Liu, C.; Yu, Y.; Zhang, B. Electrosynthesis of Formamide from Methanol and Ammonia under Ambient Conditions. *Nat. Commun.* **2022**, *13* (1), 5452. https://doi.org/10.1038/s41467-022-33232-w.

(170) Prieto, G.; Martínez, A.; Murciano, R.; Arribas, M. A. Cobalt Supported on Morphologically Tailored SBA-15 Mesostructures: The Impact of Pore Length on Metal Dispersion and Catalytic Activity in the Fischer–Tropsch Synthesis. *Appl. Catal. A Gen.* **2009**, *367* (1–2), 146–156. https://doi.org/10.1016/j.apcata.2009.08.003.

(171) Prieto, G.; De Mello, M. I. S.; Concepción, P.; Murciano, R.; Pergher, S. B. C.; Martínez, A. Cobalt-Catalyzed Fischer–Tropsch Synthesis: Chemical Nature of the Oxide Support as a Performance Descriptor. *ACS Catal.* **2015**, *5* (6), 3323–3335. https://doi.org/10.1021/acscatal.5b00057.

(172) Jeong, N. C.; Lee, J. S.; Tae, E. L.; Lee, Y. J.; Yoon, K. B. Acidity Scale for Metal Oxides and Sanderson's Electronegativities of Lanthanide Elements. *Angewandte Chemie International Edition* **2008**, *47* (52), 10128–10132. https://doi.org/10.1002/anie.200803837.

(173) Kim, J.; Sarma, B. B.; Andrés, E.; Pfänder, N.; Concepción, P.; Prieto, G. Surface Lewis Acidity of Periphery Oxide Species as a General Kinetic Descriptor for CO_2 Hydrogenation to Methanol on Supported Copper Nanoparticles. *ACS Catal.* **2019**, *9* (11), 10409–10417. https://doi.org/10.1021/acscatal.9b02412.

(174) Van den Berg, R.; Prieto, G.; Korpershoek, G.; van der Wal, L. I.; van Bunningen, A. J.; Lægsgaard-Jørgensen, S.; de Jongh, P. E.; de Jong, K. P. Structure Sensitivity of Cu and CuZn Catalysts Relevant to Industrial Methanol Synthesis. *Nat. Commun.* **2016**, *7* (1), 13057. https://doi.org/10.1038/ncomms13057.

(175) Vogt, C.; Weckhuysen, B. M. The Concept of Active Site in Heterogeneous Catalysis. *Nat. Rev. Chem.* **2022**, *6* (2), 89–111. https://doi.org/10.1038/s41570-021-00340-y.

(176) Hammer, B.; Norskov, J. K. Why Gold Is the Noblest of All the Metals. *Nature* **1995**, *376* (6537), 238–240. https://doi.org/10.1038/376238a0.

(177) Fechete, I. Paul Sabatier– The Father of the Chemical Theory of Catalysis. *Comptes Rendus Chimie* **2016**, *19* (11–12), 1374–1381. https://doi.org/10.1016/j.crci.2016.08.006.

(178) Medford, A. J.; Vojvodic, A.; Hummelshøj, J. S.; Voss, J.; Abild-Pedersen, F.; Studt, F.; Bligaard, T.; Nilsson, A.; Nørskov, J. K. From the Sabatier Principle to a Predictive Theory of Transition-Metal Heterogeneous Catalysis. *J. Catal.* **2015**, *328*, 36–42. https://doi.org/10.1016/j.jcat.2014.12.033.

(179) Jacobsen, C. J. H.; Dahl, S.; Clausen, B. S.; Bahn, S.; Logadottir, A.; Nørskov, J. K. Catalyst Design by Interpolation in the Periodic Table: Bimetallic Ammonia Synthesis Catalysts. *J. Am. Chem. Soc.* **2001**, *123* (34), 8404–8405. https://doi.org/10.1021/ja010963d.

(180) Titmuss, S.; Wander, A.; King, D. A. Reconstruction of Clean and Adsorbate-Covered Metal Surfaces. *Chem. Rev.* **1996**, *96* (4), 1291–1306. https://doi.org/10.1021/cr950214c.

(181) Kayode, G. O.; Montemore, M. M. Factors Controlling Oxophilicity and Carbophilicity of Transition Metals and Main Group Metals. *J. Mater. Chem. A Mater.* **2021**, *9* (39), 22325–22333. https://doi.org/10.1039/D1TA06453C.

(182) Furukawa, S.; Komatsu, T. Intermetallic Compounds: Promising Inorganic Materials for Well-Structured and Electronically Modified Reaction Environments for Efficient Catalysis. *ACS Catal.* **2017**, *7* (1), 735–765. https://doi.org/10.1021/acscatal.6b02603.

(183) Shan, S.; Petkov, V.; Yang, L.; Mott, D.; Wanjala, B. N.; Cai, F.; Chen, B. H.; Luo, J.; Zhong, C.-J. Oxophilicity and Structural Integrity in Maneuvering Surface Oxygenated Species on Nanoalloys for CO Oxidation. *ACS Catal.* **2013**, *3* (12), 3075–3085. https://doi.org/10.1021/cs400700r.

(184) Kepp, K. P. A Quantitative Scale of Oxophilicity and Thiophilicity. *Inorg. Chem.* **2016**, *55* (18), 9461–9470. https://doi.org/10.1021/acs.inorgchem.6b01702.

(185) Chavez, S.; Werghi, B.; Sanroman Gutierrez, K. M.; Chen, R.; Lall, S.; Cargnello, M. Studying, Promoting, Exploiting, and Predicting Catalyst Dynamics: The Next Frontier in Heterogeneous Catalysis. *The Journal of Physical Chemistry C* **2023**, *127* (5), 2127–2146. https://doi.org/10.1021/acs.jpcc.2c06519.

(186) Global Market Insights Inc. *Metal alloys market size*.

(187) Kumar, A.; Bui, V. Q.; Lee, J.; Wang, L.; Jadhav, A. R.; Liu, X.; Shao, X.; Liu, Y.; Yu, J.; Hwang, Y.; Bui, H. T. D.; Ajmal, S.; Kim, M. G.; Kim, S.-G.; Park, G.-S.; Kawazoe, Y.; Lee, H. Moving beyond Bimetallic-Alloy to Single-Atom Dimer Atomic-Interface for All-PH Hydrogen Evolution. *Nat. Commun.* **2021**, *12* (1), 6766. https://doi.org/10.1038/s41467-021-27145-3.

(188) Cortés-Reyes, M.; Azaoum, I.; Molina-Ramírez, S.; Herrera, C.; Larrubia, M. Á.; Alemany, L. J. NiGa Unsupported Catalyst for CO_2 Hydrogenation at Atmospheric Pressure. Tentative Reaction Pathways. *Ind Eng Chem Res* **2021**, *60* (51), 18891–18899. https://doi.org/10.1021/acs.iecr.1c03115.

(189) Mittasch, A.; Frankenburger, W. The Historical Development and Theory of Ammonia Synthesis. *J. Chem. Educ.* **1929**, *6* (12), 2097. https://doi.org/10.1021/ed006p2097.

(190) Kojima, R.; Aika, K. Cobalt Molybdenum Bimetallic Nitride Catalysts for Ammonia Synthesis. *Appl. Catal. A Gen.* **2001**, *215* (1–2), 149–160. https://doi.org/10.1016/S0926-860X(01)00529-4.

(191) Rai, R. K.; Al Maksoud, W.; Morlanés, N.; Harb, M.; Ahmad, R.; Genovese, A.; Hedhili, M. N.; Cavallo, L.; Basset, J.-M. Iron–Cobalt-Based Materials: An Efficient Bimetallic Catalyst for Ammonia Synthesis at Low Temperatures. *ACS Catal.* **2022**, *12* (1), 587–599. https://doi.org/10.1021/acscatal.1c05078.

(192) Hannagan, R. T.; Giannakakis, G.; Flytzani-Stephanopoulos, M.; Sykes, E. C. H. Single-Atom Alloy Catalysis. *Chem. Rev.* **2020**, *120* (21), 12044–12088. https://doi.org/10.1021/acs.chemrev.0c00078.

(193) Hume-Rothery, W.; Mabbott, G. W.; Evans; K. M. Channel. The Freezing Points, Melting Points, and Solid Solubility Limits of the Alloys of Sliver and Copper with the Elements of the b Sub-Groups. *Philosophical Transactions of the Royal Society of London. Series A, Containing Papers of a Mathematical or Physical Character* **1934**, *233* (721–730), 1–97. https://doi.org/10.1098/rsta.1934.0014.

(194) Massalski, T. B. Structure and Stability of Alloys. In *Physical Metallurgy*; Elsevier, 1996; pp 135–204. https://doi.org/10.1016/B978-044489875-3/50007-7.

(195) Nakaya, Y.; Furukawa, S. Catalysis of Alloys: Classification, Principles, and Design for a Variety of Materials and Reactions. *Chem. Rev.* **2023**, *123* (9), 5859–5947. https://doi.org/10.1021/acs.chemrev.2c00356.

(196) Chen, J. G. Carbide and Nitride Overlayers on Early Transition Metal Surfaces: Preparation, Characterization, and Reactivities. *Chem. Rev.* **1996**, *96* (4), 1477–1498. https://doi.org/10.1021/cr950232u.

(197) Sun, W.; Bartel, C. J.; Arca, E.; Bauers, S. R.; Matthews, B.; Orvañanos, B.; Chen, B.-R.; Toney, M. F.; Schelhas, L. T.; Tumas, W.; Tate, J.; Zakutayev, A.; Lany, S.; Holder, A. M.; Ceder, G. A Map of the Inorganic Ternary Metal Nitrides. *Nat. Mater.* **2019**, *18* (7), 732–739. https://doi.org/10.1038/s41563-019-0396-2.

(198) Meschel, S. V.; Kleppa, O. J. Standard Enthalpies of Formation of Some 3d Transition Metal Carbides by High Temperature Reaction Calorimetry. *J. Alloys Compd.* **1997**, *257* (1–2), 227–233. https://doi.org/10.1016/S0925-8388(97)00023-6.

(199) Jaf, Z. N.; Miran, H. A.; Jiang, Z.-T.; Altarawneh, M. Molybdenum Nitrides from Structures to Industrial Applications. *Reviews in Chemical Engineering* **2023**, *39* (3), 329–361. https://doi.org/10.1515/revce-2021-0002.

(200) Jehn, H.; Ettmayer, P. The Molybdenum-Nitrogen Phase Diagram. *Journal of the Less Common Metals* **1978**, *58* (1), 85–98. https://doi.org/10.1016/0022-5088(78)90073-5.

(201) Hägg, G. Regularities in the Crystal Structure with Hydrides, Borides, Carbides and Nitrides of the Transition Elements. *Journal of Physical and Chemistry. Abt. B* **1931**, *12*, 33–56.

(202) Blank, H. Hägg's Rule and Fast Solute Diffusion in Cubic Transition-Metal Phases. *Philosophical Magazine B* **1996**, *73* (5), 833–844. https://doi.org/10.1080/13642819608239156.

(203) Xie, C.; Yan, D.; Li, H.; Du, S.; Chen, W.; Wang, Y.; Zou, Y.; Chen, R.; Wang, S. Defect Chemistry in Heterogeneous Catalysis: Recognition, Understanding, and Utilization. *ACS Catal.* **2020**, *10* (19), 11082–11098. https://doi.org/10.1021/acscatal.0c03034.

(204) Fuertes, A. Metal Oxynitrides as Emerging Materials with Photocatalytic and Electronic Properties. *Mater. Horiz.* **2015**, *2* (5), 453–461. https://doi.org/10.1039/C5MH00046G.

(205) Ted Oyama, S. Crystal Structure and Chemical Reactivity of Transition Metal Carbides and Nitrides. *J Solid State Chem* **1992**, *96* (2), 442–445. https://doi.org/10.1016/S0022-4596(05)80279-8.

(206) Sasaki, T.; Yamamoto, T.; Asano, S.; Niwa, K.; Hasegawa, M. High-Pressure Synthesis and Crystal Structures of Molybdenum Nitride Mo_3N_5 with Anisotropic Compressibility by a Nitrogen Dimer. *Dalton Transactions* **2023**, *52* (2), 469–475. https://doi.org/10.1039/D2DT03433F.

(207) Levy, R. B.; Boudart, M. Platinum-Like Behavior of Tungsten Carbide in Surface Catalysis. *Science (1979)* **1973**, *181* (4099), 547–549. https://doi.org/10.1126/science.181.4099.547.

(208) Teschner, D.; Borsodi, J.; Kis, Z.; Szentmiklósi, L.; Révay, Z.; Knop-Gericke, A.; Schlögl, R.; Torres, D.; Sautet, P. Role of Hydrogen Species in Palladium-Catalyzed Alkyne Hydrogenation. *The Journal of Physical Chemistry C* **2010**, *114* (5), 2293–2299. https://doi.org/10.1021/jp9103799.

(209) Kojima, R.; Aika, K. Molybdenum Nitride and Carbide Catalysts for Ammonia Synthesis. *Appl. Catal. A Gen.* **2001**, *219* (1–2), 141–147. https://doi.org/10.1016/S0926-860X(01)00676-7.

(210) Oyama, S. T. Preparation and Catalytic Properties of Transition Metal Carbides and Nitrides. *Catal. Today* **1992**, *15* (2), 179–200. https://doi.org/10.1016/0920-5861(92)80175-M.

(211) Klimashin, F. F.; Koutná, N.; Euchner, H.; Holec, D.; Mayrhofer, P. H. The Impact of Nitrogen Content and Vacancies on Structure and Mechanical Properties of Mo–N Thin Films. *J. Appl. Phys.* **2016**, *120* (18). https://doi.org/10.1063/1.4966664.

(212) Marquart, W.; Morgan, D. J.; Hutchings, G. J.; Claeys, M.; Fischer, N. Oxygenate Formation over K/β-Mo_2C Catalysts in the Fischer–Tropsch Synthesis. *Catal. Sci. Technol.* **2018**, *8* (15), 3806–3817. https://doi.org/10.1039/C8CY01181H.

(213) Anderson, R. B. Iron Nitrides as Fischer-Tropsch Catalysts. In *Advances in Catalysis*; **1953**, 5, 355–384. https://doi.org/10.1016/S0360-0564(08)60645-8.

(214) Shultz, J. F.; Abelson, Manuel.; Shaw, Leonard.; Anderson, R. B. Fischer-Tropsch Synthesis. Nitrides and Carbonitrides of Iron as Catalysts. *Ind Eng Chem* **1957**, *49* (12), 2055–2060. https://doi.org/10.1021/ie50576a048.

(215) Wang, C.; Zhang, J.; Chen, J. Preparation of Single-phase Iron Nitrides and Investigation of Their Fischer-Tropsch Synthesis Performance. *ChemistrySelect.* **2020**, *5* (13), 3953–3958. https://doi.org/10.1002/slct.202000456.

(216) Volpe, L.; Boudart, M. Ammonia Synthesis on Molybdenum Nitride. *J. Phys. Chem.* **1986**, *90* (20), 4874–4877. https://doi.org/10.1021/j100411a031.

(217) Podila, S.; Zaman, S. F.; Driss, H.; Alhamed, Y. A.; Al-Zahrani, A. A.; Petrov, L. A. Hydrogen Production by Ammonia Decomposition Using High Surface Area Mo_2N and Co_3Mo_3N Catalysts. *Catal. Sci. Technol.* **2016**, *6* (5), 1496–1506. https://doi.org/10.1039/C5CY00871A.

(218) Marquart, W.; Raseale, S.; Prieto, G.; Zimina, A.; Sarma, B. B.; Grunwaldt, J.-D.; Claeys, M.; Fischer, N. CO_2 Reduction over Mo_2C-Based Catalysts. *ACS Catal.* **2021**, *11* (3), 1624–1639. https://doi.org/10.1021/acscatal.0c05019.

(219) Vogt, C.; Groeneveld, E.; Kamsma, G.; Nachtegaal, M.; Lu, L.; Kiely, C. J.; Berben, P. H.; Meirer, F.; Weckhuysen, B. M. Unravelling Structure Sensitivity in CO_2 Hydrogenation over Nickel. *Nat. Catal.* **2018**, *1* (2), 127–134. https://doi.org/10.1038/s41929-017-0016-y.

(220) Nagai, M.; Zahidul, A. Md.; Matsuda, K. Nano-Structured Nickel–Molybdenum Carbide Catalyst for Low-Temperature Water-Gas Shift Reaction. *Appl. Catal. A Gen.* **2006**, *313* (2), 137–145. https://doi.org/10.1016/j.apcata.2006.07.006.

(221) Lausche, A. C.; Schaidle, J. A.; Schweitzer, N.; Thompson, L. T. Nanoscale Carbide and Nitride Catalysts. In *Comprehensive Inorganic Chemistry II*; Elsevier, **2013**, 371–404. https://doi.org/10.1016/B978-0-08-097774-4.00730-0.

(222) Tyutyunnik, A.; Grins, J.; Svensson, G. Rietveld Refinement Studies of Nb_4N_5- and Nb_5N_6-Related Phases in the (Mn)–Nb–O–N System. *J. Alloys Compd.* **1998**, *278* (1–2), 83–91. https://doi.org/10.1016/S0925-8388(97)00496-9.

(223) Yamamoto, S.; Ohashi, Y.; Masubuchi, Y.; Takeda, T.; Motohashi, T.; Kikkawa, S. Niobium–Aluminum Oxynitride Prepared by Ammonolysis of Oxide Precursor Obtained through the Citrate Route. *J. Alloys. Compd.* **2009**, *482* (1–2), 160–163. https://doi.org/10.1016/j.jallcom.2009.03.151.

(224) Kartachova, O.; Glushenkov, A. M.; Chen, Y.; Zhang, H.; Chen, Y. Bimetallic Molybdenum Tungsten Oxynitride: Structure and Electrochemical Properties. *J. Mater. Chem. A Mater.* **2013**, *1* (27), 7889. https://doi.org/10.1039/c3ta10836h.

(225) Ruan, D.; Lin, R.; Jiang, K.; Yu, X.; Zhu, Y.; Fu, Y.; Wang, Z.; Yan, H.; Mai, W. High-Performance Porous Molybdenum Oxynitride Based Fiber Supercapacitors. *ACS Appl. Mater. Interfaces* **2017**, *9* (35), 29699–29706. https://doi.org/10.1021/acsami.7b07522.

(226) Pandey, S. A.; Zhang, C.; Ibrahim, D. H.; Goldfine, E. A.; Wenderott, J. K.; dos Reis, R.; Paul, R. L.; Spanopoulos, I.; Kanatzidis, M.; Bedzyk, M. J.; Dravid, V. P.; González, G. B.; Haile, S. M. Hidden Complexity in the Chemistry of Ammonolysis-Derived "γ-Mo_2N": An Overlooked Oxynitride Hydride. *Chemistry of Materials* **2021**, *33* (17), 6671–6684. https://doi.org/10.1021/acs.chemmater.1c00617.

(227) Miga, K.; Stanczyk, K.; Sayag, C.; Brodzki, D.; Djéga-Mariadassou, G. Bifunctional Behavior of Bulk MoO_xN_y and Nitrided Supported NiMo Catalyst in Hydrodenitrogenation of Indole. *J. Catal.* **1999**, *183* (1), 63–68. https://doi.org/10.1006/jcat.1998.2381.

(228) Sellem, S.; Potvin, C.; Manoli, J. M.; Contan, R.; Djéga-Mariadassou, G. Synthesis and Catalytic Bifunctional Properties of Tungsten Oxynitrides. *J. Chem. Soc., Chem. Commun.* **1995**, No. 3, 359–360. https://doi.org/10.1039/C39950000359.

(229) Ji, S.; Chen, W.; Zhao, Z.; Yu, X.; Park, H. S. Molybdenum Oxynitride Nanoparticles on Nitrogen-Doped CNT Architectures for the Oxygen Evolution Reaction. *Nanoscale Adv.* **2020**, *2* (12), 5659–5665. https://doi.org/10.1039/D0NA00648C.

(230) Dasgupta, A.; Rioux, R. M. Intermetallics in Catalysis: An Exciting Subset of Multimetallic Catalysts. *Catal. Today* **2019**, *330*, 2–15. https://doi.org/10.1016/j.cattod.2018.05.048.

(231) Hodnik, N.; Jeyabharathi, C.; Meier, J. C.; Kostka, A.; Phani, K. L.; Rečnik, A.; Bele, M.; Hočevar, S.; Gaberšček, M.; Mayrhofer, K. J. J. Effect of Ordering of $PtCu_3$ Nanoparticle Structure on the Activity and Stability for the Oxygen Reduction Reaction. *Phys. Chem. Chem. Phys.* **2014**, *16* (27), 13610–13615. https://doi.org/10.1039/C4CP00585F.

(232) Li, C.; Chen, Y.; Zhang, S.; Xu, S.; Zhou, J.; Wang, F.; Wei, M.; Evans, D. G.; Duan, X. Ni–In Intermetallic Nanocrystals as Efficient Catalysts toward Unsaturated Aldehydes Hydrogenation. *Chemistry of Materials* **2013**, *25* (19), 3888–3896. https://doi.org/10.1021/cm4021832.

(233) Chen, X.; Jin, J.; Sha, G.; Li, C.; Zhang, B.; Su, D.; Williams, C. T.; Liang, C. Silicon–Nickel Intermetallic Compounds Supported on Silica as a Highly Efficient Catalyst for CO Methanation. *Catal. Sci. Technol.* **2014**, *4* (1), 53–61. https://doi.org/10.1039/C3CY00743J.

(234) Studt, F.; Sharafutdinov, I.; Abild-Pedersen, F.; Elkjær, C. F.; Hummelshøj, J. S.; Dahl, S.; Chorkendorff, I.; Nørskov, J. K. Discovery of a Ni-Ga Catalyst for Carbon Dioxide Reduction to Methanol. *Nat. Chem.* **2014**, *6* (4), 320–324. https://doi.org/10.1038/nchem.1873.

(235) Takanashi, T.; Nakagawa, Y.; Tomishige, K. Amination of Alcohols with Ammonia in Water over Rh–In Catalyst. *Chem. Lett.* **2014**, *43* (6), 822–824. https://doi.org/10.1246/cl.140051.

CHAPTER 2.

OBJECTIVES

As discussed in the focused introduction (**Chapter 1**), the industrial landscape is undergoing a profound shift towards decarbonization and electrification, aiming to achieve net zero emissions by moving away from conventional feedstocks. Additionally, there is growing industrial interest in short-chain nitriles such as acid cyanide and acetonitrile, while lower rates of global demand increase are expected for acrylonitrile. Hence, there is a compelling case for disconnecting the production of short-chain nitriles from conventional propylene ammoxidation routes, such as the well-established SOHIO process. Leveraging bio/e-*syngas*, or its methanol derivative, and green ammonia presents an opportunity for integrating future renewable C_1 and N_1 cycles in connection to established value chains of the chemical industry. Indispensable towards these developments is the rational development of selective and stable solid catalysts. This requires a comprehensive understanding of the active (working) species in solid catalysts able to concomitantly steer C-N and C-C coupling reactions. This thesis specifically aims to provide this type of information for the process of N-compound formation from NH_3/syngas mixtures. This shall inform catalyst design efforts to progress beyond the current state of the art. Additionally, the formation of C_{2+} nitrogen compounds from the reaction of methanol (as the C_1 source) and ammonia is an emerging and immature approach that requires fundamental studies to understand the nature of the active catalyst and how to stabilize it under process conditions.

The overarching objective of this thesis is to elucidate the working principle of promotional bimetallic effects in processes for the simultaneous conversion of potentially renewable C_1 and N_1 feedstocks to C_{2+} N-compounds, via the integration of C-C and C-N coupling reactions. Specifically, industrially relevant aliphatic nitriles, primarily acetonitrile, are considered as target products. To this end, the study aims to gain bulk and near-surface compositional and structural information on mono- and bimetallic catalysts under *operando* conditions, i.e., while exposed to relevant activation and catalysis conditions. The thesis is structured as follows:

The experimental and computational (Density Functional Theory (DFT) and first principles thermochemistry) methods are described in **Chapter 3**. Emphasis is given to *in situ* and *operando* diffraction and spectroscopy methods reliant on high-coherence and modulable synchrotron radiation. This chapter additionally provides details on the online analytics, based on gas chromatography and mass spectrometry, applied to monitor the catalytic performance of solid catalysts under industrially relevant operation settings.

The results are discussed in **Chapters 4** to **6**. **Chapters 4** and **5** are devoted to studying the conversion of syngas (CO and H_2) and ammonia for the selective synthesis of acetonitrile and higher nitriles on molybdenum-based catalysts. **Chapter 4** integrates the findings from catalytic testing, employing a monometallic molybdenum catalyst, with Density Functional Theory calculations to provide insights into the mechanism underlying the activation of H_2, CO and NH_3 reactants, the sequential C-N and C-C reactions and the role of HCN as key reaction intermediate towards higher nitriles. **Chapter 5** further elaborates on the results presented in **Chapter 4** and discusses the effects of the promotion of molybdenum with first-row divalent transition metals on acetonitrile synthesis. A bimetallic Mn-Mo oxynitride catalyst, derived from a crystalline mixed-metal ammonium molybdate precursor, is shown to provide enhanced nitrile selectivity and stability. For this catalyst, deeper catalytic and *in situ* characterization studies are presented to elucidate the structural evolution of the pre-catalyst into its real active form, as well as to rationalize feasible modes of promotion brought about by the manganese promoter.

Finally, **Chapter 6** extends the study space to the conversion of vapor mixtures of methanol (C_1) and ammonia (N_1) to N-compounds. Focus is placed on performance differences between disordered alloy and ordered intermetallic solid-state solutions, using the Ni-Ga bimetallic system as a showcase. *In situ* and *operando* X-ray diffraction and X-ray absorption spectroscopy are applied to gain insights into the short- and long-range atomic order of selected alloy and intermetallic $NiGa/SiO_2$ bimetallic supported catalysts. Emphasis is given to tracking chemical (e.g. oxidation state) and (nano)structural changes driven by

catalyst activation and usage under relevant process conditions. Structure-performance relations are sought to connect alloy and intermetallic nanostructures to the production of specific N-compounds, i.e., aliphatic nitriles and amines.

CHAPTER 3.

METHODS

3.1 CATALYST SYNTHESIS

In this section, experimental details are provided for catalyst synthesis and conditioning.

3.1.1 Co-precipitation method

The co-precipitation method has emerged as one of the most widely used methods for catalyst synthesis due to its versatile nature and technical simplicity. It involves the simultaneous precipitation of multiple metal ions or compounds from a solution, resulting in the formation of a mixed or composite catalyst material. In this process, two or more precursor compounds containing the desired metal components are dissolved in a common solvent. By adding a precipitating agent, conditions are created that lead to the formation and precipitation of metal hydroxides, oxides, or other solid phases, as catalyst precursors. The concentration and nature of the metal precursors, or/and tensioactive compounds, which may be deliberately added to the synthesis medium, are determinants for the rates of solid nucleation, crystallization, and crystal growth, e.g., via Ostwald ripening mechanisms. In addition, various experimental parameters, including pH, pressure, temperature, stirring speed, aging time of the precipitate in the mother liquors, among others, can also be jointly adjusted to control catalyst composition, particle size and morphology.

This co-precipitation route was used to synthesize a series of ammonium metal (II) molybdate materials (M= Zn, Cu, Ni, Co or Mn),[1] which are discussed in **Chapter 5**. 100 mL of $(NH_4)_6Mo_7O_{24}{\cdot}4H_2O$ aqueous solution (0.04 M, ≥99.3 %, Merck) was prepared and its pH was adjusted to 9.8 by addition of an ammonium hydroxide aqueous solution (25 %). 100 mL of this solution was magnetically stirred and heated to 363 K in an oil bath. Next, 15 mL of a 1.4 M aqueous solution of the corresponding metal nitrate precursor for the divalent first-row transition metal M ($Zn(NO_3)_2.6H_2O$, ≥99 % Sigma-Aldrich; $Cu(NO_3)_2.2.5H_2O$, ≥98 % Alfa Aesar; $Ni(NO_3)_2.6H_2O$, 99.999 % Sigma-Aldrich; $Co(NO_3)_2.6H_2O$, ≥98 % ACROSS organics; or $Mn(NO_3)_2.4H_2O$, 99.999 % Merck) was added drop-wise on

the molybdate solution at a constant rate of 0.5 mL min^{-1} at 363 K. The precipitate was aged in the liquors for 30 min at same temperature, isolated by filtration, washed extensively with boiling water and dried in an oven at 373 K overnight. Different precipitation colors, except Zn (white), were produced depending on the metal used, such as pea green, olive green, purple and sand color for Cu, Ni, Co and Mn, respectively.

3.1.2 Thermal treatment under NH_3/syngas mixture

A series of thermal treatments were performed on selected ammonium manganomolybdate and MoO_3 catalyst precursors under flow $NH_3/CO/H_2$ gas mixtures, which mimics relevant gas feeds for the synthesis of acetonitrile. The aim of these *in situ* thermal treatments is to elucidate the evolution of the chemical composition and crystalline structure with temperature, as it is discussed in **Chapter 5**. Circa 200 mg of the precursor, sieved in the range of 0.2-0.4 μm, were loaded into a packed-bed quartz reactor and exposed to a flow with molar composition of 3 $NH_3/CO/H_2$ for 10 min, stepwise, at temperatures of 523 K, 598 K and at intervals of 50 K from 673 K to 873 K (3 K min^{-1}). Furthermore, longer times on stream (1 h and 10 h) were applied at the finally selected reaction temperature of 723 K. Subsequently to the treatment, the samples were quenched in Argon flow and cooled down to RT by convection. The resulting samples were transferred under exclusion of air and stored in a N_2-filled glove box (O_2 <1 ppm, H_2O<1 ppm).

3.1.3 Reduction-nitridation treatment

A γ-Mo_2N standard material was synthesized from MoO_3 nanopowder (>99.5 %, Merck) by a thermal treatment at 973 K for 5 h (5 K min^{-1}) under flow of 40 vol% N_2 in H_2,[2] in a packed-bed quartz reactor. The resulting molybdenum nitride was applied as reference material for structural characterizations discussed in **Chapters 4** and **5**.

3.1.4 Impregnation method

Impregnation is a catalyst synthesis method that involves the deposition of metal, more generally active species, onto a support material. In this technique, a support material, often porous, is brought in contact with a solution containing precursors of the catalytically active species to be incorporated thereon. In its *incipient wetness* version, the volume of impregnating solution equals the pore volume available in the support material. Therefore, this technique requires previous prior knowledge of the textural properties of the support material. The solution is driven inside the pores of the carrier by capillarity forces. Following liquid uptake, the solid appears macroscopically "dry". Alternatively, the support material is brought in contact with an excess of solution relative to the available pore volume and the solvent is thereafter removed by controlled evaporation, e.g., in a rotary evaporator. This method was employed in the synthesis of a series of SiO_2-supported Ni and NiGa catalysts discussed in **Chapter 6**.

Experimentally, the series of supported $Ni_{(1-x)}Ga_x/SiO_2$ (x= 0.02, 0.05, 0.1, 0.2, 0.3, 0.4, 0.5, 0.6) was synthesized by incipient wet impregnation of Silica gel (110 $m^2\ g^{-1}$, 28.5 nm, 0.83 $cm^3\ g^{-1}$, Silicycle Inc.) with nickel nitrate and gallium nitrate aqueous solutions (4 M, in 0.1 M HNO_3(aq)). Nitrate precursors were selected to yield higher metal contents, compared to alternative organic metal precursors, owing to the high solubility of the former in water. To obtain the precursor stock solutions, $Ni(NO_3)_3.\ 6H_2O$ (Sigma-Aldrich, 99.999 %) and $Ga(NO_3)_2.\ XH_2O$ (X= 9) (Sigma-Aldrich, 99.9 %) were dissolved in 0.1 M HNO_3(aq)) at individual concentrations to attain preset Ni/Ga atomic ratios from 0 to 0.7. Following impregnation to incipient wetness, the pore-confined nitrate precursors were converted into the corresponding oxide derivatives following the NO-assisted nitrate decomposition method developed by de Jong and coworkers.[3–5] The powder solids were loaded into a quartz packed-bed reactor, wherein a flow of 2 vol% NO in He was established (60 mL min^{-1}). Finally, the temperature was increased to 623 K with a heating rate of 2 K min^{-1}, followed by 3 h dwell time at this temperature to enable metal nitrate decomposition.

3.1.5 Reduction treatment

The series of supported $Ni_{(1-x)}Ga_x/SiO_2$ (x= 0.02, 0.05, 0.1, 0.2, 0.3, 0.4, 0.5, 0.6) were *ex situ* reduced and handled under exclusion of air for a first crystal structure elucidation after activation. The results thereof are discussed in **Chapter 6**. 0.15 g were placed in a U-shape reactor under 75 mL min^{-1} of pure H_2 (Linde, 99.9999%). The temperature was raised to 1023 K with a heating rate of 2 K min^{-1}, followed by 5 h dwell time. Finally, the samples were cooled down at room temperature and exposed to 10 mL min^{-1} of 1 vol% O_2 in N_2 (Air products) feed atmosphere for 30 min for surface passivation.

3.2 CATALYST CHARACTERIZATION

The nanoscale particle size and morphology, as well as bulk and near-surface composition of solid catalysts, was characterized at different stages throughout their synthesis, activation and usage, using several physicochemical techniques as detailed in this section.

3.2.1 Inductively coupled plasma optical-emission spectrometry (ICP-OES)

Bulk metal contents were determined by inductively coupled plasma optical-emission spectrometry (ICP-OES) in a Thermoscientific, iCAP PRO spectrometer, previously calibrated with commercial standard solutions. Samples were disaggregated in aqua regia (3:1 v/v HCl/ HNO_3). In the case of air sensitive samples, samples were weighed and disaggregated in a glove bag, under inert Ar atmosphere, in order to prevent uncontrolled (re)oxidation.

3.2.2 Elemental (C, N, H, S) analysis

Elemental analysis provides information about the bulk content of carbon, nitrogen, hydrogen and sulfur (alternatively also oxygen) elements. A small (few mg) sample is combusted in a high-temperature furnace, and combustion products such as carbon dioxide (CO_2), nitrogen oxides (NO_x), water (H_2O), and

sulfur dioxide (SO_2) are quantified by chromatography methods. In this thesis, elemental analysis was performed to determine the N and C content in selected catalysts, in their precursor state as well as following specific treatments or usage under potentially carbidizing and/or nitride gas atmospheres. Experiments were carried out in a Eurovector, EuroEA 3000 CHNS analyzer using sulfanilamide as standard.

3.2.3 N_2-physisorption

N_2 physisorption is widely employed in the characterization of textural properties (specific surface area, pore volume and size distribution) of catalysts and adsorbent materials. N_2 is adsorbed onto the surface of the solid at low temperatures, typically the boiling point for the adsorbate at atmospheric pressure (77 K). The uptake of adsorbed N_2 is measured under isothermal conditions, as a function of the relative pressure (P/P_0, wherein P_0 denotes the saturation pressure at the temperature of analysis). The desorption branch of the isotherm is measured by registering N_2 evaporation upon decreasing P/P_0. The IUPAC categorizes the six most common adsorption isotherms.[6]

N_2 physisorption was applied in this thesis to determine the specific surface area of selected materials, as well as to determine the total mesopore volume of catalyst support materials, as required to deposit catalytically active metals by incipient wetness impregnation, see **Section 3.1.4**. Nitrogen physisorption experiments were performed in an ASAP 2420 apparatus (Micromeritics) at 77 K with an equilibration interval of 20 s. Previous to the measurement, the sample (200 mg, 0.2-0.4 mm sieve range) were degassed at 423 K and 10^{-6} bar overnight. The Brunauer−Emmett−Teller (BET) formalism was used in a relative pressure (P/P_0) range of 0.05-0.3 to determine the specific surface area. Total pore volumes were determined from the N_2 uptake at a relative pressure P/P_0 of 0.95. Average mesopore diameters were determined by applying the Barrett-Joyner-Halenda (BJH) formalism to the desorption branch of the isotherm.

3.2.4 Temperature programmed reduction (H_2-TPR)

The sample reducibility was studied by hydrogen temperature programmed reduction (H_2-TPR). Experiments were carried out in an AMI-200 (Altamira Instruments) equipment. Prior to the experiment, 50 mg of the calcined catalyst was pretreated in argon at 298 K for 15 min. H_2-TPR profiles were recorded when heating the samples from 313 to 1173 K using a heating ramp of 10 °C min^{-1} in 50 mL min^{-1} of 10 % H_2 in Ar flow. The exhaust gases were analyzed by a thermal conductivity detector (TCD).

3.2.5 Raman spectroscopy

Raman spectroscopy is based on the interaction of an incident monochromatic laser light with matter and the study of the frequency shift (Stokes or Anti-Stokes) in the scattered photons. This technique provides insights into vibrational and rotational frequency transitions, offering chemical and structural information. Raman spectroscopy was applied to study the development and assess the graphitic character of carbonaceous deposits on selected catalysts following exposure to reaction conditions. Experimentally, spectra were recorded in a Renishaw inVia "Reflex" Raman spectrometer equipped with an Olympus microscope, a CCD Detector, a He-Ne green laser (514 nm), and a diode laser (785 nm).

3.2.6 X-Ray Diffraction

X-ray diffraction technique relies on the diffraction pattern generated by constructive interferences of a monochromatic beam of X-rays with a periodic lattice structure possessing long-range order. X-rays exhibit wavelengths in the Angstrom (Å) magnitude comparable to the interplanar distances (d_{hkl}) of the parallel lattice planes in crystalline materials (**Figure 3.1. a**), which are described by the Miller index (hkl). A diffraction peak emerges exclusively at certain conditions which fulfill the Bragg´s law (see **Equation 3.1**).

$$n\lambda = 2d_{hkl}\, sin\theta \qquad \textbf{Eq. 3.1}$$

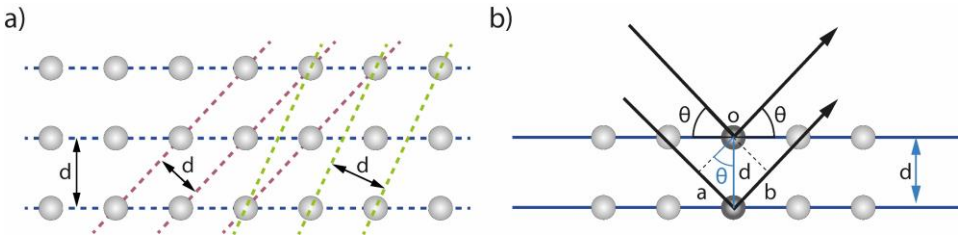

Figure 3.1: *a) Interplanar distances between periodically arranged lattice planes of atoms in a crystal structure. b) Geometric correlation between the interplanar distance (d) and the diffraction angle (θ) of Bragg´s law. Adapted from ref.*[7]

In this context, λ and θ denote the wavelength and the angle of the incident radiation relative to the crystal plane, respectively. The term d_{hkl} represents the interplanar distance between parallel crystal lattice planes defined by Miller indices (hkl). This **equation 3.1** can be derived from geometric correlations between the spacing *d* and the diffraction angle θ, as depicted in **Figure 3.1. b**. As a wave must travel a longer distance (a+b) than the adjacent wave, a constructive interference results when the delay between waves reflecting from adjacent planes is an integer number of the wavelength ($n\lambda$, n= 1, 2, 3, …,).

Powder X-ray diffraction has been applied as a characterization method in the present thesis in two different settings, which are presented in **Sections 3.2.6.1** and **3.2.6.2** below, respectively.

3.2.6.1 Ex situ powder X-ray diffraction (XRPD)

Powder X-ray diffraction is one of the most widely applied methods to determine the structure of polycrystalline powder materials. The diffraction peaks of large and perfect three-dimensional crystallites with undisturbed periodicity are very narrow. Instrumental factors and deviation from the ideal crystalline structure

in nanocrystallites lead to broadening of the diffraction signals. Peak broadening encompasses contributions from strains, dislocations, twinning, stacking faults, antiphase domains and crystallite size (distribution) and shape.

Factors other than crystallite (more precisely crystalline domain) size are disregarded when applying the Scherrer equation, see **Equation 3.2**, to estimate the volume-averaged crystallite size from the analysis of line broadening in powder XRD patterns.[7] This relation reads as follows:

$$L_{hkl} = \frac{k\lambda}{\beta cos\theta} \qquad \textit{Eq. 3.2}$$

Where *L* is the average crystal size, *k* is the Scherrer constant which describes deviations of crystallite shape from sphericity, λ is the wavelength, β is the integral breadth and θ is the angular peak position. The integral breadth is defined as the area under the peak divided by the maximum intensity, and it is often assimilated to the peak full width at half maximum (FWHM), subject to correction by the instrumental line broadening, which is sample independent.[7]

The conventional method for X-rays generation in laboratory devices is based on a cathode and anode in a vacuum chamber. The cathode is the source of high-energy electrons, which are generated by passing a current through a filament typically composed of tungsten. These high-energy electrons are driven by a potential difference towards the anode, based on a metal responsible for the X-ray radiation generation. The anode can consist of Co, Fe, Cr, but most commonly is based on Cu and Mo, with respective X-ray emission wavelengths (λ) of 1,54 and 0.71 Å.[8] As the atomic number of the metal increases, the wavelength of the emitted photon decreases, as dictated by the Moseley´s law. Consequently, heavier metals will produce the shortest wavelengths. This X-ray spectrum is formed by two types of radiation, the continuous spectrum or “bremsstrahlung” and the characteristic radiation of the anode. The latter is produced by the relaxation of the outer electrons into the previously generated vacancies in inner electronic levels of the atom, and it, therefore, is characteristic

of the metal used as anode. If the ionized level is K, the electronic vacancy can be filled by an electron of a M level (K_β radiation) or from a L level (K_α radiation), see **Figure 3.2. a**. The latter is the useful line for diffraction experiments, and it is composed of $K_{\alpha1}$ and $K_{\alpha2}$ components, in which the intensity for the former is double than for the latter, while the $K_{\alpha1}$/ K_β intensity ratio is around 5/1 as summarized in **Figure 3.2, b**. The K_β-line can be partially eliminated using filters (the simplest type of monochromator), such as Ni and Zr filters for Cu and Mo anodes, respectively, or optics elements that limit the divergence of the X-ray beam, focalize the beam in parallel X-rays, remove undesired wavelengths and refocus the parallel producing a better resolution with narrower diffraction peaks but at the price of beam intensity. These optics elements can be formed by Sollers, parallel plane crystal monochromators, slits, parabolic mirrors (Göbel), lenses and monochromators, among others. Regarding X-ray detection, the so-called Bragg-Brentano geometry is the most common in laboratory diffractometers. It involves

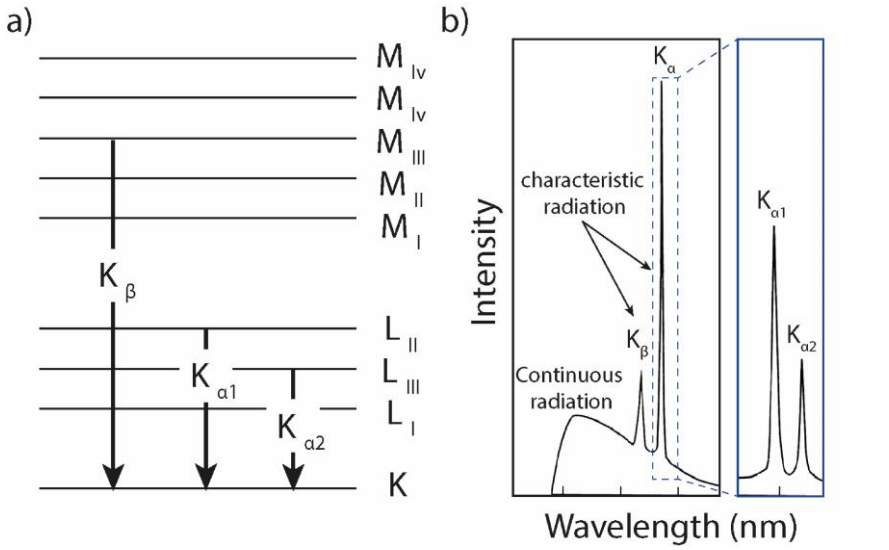

Figure 3.2: *a) Schematic representation of the L and M levels and the generated K_α radiation and K_β radiation by electron relaxation after K level ionization. b) X-ray spectrum scheme of a metallic anode showing the continuously radiation or "Bremsstrahlung" and characteristic radiation. Blue inset provides a magnified view of the K_α radiation. Adapted from ref.*[9]

directing the X-ray beam onto the top, flat surface of the polycrystalline sample at an angle θ and detecting diffracted beams at an angle 2θ using, typically, a scintillation detector.*Ex situ* laboratory X-ray powder diffractograms, i.e., without the concomitant control over the gas atmosphere and temperature the sample is exposed to, were recorded in Bragg-Brentano geometry using a PANalytical CUBIX diffractometer (Cu K_α radiation, λ = 1.5406 Å, λ = 1.5444 Å, I_2/I_1 = 0.5, goniometer radius 200 mm) equipped with a X'Celerator detector. For each measurement, samples were finely grounded and filled in a stainless-steel round holder. Once mounted in the diffractometer, the holders were spined at 20 rpm and the measurement was performed with a fixed divergence slit with a 1/8º aperture, from 3.5 to 90.0 degrees (2θ), with 0.020˚ step^{-1}(2θ) and 35 s step^{-1}.

Following exposure to activation/ reaction conditions or *ex situ* thermal treatments, such as reduction of exposure to reactive atmospheres, air-sensitive samples were handled in a nitrogen-filled glove box (O_2 < 1 ppm, H_2O< 1 ppm) and mounted on an air-tight Si(911) plate holder sealed with Kapton. In this case, measurements were performed with a variable divergence slit irradiating a 3 mm x 10 mm (length x width) sample area, using 0.020 step^{-1} (2θ), 17 s step^{-1} step sizes and scanning speed, respectively.

3.2.6.2 In situ temperature-resolved X-ray powder diffraction

Particularly in catalyst materials, the materials short and long-range structure may change significantly in response to the surrounding chemical potentials of various compounds/elements as well as to operational variables such as total pressure and temperature. This calls for *in situ*/*operando* experimentation to reliably monitor those material structures that exist under relevant conditions for catalyst activation, conditioning, or usage. In **Chapter 6** of this thesis, the effects of ammonia-containing gas atmospheres on the crystalline structure of metal species in selected supported Ni/SiO_2 and $Ni_{0.95}Ga_{0.05}$/SiO_2 catalysts were studied by *in situ* powder XRD, as a function of temperature.

Experimentally, a reaction chamber (Anton Paar XRK900) was mounted in a Rigaku SmartLab diffractometer equipped with a rotating anode (9 kW, 45 kV,

200 mA) and operating in Bragg-Brentano-geometry (CuK$\alpha_{1,2}$, 1.541862 Å) at the Max-Planck-Institut für Kohlenforshung, Mülheim an der Ruhr, Germany. The powder samples were filled in a ceramic holder with a sieve plate at bottom, allowing the gases to flow through the sample. Gas flow was supplied to the chamber system by means of mass-flow controllers (MFCs, Bronkhorst) connected to He line (99.999 %, Air liquide), NH_3 (99.98 %, Air liquide) and H_2 (99.999 %, Air liquide) gas cylinders. The experiment was performed at atmospheric pressure. First, catalyst reductive activation was performed *in situ*, by heating the sample from room temperature to 523 K at a heating rate of 5 K min^{-1}, followed by a slower heating ramp of 3 K min^{-1} to 1023 K under flow of 20% H_2/He (50 mL min^{-1}). Diffractograms were recorded at isothermal conditions, in the 2θ range from 30 to 82°, every 25 K from 523 to 623 K, then every 100 K up to 1023 K.

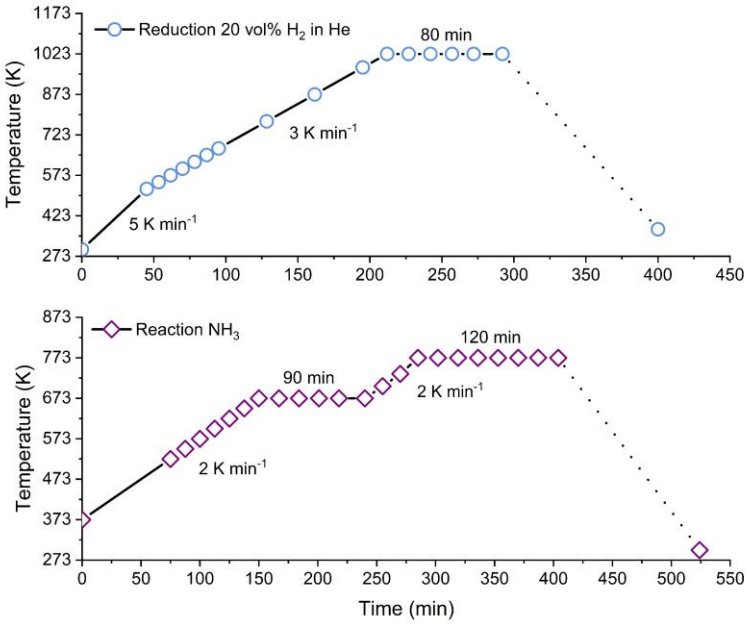

Figure 3.3: *Temperature program applied for in situ, laboratory powder XRD analysis during catalyst reduction (top) and exposure to NH_3 atmosphere (bottom). Scatter data points mark specific times along the experiment when the temperature was held steady to record XRD patterns.*

Subsequently, the *in situ* XRD experiment was extended to exposure of the catalyst to an NH_3 atmosphere. In this case, a flow of pure gaseous NH_3 (10 mL min^{-1}) was accepted into the reaction chamber. Then temperature was increased to 673 K using a heating ramp of 2 K min^{-1}, and XRD patterns were recorded isothermally every 25 K. Next, the temperature was kept constant at 673 K for 90 min, while continuously registering the XRD pattern. Next, a similar procedure was applied to further increase the temperature up to 773 K, recording at 703, 733 and 773 K and continuously at 773 K. **Figure 3.3** shows the temperature profile program employed during *in situ* XRD reduction and reaction under ammonia conditions. Diffraction patterns were recorded with a HyPix-7503000 multi-dimensional detector (1D mode), in the 2θ range from 25° to 82° at a scan speed of 5° min^{-1} (step size, 0.01°). During data collection, the incident slit was set to 1/8°, a RS1 was set at 20 mm, RS2 was open, the Soller slit was set to 2.5°, and a 5 mm mask was applied.

3.2.7 X-ray photoelectron spectroscopy (XPS)

X-ray photoelectron spectroscopy is a non-destructive and near-surface sensitive technique based on the photoelectric effect. This technique measures photoelectrons emitted from an energy level with a kinetic energy E_k, when an incoming photon, with an energy hv, is adsorbed as referred in the **Equation 3.3**:

$$E_k = hv - E_B - \Phi \qquad \textit{Eq. 3.3}$$

where Φ represents the work-function of the spectrometer and is the difference between the Fermi level and the vacuum energy, and E_B is the initial binding energy of the photoelectron in its fundamental state. The emission of the photoelectron creates a vacancy, which is subsequently filled by the relaxation of an electron of an outer level. This relaxation process releases energy, which can excite an Auger electron with the characteristic energy of the difference between binding energy of the emitted photoelectron and the binding energy level energy of the electron that fills the vacancy. This technique enables the quantitative

examination of the near-surface composition and the chemical state of a solid, as it is sensitive to the oxidation state, which is discernible through binding energy analysis.

As schematically shown in **Figure 3.4**, an XPS spectrometer incorporates a monochromatic X-ray source, typically employing an Al K_α (1486.6 eV) or Mg K_α (1253.6 eV) emission to irradiate a flat sample specimen within an ultra-high vacuum (10^{-4} to 10^{-7} mbar) chamber. A monochromator ensures energy specificity of the incident X-rays. The emitted photoelectrons undergo analysis using a photoelectron analyzer, which can be either a hemispherical or cylindrical mirror analyzer, to measure their kinetic energy and angular distribution. Detectors, often multi-channel detectors or electron energy analyzers, capture the photoelectrons' intensity and kinetic energy (KE) distribution, which can then be translated into binding energy (BE) as shown in **Equation 3.3** above.

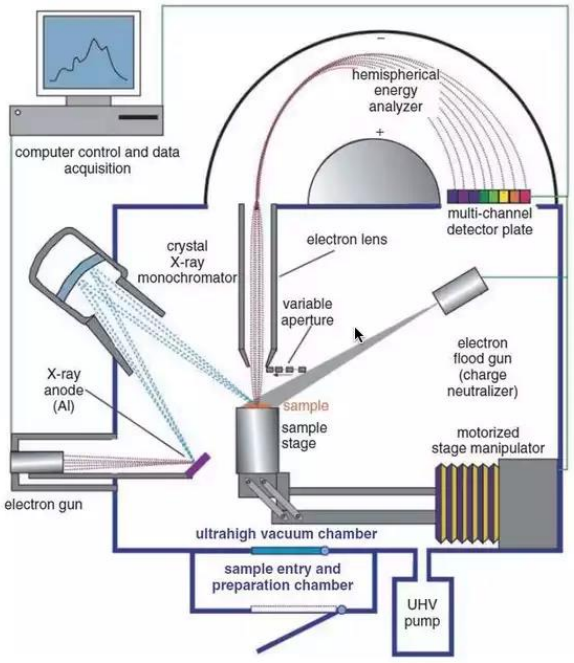

Figure 3.4: *Schematics of the operation principle of X-ray photoelectron spectroscopy (XPS). Reproduced from ref.*[10]

The analysis escape depth in XPS, i.e., the depth from which photoelectrons contribute to the signal, depends on factors such as the kinetic energy of the photoelectrons, the atomic density and composition of the materials near-surface region, which are determinant for the electron inelastic mean free path. This analysis depth ranges typically from a few angstroms to a few nanometers, emphasizing the fact that the technique provides information on the near-surface region of the specimen.

In this thesis, standard laboratory XPS has been applied to assess the near-surface composition of selected catalysts at different stages throughout their synthesis, activation and usage. X-ray photoelectron spectra were collected in a SPECS spectrometer equipped with a Phoibos 150 MCD-9 detector and using a non-monochromatic (Al K_α= 1486.6 eV) X-ray source, an analyzer pass energy of 30 eV, and an X-ray power of 100 W under an operating pressure of 10^{-4} mPa. Following exposure to activation/reaction conditions, samples were transferred to a N_2-filled glove box (O_2 < 1 ppm, H_2O< 1 ppm) under exclusion of air, mounted onto double copper film-stainless steel holders and then transferred to the UHV line connected to the spectrometer in an air-tight transfer suitcase (Specs) under protective inert atmosphere. XPS spectra were analyzed using the CASA XPS software applying Shirley-type spectral backgrounds and Gaussian/Lorentzian curves for spectra fitting. Binding energies for molybdenum-based catalysts in **Chapters 4** and **Chapter 5** were calibrated to the signal for adventitious carbon at 284.6 eV. In the case of the series of NiGa/SiO_2 catalysts studied in **Chapter 6**, binding energies were calibrated to the Si2p signal at 103.5 eV.

To investigate selected NiGa/SiO_2 catalysts in their activated state (**Chapter 6**), experiments were performed at Max-Planck-Institut für Kohlenforshung, Mülheim an der Ruhr, Germany, in a SPECS spectrometer equipped with a PHOIBOS 150 1D-DLD hemispherical analyzer and a monochromatized Al K_α X-ray source (E= 1486.6 eV) and operated at 200 W with a pass energy of 20 V under a pressure of ca. 10^{-4} mPa The catalyst specimen was *in situ* reduced in a reaction chamber, connected to the UHV line of the spectrometer. For reduction, a flow of 50 mL min^{-1} of 20 vol% H_2/ Ar was

established into the reduction chamber and the temperature of the sample was increased up to 1023 K using a heating rate of 3 K min^{-1}. Next, the activated sample specimen was transferred *in vacuo* to the XPS analysis chamber. XPS spectra were analyzed using the CASA XPS software applying Shirley-type spectral backgrounds and Gaussian/Lorentzian curves for spectra fitting. As indicated above, binding energies were calibrated to the Si2p signal from the irreducible catalyst support at 103.5 eV.

3.2.8 Synchrotron radiation techniques

Synchrotron installations are singular research infrastructures which generate a highly collimated, low-divergence, polarized, monochromatic pulsed light with high brilliance (typically 10^{12} to 10^{21} photons s^{-1} mm^{-2} $mrad^{-2}$·0.1 % of band width). This beam is typically exploited at different beam lines to study different light-matter interactions: absorption, diffraction, and reflection-refraction in imaging techniques. Compared to conventional laboratory techniques, major advantages of employing synchrotron facilities lie in the capability to modulate the photon energy in a broad range of energies (0.1-50 KeV) and the high photon flux.

In this thesis, a number of different synchrotron-based techniques have been leveraged. Total X-ray scattering, high-resolution X-ray powder diffraction (HR-XRPD), and X-ray adsorption spectroscopy (XAS) have been applied to investigate long- and short-atomic range structural features. In turn, synchrotron-radiation X-ray photoelectron spectroscopy (SR-XPS) has been utilized to investigate depth-resolved near-surface compositional properties of selected catalysts at different stages of catalyst activation and usage. All experiments have been performed at different beamlines of the ALBA synchrotron (Cerdanyola del Vallès, Spain) with assistance from ALBA staff members.

3.2.8.1 Total X-ray scattering analysis

Understanding the structure of the working catalyst is particularly complex when catalysts adopt nanocrystalline or amorphous structures, with limited or no long-range coherence, under relevant activation or reaction conditions. Total X-ray scattering is a scattering technique that captures the full scattering pattern as

a function of the scattering angle or momentum transfer. Data is typically represented in reciprocal space. Total X-ray scattering analysis encompasses two components, corresponding to Bragg and diffuse intensities. The latter can provide short-range structural information that can be extracted by Pair Distribution Function (PDF) analysis. Unlike diffraction methods, total X-ray scattering does not require long-range atomic ordering and the PDF analysis provides information about the probability of finding an atom at a certain radial distance from another given atom.[11]

Total X-ray scattering data were collected at the BL04-MSPD beamline of the ALBA synchrotron (Cerdanyola del Vallès, Spain).[12] MoMn bimetallic catalyst samples, in powder form, were first treated, *ex situ*, mimicking exposure to reaction conditions for the synthesis of nitriles from syngas/NH_3 mixtures, as discussed in **Chapter 5**. The activated materials were transferred into glass capillaries (outer diameter 0.5 mm, wall thickness 0.01 mm), the capillaries sealed with clay under exclusion of air, and finally flame-sealed. Measurements were performed at the ALBA-MSPD beamline in Debye-Scherrer geometry at 30 keV photon energy (wavelength 0.4125 Å refined using NIST 640e standard) using a MYTHEN position sensitive detector[13] in the 2θ range of 2-120 degree, corresponding to a Q range of 0.5-26 $Å^{-1}$. Four diffraction patterns (45 min $scan^{-1}$) were collected for each sample and averaged to improve signal/noise ratio.

3.2.8.2 Synchrotron-radiation X-ray photoelectron spectroscopy (SR-XPS)

The tunability of the synchrotron radiation energy allows the adjustment of the photoelectron scape depth in XPS experiments, enabling the assessment of the near-surface chemical composition of powder catalysts with (sub)-nm depth resolution.

For selected MnMo catalysts and following *ex situ* thermal treatments which mimicked exposure to reaction conditions for the synthesis of nitriles from syngas/NH_3 mixtures (see **section 3.1.2)** in **Chapter 5**, near-surface depth-profiling compositional analyses were performed with SR-XPS at the near-ambient pressure X-ray photoelectron spectroscopy NAP-XPS B24-CIRCE

beamline of the ALBA synchrotron. This is an undulator beamline wherein a plane mirror and three diffraction gratings are used to cover the source energy range from 100 to 2000 eV. Data acquisition was performed using a PHOIBOS 150NAP electron energy analyzer (SPECS). Spectra were acquired with an exit slit of 60 mm and a pass energy of 20 eV irradiating a spot on the powder samples mounted onto copper film-stainless steel holders and transferred from a glove box to the UHV line of the end-station under exclusion of air. Incident photon energies of 400, 500, 600 and 750 eV were applied to record Mo3d, Mn3p, N1s/Mo3p, and C1s core-levels with variable photoelectron escape depths, as determined with electron inelastic mean free paths predicted by the Tanuma-Powell-Penn formalism (TTP2M).[14] The XPS data were analyzed using CASA XPS Software and applying Shirley-type spectral backgrounds and Gaussian/Lorentzian curves for spectra fitting. Binding energies were calibrated to the C1s signal for adventitious carbon at 284.6 eV.

3.2.8.3 X-ray absorption spectroscopy (XAS)

X-ray absorption spectroscopy (XAS) provides volume-averaged information into the local coordination and electronic environment of element-specific atoms within a material, e.g., solid catalysts in this thesis. XAS utilizes a monochromatic, generally synchrotron, X-rays beam with energies typically ranging from several hundred to several tens of thousands of electron volts (eV). The incoming X-rays are tuned to specific energies corresponding to the absorption edges of the elements of interest. The energy transfer of the incoming hard X-ray photons to depth-core electrons (L or K edge) results in electron promotion phenomena to above the Fermi energy (continuum). In XAS, electronic transitions are element-characteristic and correspond to the atom core-level energy as schematically represented in **Figure 3.5. a**. Therefore, XAS measurements can be performed either in transmission or fluorescence modes. X-rays transmittance can be described according to the Lambert-Beer law, **Equation 3.4**:

$$I = I_0 e^{(-\mu t)} \qquad \textbf{Eq. 3.4}$$

Wherein I_0 represents intensity of the incident beam, μ stands for the absorption coefficient, and t the thickness, as depicted in the **Figure 3.5. b**. The absorption coefficient μ depends on the atomic number, (Z^4) the density and the atomic mass (A), and the energy of the X-ray radiation, as indicated in **Equation 3.5**.

$$\mu \approx \frac{\rho Z^4}{AE^3} \qquad \textbf{Eq. 3.5}$$

A sharp increase in absorption occurs when the incident X-ray energy is large enough to promote the core-level electron to the continuum.

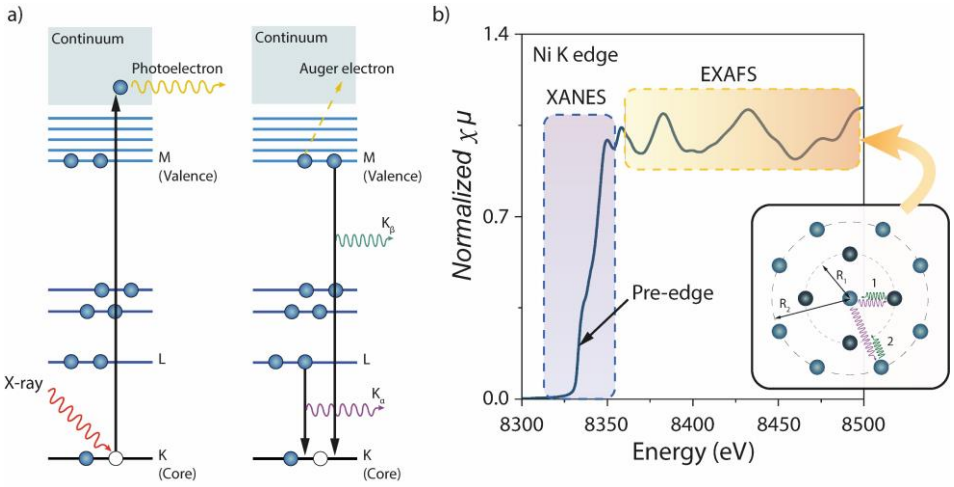

Figure 3.5: *a, right) Ejection of a photoelectron to the continuum by the electron absorption in the K edge of an X-ray photon. a, left) Consequently, the production of X-ray fluorescence (K_α and K_β) and Auger emission by the relaxation of an electron to the core-hole. b) K-edge XAS spectrum of Ni foil. Inset represents the interference effect produced by the back-scattered photoelectron with its shelf when interacting with adjacent neighbors at distances R_1 and R_2. Adapted from ref.*[15]

Two main electronic phenomena are analyzed, at two different energy regions of the absorption spectrum:

(i) X-ray Absorption Near Edge Structure (XANES) focuses on the immediate vicinity of the absorption edge, where inner-shell electrons are excited to unoccupied states (see **Figure 3.5. b**). The fine details of the XANES spectrum provide information about the electronic structure, oxidation states, and coordination environment of the absorbing atoms. Ions with partially filled *d* orbitals may display a pre-edge peak in the XAS spectrum, as a result of changes in the *p-d* hybridization in tetrahedral and distorted octahedral coordination environments. Shifts in the edge position to lower energies may be interpreted as indicative of sample reduction, a phase transition, or electron-donating contributions. Conversely, shift towards higher energies may suggest the opposite scenarios. Therefore, the oxidation state of a compound can be determined through the edge energy, subject to calibration of reference compounds wherein the element of interest shows known oxidation states.

(ii) Extended X-ray Absorption Fine Structure (EXAFS) analyzes the oscillatory features oscillation of the absorption μ(E), at energies ca. 20-50 eV higher than the absorption edge, generated by interference effects (constructive and destructive) of the photon-electron backscattered by atoms in the most direct coordination shells around the emitter atom. The inset to **Figure 3.5. b** sketches those interferences of the emitted electron with the first and second coordination shells, at atomic distances, R_1 and R_2, respectively, from the emitter atom. Through the modelling of the spectral features in the EXAFS region, it is possible to elucidate the average coordination number (CN) for the absorber atom, and the average radial distances to neighboring atoms (R), among others short-range structural information.

In **Chapters 4** and **5** of this thesis, XAS has been applied to investigate temperature resolved changes in Mo and Mn average oxidation states during catalyst activation, as well as to assess differences in the local structure of the

working (mixed) metal nitride catalysts, in the synthesis of nitriles from syngas/NH_3 mixtures. X-ray absorption spectra were recorded at the Mo K (19.9995 keV) and Mn K (6.539 keV) absorption edges at the BL22-CLÆSS beamline station of the ALBA synchrotron light source, Barcelona (Spain). The beam was monochromatized using a (311) double crystal monochromator, and harmonic rejection was performed using Pt-coated silicon mirrors. Samples and air-sensitive standards were ground, diluted in boron nitride (to circumvent self-absorption effects) and mounted in air-tight holders sealed with Kapton film in an Argon-filled glove box (O_2<1 ppm, H_2O<1 ppm). Measurements were performed at room temperature in fluorescence mode using a fluorescence solid Silicon Drift detector. Reference metal oxide materials were prepared in the same way, shaped into pellets (Ø= 13.2 mm) and measured in transmission mode employing ion chambers filled with appropriate gases in order to absorb 15 % and 80 % in the I_0 and I_1, respectively. At least 3 scans were recorded to ensure spectral reproducibility and appropriate signal-to-noise ratio.

Data reduction and extraction of the χ(k) function were performed using the Athena code from the Demeter software package (version 0.9.26).[16] In the data reduction process, a k range of 1< k(Å^{-1})< 8 or 1< k(Å^{-1})< 11 was considered for extracting the Fourier transform FT-χ(k) signal of the spectra collected at the Mn and Mo k edge, respectively. In all cases, a R_{bkg} value of 1 was considered. To provide straightforward qualitative information on the relative scattering contribution of the EXAFS components in both the reciprocal (k) and the real (R-uncorrected for phase-shifts) spaces, Continuous Cauchy Wavelet Transforms (CCWT) were performed on the extracted Mo K EXAFS spectra by applying the method developed by M. Muñoz et al.[17]. The CCWT, presented in the form of 2D contour plots, were calculated with a Cauchy order n= 200, and a Hanning apodization window was applied in the range 1< k(Å^{-1})< 11 to extract the FT-χ(k) signals in the R-space.

Changes in the Mn and Mo formal oxidation states (OS_{Mn}, OS_{Mo}) were assessed by linear regression analysis of the energy edge position shift of the samples relative to the corresponding metallic foil ($\Delta E_0 = E_{0,\,sample} - E_{0,\,foil}$))

employing reference metal oxides with well-known oxidation states. The edge position was taken either at the first or the second maximum of the derivative XANES spectra collected at Mn and Mo k edge, respectively, according to previous studies in the literature.[18,19]

3.2.8.4 In situ/operando high-resolution X-ray powder diffraction and X-ray adsorption spectroscopy

The long-range structural evolution of Ni-based supported metal catalysts, during their activation and subsequent application in the synthesis of acetonitrile from methanol/NH_3 mixtures, was monitored by *in situ*/*operando* high-resolution XRD. These results are discussed in **Chapter 6**. Experiments have been performed at the BL16-NOTOS beamline of the ALBA synchrotron (Cerdanyola del Vallès, Spain).

The experiments were performed in a capillary flow cell-microreactor. This setup enables quasi-simultaneous X-ray diffraction and absorption (EXAFS) experiments with synchrotron radiation. **Figure 3.6. a** shows a picture and simplified schematics of the relative orientation of the horizontal capillary reactor, the incoming X-ray beam and the transmitted and diffracted X-ray beams, respectively. **Figure 3.6. b** shows a picture of the setup, installed at the BL16-NOTOS beamline, and it identifies its major sections/components. The cell is equipped with high-precision gas mass flow controllers (MFC, Bronkhorst) to provide a reliable gas feed supply and it holds a low total void volume, ca. 17 mL. Besides, the setup comprises a 10 cm length quartz glass capillary, which is mounted horizontally onto a flow cell and aligned with the X-ray beam. The catalyst bed is heated by a hot air blower (Mistral System 230 V/3400 W, nozzle Ø 50 mm ID, Leister®) positioned orthogonal to the capillary, providing an isothermal packed bed length of 5 mm.

Experimentally, the catalyst samples were sieved in a 0.1-0.2 μm range and filled into glass capillaries (outer diameter 1.0 mm, wall thickness of 0.01 mm). The sieved samples were packed with a length of 3 mm between 2 cm of SiC (ø= 0.1-0.2 μm), placed up- and down-stream from the catalyst packed bed to pre-

heat the gases and avoid product condensation after the catalyst bed. Quartz wool plugs were mounted at both ends of the capillary filling to fix the catalyst bed in place. The hot air blower was placed 5 mm beneath to the center of the capillary, operated with 500 L h^{-1} air flow and 1.5 L min^{-1} cooling water flow, and it was calibrated using a type-K SS316-coated thermocouple (OD= 1.6 mm) placed in the middle of a packed bed of the SiO_2 catalyst support, while flowing 8.5 mL min^{-1} of He and in the temperature range from 303 to 1073 K.

Mass flow controllers (MFC Bronkhorst) were connected to 25 % NH_3 in He (Linde, 99.98 %), He (Linde, 99.99 %) and H_2 (Linde, 99.9999 %) gas cylinders. *In situ* catalyst reduction was performed in three steps while exposing the catalyst bed to a 10 mL min^{-1} flow rate of 20 vol% H_2 in He. First, the temperature was increased to 423 K at a heating rate of 5 K min^{-1}, then the ramp was set at 3 K min^{-1} to reach 1023 K, and finally, this temperature was maintained for 90 minutes before letting the capillary microreactor cool down to 313 K at - 10 K min^{-1}. Next, the gas feed mixture was accepted into the capillary reactor. Said feed mixture was generated by mixing a flow of 4.8 mL min^{-1} of 25 vol% NH_3 in He and an additional flow of 6.2 mL min^{-1} of He saturated with methanol (99.99 %). The saturation of the second gas stream in methanol vapors was achieved in a high-pressure double-stage saturator, with a similar design albeit lower void volume compared to the one described in **Section 3.4.1.2** (*vide infra*). The He carrier gas was bubbled through liquid methanol (Scharlab, 99.99 %) in a first SS cylinder which was kept at RT (297 K). Excess vapor was removed in a second condenser cylinder operated at 288 K. This temperature was selected to attain a preset methanol vapor pressure in the carrier gas to attain a NH_3/MeOH molar ratio of 2 in the feed mixture into the capillary reactor. Methanol vapor pressure was estimated using Antoine's equation (see **Section 3.4.1.2** below for details on Antoine parameters). The temperature of the catalyst-packed bed was increased from RT to 673 K at 2 K min^{-1} and held at this temperature for 120 min. Next, the temperature was further increased to 773 K and this reaction temperature sustained for 240 min. Finally, the reactor was cooled down to RT using a programmed cooling rate of - 10 K min^{-1}.

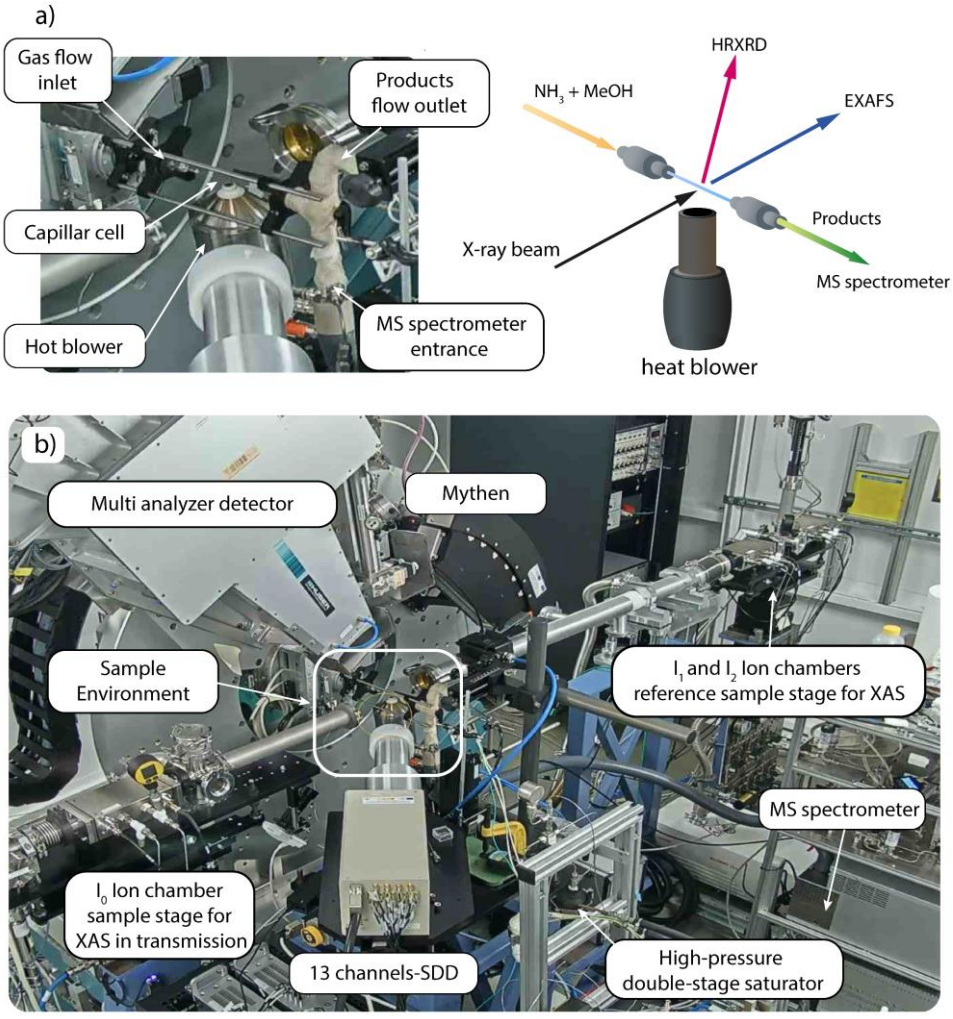

Figure 3.6: *Capillary cell configuration of the In-situ/Operando High-resolution XRD and X-ray absorption experiments pressure under ammonia/methanol feed at atmospheric. The products were analyzed downstream by a MS spectrometer.*

The X-ray beam was monochromatized using a double crystal monochromator (DCM) with two sets of crystals Si(111) and Si(220), and harmonic rejection was performed using silicon Si(111) mirrors. HR-XRD measurements were carried out in a Debye-Scherrer geometry at 13 keV photon energy (wavelength 0.95342 Å) using a Mythen position sensitive (6 modules)

detector in the 2θ range of 5-58 degrees, corresponding to a Q range of 0.57-6.4 $Å^{-1}$. Diffraction data were collected continuously during the exposure of the catalysts to reduction and reaction conditions.

Moreover, during the *operando* catalysis experiments, the outlet stream from the capillary reactor was continuously monitored using a mass spectrometer (MKS104-J0722089).

Prior to and following catalyst reduction and reaction, XAS spectra were additionally recorded, *in situ*, at room temperature, at the Ni K (8330 keV) and Ga K (10370 keV) absorption edges, respectively. Spectra were recorded in fluorescence mode before using a 13-element Silicon Drift detector (SDD). Reference metal oxides and nitrides, i.e., Ga_2O_3, (Sigma-Aldrich, ≥99.99 %), GaN (Thermofisher Scientific, 99.99 %), NiO (NanoShel-UK Ltd, 99.9 %, <80 nm), were diluted with boron nitride (Aldrich, 98 %), shaped into pellets (ø= 13.2 mm) and measured in transmission mode employing three ion chambers filled with appropriate gases to absorb 15 % and 80 % in the I_0 and I_1, respectively. At least three scans were recorded to ensure spectral reproducibility and appropriate signal-to-noise ratio. Data treatment has been carried out using Athena for χ(k) function extraction and Artemis (Demeter software package) for EXAFS data analysis as detailed above.

3.2.9 Electron microscopy techniques

In the field of catalysis research, electron microscopy techniques have become essential tools as they deliver nanoscale information on (nano)materials size, shape and nano-mesoscale spatial distribution, using the interaction of electrons with matter under high vacuum conditions. When integrated to spectroscopic methods based on secondary X-ray emission, such as energy-dispersive X-ray spectroscopy (EDS), nanoscale compositional information is additionally retrieved. In the present thesis, scanning electron microscopy (SEM) and (scanning)-transmission electron microscopy ((S)TEM), have been applied to investigate microscale crystal morphologies, as well as nanoscale speciation, size

distribution and elemental spatial distribution in selected catalysts, and precursors therefor, at various stages throughout their synthesis, activation and usage.

3.2.9.1 Scanning electron microscopy (SEM)

Scanning electron microscopy is based on the interaction between a high-intensity electron probe and matter, and the consequent detection of secondary or backscattered electrons. This detection enables the reconstruction of the surface topology of the sample in x-y directions into images (micrographs) with correlated grayscale. Backscattered electrons exhibit a strong correlation with the element's atomic number, resulting in brighter (higher e-contrast) areas that are richer in elements with higher atomic numbers. Alternatively, secondary electrons are influenced by the surface topography, as well as by possible electric and magnetic fields created within the sample, depending on the insulating characteristics of the material. SEM microscopes utilize diverse electron sources. Traditional sources are based on tungsten or LaB_6 filaments, which generate electrons through thermionic emission upon heating. These filaments provide a reliable and cost-effective solution for routine imaging. Alternatively, Field-Emission SEM leverages a field-emission electron source, often a sharp metal tip or a field-emission gun. Field emission sources require a high operating vacuum range (10^{-9} Torr), attaining smaller electron source sizes (~1 nm), than instruments equipped with conventional thermionic filaments.[20]

In this thesis, FE-SEM has been employed to assess the crystal size and morphology for the series of ammonium M (II) molybdate (M= Zn, Cu, Ni, Co or Mn) catalyst precursors which are studied in **Chapter 5**. Experiments were performed in a FE-SEM ZEISS ULTRA 55 microscope. Samples were finely grounded and deposited on a double-adhesive-face conductive carbon-tab stuck on the SEM sample holder and imaged without any additional sputter coating.

3.2.9.2 High-resolution transmission electron microscopy (HR-TEM) and high-angle annular dark-field scanning-transmission electron microscopy (HAADF-STEM)

Transmission Electron Microscopy (TEM) is a microscopy technique that utilizes a beam of electrons transmitted through a nm-thin specimen to achieve high-resolution imaging, providing detailed insights into nanoscale structures. Electron sources, typically thermionic guns with tungsten filaments or advanced Field-Emission Electron Guns (FEGs), generate electron beams. A vacuum system (10^{-3}-10^{-7} mbar) prevents electron scattering, while electromagnetic lenses and apertures control and limit the electron beam for improved resolution. Condenser lenses direct the beam onto a nm-thin sample specimen, which is often deposited onto a metallic grid coated by a thin carbon layer. Objective lenses focus transmitted electrons, while projector lenses magnify and project the electron image onto a detector, which is typically a digital CCD camera. Transmission electron microscopy is based on the transmitted incident electron beam through the sample, creating micrograph images with image resolution better than 0.2 nm of thin foil samples. This technique is characterized by element atomic number, mass thickness, and diffraction contrast, able to identify defects and deviation from crystallinity that allows high-resolution imaging.

Two typical operating modes can be discerned TEM, known as bright field (BF) and dark field (DF), respectively. BF-TEM generates micrographs using transmitted electrons, hence providing local thickness and density-based contrast maps. In contrast, DF-TEM selectively captures electrons scattered by structural irregularities, highlighting defects or features with a different electron density against a bright background.

In scanning-transmission electron microscopy, the combination of advanced electromagnetic lens designs and electron optics enables the creation of highly focused electron probes, with sizes down to a few picometers. This highly focused e-beam scan-rasters across the specimen in order to create 2D maps, with down to atomic resolution. STEM is commonly integrated with so-called high-angle annular dark-field (HAADF) detectors. The HAADF detector physically

consists of an annular ring positioned around the central beam. This annular geometry collects Rutherford electrons, which are scattered from the sample specimen at high angles (typically greater than 70 degrees) relative to the incident beam. The contrast in HAADF imaging is described by the Z-contrast law, which relates the intensity of the collected electrons to the atomic number (Z) of the specimen atoms. The intensity (I) in HAADF is proportional to Z^a, where Z is the atomic number and *a* an exponent which typically takes values in the range of 1.5-1.8. This power-law dependence results in brighter contrast for regions with higher atomic number elements, enhancing the visibility of heavy elements and facilitating the imaging of individual atomic columns with superior sensitivity to variations in composition.

Both TEM and particularly (S)TEM methods can be integrated with nanoscale spectroscopy techniques in the microscope, to create compositional maps with chemical and electronic nanostructure information with down to atomic resolution. Electron Energy Loss Spectroscopy (EELS) operates in two distinct modes within the TEM environment. The core-loss mode involves high-energy electrons interacting with specimen atoms, resulting in inelastic scattering and energy loss. The measured energy loss is then utilized to characterize elemental composition and bonding states. Conversely, low-loss EELS focuses on smaller energy losses associated with electronic excitations, offering valuable information about the electronic structure of materials. Alternatively, Energy-Dispersive X-ray Spectroscopy (EDS) functions based on the principles of X-ray emission resulting from the interaction of high-energy electrons with the specimen in the microscope. When incident electrons hit the specimen, they displace inner-shell electrons from their orbits. As outer-shell electrons transition to fill these vacancies, characteristic X-rays are emitted. The energy of these emitted X-rays is directly proportional to the energy difference between the involved electron shells and is characteristic of the elements present. EDS offers rapid elemental analysis through point analysis and mapping modes. In the point analysis mode, a focused electron beam scans the specimen, and the emitted X-rays are collected by an energy-dispersive detector. EDS mapping extends this capability by scan-rastering the electron beam across the specimen's surface, creating spatially resolved elemental maps.

In **Chapters 4-6** of this thesis, electron microscopy and nanoscale EDS spectroscopy methods have been applied to gain insight into nanoscale features such as particle size and shape distributions, as well as cross-sectional distributions of elements across selected catalysts and precursors therefor, at various stages throughout their synthesis, activation and usage. High-resolution Transmission Electron microscopy (HR-TEM) and High-Angle Annular Dark-Field Scanning-Transmission electron microscopy (HAADF-STEM) experiments were carried out in a FEI TITAN G2 microscope equipped with a Schottky-type Field-Emission Gun and operated at an acceleration voltage of 300 kV. Prior to observation, the samples were embedded in a low-viscosity epoxy resin (Spurr) under exclusion of air. Then, slices of the embedded material were produced, with nominal thickness of 250 nm, on a Reichert Ultracut ultramicrotome mounting a Diatome diamond knife and deposited onto Cu and Au TEM grids (150 mesh) coated with a continuous formvar film. Cross-sectional compositional maps were generated from the ultramicrotomed specimens by means of a Super X quadruple Energy-Dispersive Spectroscopy (EDS) detector with automated drift correction.

3.3 COMPUTATIONAL METHODS

3.3.1 Mechanistic studies on NH_3/syngas conversion reaction on $Mo_2N(100)$

In **Chapter 4**, Periodic Density Functional Theory (DFT) calculations were performed using the Vienna Ab-initio Simulation Package (VASP)[21,22] in version 5.4.4. The exchange-correlation energy was calculated with the PBE form of the generalized gradient approximation (GGA) functional.[23] The electron-ion interaction was modeled by the projector-augmented wave (PAW) method.[24] A plane-wave basis set was used with a cut-off energy of 400 eV. Fractional occupancies were calculated using a first order Methfessel–Paxton smearing function[25] with a width of 0.2 eV. To model high surface coverage, which is expected to be the experimentally relevant condition, a p(1x1) slab has been used as the repeating unit in *x* and *y* directions. To check the effect of the unit cell size, CO and N adsorption structures were calculated as test parameters on both p(1x1) and p(2x2) slabs. The difference in adsorption energies were found to be less than 10 kJ mol^{-1}, which indicates that the p(1x1) unit cell size is relevant to model a $Mo_2N(100)$ surface at high surface coverages. Optimization of structures was performed with an energy convergence criterion of 10^{-4} eV and a force convergence criterion of 0.02 eV $Å^{-1}$. The reciprocal space was sampled with a (4 × 4 × 1) *k*-points grid, which were automatically generated using the Monkhorst–Pack method.[26] During optimization, the two bottom layers of the slab were fixed, while all remaining atoms were fully relaxed. The parameters that can affect the DFT generated results such as energy cut-off, number of layers and number of *k*-points were optimized. CO adsorption energy was used as a test parameter to check the effect of these parameters. An increase of the mentioned parameters, compared to the values used in our calculations, resulted in a change of CO adsorption of less than 7 kJ mol^{-1}. After optimization of initial and final state configurations for elementary reactions, saddle points in the minimum energy path were optimized using the Climbing Image-Nudged Elastic Band (CI-NEB) method[27] until the forces acting on the image with the highest energy were lower

than 0.04 eV $Å^{-1}$. For vibrational frequency analysis, the atoms were displaced from their equilibrium positions by 0.015 Å. All transition states were further confirmed by vibrational frequency analysis, which indicated a single imaginary vibrational frequency.

Adsorption energies were calculated with respect to gas-phase species according to **Equation 3.6**:

$$E_{ad} = E_{slab+ad} - E_{slab} - E_{vac} \qquad \textit{Eq. 3.6}$$

Where $E_{slab+ad}$ is the energy of the slab with adsorbate, E_{slab} is the energy of the neat slab (without adsorbates) and E_{vac} is the energy of the isolated molecule in vacuum. Adsorption energies of dehydrogenated NH_x (x= 2,1 and 0) species have been calculated with respect to gas phase NH_3 according to **Equation 3.7**:

$$E_{ad,NHx} = E_{slab+ad} + (3-x)E_{Had} - (4-x)E_{slab} - E_{vac,NH3} \qquad \textit{Eq. 3.7}$$

Where EH_{ad} is the energy of the slab with atomic hydrogen adsorbed.

3.3.2 First principles thermochemistry of (Mn-doped) Mo oxynitride catalysts

In **Chapter 5**, Periodic Density Function Theory (DFT) calculations, in connection also to first principles thermochemistry simulations, were performed using Quantum Espresso code suite in version 7.2.[28,29] Calculations have been carried out adopting the generalized gradient approximation (GGA) with the revised Perdew-Burke-Ernzerhof (RPBE) density functional.[30] The semi-empirical method of Grimme-D3 was employed to describe long-range dispersion interactions. The interaction between valence and core electrons was described with the Projected Augmented Wave method (PAW).[31] A plane-wave basis set

was used with a cut-off energy of 650 eV. Fractional occupancies were calculated using a Gaussian smearing function with a width of 0.10 eV. All calculations were performed considering spin polarization. A Broyden-Fletcher-Goldfarb-Shanno algorithm has been applied for geometry optimizations with an interatomic force threshold of $2.5 \cdot 10^{-2}$ eV $Å^{-1}$. Monkhorst-Pack grids were used to approximate the value of an integral over the Brillouin zone with 6 × 6 × 6 k-point meshes to sample the reciprocal space for 2 x 2 x 2 supercells. All atoms were allowed to relax when optimizing cubic supercells. Gas-phase molecules were optimized in a 10^3 $Å^3$ cubic vacuum box to minimize lateral interactions and reciprocal space sampling was applied to the gamma point. A 4 × 4 × 1 k-point mesh was used to sample the reciprocal space for slabs. The latter were constructed in 2 x 2 cells with four atomic layers and spaced by a perpendicular vacuum size greater than 15 Å to avoid spurious interactions with periodic replicas. The two top atomic layers, and all atoms for adsorbate molecules, were allowed to relax fully during geometry optimization, while the two layers at the bottom of the metal slab were kept frozen.

Adsorption energies were calculated as the difference between the energy of the slab with the adsorbed molecule and the sum of the energies of the clean metal slab and the isolated adsorbate molecule as shown in **Equation 3.8**:

$$E_{ads} = E_{molecule/slab} - (E_{slab} + E_{molecule}) \qquad \textbf{Eq. 3.8}$$

For atomic oxygen adsorbates, the gas-phase reference energy was considered as ½E(O_2) for the O_2 molecule relaxed in a vacuum box.

Formation Gibbs free energies were determined as:

$$G_f\left(\left[Mo_xMn_yN_zO_w\right], T, P\right) = E\left[Mo_xMn_yN_zO_w\right] \qquad \textbf{Eq. 3.9}$$
$$-\left(\frac{x}{2}E[Mo_{bcc}] + \frac{y}{2}E[Mn_{bcc}] + \frac{z}{2}\mu_{N2}(T,P) + \frac{w}{2}\mu_{O2}(T,P)\right)$$

Wherein E stands for total electronic energies and μ_i represents the chemical potential of the *i* compound in the gas phase. Body centered Mo and Mn (*Im-3m*) metallic phases were considered as reference states for molybdenum and manganese, respectively. Values for the chemical potential as a function of temperature and pressure were obtained using standard statistical thermodynamics:

$$\mu_i(T,P) = 1/n \cdot \left[E + ZPE + \left(\Delta G_{i-mol}(T,P) - \Delta G_{i-mol}(0K,P^0)\right) + k_b T \cdot ln\frac{P}{P^0}\right] \quad \textbf{Eq. 3.10}$$

Where *n* stands for the number of atoms of element *i*, e.g. N, O in the *i*-mol molecule, e.g. N_2, O_2, E and ZPE are the electronic and zero-point energy of the gas-phase compound as derived from DFT, the ΔG term is the difference in Gibbs free energy between 0 K and a i-molecule reference pressure P^0= 1 atm and at a temperature T (K) and a partial pressure P as calculated from the partition function of the molecule, and the last term is the pressure dependency of the Gibbs free energy. Vibrational analysis for the determination of partition functions and entropic contributions was performed using a harmonic approximation with 0.005 Å atom displacements as implemented in ORCA, in version 5.0.4.

The Gibbs free energy change of point-defect formation was determined as follows:

$$\Delta G_{def} = \Delta G_f^{def} - \Delta G_f^{perf} + \sum_i n_i^{vac} \cdot \mu_i \quad \textbf{Eq. 3.11}$$

Wherein the super indexes *def* and *perf* denote the defective and perfect reference solid compounds, respectively, and the last summatory term is only applied in the case of point defects associated to the occurrence of vacancies, e.g. nitrogen vacancies. For cationic vacancies and Schottky pair defects, body

centered Mo and Mn (*Im-3m*) metallic phases were considered as reference states for molybdenum and manganese, respectively. Entropic contributions for solid materials were neglected in the calculations.

3.4 CATALYST TESTING

3.4.1 Microactivity XS15 reactor

Catalysis tests were performed in an XS15-Microactivity reactor (Micromeritics) equipped with a 316L-grade stainless steel tubular reactor inserted axially in a furnace. The catalyst particles (Ø = 200-400 µm) were diluted with SiC granules (Ø = 600-800 µm) to improve the overall heat conductivity and packed in a fixed-bed with a total volume of 1.4 cm^3. The tubular reactor is equipped with chemically inert quartz in-liner (I.D.= 7 mm) and a sapphire sheath hosting a type-K SS316-coated thermocouple (O.D.= 2.9 mm), inserted axially to provide the temperature reading at the center of the catalyst bed. Temperature was controlled in the range of 293-1023 K by means of a PID controller, while pressure was controlled (1.2-3 bar) by a servocontrolled micrometering valve located downstream of the reactor.

All transfer lines to the GC (or alternatively the MS) were heat traced to 453 K to prevent product condensation as well as deposition of $(NH_4)_2CO_3$ or urea, which may form by reaction of NH_3 and CO_2 (side-product of the syngas conversion reaction) and can cause clogging of the flow lines, constituting a safety concern. Additional safety measures were implemented to ensure the highest level of protection of the user to hazardous compounds like CO (reactant or potential reaction product depending on the specific process investigated) and HCN (potential reaction product). The entire reactor setup and its gas conditioning and feeding system were placed inside a fume hood with forced convection ventilation to an exhaust line, to mitigate risks associated with gas leakages. Additionally, a fixed Dräger Polytron CO detector was installed in the laboratory, adjacent to the fume hood, and connected to an acoustic alarm system. Moreover,

personal, portable Dräger PAC 6000 detectors specific for HCN and CO were carried by the experimentalist.

Figure 3.7 shows a P&ID diagram of the reactor setup. A close-up view and scheme for the reactor's internals are also provided for clarity.

Depending on the C_1 compound (methanol or carbon monoxide) included in the gas feed, different setup configurations were required for the catalytic tests, as detailed in **Sections 3.4.1.1** and **3.4.1.2**, below.

3.4.1.1 Reactor configuration for conversion tests with syngas and ammonia gas feeds

Pure NH_3 (Linde, 99.9 %), a synthetic syngas mixture (Linde, 45 %. CO, 45 % H_2, 10 % Ar (vol)) and H_2 (Linde, 99.9999 %) were fed from gas cylinders through mass-flow controllers (MFCs, Bronkhorst). The synthetic syngas stream was purified in a high-pressure filter, filled with activated carbon pellets (3 mm), located upstream of the corresponding MFC, in order to retain any volatile metal carbonyl compounds, which may be entrained from the gas cylinder.

3.4.1.2 Reactor configuration for conversion tests with methanol and ammonia gas feeds

Pure NH_3 (Linde, 99.9 %), and H_2 (Linde, 99.9999 %) were fed from gas cylinders through mass-flow controllers (MFCs, Bronkhorst) into the reactor, while an Ar/ He mixture (10 % Ar in He (vol)), Linde) was fed from cylinders through mass-flow controllers (MFCs, Bronkhorst) into the dual-stage, high pressure saturator (**Figure 3.7,** green frame). The saturator is composed of two sampling stainless steel 316L cylinders connected in series. The first cylinder was operated as a gas bubbler and it features an axial immersion inlet tube (1/4 inch OD) with a porous frit at the tip to bubble the incoming carrier gas in the liquid filling the cylinder. This cylinder was filled with methanol (multisolvent®, HPLC Grade, Sharlab, 99.99 %,) and its temperature was controlled to 313 K by means of a heat tracing element. The outlet stream from the first cylinder enters the second cylinder which operates as a condenser. In this case, the temperature in the cylinder is controlled by means of a metallic serpentine jacketing the cylinder, which is connected to a

circulating cryostat bath using ethylene glycol (antifreeze Repsol, 30 %) as the circulating cooling medium. The cylinder is empty, and it also features an immersion tube for the incoming gas. This second stage of the gas saturator was operated at a lower temperature than the first stage, in the range of 308 K, and it therefore serves to fine-adjust the vapor content in the gas stream, leaving the second stage of the saturator by partially condensing out methanol. The entire dual-stage saturator may be bypassed to feed a methanol-free carrier gas stream to the reactor.

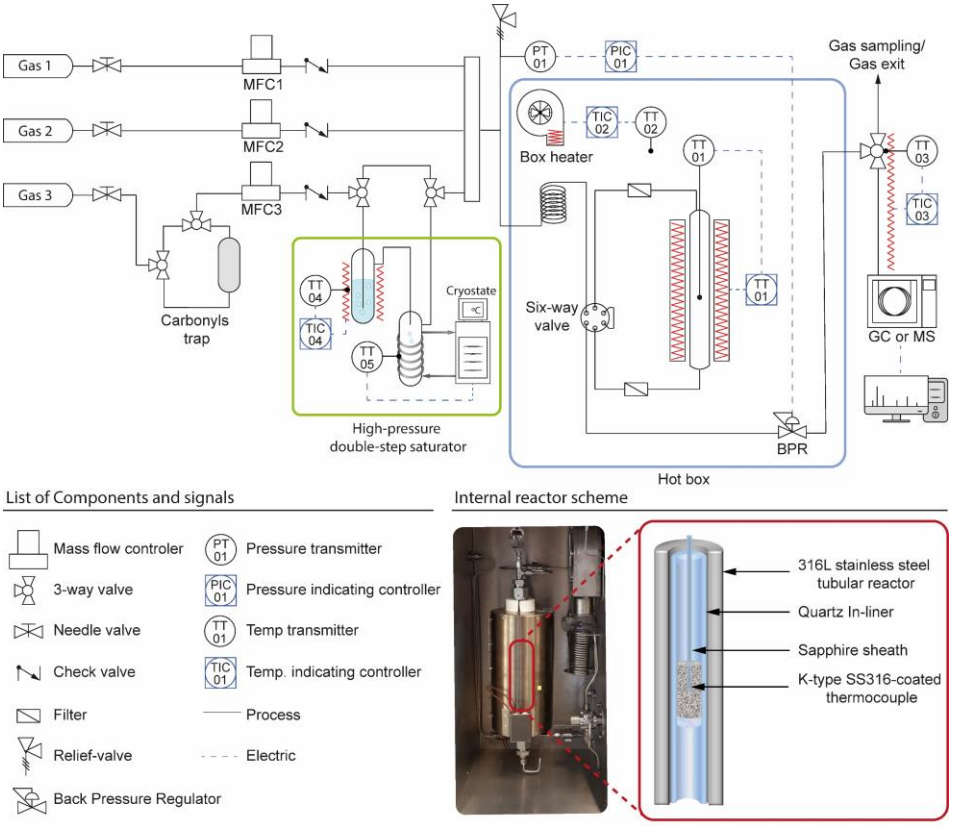

Figure 3.7: *P&ID diagram of the reactor setup applied for catalytic conversion tests, with a close-up view in the packed-bed reactor.*

The methanol concentration in the gas stream leaving the saturator was determined from the flow rate of the carrier gas, and the methanol partial pressure at the temperature of the second saturator stage, as estimated by applying Antoine's equation, according to **Equation 3.12**. with the parameters A= 8.0724, B= 1574.99 and C= 238.87. These parameters can be used in the temperature range of 257 to 364 K.

$$P_v(mmHg) = 10^{\left(A - \frac{B}{C+T(^\circ C)}\right)} \qquad \textit{Eq. 3.12}$$

3.4.2 Analytics

3.4.2.1 Gas Chromatography

The product stream leaving the reactor was depressurized and directed to a gas chromatograph (GC), connected online, downstream of the reactor setup. Two different gas chromatographs were used, depending on the reaction under study.

A Scion 456 gas chromatograph was used for those catalytic tests discussed in **Chapters 4** and **5**. The GC was equipped with a SCION-BOND Q (25 m x 0.32 mm x 5 µm) precolumn and a Molsieve 5A 80/100 Mesh (15 m x 0.32 mm x 30 µm) column to resolve permanent gases, CO_2, NH_3 and HCN along a first channel, which feeds to a thermal conductivity detector (TCD) and two MetAmine-VOL (60 m x 0.32 mm) columns, connected in series along a second channel, to analyze hydrocarbons, oxygenates and nitrogen organic compounds in a flame ionization detector (FID). **Figure 3.8** shows a representative chromatogram.

An Agilent 8860 System gas chromatograph was applied for those catalytic tests presented in **Chapters 4-6**. The chromatograph is equipped with a CP-Volamine (15 m x 0.32 mm) as a guard-column, a column HP-Plot Q (30 m x 0.32 mm x 20 µm) as precolumn and a HP-Molsieve (30 m x 0.32 mm x 12 µm) column to resolve permanent gases CO, CO_2, NH_3, Ar, and HCN along a first

channel, which feeds to a thermal conductivity detector (TCD); and a CP-Volamine (60 m x 0.32 mm) column, along a second analysis channel, to analyze hydrocarbons, oxygenates and nitrogenated organic compounds in a flame ionization detector (FID).

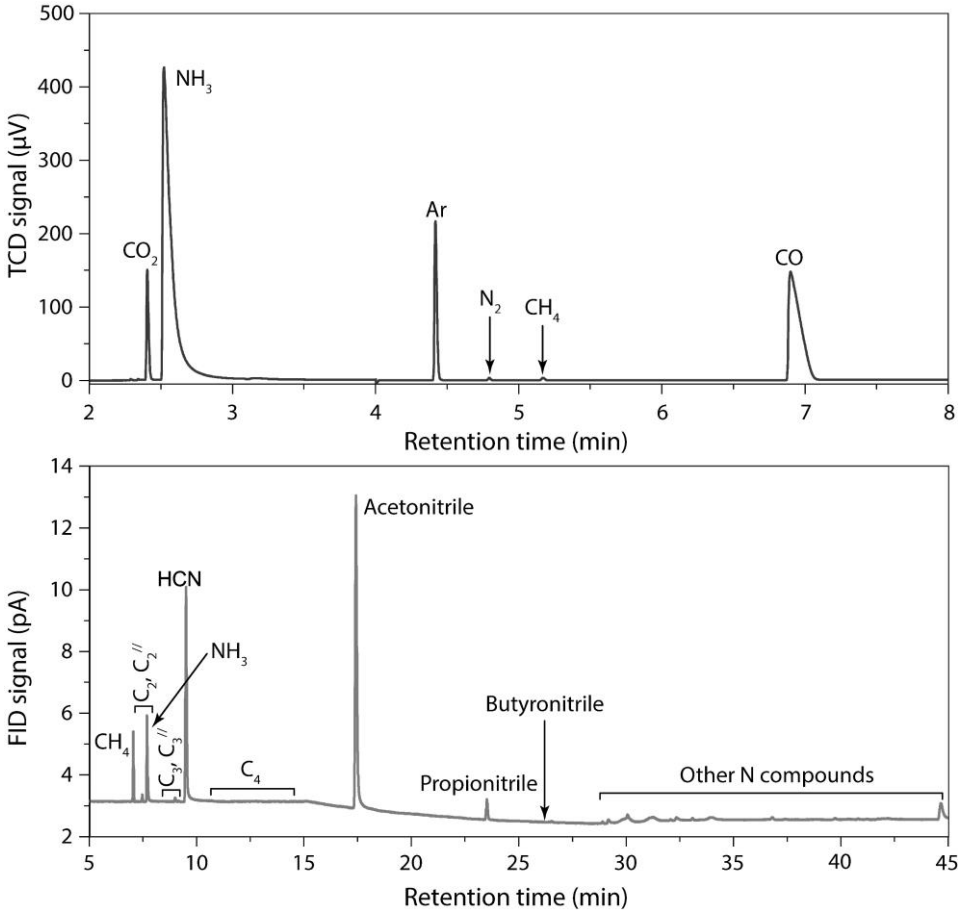

Figure 3.8: *Representative Scion 456 gas chromatogram for a test of the catalytic synthesis of acetonitrile from syngas/NH_3 mixtures. a) TCD channel, b) FID channel. Major compounds have been labelled on the figure. Light hydrocarbons are represented as C_2, $C_2^{//}$, C_3, $C_3^{//}$, C_4 corresponding to ethane, ethylene, propane, propene and racemic C_4 hydrocarbons, respectively.*

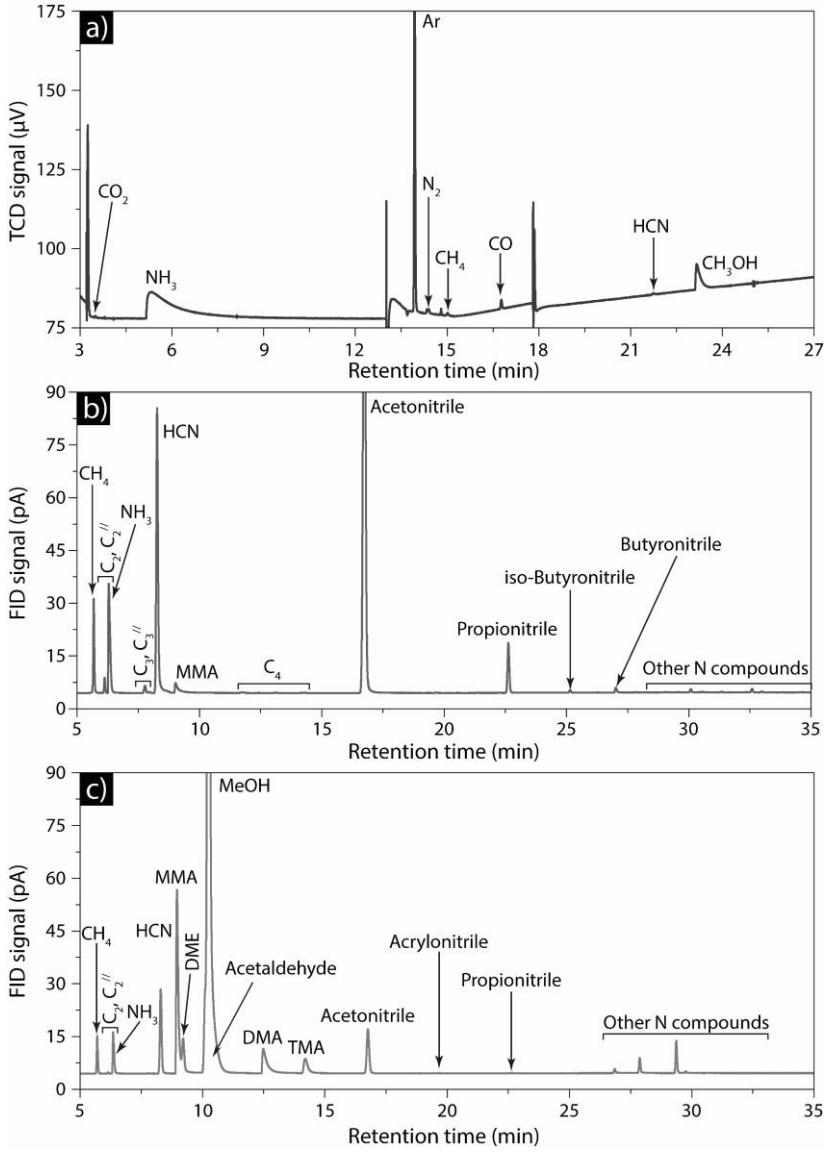

Figure 3.9: *Representative Agilent 8860 System gas chromatograms along a) the TCD channel and b,c) the FID channel for tests of the catalytic synthesis of acetonitrile from b) syngas/NH_3 mixtures and c) methanol/NH_3 mixtures. Major compounds have been labelled on the figure. Light hydrocarbons are represented as C_2, $C_2^{//}$, C_3, $C_3^{//}$, C_4, corresponding respectively to ethane, ethylene, propane, propene and racemic C_4 hydrocarbon. MMA, DMA and TMA represent the methylamines that comprise mono-, di-, and tri-methylamine, respectively. Additionally, DME represents dimethyl ether.*

Table 3.1: *Details on analysis settings at the SCION 456 and Agilent 8860 System gas chromatographs applied for online analytics during catalysis tests.*

SCION GC

	FID-channel	TCD-channel		
Split ratio	20:1	10:1		
		Rate (psi min^{-1})	Value (psi)	Hold time (min)
Program column pressure	Constant	Initial	17.0	3.7
		400.0	2.0	0.0

	Rate (K min^{-1})	Value (K)	Hold time (min)
Program temperature oven	Initial	313	15
	10	463	16

Agilent 8860 GC

	FID-channel	TCD-channel		
Makeup flow (He)	25 mL min^{-1}	5 mL min^{-1}		
Split ratio	18:1	8:1		
		Rate (psi min^{-1})	Value (psi)	Hold time (min)
Program column pressure	Constant	Initial	10.0	1.0
		15.0	35.0	18.4

	Rate (K min^{-1})	Value (K)	Hold time (min)
Program temperature oven	Initial	313	15
	10	463	5

Table 3.1 provides details on the chromatographic programs and experimental settings. Representative online TCD (**Figure 3.9. a**) and FID chromatograms for a catalytic test of acetonitrile synthesis from syngas/NH_3 mixtures and methanol/NH_3 feeds are shown in **Figure 3.9. b** and **c**, respectively. Ar was used as internal standard for quantifications. Molar based-response factors for those compounds detected at the TCD, i.e., permanent gases such as CO, CO_2, CH_4, Ar, N_2, as well as ethane and ethylene, relative to Ar, were determined by injection of certified gas mixtures (Abelló-Linde). Regarding those compounds detected at the FID, a weight-based response factor of 1.0, relative to CH_4, was applied to all hydrocarbon compounds lacking heteroatoms. ***Table A.III.1*** *in* ***Appendix III*** provides details on the experimental chromatographic response factors employed for product quantification.

For organic nitriles containing C_2 to C_5, such as acetonitrile, response factors were experimentally determined by injecting liquid mixtures of known composition, using *n*-heptane as reference hydrocarbon. In cases where experimental response factor determination was not possible, e.g., in the case of HCN, chromatographic responses were predicted using the effective carbon number (ECN). [32–34] A summary of response factors is available in **Table A. III. 1**, see **Appendices**.

The molar flow ($\widetilde{W}_{i,TCD}$) of compounds detected in the TCD was determined employing **Equation 3.13**, wherein $\widetilde{W}_{Ar,in}$, A_i and $f_{i/Ar}$ correspond to the molar flow of Ar (internal standard) in the gas feed stream, the area of a compound *i* and the molar-based response factor of said compound *i* relative to Ar, respectively.

$$\widetilde{W}_{i,TCD} = \frac{\widetilde{W}_{Ar,in}}{f_{i/Ar}} \cdot \frac{A_i}{A_{Ar}} \qquad \textit{Eq. 3.13}$$

$$\widetilde{W}_{i,FID} = \frac{A_i}{A_{CH_4}} \cdot \frac{\widetilde{W}_{CH_4,out}}{f_{i/CH_4}} \cdot \frac{Mw_{CH_4}}{Mw_i} \qquad \textit{Eq. 3.14}$$

$$X_{NH_3}(\%) = \frac{\left(\frac{A_{NH_3}}{A_{Ar}}\right)_{in} - \left(\frac{A_{NH_3}}{A_{Ar}}\right)_{out}}{\left(\frac{A_{NH_3}}{A_{Ar}}\right)_{in}} . 100 \qquad \textbf{Eq. 3.15}$$

Additionally, methane, which was detected at both TCD and FID channels, was used as *inter-detector transfer compound*. Therefore, the quantification of the molar flow ($\widetilde{W}_{i,FID}$) for compounds (other than methane) analyzed in the FID channel was performed as described in **Equation 3.14,** using the corresponding weight-based response factor for each compound *i* relative to methane ($f_{i/CH4}$), and the respective molecular weights (M_w).The conversion of ammonia (X_{NH_3}) was determined by using the ratio of the ammonia and Ar at the feed (inlet) and reactor's outlet streams, respectively, as shown in **Equation 3.15**.

3.4.2.2 Calculation of catalytic performance parameters

The molar flows of different reactant and product compounds were used to derive the conversion of any *j*-reactant (X_j), product selectivities to each *i*-product (S_i), expressed in a carbon molar basis, *i*-product formation rates (r_i), as well as the overall carbon balance, as shown in **Equations 3.16-19**. In this thesis, all product selectivities are reported on a carbon molar basis.

$$X_j\ (C\ \%) = \frac{\widetilde{W}_{j,in} - \widetilde{W}_{j,out}}{\widetilde{W}_{j,out}} . 100 \qquad \textbf{Eq. 3.16}$$

$$S_i(C\ \%) = \frac{\widetilde{W}_{i,out} . N(C)_i}{\sum_i (\widetilde{W}_{i\ ,out} . N(C)_i)} \qquad \textbf{Eq. 3.17}$$

$$r_i\ (mmol\ g_{cat} min^{-1}) = \frac{\widetilde{W}_{i\ ,out}}{m_{cat}} \qquad \textbf{Eq. 3.18}$$

$$C\ balance(C\ \%) = \left[\frac{\sum_i (\widetilde{W}_{i\ ,out} . N(C)_i)}{\widetilde{W}_{CO,\ in}}\right] . 100 \qquad \textbf{Eq. 3.19}$$

3.4.2.3 Mass spectrometry

Initial reaction transients were studied in the same setup, monitoring the composition of the outlet stream by means of mass spectrometry in an OmniStar GSD320 mass spectrometer (Pfeiffer) equipped with C-SEM and Faraday detectors and connected online.

Acetonitrile and HCN mass spectrometry signals were recorded during the earliest stages of the reaction of conversion of NH_3/syngas mixtures on a MnMo bimetallic catalyst. The applied reaction conditions were T= 723 K, P= 1.5 bar, molar gas feed composition $2NH_3$:1CO:$1H_2$, GHSV= 7.5 h^{-1}. The ammonium manganomolybdate catalyst precursor was first calcined *ex situ* under air flow (150 mL min^{-1}) at 673 K (heating ramp of 3 K min^{-1}) for 2 h, to obtain $MnMoO_4$. Then the oxide pre-catalyst was heated up to the reaction temperature of 723 K, under N_2 flow (17.2 mL min^{-1}).

After stabilization of the MS signal, a CO/H_2/Ar gas mixture was fed into the reactor and stabilized for 5 min. Next, the reactor was bypassed, and a flow of Ar/ CO/ H_2/ NH_3 with molar composition 0.2/ 1.0/ 1.0/ 2.0 was established along the reactor's bypass, kept at 723 K, and maintained until the stabilization of the MS signal. Next, the reaction gas mixture was directed to the reactor following a rapid valve switch, and the composition of the outlet stream was monitored by online mass spectrometry. To prevent any condensation, the gas stream leaving the reactor was diluted with N_2 (105 mL min^{-1}) and the transfer line to the MS was maintained at 453 K. The temporal evolution of the volumetric concentration of acetonitrile and HCN in the reactor's outlet was determined based on the MS signal for fragments with mass-to-charge ratio (m/z) of 41 and 27, respectively, after correction for contributions expected from the fragmentation of additional reaction products, i.e., methylamine, higher nitriles, and hydrocarbons, in the quadrupole mass analyzer. **Table A.III. 2** in **Appendix III** summarizes the relative abundances of the m/z signals expected for the different fragmentation ions of the relevant reaction products following electron impact ionization, as implemented in the applied OmniStar GSD320 mass spectrometer.

3.5 REFERENCES

(1) Prieto, G.; Beijer, S.; Smith, M. L.; He, M.; Au, Y.; Wang, Z.; Bruce, D. A.; de Jong, K. P.; Spivey, J. J.; de Jongh, P. E. Design and Synthesis of Copper–Cobalt Catalysts for the Selective Conversion of Synthesis Gas to Ethanol and Higher Alcohols. *Angewandte Chemie International Edition* **2014**, *53* (25), 6397–6401. https://doi.org/10.1002/anie.201402680.

(2) Wise, R. S.; Markel, E. J. Synthesis of High Surface Area Molybdenum Nitride in Mixtures of Nitrogen and Hydrogen. *J. Catal.* **1994**, *145* (2), 344–355. https://doi.org/10.1006/jcat.1994.1043.

(3) Wolters, M.; van Grotel, L. J. W.; Eggenhuisen, T. M.; Sietsma, J. R. A.; de Jong, K. P.; de Jongh, P. E. Combining Confinement and NO Calcination to Arrive at Highly Dispersed Supported Nickel and Cobalt Oxide Catalysts with a Tunable Particle Size. *Catal. Today* **2011**, *163* (1), 27–32. https://doi.org/10.1016/j.cattod.2010.02.052.

(4) Prieto, G.; Zečević, J.; Friedrich, H.; de Jong, K. P.; de Jongh, P. E. Towards Stable Catalysts by Controlling Collective Properties of Supported Metal Nanoparticles. *Nat. Mater.* **2013**, *12* (1), 34–39. https://doi.org/10.1038/nmat3471.

(5) Sietsma, J. R. A.; Meeldijk, J. D.; den Breejen, J. P.; Versluijs-Helder, M.; van Dillen, A. J.; de Jongh, P. E.; de Jong, K. P. The Preparation of Supported NiO and Co_3O_4 Nanoparticles by the Nitric Oxide Controlled Thermal Decomposition of Nitrates. *Angewandte Chemie International Edition* **2007**, *46* (24), 4547–4549. https://doi.org/10.1002/anie.200700608.

(6) Thommes, M.; Kaneko, K.; Neimark, A. V.; Olivier, J. P.; Rodriguez-Reinoso, F.; Rouquerol, J.; Sing, K. S. W. Physisorption of Gases, with Special Reference to the Evaluation of Surface Area and Pore Size Distribution (IUPAC Technical Report). *Pure and Applied Chemistry* **2015**, *87* (9–10), 1051–1069. https://doi.org/10.1515/pac-2014-1117.

(7) Weidenthaler, C. Pitfalls in the Characterization of Nanoporous and Nanosized Materials. *Nanoscale* **2011**, *3* (3), 792. https://doi.org/10.1039/c0nr00561d.

(8) Hölzer, G.; Fritsch, M.; Deutsch, M.; Härtwig, J.; Förster, E. $K\alpha_{1,2}$ and $K\beta_{1,3}$ X-Ray Emission Lines of the 3d Transition Metals. *Phys. Rev. A (Coll Park)* **1997**, *56* (6), 4554–4568. https://doi.org/10.1103/PhysRevA.56.4554.

(9) Pifferi, A. X-Ray Sources. In *Encyclopedia of Condensed Matter Physics*; Elsevier, **2005**, 323–329. https://doi.org/10.1016/B0-12-369401-9/00631-8.

(10) Vickerman, J. C.; Gilmore, I. S. *Surface Analysis – The Principal Techniques, 2nd Edition*, 2nd ed.; Vickerman, J. C., Gilmore, I. S., Eds.; John Wiley & Sons, **2009**.

(11) Terban, M. W.; Billinge, S. J. L. Structural Analysis of Molecular Materials Using the Pair Distribution Function. *Chem. Rev.* **2022**, *122* (1), 1208–1272. https://doi.org/10.1021/acs.chemrev.1c00237.

(12) Fauth, F.; Boer, R.; Gil-Ortiz, F.; Popescu, C.; Vallcorba, O.; Peral, I.; Fullà, D.; Benach, J.; Juanhuix, J. The Crystallography Stations at the Alba Synchrotron. *The European Physical Journal Plus* **2015**, *130* (8), 160. https://doi.org/10.1140/epjp/i2015-15160-y.

(13) Bergamaschi, A.; Cervellino, A.; Dinapoli, R.; Gozzo, F.; Henrich, B.; Johnson, I.; Kraft, P.; Mozzanica, A.; Schmitt, B.; Shi, X. The MYTHEN Detector for X-Ray Powder Diffraction Experiments at the Swiss Light Source. *J Synchrotron Radiat* **2010**, *17* (5), 653–668. https://doi.org/10.1107/S0909049510026051.

(14) Tanuma, S.; Powell, C. J.; Penn, D. R. Calculations of Electron Inelastic Mean Free Paths. IX. Data for 41 Elemental Solids over the 50 EV to 30 KeV Range. *Surface and Interface Analysis* **2011**, *43* (3), 689–713. https://doi.org/10.1002/sia.3522.

(15) Iglesias-Juez, A.; Chiarello, G. L.; Patience, G. S.; Guerrero-Pérez, M. O. Experimental Methods in Chemical Engineering: X-ray Absorption Spectroscopy—XAS, XANES, EXAFS. *Can J. Chem. Eng.* **2022**, *100* (1), 3–22. https://doi.org/10.1002/cjce.24291.

(16) Ravel, B.; Newville, M. *ATHENA* , *ARTEMIS* , *HEPHAESTUS* : Data Analysis for X-Ray Absorption Spectroscopy Using *IFEFFIT*. *J. Synchrotron Radiat.* **2005**, *12* (4), 537–541. https://doi.org/10.1107/S0909049505012719.

(17) Muñoz, M.; Argoul, P.; Farges, F. Continuous Cauchy Wavelet Transform Analyses of EXAFS Spectra: A Qualitative Approach. *American Mineralogist* **2003**, *88* (4), 694–700. https://doi.org/10.2138/am-2003-0423.

(18) Kurlov, A.; Deeva, E. B.; Abdala, P. M.; Lebedev, D.; Tsoukalou, A.; Comas-Vives, A.; Fedorov, A.; Müller, C. R. Exploiting Two-Dimensional Morphology of Molybdenum Oxycarbide to Enable Efficient Catalytic Dry Reforming of Methane. *Nat. Commun.* **2020**, *11* (1), 4920. https://doi.org/10.1038/s41467-020-18721-0.

(19) Zarrabeitia, M.; Gonzalo, E.; Pasqualini, M.; Ciambezi, M.; Lakuntza, O.; Nobili, F.; Trapananti, A.; Di Cicco, A.; Aquilanti, G.; Katcho, N. A.; López del Amo, J. M.; Carrasco, J.; Muñoz-Márquez, M. Á.; Rojo, T. Unraveling the Role of Ti in the Stability of Positive Layered Oxide Electrodes for Rechargeable Na-Ion Batteries. *J. Mater. Chem. A Mater.* **2019**, *7* (23), 14169–14179. https://doi.org/10.1039/C9TA02710F.

(20) Wang, Z. L.; Lee, J. L. Electron Microscopy Techniques for Imaging and Analysis of Nanoparticles. In *Developments in Surface Contamination and Cleaning*; Elsevier, 2008, 395–443. https://doi.org/10.1016/B978-0-323-29960-2.00009-5.

(21) Kresse, G. Ab Initio Molecular Dynamics for Liquid Metals. *J. Non Cryst. Solids* **1995**, *192–193*, 222–229. https://doi.org/10.1016/0022-3093(95)00355-X.

(22) Kresse, G.; Furthmüller, J. Efficient Iterative Schemes for *Ab Initio* Total-Energy Calculations Using a Plane-Wave Basis Set. *Phy.s Rev. B* **1996**, *54* (16), 11169–11186. https://doi.org/10.1103/PhysRevB.54.11169.

(23) Perdew, J. P.; Burke, K.; Ernzerhof, M. Generalized Gradient Approximation Made Simple. *Phys. Rev. Lett.* **1996**, *77* (18), 3865–3868. https://doi.org/10.1103/PhysRevLett.77.3865.

(24) Blöchl, P. E. Projector Augmented-Wave Method. *Phys. Rev. B* **1994**, *50* (24), 17953–17979. https://doi.org/10.1103/PhysRevB.50.17953.

(25) Methfessel, M.; Paxton, A. T. High-Precision Sampling for Brillouin-Zone Integration in Metals. *Phys. Rev. B* **1989**, *40* (6), 3616–3621. https://doi.org/10.1103/PhysRevB.40.3616.

(26) Monkhorst, H. J.; Pack, J. D. Special Points for Brillouin-Zone Integrations. *Phys. Rev. B* **1976**, *13* (12), 5188–5192. https://doi.org/10.1103/PhysRevB.13.5188.

(27) Henkelman, G.; Uberuaga, B. P.; Jónsson, H. A Climbing Image Nudged Elastic Band Method for Finding Saddle Points and Minimum Energy Paths. *J. Chem. Phys.* **2000**, *113* (22), 9901–9904. https://doi.org/10.1063/1.1329672.

(28) Giannozzi, P.; Baroni, S.; Bonini, N.; Calandra, M.; Car, R.; Cavazzoni, C.; Ceresoli, D.; Chiarotti, G. L.; Cococcioni, M.; Dabo, I.; Dal Corso, A.; de Gironcoli, S.; Fabris, S.; Fratesi, G.; Gebauer, R.; Gerstmann, U.; Gougoussis, C.; Kokalj, A.; Lazzeri, M.; Martin-Samos, L.; Marzari, N.; Mauri, F.; Mazzarello, R.; Paolini, S.; Pasquarello, A.; Paulatto, L.; Sbraccia, C.; Scandolo, S.; Sclauzero, G.; Seitsonen, A. P.; Smogunov, A.; Umari, P.; Wentzcovitch, R. M. QUANTUM ESPRESSO: A Modular and Open-Source Software Project for Quantum Simulations of Materials. *Journal of Physics: Condensed Matter* **2009**, *21* (39), 395502. https://doi.org/10.1088/0953-8984/21/39/395502.

(29) Giannozzi, P.; Andreussi, O.; Brumme, T.; Bunau, O.; Buongiorno Nardelli, M.; Calandra, M.; Car, R.; Cavazzoni, C.; Ceresoli, D.; Cococcioni, M.; Colonna, N.; Carnimeo, I.; Dal Corso, A.; de Gironcoli, S.; Delugas, P.; DiStasio, R. A.; Ferretti, A.; Floris, A.; Fratesi, G.; Fugallo, G.; Gebauer, R.; Gerstmann, U.; Giustino, F.; Gorni, T.; Jia, J.; Kawamura, M.; Ko, H.-Y.; Kokalj, A.; Küçükbenli, E.; Lazzeri, M.; Marsili, M.; Marzari, N.; Mauri, F.; Nguyen, N. L.; Nguyen, H.-V.; Otero-de-la-Roza, A.; Paulatto, L.; Poncé, S.; Rocca, D.; Sabatini, R.; Santra, B.; Schlipf, M.; Seitsonen, A. P.; Smogunov, A.; Timrov, I.; Thonhauser, T.; Umari, P.; Vast, N.; Wu, X.; Baroni, S. Advanced Capabilities for Materials Modelling with Quantum ESPRESSO. *Journal of Physics: Condensed Matter* **2017**, *29* (46), 465901. https://doi.org/10.1088/1361-648X/aa8f79.

(30) Perdew, J. P.; Burke, K.; Ernzerhof, M. Generalized Gradient Approximation Made Simple. *Phys. Rev. Lett.* **1996**, *77* (18), 3865–3868. https://doi.org/10.1103/PhysRevLett.77.3865.

(31) Blöchl, P. E. Projector Augmented-Wave Method. *Phys. Rev. B* **1994**, *50* (24), 17953–17979. https://doi.org/10.1103/PhysRevB.50.17953.

(32) Robert Raymond, C. Flame Ionization Detection of Hydrocyanic Acid, Analysis of Trace Aqueous Solutions, **1968**.

(33) Dietz, W. A. Response Factors for Gas Chromatographic Analyses. *J. Chromatogr. Sci.* **1967**, *5* (2), 68–71. https://doi.org/10.1093/chromsci/5.2.68.

(34) Kretzschmar, N.; Seifert, M.; Busse, O.; Weigand, J. J. Prediction of Retention Indices and Response Factors of Oxygenates for GC-FID by Multilinear Regression. *Data (Basel)* **2022**, *7* (9), 133. https://doi.org/10.3390/data7090133.

CHAPTER 4.

NITRILE SYNTHESIS BY REACTION OF NH_3/SYNGAS MIXTURES ON MOLYBDENUM NITRIDE: INSIGHTS INTO THE REACTION MECHANISM

4.1 INTRODUCTION

Transition metal nitrides (TMN) currently attract an increasing deal of attention in various catalysis areas. These interstitial materials bear surface electronic and catalytic features, which resemble those of group VIII elements in their metallic state.[1,2] Indeed, they have been proven to show H_2 activation and C-C chain-growth activities, which are prototypical for metallic surfaces.[3–5] Besides, they are known to withstand aggressive reaction conditions, e.g., in the presence of gaseous ammonia and under specific settings, and have been proposed to act as reservoirs and solid transfer agents for active nitrogen species.[6–8]

These properties make transition metal nitrides attractive for transformations, which require the integration of C-C and C-N coupling reactions, for instance, for the bottom-up conversion of (renewable) syngas and ammonia feedstocks into added-value nitrogenated compounds. The development of such unconventional conversion routes is appealing in the quest for a de-fossilization of bulk chemicals production. Exemplarily, nitriles are important commodities at the entry point to several value chains. In particular, acetonitrile (MeCN) finds a wide array of applications as solvent, extractive distillation agent in olefin purification processes, as electrolyte in lithium batteries[9,10] or as precursor for specialties and pharmaceutical compounds, among others.[11]

The direct synthesis of nitrile compounds by conversion of NH_3/syngas mixtures was first reported by researchers at Monsanto[12] and others.[13–16] Both iron and molybdenum-based catalysts have been reported for this reaction. Mo-based catalysts have been proposed to generally deliver higher selectivity to C_{2+} nitriles.[12] However, limited attention has been devoted to elucidating the structure of the working catalysts and the reaction mechanism, in spite of their significance to progress towards improved catalyst formulations and performances.

Common to both iron and molybdenum is that these metals can form nitride compounds under nitrogen-sourcing reactive atmospheres. Both Fe and Mo nitrides have been shown to be catalytically active for syngas activation and C-C chain propagation in the Fischer-Tropsch synthesis of synthetic

hydrocarbons.[17,18] Herein we experimentally verify that an oxidic molybdenum catalyst precursor undergoes *in situ* (near surface) nitridation and evolves spontaneously into Mo_2N upon exposure to relevant reaction conditions for the direct conversion of syngas/NH_3 mixtures to acetonitrile. As a result, the metal nitride compound is identified as the working catalyst. Periodic Density Functional Theory (DFT) calculations are performed to elucidate the possible reaction mechanism on a molybdenum nitride model surface. The reaction entails a complex network of carbon monoxide and ammonia dissociative activation, followed by C-N and C-C coupling from C_1 and N_1 monomeric adspecies towards C_{2+} nitrile products. The results suggest the dehydrogenation of HCN, a particularly stable intermediate product, as a kinetically controlling step towards nitrile formation.

4.2 RESULTS AND DISCUSSION

In silico thermodynamic simulations supported the feasibility to produce HCN and higher nitriles (e.g. acetonitrile) by conversion of syngas/ammonia mixtures at temperatures in the range of 673-873 K and pressures in the range of 1-10 bar, see **Appendix VII** in **Appendices**. It stemmed from the equilibrium simulations that catalyst development faces the challenge of inhibiting nitrogen recombination into N_2, which is thermodynamically preferred to C-N coupling, as well as methanation and WGS reactions, given that CH_4 and CO_2 are thermodynamically favored over C_{2+} products, including N-compounds.

The oxidic catalyst precursor showed the *Pbnm* structure for MoO_3. The average crystallite size, as determined by line broadening analysis of XR diffractions, was >100 nm. The catalytic performance for the direct synthesis of acetonitrile was assessed by exposure to a CO: H_2: NH_3 (25: 25: 50 % vol) feed stream at 723 K.

First, performance was studied as a function of the gas weight hourly space velocity WHSV (**Figure 4.1. a**). Hydrogen cyanide was the major organic product at the highest space velocity of 7.1 h^{-1}, i.e., the lowest contact time corresponding to a CO conversion level <10 %. Progressively decreasing WHSV,

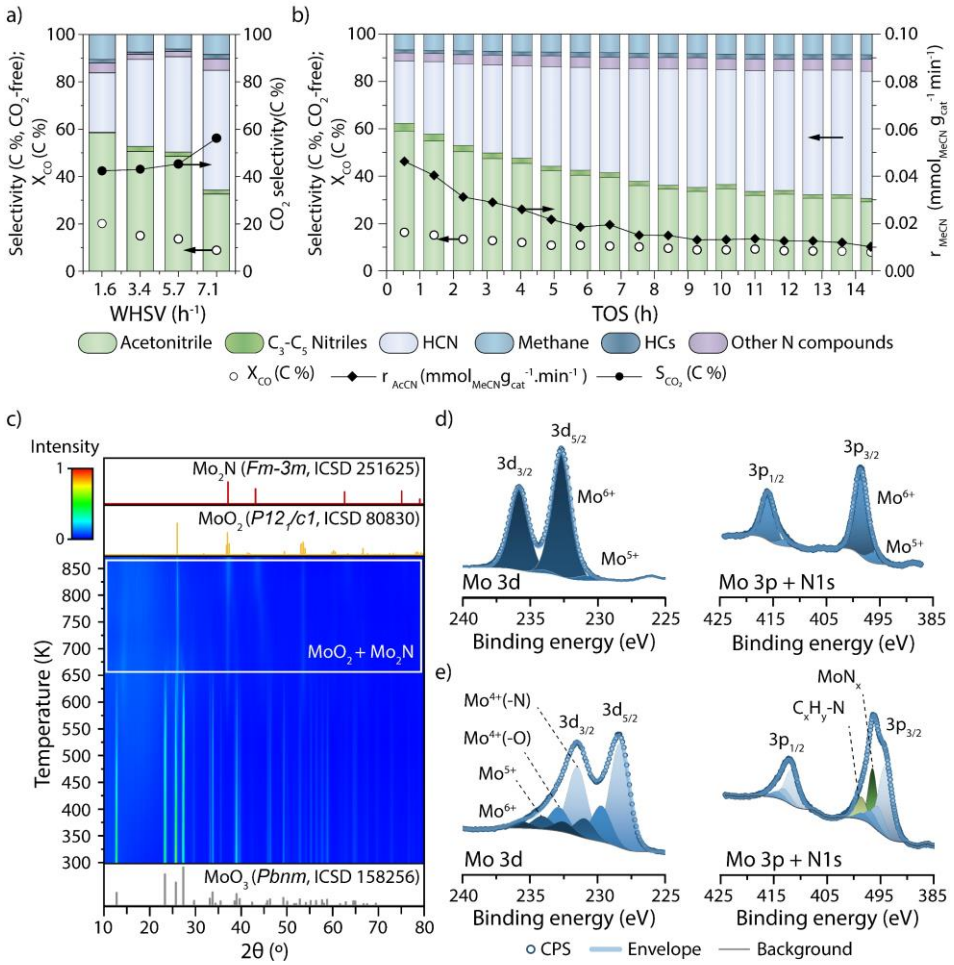

Figure 4.1: *a) Dependence of CO conversion (X_{CO}) and product selectivity with WHSV and b) evolution of CO conversion, acetonitrile formation rate (r_{MeCN}) and product selectivity (within organic products, CO_2-free basis) with time on stream (TOS) for the direct synthesis of acetonitrile from a NH_3/syngas mixture. Reaction conditions: T=723 K, P=3 bar, gas feed molar composition NH_3: CO: H_2=2: 1: 1. c) Temperature-resolved X-ray diffraction patterns recorded during the exposure of the MoO_3 catalyst precursor to the NH_3/syngas reactive atmosphere in the temperature range of 523-873 K and P= 1 bar. d, e) X-ray photoemission spectra, in the Mo3d and Mo3p + N1s core level spectral regions, for d) the pristine MoO_3 catalyst precursor and, e) the Mo-based catalyst after exposure to reaction conditions for 10 hours-on-stream.*

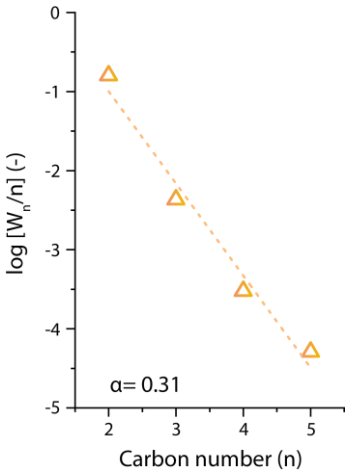

Figure 4.2: *Linearized Anderson-Schulz-Flory plot and the corresponding chain-growth probability (α) for nitrile products obtained in the direct conversion of a NH_3/syngas mixture on the Mo nitride catalyst. Reaction conditions: T=723 K, P=3 bar, gas feed molar composition $2NH_3$: 1CO: $1H_2$, WHSV= 7.1 h^{-1}. W_n stands for the weight fraction of nitrile products with n carbon atoms within the products. The dotted line corresponds to the linear regression of the data set.*

i.e., increasing the gas-catalyst contact time, the share of acetonitrile in the products increased steadily, at the expense of HCN, suggesting that the latter is an intermediate product along the acetonitrile production path. The share of C_{3+} nitriles was significantly lower (<4 % within the nitrile products), indicating a limited C-C chain-growth activity from C_2 intermediates. The nitrile Anderson-Schulz-Flory chain growth probability (α) was found to be 0.31 (**Figure 4.2**). Methylamine was the major product among the nitrogen containing organic compounds other than nitriles, with a selectivity in the range of 2.3-4.8 %, while only minor amounts of methane and other light (C_{4-}) hydrocarbons were detected (<12.0 %). A fraction of the oxygen in the syngas feed was rejected in the form of CO_2, via the water gas shift reaction (WGSR). The selectivity to CO_2 was in the range of 42.3-45.2 % for WHSV ≤5.7 h^{-1} and increased to 56.2 % at the highest studied space velocity (7.1 h^{-1}).

A longer catalysis test was performed at a fixed WHSV of 7.1 h^{-1} to evaluate stability (**Figure 4.1. b**). Initially, a MeCN formation rate of

0.046 mmol g_{cat}^{-1} min^{-1} was registered. This production rate decreased progressively over the first ca. 10 hours on-stream, beyond which a pseudo-steady state was attained. Next to a progressive drop in CO conversion rate, the major contribution to deactivation was associated to a decline in the selectivity to acetonitrile within the organic products, from 59.1 % initially to 32.2 % in the pseudo-steady state. This decrease in MeCN selectivity took place in favor of an increasing share of HCN within the organic products, suggesting the deactivation of active sites involved in C-C coupling from the HCN intermediate.

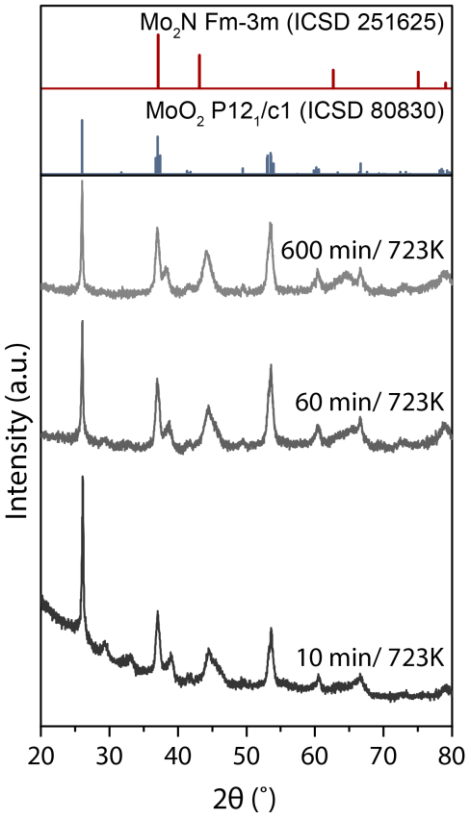

Figure 4.3: *Ex situ XRD of MoO_3 exposed to reaction conditions for the direct conversion of a NH_3/syngas (T=723 K, gas feed molar composition $2NH_3$:1CO:$1H_2$) for different times on stream (10, 60 and 600 min, respectively). On the top side of the plot, simulated diffraction patterns for MoO_2 (ICSD 80830) and γ-Mo_2N (ICSD 251625) are shown for reference purposes.*

The evolution of the catalyst structure upon exposure to the syngas/NH_3 reactive atmosphere was assessed by temperature-resolved X-ray diffraction. As shown in **Figure 4.1. c**, the oxidic MoO_3 precursor became unstable at temperatures ≥600 K. Beyond this temperature, diffractions for MoO_3 progressively vanished and new diffractions emerged, which could be indexed to MoO_2 (*P 1 2₁/c 1*) and γ-Mo_2N_{1-x} (*Fm-3m*), indicating reductive nitridation of the molybdenum catalyst. This nitridation did not proceed to completion in the temperature range studied (up to 873 K), as indicated by the persistence of diffraction signals for MoO_2. Similarly, the coexistence of MoO_2 and Mo_2N crystalline domains was ascertained following an isothermal catalysis test at 723 K (**Figure 4.3**), indicative that this microstructure is representative for the working catalyst.

Complementarily, X-ray photoelectron spectroscopy was applied to study the near-surface Mo speciation (**Figure 4.1. d-e**). The Mo3d core level spectrum for the MoO_3 catalyst precursor showed a dominant contribution at a binding energy (BE) of 232.72 eV, corresponding to the expected Mo^{6+} oxidation state. A minor additional contribution was found at 230.92 eV, which may be ascribed to

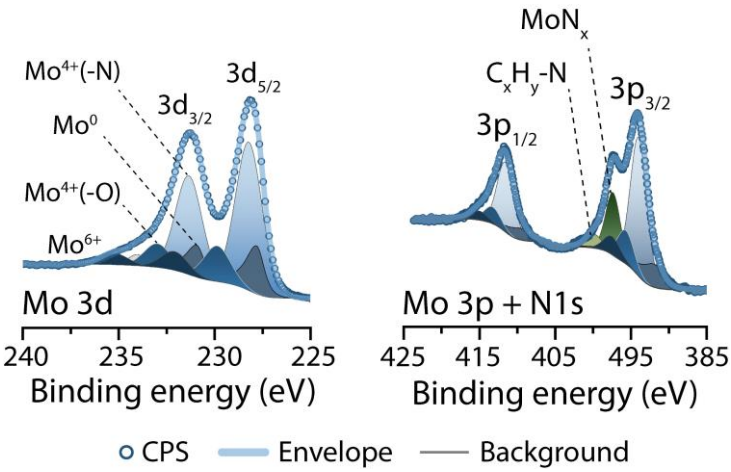

Figure 4.4: *X-ray photoemission spectra in the Mo3d and Mo3p + N1s core level spectral regions for a γ-Mo_2N standard.*

partially reduced Mo species, possibly originated from an *in situ* partial surface reduction under the incident X-ray beam. In contrast, the catalyst following prolonged (10 h) exposure to reaction conditions showed a diversity of Mo3d contributions, corresponding to different Mo oxidation states.

The major component, at a BE of 228.35 eV, accounted for 60 % of the near-surface Mo species and it is ascribed to Mo^{4+} in a nitrided direct coordination environment. Additional components were also detected with BEs of 232.44 eV, 230.85 eV and 229.66 eV, which can be ascribed to Mo^{6+}, Mo^{5+} and Mo^{4+} in (partially) oxidic environments, respectively. A comparable near-surface Mo speciation pattern was observed for a reference γ-Mo_2N material obtained by *ex situ* nitridation (**Figure 4.4,** and **Table A. IV.1**, *see* **Appendices A.IV**), confirming that the near-surface composition of the working catalyst is compatible with the Mo_2N phase detected with XRD too.

Regarding the N1s core level spectral region, two different species could be discerned, with BEs of 396.5 and 398.7 eV, respectively. These binding energies are characteristic for metal nitrides[19,20] and sp^2 nitrogen atoms in carbonaceous compounds,[21,22] correspondingly. While the former is ascribed to the Mo nitride phase developed under reaction conditions, the latter may be associated to nitrogenated hydrocarbon/coke species strongly bounded to the catalyst surface. No signs for carbidic carbon species (C1s BE~282.7 eV) were detected, indicating that, under process conditions, the Mo-based catalyst takes interstitial nitrogen up, but not carbon.

(Scanning) transmission electron microscopy ((S)TEM) was applied to assess nanostructural changes driven by the reactive atmosphere. Prolonged exposure to reaction conditions resulted in sintering, from the starting, markedly faceted MoO_3 nanocrystals (194 ±130 nm) into comparatively larger (429± 178 nm) particles with smoothed edges (**Figure 4.5**). **Figure 4.6** shows TEM and HAADF-STEM micrographs for representative catalyst particles following 10 hours under catalysis conditions. Energy Dispersive X-ray Spectroscopy (EDS) maps and linescans were recorded to assess nanoscale compositional gradients.

Figure 4.6. f shows the radial evolution of the Mo content and N/O signal ratio for a catalyst particle. The near-surface rim was found to be richer in nitrogen, while the N/O atomic ratio decreased towards the inner bulk and it was minimum at the center of the particle. Additional regions were inspected with similar results (**Figure A.IV.1**, see **Appendix IV**). This radial compositional gradient indicates a partial, near-surface nitridation of the MoO_3 crystals.

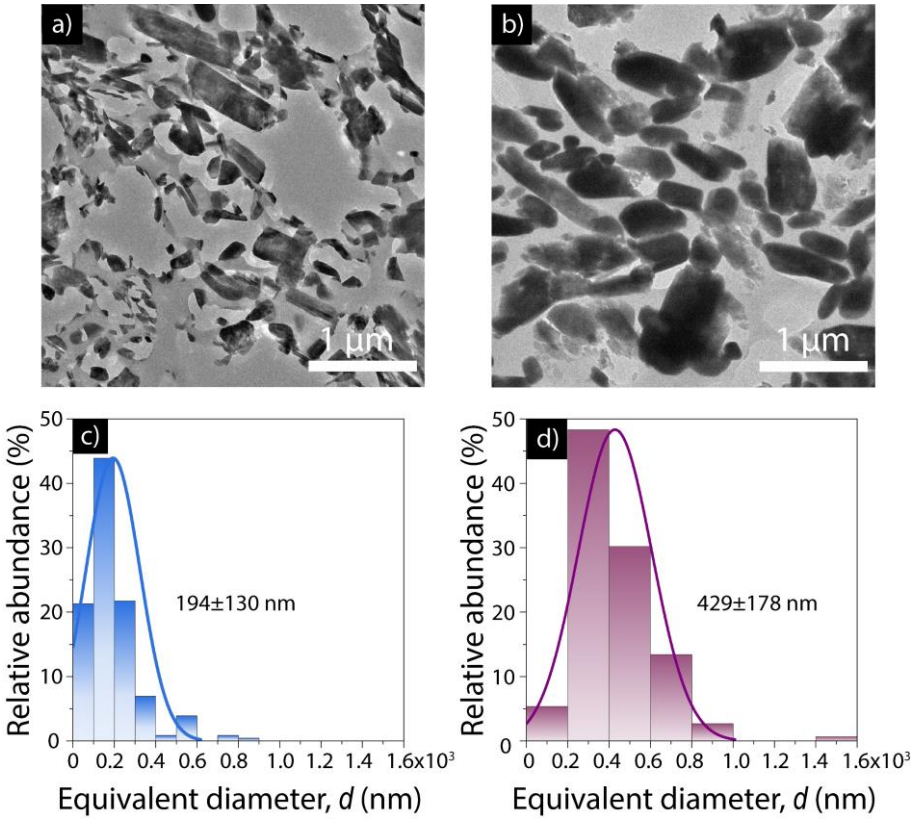

Figure 4.5: *Transmission electron micrographs and the corresponding particle size distributions for a,c) the pristine MoO_3 catalyst precursor and b,d) following exposure to reaction conditions for the conversion of a NH_3/syngas mixture to acetonitrile ($3NH_3$:$1CO$:$1H_2$ feed stream, T=723 K) for 10 h. Given the anisotropic shape of the particles, individual particle sizes (d) were assessed as $d = (4A/\pi)^{1/2}$, wherein d is the equivalent particle diameter and A is the projected particle area.*

Taken together, the above characterization results furnish evidence for an extensive nitridation of the catalyst upon exposure to the reactive syngas/NH_3 atmosphere at relevant catalysis conditions. Crystal domains for MoO_2 endure this catalyst transformation. However, they correspond to the innermost core of the catalyst particles, which the nitridation front does not penetrate. The outer surface of the working catalyst is best described as molybdenum nitride.

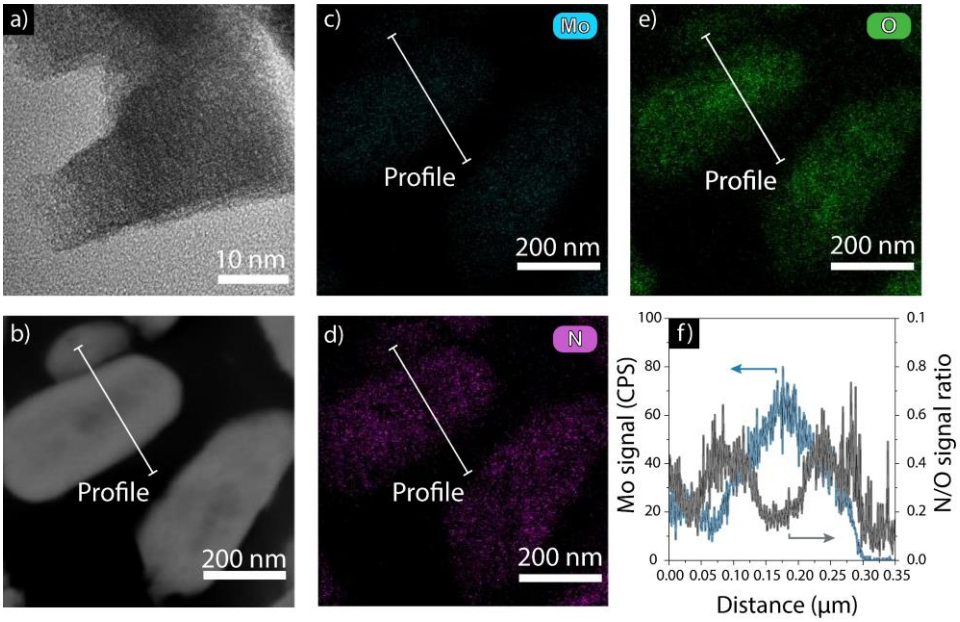

Figure 4.6: *a) Representative high-resolution transmission electron microscopy (HR-TEM) and, b) high-angle annular dark-field scanning-transmission electron microscopy (HAADF-STEM) micrographs for the molybdenum catalyst following 10 h of exposure to reaction conditions for the synthesis of acetonitrile from syngas/NH_3 mixtures. Feed composition: $3NH_3$: 1CO: $1H_2$ (vol), reaction temperature= 723 K. c-e) EDS compositional maps collected for the area imaged in (b). f) Spatial evolution of the Mo signal and the N/O signal ratio along the linescan EDS compositional profile recorded across a representative particle (see segment marked on panels b-d). Distance expressed from left to right along the profile segment.*

4.3 THEORETICAL INSIGHTS INTO THE REACTION MECHANISM

Periodic DFT calculations were performed, at the GGA-PBE level of theory, to get molecular-level insights into the reaction mechanism. A γ-Mo_2N(100) surface was selected as a catalyst model given that {100} planes are parallel to the basal plane in the platelet-like crystallite morphology, which is characteristic for γ-Mo_2N.

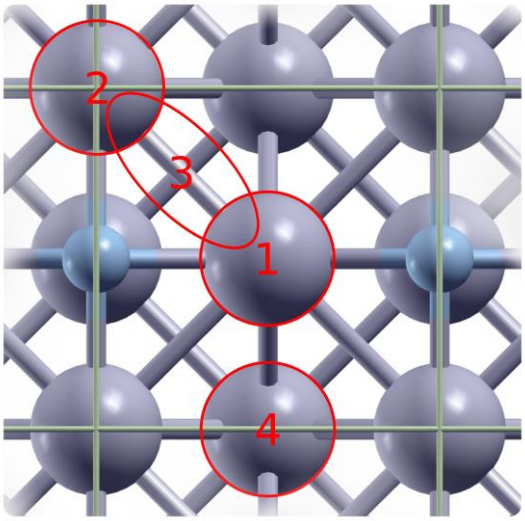

Figure 4.7: *Top view of the γ-Mo_2N(100) surface showing a p(1x1) unit cell and adsorption sites, 1) Atop (Mo^{III}), 2) Top (Mo^{II}), 3) Bridged, 4) Hollow. Mo atoms are depicted gray and N atoms in blue.*

First, the (co)adsorption of CO and NH_3 reactants was investigated. Adsorption centers on the Mo_2N(100) surface include hollow, bridge, and atop sites on two inequivalent Mo cations, directly coordinated to either two or three N atoms, which we shall denote Mo^{II} and Mo^{III}, respectively (**Figure 4.7**). Molecular CO binds to different sites on Mo_2N(100), i.e., atop, bridged, and significantly more strongly ($E_{ad,\,CO}$= -156 kJ mol^{-1}) than NH_3 ($E_{ad,\,NH3}$= -93 kJ mol^{-1}) or any NH_x (x=0-2) species ($E_{ad,\,NHx}$ >-130 kJ mol^{-1}). Unlike CO, the latter shows a remarkable site

specificity, with NH species and N adatoms showing a strong preference for hollow sites. The co-adsorption of CO and NH_x species was also studied to ascertain how lateral interactions between adsorbates affect their binding to the catalyst surface (**Table 4.1**). Co-adsorption of molecular CO and NH_3 reactants leads to comparatively minor drops (7 kJ mol^{-1}) in their individual adsorption energies. A notably higher destabilization of CO was found in presence of NH_2 and particularly NH species derived from ammonia decomposition, by 71 and 114 kJ mol^{-1}, respectively, while CO co-adsorption showed again a lower effect on the binding of N adatoms on hollow sites. Nevertheless, the effect of CO on the E_{ad} of nitrogen species outweighs in all cases and $E_{ad,\,CO}$ is higher for any co-adsorption combination. Similarly to what is known for e.g., metallic cobalt surfaces upon co-adsorption of syngas and NH_x,[23] these results suggest molecular CO as a dominant adsorbate on the working catalyst.

Table 4.1: *Individual adsorption and co-adsorption energies of CO and NH_x species, on γ-Mo_2N(100) as determined by DFT calculations (GGA-PBE). All adsorption energies are expressed in kJ mol^{-1}.*

Species	CO or NH_x	CO and NH_3	CO and NH_2	CO and NH	CO and N
CO	-156	-149	-85	-42	-112
NH_3	-93	-86	NA	NA	NA
NH_2	-126	NA	-55	NA	NA
NH	-79	NA	NA	35	NA
N	-130	NA	NA	NA	-87

4.3.1 Reactant activation

Having established the binding behavior of relevant surface species, different mechanistic routes for the synthesis of acetonitrile were assessed. The first necessary step is the dissociation of both CO and NH_3 reactants. Moreover, the experimental evolution of product selectivity with the gas-catalyst contact time points to HCN as a major primary product of the reaction. Hence, we have first studied reaction pathways from syngas and NH_3 to HCN.

Regarding CO dissociation, both direct scission and hydrogen-assisted pathways have been extensively discussed for syngas conversion via the Fischer-Tropsch synthesis.[24,25] As shown in **Figure 4.8**, on the herein considered $Mo_2N(100)$ surface, the activation barrier (E_a) for direct CO dissociation was found to be 160 kJ mol^{-1}. H_2-assisted CO hydrogenation to HCO and H_2CO showed plausible barriers lower than 100 kJ mol^{-1}. These species could deoxygenate with reaction barriers of 152 and 101 kJ mol^{-1}, respectively. Therefore, the results show that the H-assisted pathway is preferred for CO dissociation on the metal nitride surface, via the sequential formation of H_2CO and its dissociation to H_2C and O adspecies.

Hydrogenation of atomic C can compete with C-N and C-C coupling reactions, which are necessary for the formation of HCN and MeCN. As summarized in **Figure 4.9**, the stepwise hydrogenation of CH_x species on the molybdenum nitride surface is subjected to energy barriers lower than 100 kJ mol^{-1}. Nevertheless, as our results on CO dissociation indicated that CH_2 is the primary CH_x product from the H-assisted CO dissociation, we have focused on those steps for the (de)hydrogenation of CH_2 species. Hydrogenation to CH_3 requires surmounting an E_a of 77 kJ mol^{-1}, while the energy barrier determined for CH_2 dehydrogenation to CH is slightly lower (56 kJ mol^{-1}). Therefore, the dehydrogenative pathway is expected to proceed with slightly higher intrinsic rates.

The stepwise ammonia dehydrogenative dissociation was investigated next (**Figure 4.10**). Full NH_3 dissociation was found to be subjected to a comparatively high energy barrier of 151 kJ mol^{-1}, particularly for NH_2 dissociation.

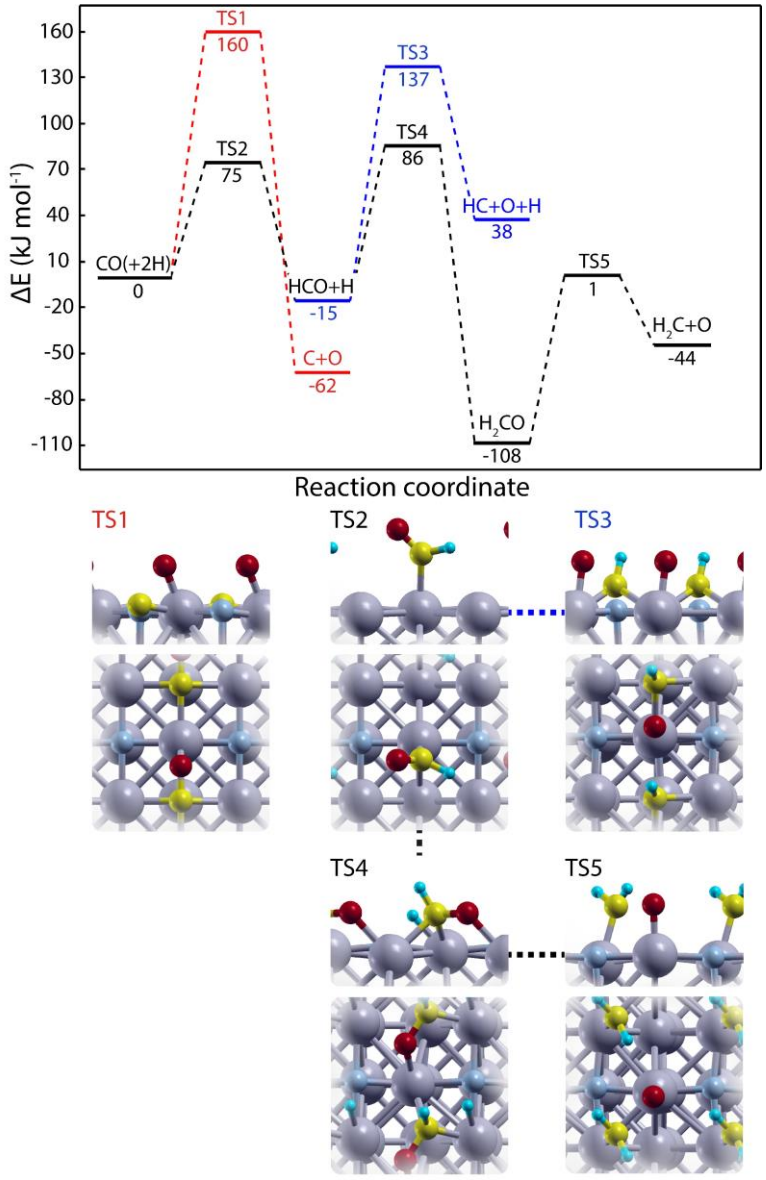

Figure 4.8: *Potential energy diagram for CO dissociation pathways on the Mo_2N (100) surface, via direct dissociation (red trace) and via hydrogen-assisted CO hydrogenation pathway to HCO (blue trace) and H_2CO formation (black trace) followed by dissociation into HC, O and H species and H_2C and O species, respectively. Zenithal and side views over the optimized transition states (TS) along the different reaction pathways are included on the bottom side. Mo, N, C, O and H atoms are shown in gray, blue, yellow, red and cyan, respectively.*

This result contrasts to the experimental finding of a relatively fast catalyst (near-surface) nitridation on exposure to reaction conditions. Hence, additional effects from CO and its dissociation products on NH_3 dissociation were studied. Atomic

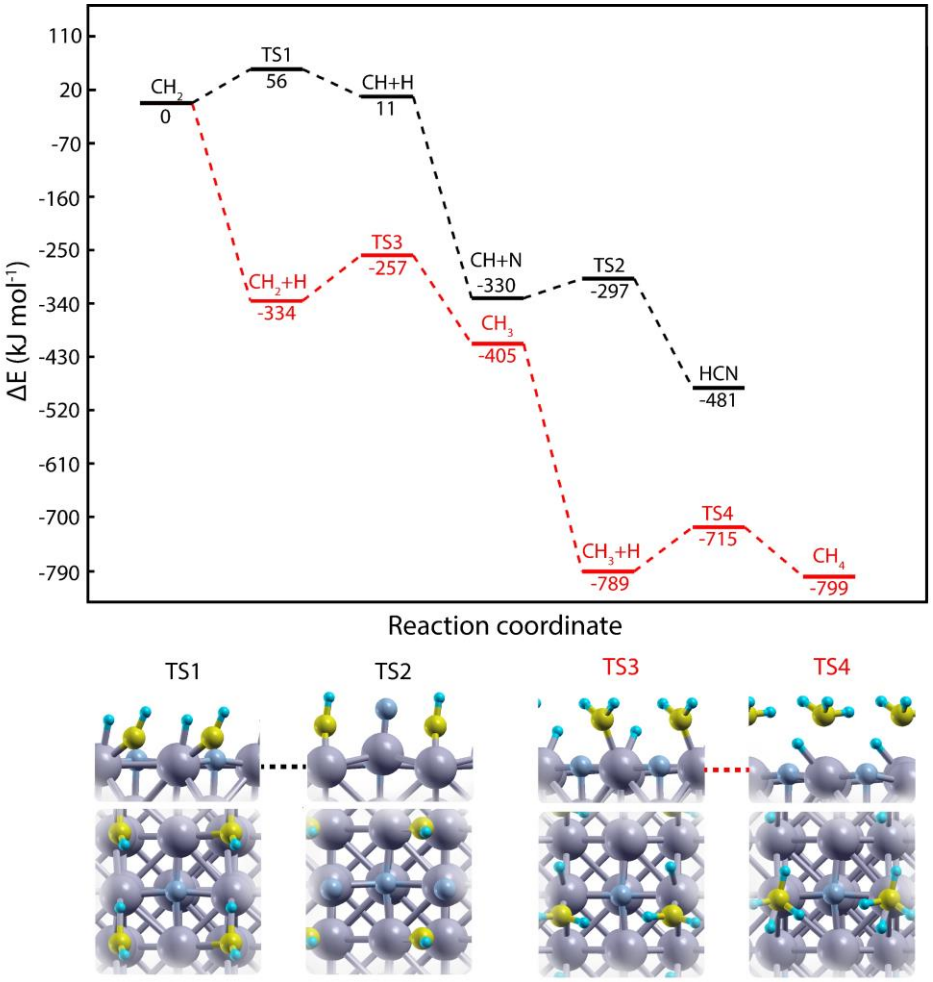

Figure 4.9: *Potential energy diagram for the hydrogenation of CH_2 adspecies to methane (red trace) and coupling of HC species to N adatoms to produce HCN (black trace) on the Mo_2N (100) surface. Zenithal and side views over the optimized transition states are included on the bottom side. Mo, N, C, O and H atoms are shown in gray, blue, yellow, red and cyan, respectively.*

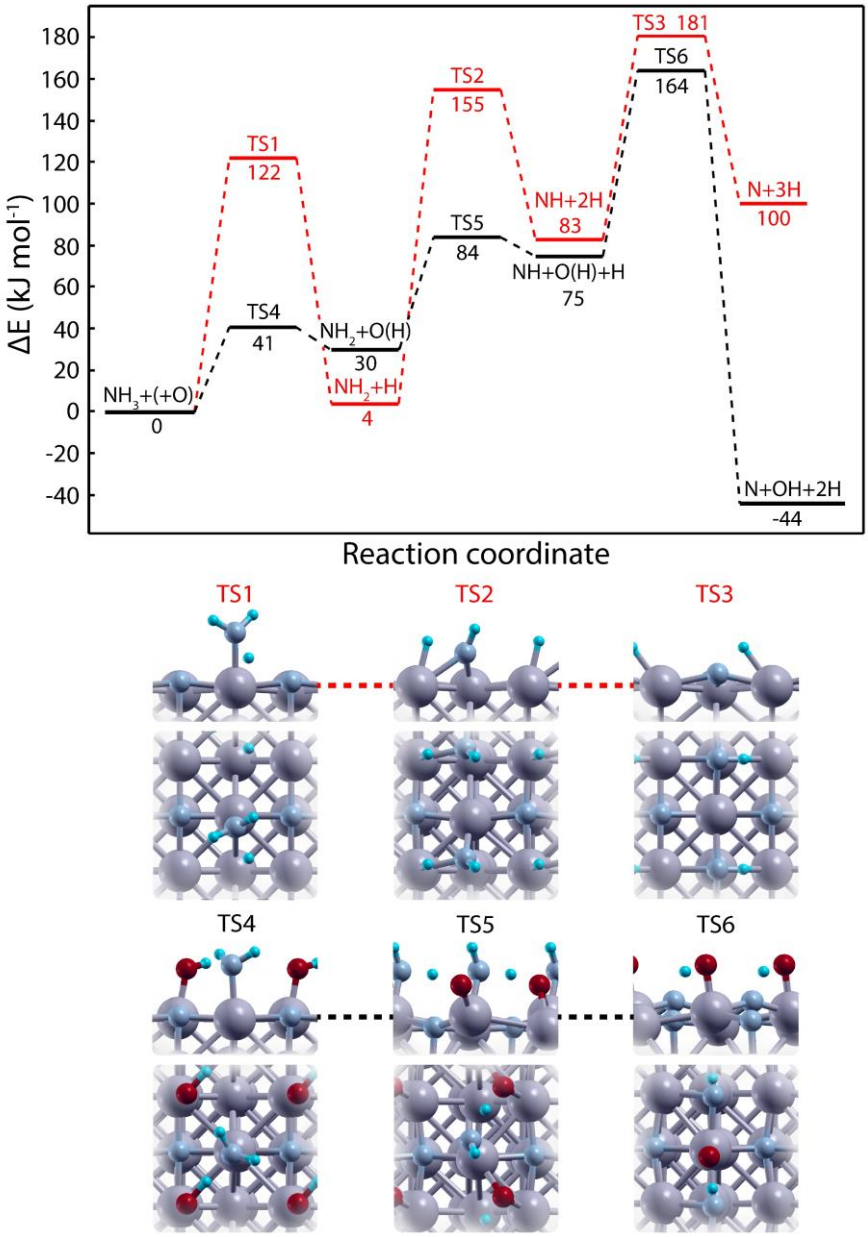

Figure 4.10: *Potential energy diagram for NH_3 dissociation, i.e., direct (red trace) vs O-assisted (black trace) on the $Mo_2N(100)$ surface. Zenithal and side views over the optimized transition states (TS) along the different reaction pathways are included on the bottom side. Mo, N, C, O and H atoms are shown in gray, blue, yellow, red and cyan, respectively.*

O species, formed as a result of CO dissociation, can affect the mechanism for HCN formation, as reported previously on Pt(111) surfaces.[26] Our results indicate that O hydrogenation to OH and H_2O may occur with barriers of 99 and 87 kJ mol^{-1}, respectively, suggesting that O may be removed from the catalyst surface by hydrogenation to water. However, as an alternative pathway, O can also be reduced by abstracting hydrogen from other surface species such as NH_x. Therefore, we have further investigated O hydrogenation by NH_x species.

On the herein investigated molybdenum nitride catalyst, O adspecies originate from CO dissociation. Remarkably, the predicted energy barriers for NH_3 and NH_2 dissociation steps (into NH_2 and NH, in turn) were vastly reduced from 122 and 151 kJ mol^{-1} to 41 and 54 kJ mol^{-1}, respectively, when surface O was considered as hydrogen acceptor. Moreover, the direct hydrogenation of surface O by reaction with NH_3 (**Equation 4.1**) was found to be subjected to a comparable (slightly lower) E_a than the alternative pathway with atomic H (**Equation 4.2**) to OH (89 vs 99 kJ mol^{-1}), supporting the proposal that surface oxygen species play a central role in facilitating the dehydrogenative activation of NH_3 on the nitride surface.

$$NH_3 + O \rightarrow NH_2 + OH \qquad \textit{Eq. 4.1}$$

$$H + O \rightarrow OH \qquad \textit{Eq. 4.2}$$

$$OH + H \rightarrow H_2O \qquad \textit{Eq. 4.3}$$

For the postulated O-assisted NH_3 dissociation mechanism, all elemental steps were found to proceed with barriers <90 kJ mol^{-1}, whilst the highest-barrier step is shifted from NH_2 decomposition (O-unassisted path) to NH dissociation in the O-assisted route, as shown in **Figure 4.10**. Further hydrogenation of OH groups to water (**Equation 4.3**) requires surmounting a reaction barrier of 87 kJ mol^{-1}, supporting a kinetically feasible removal of surface oxygen as water.

4.3.2 C-N coupling reactions

The stepwise hydrogenation of CH_2 monomeric species to methane has been found to proceed with elemental barriers of ca. 75 kJ mol^{-1}. However, as discussed above, a dehydrogenative pathway to CH is energetically preferred. As shown in **Figure 4.10**, further coupling of CH species to N adatoms to produce HCN was predicted to be particularly facile. For this reaction, the availability of hollow adsorption sites and the resulting structures for N and CH co-adsorption have strong effects on kinetics. On the neat $Mo_2N(100)$ surface, N atoms occupy preferentially hollow sites, while CH sits preferentially on the vicinal atop Mo^{III} sites. From this initial state, HCN formation proceeds with an energy barrier of 131 kJ mol^{-1}.

The most stable adsorption configuration for the resulting HCN product is bridge-type, bonded by N and CH groups to atop Mo^{II} and Mo^{III} sites, respectively, indicating that HCN formation does not require free hollow sites. Therefore, we also investigated the C-N coupling mechanism when the hollow site is free. In that state, N and CH species adsorb on Mo^{II} and Mo^{III} sites, respectively, leading to an initial state, which proceeds to HCN with a remarkably low barrier of 33 kJ mol^{-1}. Alternative pathways, e.g., via coupling of H_2C and N species followed by H_2CN dehydrogenation were found to be subjected to both kinetic (high E_a) and steric (entropic) hindrance, as indicated by a dissociation reaction energy of 97 kJ mol^{-1} and the lack of free sites for the dissociating hydrogen to adsorb, at the high surface coverage conditions investigated. These results strongly suggest that the formation of HCN may proceed via the coupling of atomic N and CH with high rates, even when hollow sites are occupied by atomic species with high preference for these binding centers, e.g., N, O or C adatoms, which is more likely to represent the catalyst surface under reaction conditions. The fact that C-N coupling provides a preferential conversion route for CH_x species, compared to full hydrogenation, agrees well with the modest rates of methane formation observed experimentally on the nitride catalyst surface (selectivity to CH_4< 11 %).

4.3.3 Acetonitrile formation

As discussed from the experimental results, and in line with earlier observations,[27] the selectivity pattern for HCN and MeCN as a function of the gas-catalyst contact time strongly suggests the former to be an important intermediate product towards acetonitrile synthesis. Mechanistically, this is considered to imply HCN readsorption and dissociation to CN + H surface species, followed by coupling of CN with CH_x species and subsequent hydrogenation to acetonitrile (MeCN), as considered in the elementary reaction steps summarized in **Figure 4.11**.

Although lesser compared to NH_3 dissociation, surface oxygen contributes also to lower the energy barrier for HCN dissociation, from 143 kJ mol^{-1} on bare $Mo_2N(100)$ to 122 kJ mol^{-1} in presence of surface O as hydrogen scavenger. Hence, HCN dissociation is subjected to a sizeable energy barrier. The resulting surface CN species may couple to CH_3 groups with a comparable energy barrier of 132 kJ mol^{-1}, resulting in the formation of CH_3CN. These computed energy barriers are in reasonable agreement with the E_{app} for acetonitrile formation of 151 kJ mol^{-1} determined experimentally (**Figure 4.12**). Therefore, our calculations suggest HCN dissociation and further C-C coupling as those elementary reaction steps subjected to the highest energy barriers. These elementary steps are, therefore, likely to hold the highest degree of rate control for the overall reaction of acetonitrile formation.

Alternative mechanistic considerations, including the direct, associative addition of HCN onto the CH_2=M carbene species to attain a direct C-C coupling to MeCN were found to yield CH_2HCN adspecies with a low barrier of 17 kJ mol^{-1}. Nevertheless, the subsequent isomerization of the latter species to MeCN is subjected to an exceptionally high energy barrier of 287 kJ mol^{-1}. Consequently, it is deemed implausible to be favored over the suggested reaction path, which involves HCN dissociation. It is also worth to note that HCN is predicted to show a comparatively low adsorption energy on the O pre-covered Mo_2N surface (- 76 kJ mol^{-1}), which, in conjunction with the relatively high activation energy barrier, suggests HCN to be a particularly stable intermediate product. This ties in

well with the experimental observation that HCN consumption to acetonitrile is a rather slow process, and hence it proceeds to significant extents only at comparatively high gas-catalyst contact times.

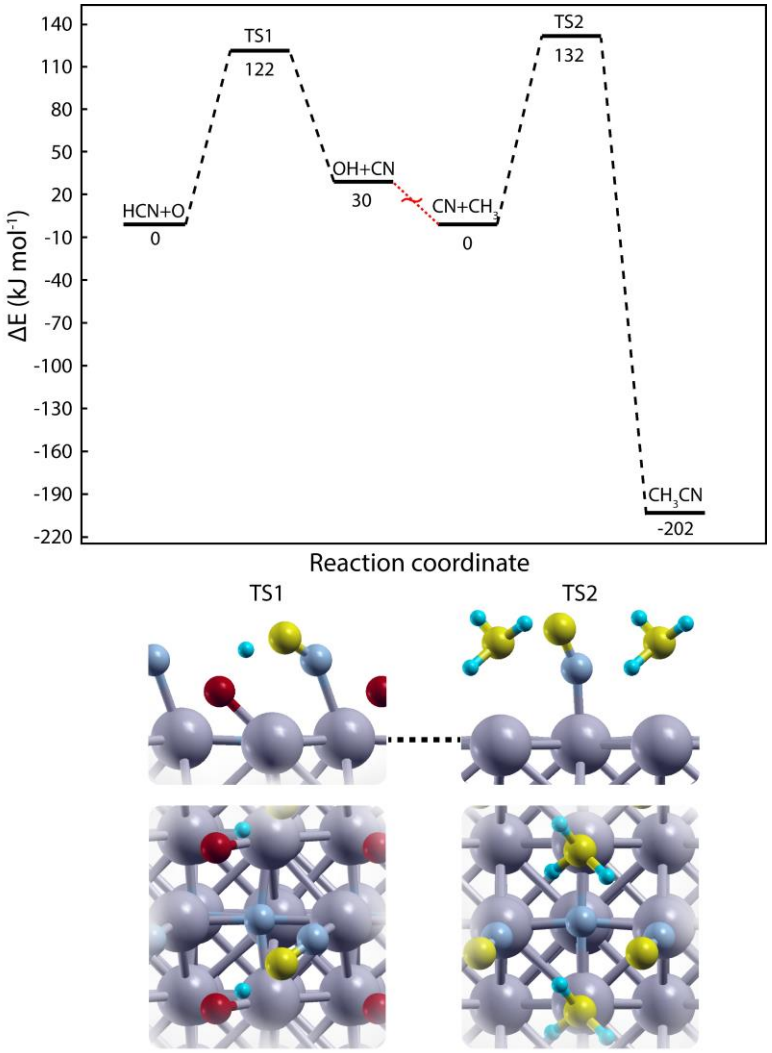

Figure 4.11: *Potential energy diagram for acetonitrile formation from HCN decomposition into -CN and -OH adspecies on the O pre-covered $Mo_2N(100)$ surface, followed by C-C coupling with CH_3 species. Zenithal and side views over the optimized transition states are included on the bottom side. Mo, N, C, O and H atoms are shown in gray, blue, yellow, red and cyan, respectively.*

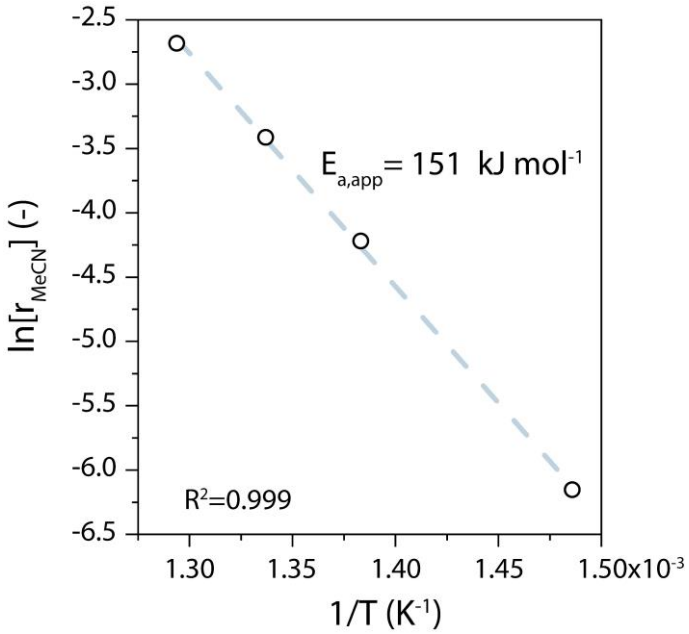

Figure 4.12: *Experimental Arrhenius plot for acetonitrile formation (formation rates determined at pseudo-steady state for X_{CO}<15 %) obtained for the studied unsupported Mo catalyst in the direct conversion of NH_3/syngas mixtures. Reaction conditions: P_{atm}, gas feed molar composition NH_3: CO: H_2=2: 1: 1. The dotted line corresponds to the linear regression of the dataset.*

4.4 CONCLUSION

Considering together the findings obtained in the chapter, the main conclusions are outlined below:

i. An oxidic MoO_3 catalyst precursor is unstable and it readily undergoes (near surface) nitridation under reaction conditions for the direct synthesis of acetonitrile from syngas and ammonia mixtures, rendering molybdenum nitride the actual working catalyst.

ii. Periodic DFT mechanistic investigations on a γ-Mo_2N(100) model surface point to H-assisted CO dissociation and O-assisted NH_3 dissociation to play central roles for the activation of both C_1 and N_1 reactants on the molybdenum nitride surface.

iii. Direct condensation of CH and N adspecies is predicted to proceed with a remarkably low energy barrier (33 kJ mol^{-1}), rendering C-N coupling kinetically irrelevant.

iv. Experimental and computational results point to HCN as a major, particularly stable intermediate product, whose dehydrogenative activation on the molybdenum nitride surface is again facilitated by H-abstraction on surface oxygen and likely determinant for the overall acetonitrile synthesis kinetics. These findings point to HCN activation as a central design criterium towards optimized Mo_2N-based catalysts.

v. Surface CN species may couple to CH_3 groups, resulting in the formation of MeCN, with a computed energy barrier of 132 kJ mol^{-1} which is in reasonable agreement with the E_{app} for acetonitrile formation of 151 kJ mol^{-1} determined experimentally.

4.5 REFERENCES

(1) S. T. Oyama; M. Boudart. Ammonia Synthesis on Surface Layers of Molybdenum Nitride. *Journal of the Research Institute for Catalysis Hokkaido University* **1980**, *28*, 305–320.

(2) Ted Oyama, S. Crystal Structure and Chemical Reactivity of Transition Metal Carbides and Nitrides. *J. Solid. State. Chem.* **1992**, *96* (2), 442–445. https://doi.org/10.1016/S0022-4596(05)80279-8.

(3) Anderson, R. B. Iron Nitrides as Fischer-Tropsch Catalysts. In *Advances in Catalysis*; 1953; Vol. 5, pp 355–384. https://doi.org/10.1016/S0360-0564(08)60645-8.

(4) Shultz, J. F.; Abelson, Manuel.; Shaw, Leonard.; Anderson, R. B. Fischer-Tropsch Synthesis. Nitrides and Carbonitrides of Iron as Catalysts. *Ind. Eng. Chem.* **1957**, *49* (12), 2055–2060. https://doi.org/10.1021/ie50576a048.

(5) Wang, C.; Zhang, J.; Chen, J. Preparation of Single-phase Iron Nitrides and Investigation of Their Fischer-Tropsch Synthesis Performance. *ChemistrySelect.* **2020**, *5* (13), 3953–3958. https://doi.org/10.1002/slct.202000456.

(6) Michalsky, R.; Avram, A. M.; Peterson, B. A.; Pfromm, P. H.; Peterson, A. A. Chemical Looping of Metal Nitride Catalysts: Low-Pressure Ammonia Synthesis for Energy Storage. *Chem. Sci.* **2015**, *6* (7), 3965–3974. https://doi.org/10.1039/C5SC00789E.

(7) Hunter, S. M.; Gregory, D. H.; Hargreaves, J. S. J.; Richard, M.; Duprez, D.; Bion, N. A Study of $^{15}N/^{14}N$ Isotopic Exchange over Cobalt Molybdenum Nitrides. *ACS Catal.* **2013**, *3* (8), 1719–1725. https://doi.org/10.1021/cs400336z.

(8) Daisley, A.; Hargreaves, J. S. J. Metal Nitrides, the Mars-van Krevelen Mechanism and Heterogeneously Catalysed Ammonia Synthesis. *Catal. Today* **2023**, *423*, 113874. https://doi.org/10.1016/j.cattod.2022.08.016.

(9) Yamada, Y.; Furukawa, K.; Sodeyama, K.; Kikuchi, K.; Yaegashi, M.; Tateyama, Y.; Yamada, A. Unusual Stability of Acetonitrile-Based Superconcentrated Electrolytes for Fast-Charging Lithium-Ion Batteries. *J. Am. Chem. Soc.* **2014**, *136* (13), 5039–5046. https://doi.org/10.1021/ja412807w.

(10) Trinh, N. D.; Lepage, D.; Aymé-Perrot, D.; Badia, A.; Dollé, M.; Rochefort, D. An Artificial Lithium Protective Layer That Enables the Use of Acetonitrile-based Electrolytes in Lithium Metal Batteries. *Angewandte Chemie International Edition* **2018**, *57* (18), 5072–5075. https://doi.org/10.1002/anie.201801737.

(11) Zhong, P.; Zhang, L.; Luo, N.; Liu, J. Advances in the Application of Acetonitrile in Organic Synthesis since 2018. *Catalysts* **2023**, *13* (4), 761. https://doi.org/10.3390/catal13040761.

(12) Olive, G.; Olive, S. Process for Preparing Acetonitrile. US 4,179,462, 1979.

(13) Hamada, H.; Kuwahara, Y.; Matsuno, Y.; Wakabayashi, K. Synthesis of Acetonitrile from Syngas and Ammonia over Silica-Supported Molybdenum Catalysts Modified by Silver. *Journal of The Japan Petroleum Institute* **1987**, *30* (3), 188–194. https://doi.org/10.1627/jpi1958.30.188.

(14) Badani, M. V.; Nicholas Delgass, W. The Active Phase of Iron Catalysts for Acetonitrile Synthesis. *J. Catal.* **1999**, *187* (2), 506–517. https://doi.org/10.1006/jcat.1999.2640.

(15) Hummel, A. A.; Badani, M. V.; Hummel, K. E.; Delgass, W. N. Acetonitrile Synthesis from CO, H_2, and NH_3 over Iron Catalysts. *J. Catal.* **1993**, *139* (2), 392–405. https://doi.org/10.1006/jcat.1993.1035.

(16) Fischer, N.; Henkel, R.; Kotzé, H.; Fürst, M.; Olivier, J.; Neethling, J.; Claeys, M. Acetonitrile via CO Hydrogenation in the Presence of NH_3. *Catal. Commun.* **2016**, *87*, 14–17. https://doi.org/10.1016/j.catcom.2016.08.019.

(17) Anderson, R. B.; Shultz, J. F.; Seligman, B.; Hall, W. K.; Storch, H. H. Studies of the Fischer—Tropsch Synthesis. VII. Nitrides of Iron as Catalysts [1]. *J. Am. Chem. Soc.* **1950**, *72* (8), 3502–3508. https://doi.org/10.1021/ja01164a051.

(18) Schaidle, J. A.; Thompson, L. T. Fischer–Tropsch Synthesis over Early Transition Metal Carbides and Nitrides: CO Activation and Chain Growth. *J. Catal.* **2015**, *329*, 325–334. https://doi.org/10.1016/j.jcat.2015.05.020.

(19) Bertóti, I. Characterization of Nitride Coatings by XPS. *Surf. Coat Technol.* **2002**, *151–152*, 194–203. https://doi.org/10.1016/S0257-8972(01)01619-X.

(20) Lin, Z.; Ammal, S. C.; Denny, S. R.; Rykov, S. A.; You, K.-E.; Heyden, A.; Chen, J. G. Unraveling Unique Surface Chemistry of Transition Metal Nitrides in Controlling Selective C–O Bond Scission Pathways of Glycerol. *JACS Au* **2022**, *2* (2), 367–379. https://doi.org/10.1021/jacsau.1c00403.

(21) Jansen, R. J. J.; van Bekkum, H. XPS of Nitrogen-Containing Functional Groups on Activated Carbon. *Carbon N Y* **1995**, *33* (8), 1021–1027. https://doi.org/10.1016/0008-6223(95)00030-H.

(22) Osadchii, D. Yu.; Olivos-Suarez, A. I.; Bavykina, A. V.; Gascon, J. Revisiting Nitrogen Species in Covalent Triazine Frameworks. *Langmuir* **2017**, *33* (50), 14278–14285. https://doi.org/10.1021/acs.langmuir.7b02929.

(23) Kizilkaya, A. C. (Ali C.; Niemantsverdriet, J. W. (Hans); Weststrate, C. J. (Kees-J. Ammonia Adsorption and Decomposition on Co(0001) in Relation to Fischer–Tropsch Synthesis. *The Journal of Physical Chemistry C* **2016**, *120* (7), 3834–3845. https://doi.org/10.1021/acs.jpcc.5b11609.

(24) Weststrate, C. J.; van Helden, P.; Niemantsverdriet, J. W. Reflections on the Fischer-Tropsch Synthesis: Mechanistic Issues from a Surface Science Perspective. *Catal. Today* **2016**, *275*, 100–110. https://doi.org/10.1016/j.cattod.2016.04.004.

(25) Chen, W.; Filot, I. A. W.; Pestman, R.; Hensen, E. J. M. Mechanism of Cobalt-Catalyzed CO Hydrogenation: 2. Fischer–Tropsch Synthesis. *ACS Catal.* **2017**, *7* (12), 8061–8071. https://doi.org/10.1021/acscatal.7b02758.

(26) Gómez-Díaz, J.; López, N. Mechanistic Switch between Oxidative (Andrussow) and Nonoxidative (Degussa) Formation of HCN on Pt(111) by Density Functional Theory. *The Journal of Physical Chemistry C* **2011**, *115* (13), 5667–5674. https://doi.org/10.1021/jp1093349.

(27) Tatsumi, T.; Kunitomi, S.; Yoshiwara, J.; Muramatsu, A.; Tominaga, H. Synthesis of Acetonitrile and Related Compounds from CO-H_2-NH_3 over Mo/SiO_2. *Catal. Letters* **1989**, *3* (3), 223–226. https://doi.org/10.1007/BF00766397.

CHAPTER 5.

BIMETALLIC PROMOTIONAL EFFECTS IN MOLYBDENUM-BASED CATALYSTS FOR ACETONITRILE SYNTHESIS FROM SYNGAS AND AMMONIA

5.1 INTRODUCTION

Over the last two decades, significant progress has been witnessed towards the consolidation of carbon and nitrogen renewable cycles, disconnected from resources and energy forms of fossil origin.[1,2] The coupling of these independent chemical cycles via the development of versatile catalytic routes for the formation of carbon-nitrogen bonds from unconventional, e.g. C_1 and N_1 feedstocks, is an attractive strategy towards the sustainable production of nitrogen-containing organic compounds, which are ubiquitous in a plethora of applications, from fine chemistry to textiles and polymer production.

Aliphatic nitriles are essential building blocks for the manufacture of perfumes, pesticides, polymers and pharmaceuticals, as well as widely applied as liquid solvents for solutes of a wide range of polarity. At present, industrial nitrile production is dominated by ammoxidation[3] and hydrocyanation[4] routes from high-added-value olefin or oxygenate compounds. Alternative routes for a direct synthesis of aliphatic nitriles from cheap and abundant raw materials are highly sought. A direct alkane ammo-dehydrogenation has been recently reported on bifunctional metal-acidic catalysts.[5] This route proved highly selective to produce acetonitrile (MeCN) from ethane and ammonia mixtures, although alkane dehydrogenation equilibria under reductive conditions limit the yield attainable per reactor pass. The direct conversion of mixtures of syngas ($CO+H_2$) and ammonia is particularly appealing, as it widens the feedstock scope to essentially any carbonaceous raw material. Potentially, the latter opens the door to a fully renewable nitrile production when integrated into emerging biomass- or power-to-syngas[6] and power-to-ammonia[7] technologies.

Nitrile production from syngas and ammonia mixtures requires concerted mechanisms for CO hydrogenation as well as C-C and C-N coupling reactions, respectively. Attempts to engage ammonia as a nitrogen source in syngas conversion catalysis dates back several decades. Addition of NH_3 to a methanol synthesis process on a promoted copper chromite catalyst led to nearly quantitative selectivities to trimethylamine.[8,9] Later, co-feeding of ammonia to

Fischer-Tropsch (FT) catalysts was explored as a means to produce C_{2+} nitrogenated compounds. Typically, an unselective range of terminal aliphatic nitro-compounds (amines, nitriles, amides) was observed, along with regular *n*-hydrocarbons, under FT-standard reaction temperatures (443-573 K).[10–13] Experimental evidences suggested that nitrogenated products were produced at the expenses of oxygenates upon the addition of ammonia to the gas feed.[13,14] High selectivities to nitrile products, particularly acetonitrile, were reported at higher operation temperatures (>673 K) by researchers at Monsanto[15] and others[16–18] using supported Mo and Fe catalysts. However, long-term stability proved a challenge and decays in nitrile production rates of >50 % were observed for both Fe-based[18] and Mo[16]-based catalysts over <30 h time-on-stream. Common to both Fe and Mo-based catalysts is that they can form a variety of interstitial carbide, nitride and mixed carbo-nitride compounds. Unlike in the case of catalysts based on Co, Ru or Rh, which are active in their metallic state, for Fe and Mo, carbide and nitride compounds have been conclusively shown to be the catalytically active forms for syngas conversion reactions such as the Fischer-Tropsch synthesis.[19–22] With standard CO/H_2 syngas feeds, an initial transient restructuring of oxidic or metallic catalyst precursors has been shown to occur, developing *in situ* active carbidic species.[20–23] Under those $CO/H_2/NH_3$ atmospheres applied for the direct synthesis of nitrogen-containing compounds, contact with an additional reactive source of nitrogen broadens the catalyst speciation possibilities significantly.

Transition metal nitrides, and their oxy- and carbo-nitride analogues, are interesting candidate catalysts for transformations in the context of unconventional routes for C-N coupling with ammonia as the nitrogen source. On the one hand, they bear peculiar surface electronic and catalytic features, which resemble those of group VIII elements in metallic form.[24–26] On the other hand, they are known to withstand aggressive reaction conditions in the presence of gaseous ammonia[27–29] and, under certain conditions, have been proposed to act as reservoirs and solid transfer agents for active nitrogen species.[30,31] Despite its fundamental significance to progress towards optimal and long-standing performances, the nature of the catalyst species responsible for a direct

conversion of syngas-ammonia feeds to nitrile compounds remains an unresolved question. In previous studies, fundamentally different phenomena, such as fast decomposition of nitride species into the corresponding carbide compounds,[18] as well as metal oxide crystallite sintering,[16] have been proposed to take place under reaction conditions and connected to catalyst deactivation.

Herein we investigate a MnMo mixed-metal oxynitride material as a catalyst for the direct production of acetonitrile from ammonia-syngas mixtures with remarkable selectivity and stability. Multi-modal temperature- and time-resolved characterizations, coupled to quantum mechanics DFT simulations, offer insights into the development of the working catalyst under reaction conditions, and the reaction mechanism. The coexistence of Mn and Mo in the active catalyst brings about a synergetic effect which is responsible for a notably enhanced catalytic performance compared to either of the monometallic counterparts.

5.2 BIMETALLIC MOLYBDENUM COMPOUNDS AS CATALYST PRECURSORS

As detailed in **section 3.1.1** of **Chapter 3**, a series of crystalline bimetallic M-Mo catalyst precursors (M=Mn, Co, Ni, Cu or Zn first-row transition metals) have been synthesized by co-precipitation and crystallization methods. The as-synthesized bimetallic catalyst precursors showed experimental M:Mo ratios of 1.2± 0.2 (atomic), as-determined by ICP-OES, in fair agreement with the nominal equimolar content. In all cases, the solids showed highly crystalline structures with crystal morphologies, which depended markedly on the nature of the divalent cation (M), spanning from polyhedral crystals for MnMo, to platelet crystals for NiMo, or desert-rose morphologies in the case of CoMo, CuMo and ZnMo. X-ray diffractograms could be indexed to ammonium metal molybdates of general formula $(NH_4)_nH_mM_xMo_yO_z{\cdot}2H_2O$ in all cases (**Figure 5.1**). In these structures, M^{2+} and Mo^{6+} cations occupy octahedral (O_h) and tetrahedral (T_h) crystallographic positions, respectively, providing atomic-level metal mixing as starting point for compositionally uniform catalysts.

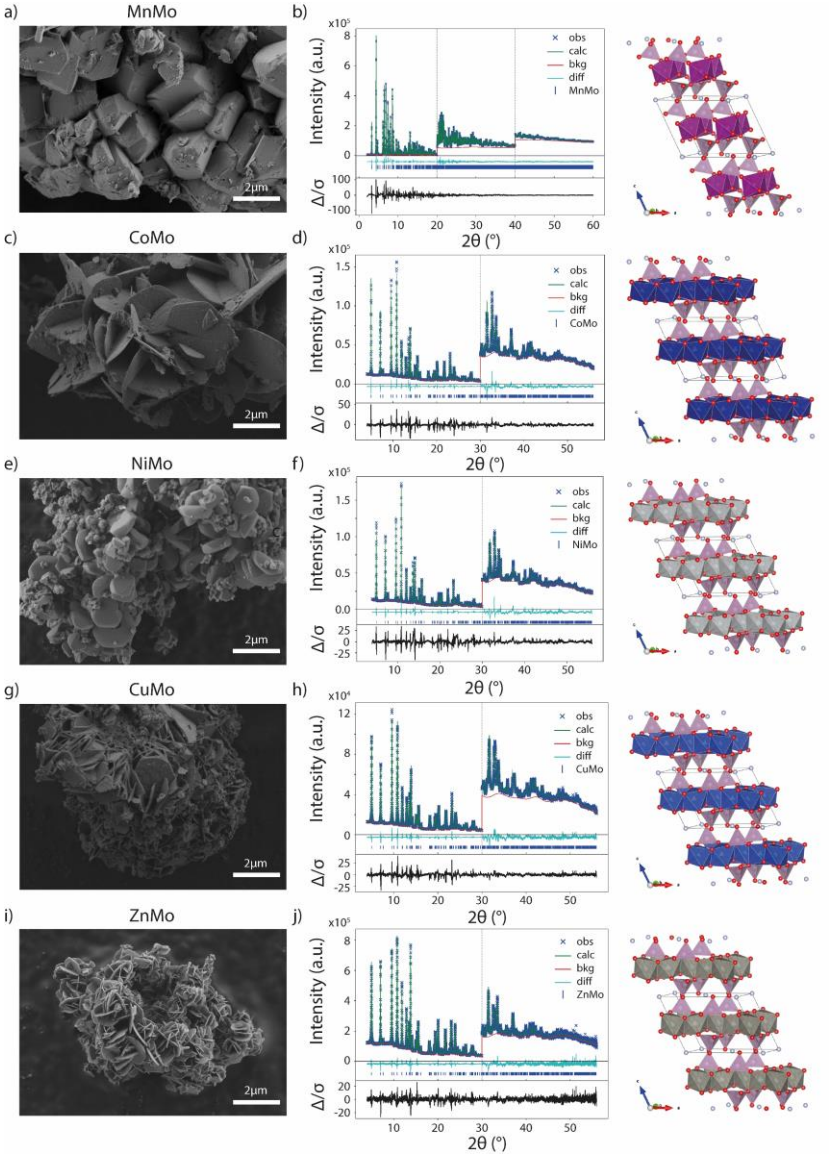

Figure 5.1: *a-i) Representative field-emission scanning electron microscopy (FE-SEM) micrographs for the series of (a) MnMo, (b) CoMo, (c) NiMo, (d) CuMo and (e) ZnMo bimetallic ammonium molybdate catalyst precursors. b-j) Rietveld refinement results and full structure solution for b) MnMo, d) CoMo, f) NiMo, h) CuMo and j) ZnMo from experimental XRD profiles (experimental data: blue scatter cross, calculated pattern: green line, residual profile: bottom blue line). Schematic representations for the corresponding crystal structures are also included.*

Assessment of the series of MMo materials as catalysts for the direct conversion of mixtures of syngas and ammonia clearly revealed the superiority of the MnMo bimetallic for a selective and stable production of acetonitrile (**Figure 5.2**).

Alternative catalysts showed either modest selectivity to acetonitrile (NiMo and CuMo) or suffered a marked deactivation over the first hours on stream (CoMo and ZnMo). For detailed information see **Table A.V.1** in **Appendices**. Therefore, further discussions focus on the catalytic performance and the nature of the active species in the bimetallic MnMo material.

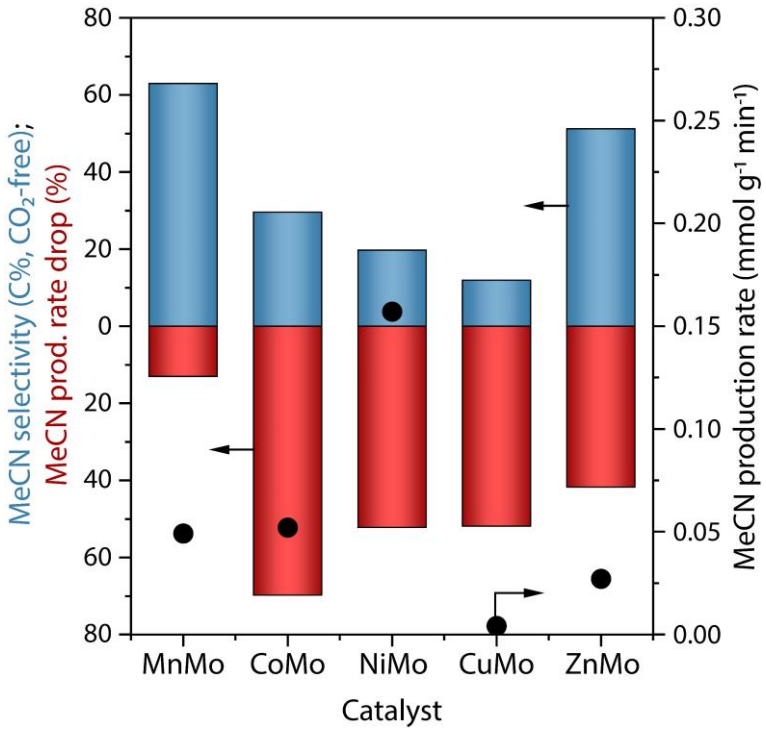

Figure 5.2: *Acetonitrile (MeCN) formation rates (black scatter), selectivity (blue bars, upwards), and percentual drop in acetonitrile (MeCN) production rate experienced over the course of 3 h on-stream (red bars, downwards) for the series of bimetallic MMo catalysts applied in the direct conversion of NH_3/syngas mixtures. Reaction conditions: T= 723 K, P=3 bar, gas feed molar composition: $2NH_3$:1CO:$1H_2$, X_{CO}<18 %.*

5.3 SYNTHESIS OF ACETONITRILE WITH A BIMETALLIC MANGANESE-MOLYBDENUM CATALYST

An initial screening of various reaction temperatures for the MnMo catalyst (P=3 bar, WHSV= 10.9 h^{-1}) showed that the highest selectivity to acetonitrile (47.6 %, CO_2-free basis) is attained at 723 K, which was therefore selected as the standard testing temperature. **Figure 5.3. a** summarizes the catalytic performance for this catalyst in an isothermal test at 723 K. Under the applied reaction conditions (P=3 bar, WHSV=7.1 h^{-1}), CO conversion remained remarkably stable for at least 14 h on-stream. Nitriles were dominant among the organic products. In this product fraction, the selectivity to acetonitrile declined from an initial 66.8 % to level off at 56.1 % after ca. 5 h on-stream, resulting in a stable acetonitrile steady production rate of ca. $5 \cdot 10^{-2}$ mmol g_{cat}^{-1} min^{-1} at longer reaction times. Hydrogen cyanide was detected as the remaining major organic product, alongside very minor amounts of methane and other light (C_{1-6}) hydrocarbons (3.3 %) and additional nitrogen compounds, primarily methylamine (5.3 %). A fraction of the oxygen in the syngas feed was rejected in the form of CO_2, via the water gas shift reaction (WGSR), with the selectivity to CO_2 being 48.5 % under steady state. The performance of the bimetallic MnMo catalyst was evidently superior to that of either of the monometallic counterparts under identical reaction conditions.

The above results notably outperformed the reference, monometallic Mo catalyst (see **section 4.2**, **Figure 4.1. b** in **Chapter 4**). For the latter, a more pronounced decline in acetonitrile formation rate was observed over the initial ca. 8 h on-stream, leading to a pseudo-steady acetonitrile production rate of 13 10^{-3} mmol g_{cat}^{-1} min^{-1}, ca. four-fold lower than for the MnMo catalyst, and a lower selectivity to MeCN of 31.7 %. HCN was the predominant organic product in this case, suggesting an intrinsically lower capacity of the catalyst to steer C-C coupling reactions. Meanwhile, very modest acetonitrile production rate ($3 \cdot 10^{-3}$ mmol g_{cat}^{-1} min^{-1}) and selectivity (23.4 %) were attained in the test using Mn_2O_3 as a monometallic catalyst precursor (**Figure 5.4. a**).

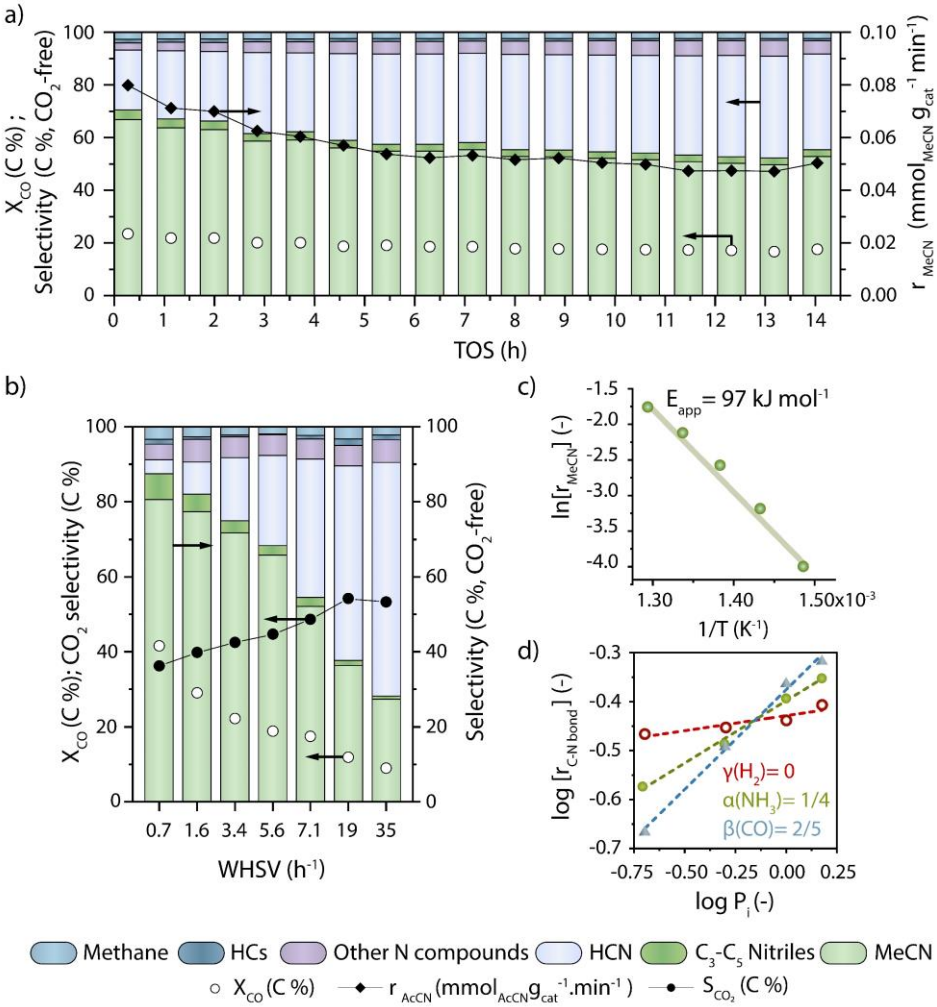

Figure 5.3: *a) Evolution of CO conversion (X_{CO}), acetonitrile formation rate (r_{MeCN}) and product selectivity (CO_2-free basis) with time on stream (TOS) for the MnMo bimetallic catalyst (space velocity= 7.1 h^{-1}); b) Dependence of CO conversion and product selectivity with WHSV for the MnMo bimetallic catalysts in the direct conversion of NH_3/syngas mixtures. Reaction conditions: T=723 K, P=3 bar, gas feed molar composition NH_3: CO: H_2= 2: 1: 1; c) Experimental Arrhenius plot for MeCN formation (formation rates determined at pseudo-steady-state for X_{CO}< 15 %). d) Log-plot for the C-N bond formation rate dependence with the partial pressure of NH_3, CO and H_2 reactants in the feed, respectively, over the bimetallic MnMo catalyst. Reaction conditions: T=723 K, P=1.2-2.5 bar, X_{CO}< 15 %. The corresponding apparent reaction orders α(NH_3), β(CO) and γ(H_2) are indicated on the figure.*

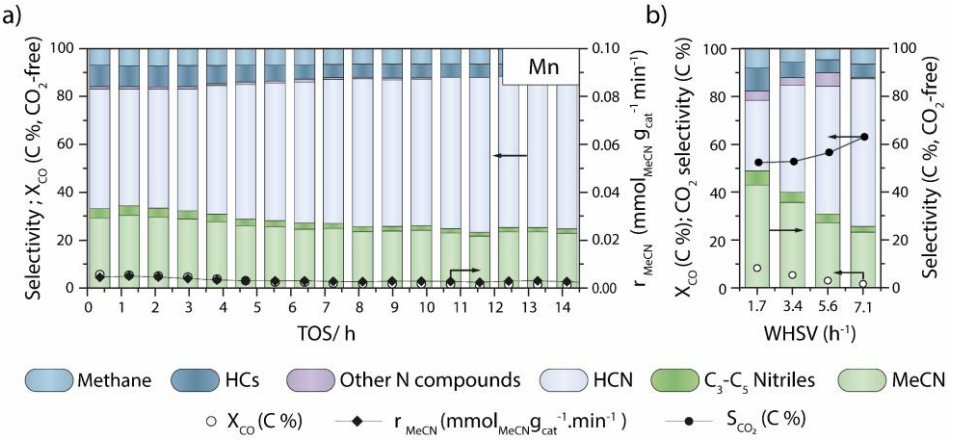

Figure 5.4: *a) Evolution of CO conversion (X_{CO}), acetonitrile formation rate (r_{MeCN}) and product selectivity (CO_2-free basis) with time on stream (TOS) for the Mn monometallic catalyst (space velocity= 7.1 h^{-1}); and b) dependence of CO conversion and product selectivity with WHSV for the Mn monometallic catalysts in the direct conversion of NH_3/syngas mixtures. Reaction conditions: T= 723 K, P= 3 bar, gas feed molar composition NH_3: CO: H_2= 2: 1: 1).*

Assessment of the performance of the MnMo catalyst at different space velocities, and thus CO conversion levels, revealed a marked and progressive shift in the selectivity pattern (**Figure 5.3. b**). While HCN dominated at shorter contact times, acetonitrile progressively became the major organic product at higher contact times. In line with the mechanistic investigations presented in **Chapter 4** with a monometallic Mo-based catalyst, these results reinforce the role of HCN as a primary product, which engages further in C-C coupling to C_{2+} nitriles.[32] Similar trends, albeit at significantly poorer nitrile selectivity levels, were observed for the Mo and Mn monometallic catalysts (**Figure 4.1 a-b** in **Chapter 4.** and **Figure 5.4**, herein above, respectively). Nitrile products obeyed an Anderson-Schulz-Flory distribution, indicative for a chain-propagation mechanism with C_1 monomer species. As shown in **Figure 5.5**, chain growth probabilities of 0.29± 0.06 were attained in all cases, indicating the production of mostly C_{2-3} nitriles, primarily acetonitrile.

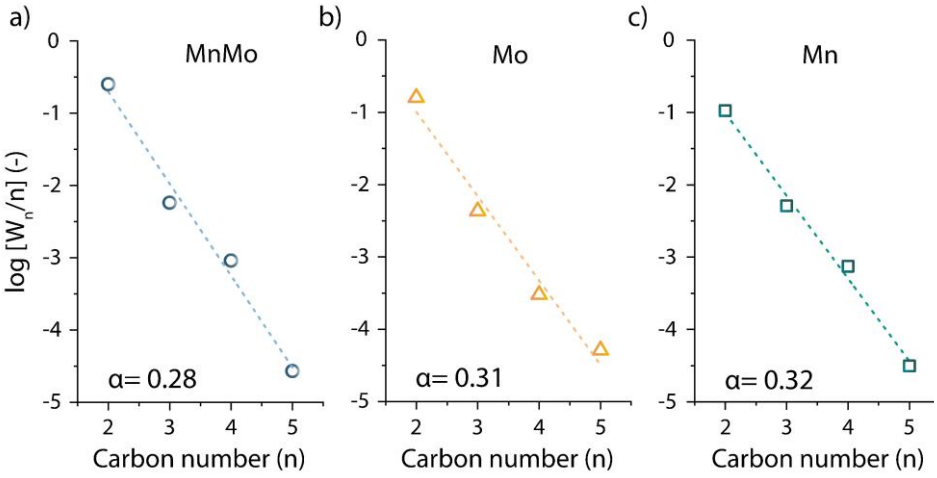

Figure 5.5: *Linearized Anderson-Schulz-Flory plots and the corresponding chain-growth probability for nitrile products for the direct conversion of NH_3/syngas mixtures on the bimetallic MnMo as well as the corresponding monometallic reference catalysts. Reaction conditions: T=723 K, P=3 bar, gas feed molar composition $2NH_3$:1CO: $1H_2$, WHSV= 7.1 h^{-1}.*

To gain further insight into the reaction kinetics, the dependence of the lumped C-N bond formation rate on the partial pressure of NH_3, CO and H_2 in the feed was studied with the bimetallic MnMo catalyst (**Figure 5.3. d**). Both NH_3 and CO reactants showed positive reaction orders of 1/4 and 2/5, respectively. On the contrary, the reaction is zero order with respect to H_2. Moreover, the application of the Arrhenius formalism to the experimental formation rates revealed an apparent activation energy (E_{app}) for acetonitrile formation of 97 kJ mol^{-1} (**Figure 5.3. c**), i.e., significantly lower than for the monometallic Mo counterpart catalyst (151 kJ mol^{-1}, *vide supra*, **Chapter 4**).

Transient analysis of the formation rates for HCN and acetonitrile products on $MnMoO_4$, i.e., the product of thermal decomposition of the ammonium manganomolybdate precursor, showed HCN to form from the onset of the reaction, while acetonitrile formation proceeded only following a 47 min long induction period (**Figure 5.6**). These observations suggest restructuring upon exposure to process conditions, and *in situ* development of the working catalyst

responsible for C-C coupling to C_{2+} nitriles. Therefore, we have adopted a multi-technique approach to assess the dynamic structural evolution and resting state of the MnMo catalyst under reaction conditions.

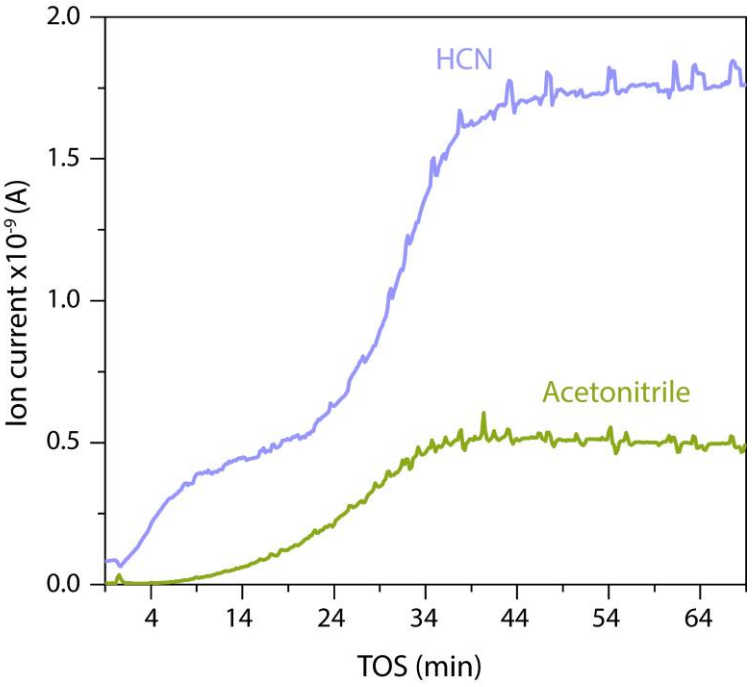

Figure 5.6: *Acetonitrile and HCN mass spectrometry signals recorded during the earliest stages of the reaction of conversion of NH_3/syngas mixtures on the MnMo bimetallic catalyst. Reaction conditions: T= 723 K, P= 1.5 bar, molar gas feed composition $2NH_3$: 1CO: $1H_2$, GHSV=7.5 h^{-1}.*

5.4 EVOLUTION OF LONG-RANGE STRUCTURE OF THE BIMETALLIC MANGANESE-MOLYBDENUM CATALYST UNDER REACTION CONDITIONS

The crystalline structure for the ammonium manganomolybdate catalyst precursor is depicted in **Figure 5.1. b.** Rietveld refinement revealed site occupancies for Mn^{2+} (O_h) and Mo^{6+} (T_h) of (1/4, 1/4, 1/2) and (0.583, 0, 0.783) coordinates of the unit cell. The evolution of the long-range structure of this catalyst precursor was investigated by means of temperature- and time-resolved XRD.

Figure 5.7. a shows the temperature-resolved X-ray diffractograms registered on exposure of this catalyst precursor to the flow of the reactive gas atmosphere (3 NH_3: 1 CO:1 H_2).

At a temperature of ca. 598 K, decomposition of the crystalline starting material was observed, leading to the monoclinic $MnMoO_4$ mixed oxide. At a higher temperature of 773 K an additional phase transition was observed into a new phase characterized by weaker and broader diffractions, i.e., smaller crystalline domains.

An essentially identical final diffractogram was observed following exposure of the catalyst to reaction conditions at the standard operation temperature of 723 K for periods of time in excess of 60 min (**Figure 5.8**), indicating that the structure corresponds to the resting state of the *ex situ* developed active catalyst. The diffraction signals are markedly asymmetric and broad, hinting at a highly defective structure with relatively small average crystalline domains. While this peak morphology hampered a refinement of the structure, the new phase could be indexed to a cubic, e.g. *Fm-3m* crystal structure.

A qualitatively similar evolution was observed starting from the monometallic MoO_3 precursor (**Figure 4.1. c**, see **Chapter 4**). In this case, the emerging new crystal phase was identified as γ-Mo_2N, known to be a stable molybdenum nitride, which crystallizes in the *Fm-3m* group (ICSD 251625). As

discussed earlier in **Chapter 4** (**Section 4.2**) nitridation was incomplete in this case, and a significant fraction of MoO_2 remained, at the inner core of the working catalyst particles, even at the highest operation temperature.

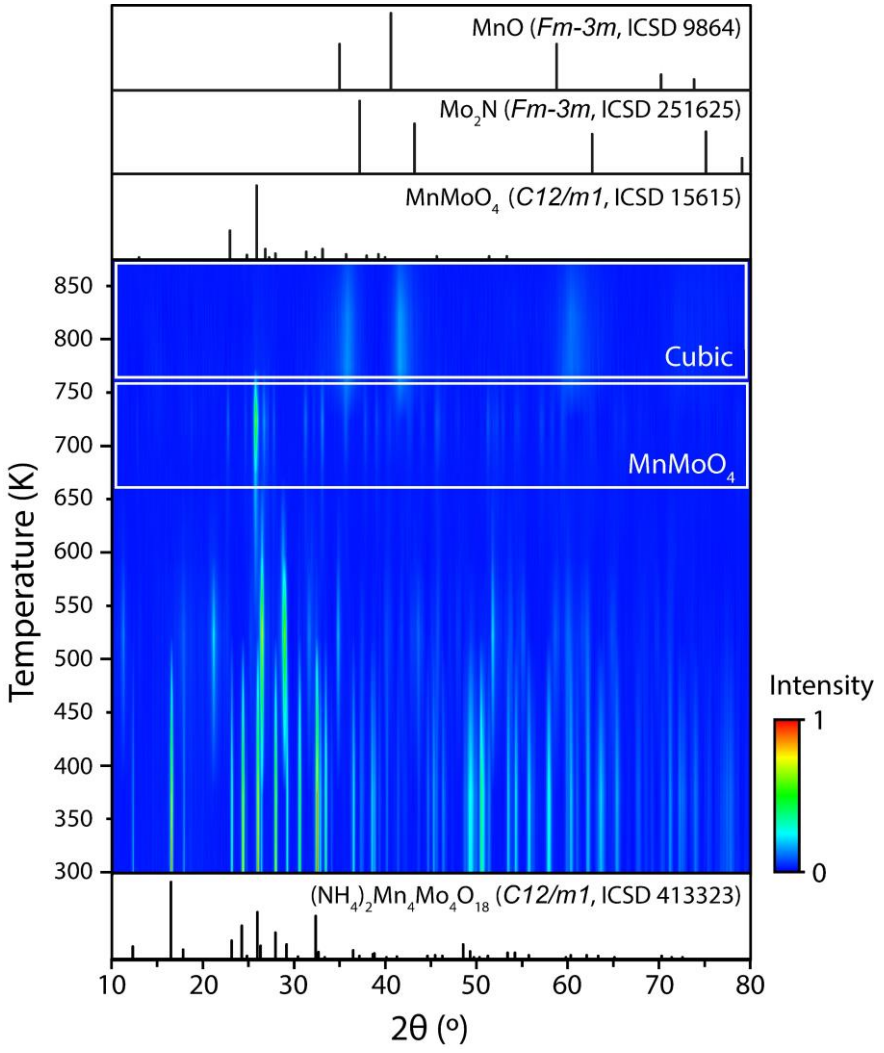

Figure 5.7: *Temperature-resolved powder X-ray diffractograms for the a) MnMo precursors during exposure to flow of the reactive NH_3/syngas atmosphere from room temperature to 873 K. Diffraction patterns for selected reference compounds have also been included.*

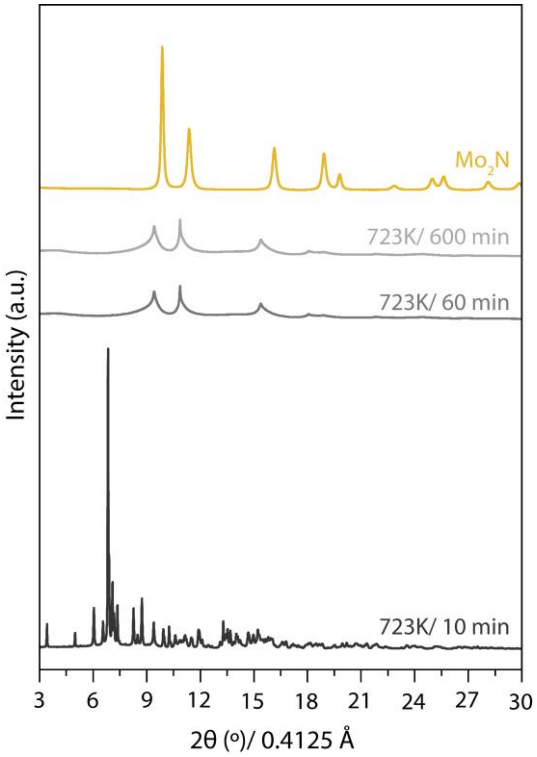

Figure 5.8: *Selected temperature-resolved powder high-resolution X-ray diffraction patterns for the MnMo catalyst after its exposure to reaction conditions in the direct conversion of NH_3/syngas mixtures for 10, 60 and 600 min. Reaction conditions: T= 723 K, P_{atm}, molar gas feed composition $3NH_3$: 1CO: $1H_2$. XRD measurement conditions: Debye-Scherrer geometry at 30 keV photon energy, λ= 0.4125 Å. Samples were sealed under inert atmosphere in a glass capillary (OD= 0.5 mm, wall thickness= 0.01 mm). The experimental pattern recorded for bulk γ-Mo_2N (Fm-3m) is included as reference*.

Further insights into the chemical modifications undergone by the mixed-metal catalyst precursor under the reaction atmosphere were gained by temperature-resolved X-ray absorption near-edge structures (XANES). This method enabled tracking the evolution of the formal oxidation state (OS) and direct coordination environment for Mo and Mn atoms as a function of temperature, during the exposure of the ammonium manganomolybdate precursor to flow of the NH_3/syngas gas feed (**Figure 5.9. a** and **b**, respectively).

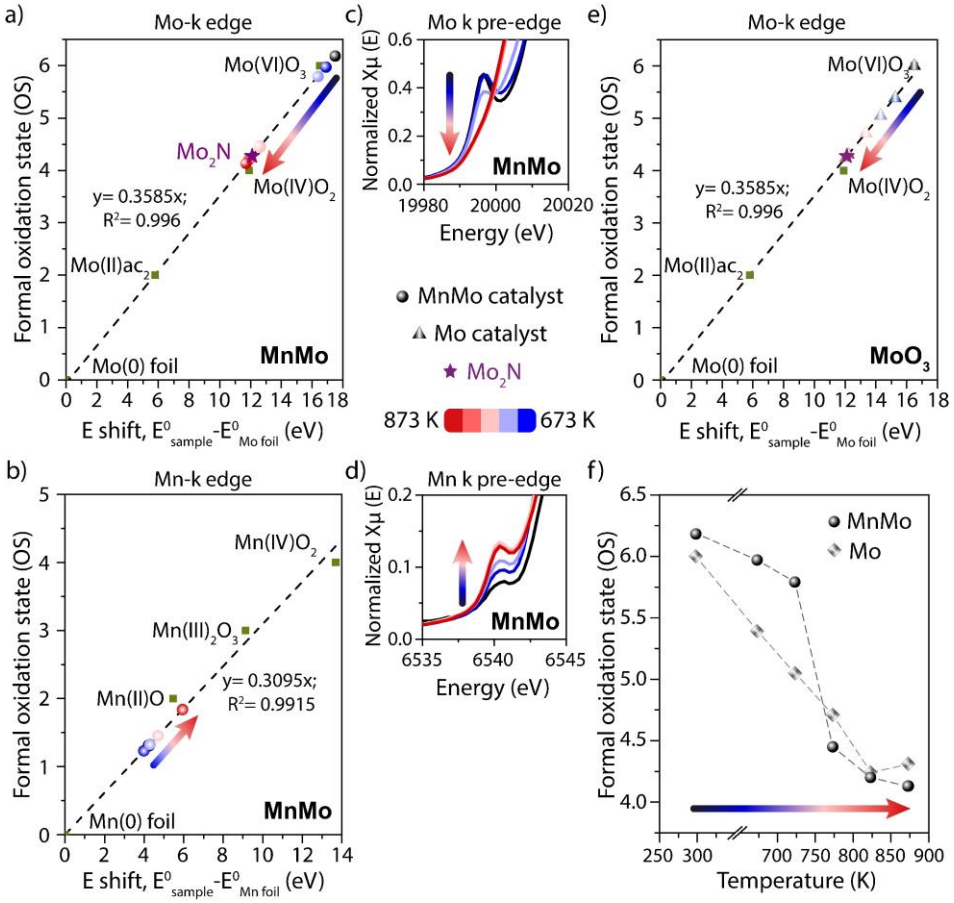

Figure 5.9: *Evolution of the average oxidation state (OS) for a, e) Mo and b) Mn, as derived from the analysis of the energy shift for Mo-k and Mn-k X-ray absorption edge energies with respect to the corresponding metallic foil (E^0_{sample}-E^0_{foil}), as a result of the exposure of the a, b) $(NH_4)_2H_2Mn_4Mo_4O_{18}{\cdot}2H_2O$ and e) MoO_3 precursor to reaction conditions at increasing temperatures. Green square data points correspond to the series of standard pure compounds with known Mo and Mn oxidate states while circles and triangle symbols represent the temperature-resolved data for the MnMo and Mo catalyst, respectively. The dashed line corresponds to the linear regression for those data points determined for the standard compounds. Detail of the temperature-resolved changes in the pre-edge XANES spectra features for the bimetallic MnMo catalyst at the c) Mo-k and d) Mn-k absorption edge energies, respectively. f) Comparison of the evolution of the OS_{Mo} with temperature for the bimetallic MnMo catalyst and a monometallic Mo counterpart. Reaction conditions: P= P_{atm}, gas feed molar composition: $3NH_3$: $1H_2$: 1CO.*

A systematic decrease in the Mo-k edge energy reflected a progressive decrease in the average OS_{Mo} on increasing temperature, from 6.0 in the $(NH_4)_2H_2Mn_4Mo_4O_{18}\cdot 2H_2O$ precursor to 4.1 at 873 K, i.e., similar to that in a γ-Mo_2N standard and thus compatible with *in situ* nitridation (**Figure 5.9. a**). A qualitatively similar behavior was observed for the MoO_3 monometallic counterpart (**Figure 5.9. e**). Remarkably, the presence of Mn in the bimetallic MnMo catalyst induces a noticeable delay in the reduction of Mo when compared to MoO_3 at temperatures below 750 K (**Figure 5.9. f**). Along with Mo reduction, a progressive dampening and eventual disappearance of the pre-edge feature in the XANES spectra suggested the evolution from a tetrahedral (T_d) Mo coordination in the catalyst precursor to a more centrosymmetric octahedral coordination environment in the final active material (**Figure 5.9. c**). In marked contrast, increasing temperatures under the reaction atmosphere led to an increase in the Mn-k edge energy, signifying a shift in the average OS_{Mn} from 1.3 to 1.8 (**Figure 5.9. b**), suggesting a slight oxidation, rather than reduction, for this metal. In this case, a noticeable exacerbation of the pre-edge feature suggested the evolution towards non-centrosymmetric Mn environments, e.g. distorted octahedral (O_h) coordination geometries (**Figure 5.9. d**).

Temperature-resolved analysis of the bulk compositional evolution showed, firstly, a decline in the nitrogen content from 2.7 wt% to 0.5 wt% up to 673 K, in correspondence with the decomposition of the starting ammonium manganomolybdate into the $MnMoO_4$ oxide (**Figure 5.10**). At higher temperatures, significant nitrogen uptake set in, and increased with increasing temperature to reach 5.4 wt% N at 873 K, indicating oxide nitridation. Carbon was also observed at temperatures ≥ 723 K, albeit at notably lower contents up to 0.5 wt% C. Isothermal exposure to reaction conditions at 723 K for extended periods of time resulted in increments in both N and C contents to 4.4 wt% N and 1.0 wt % C, respectively, after 60 min.

These contents essentially levelled off at longer times-on-stream up to 600 min. In line with the temporal evolution of the catalytic performance (**Figure 5.3**), these observations indicate the attainment of a stable composition for the

working catalyst. Remarkably, both pseudo-steady bulk N and C contents were notably lower for the bimetallic MnMo material than for any of its monometallic counterparts (**Figure 5.10**).

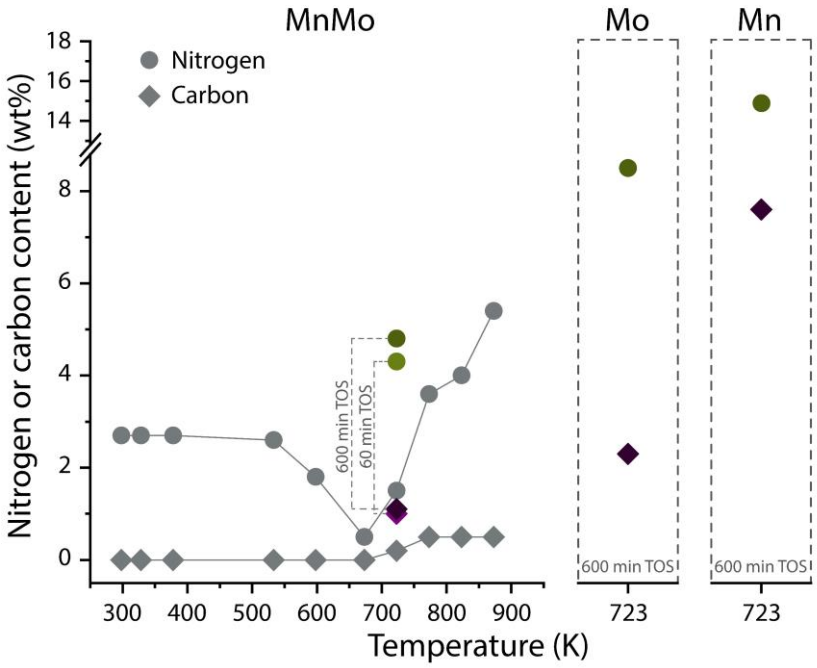

Figure 5.10: *Temperature-resolved bulk nitrogen and carbon contents, as determined by elemental analysis, for the MnMo catalyst exposed to reaction conditions for the direct conversion of NH_3/syngas mixtures. Reaction conditions: P_{atm}, gas feed molar composition: $3NH_3$: 1CO: $1H_2$. Data correspond to an exposure time of 10 min at each temperature. For selected operation temperatures, data are provided also after longer times-on-stream (TOS). For comparison data are also provided for the corresponding monometallic catalysts after 600 min on-stream at 723 K.*

5.5 FIRST-PRINCIPLES DFT AND THERMOCHEMISTRY INSIGHTS INTO METAL AND MIXED-METAL NITRIDES

The above results unequivocally support a severe nitridation of the oxidic catalyst precursors upon exposure to process conditions. Hence, a metal nitride interstitial compound with cubic structure best represents the actual working catalyst. Periodic DFT calculations were performed at the PAW-RPBE-D3 level of theory, to assess the implications of Mn doping on the thermodynamic and structural features of the metal nitrides with a cubic (*Fm-3m*) crystal structure.

It is known that *c*-MoN tends to stabilize a high density of nitrogen vacancies in its structure, leading to more stable MoN_{1-x} crystalline structures, of which γ-Mo_2N (*x*=0.5) is a commonly observed compound. **Figure 5.11. a** shows the DFT predicted evolution of the lattice parameter (*a*) for MoN_{1-x} as a function of the volumetric density of N-vacancies. An ordered arrangement of N-vacancies has been considered. Considering unordered vacancies, introduced in the primitive 2 x 2 MoN crystal supercell model through a quasi-random structure (SQS) method,[33] led to similar energetics for vacancy formation energies in the vacancy density ranged examined. Experimentally, a lattice parameter of 4.164 Å was determined for the monometallic molybdenum nitride catalyst. This average unit cell size is consistent with a stoichiometry of $MoN_{0.46}$, confirming the development of a slightly N-defective γ-Mo_2N as the working catalyst phase.

Similarly, the thermodynamic and structural effects of isomorphically incorporating Mn into the lattice structure of cubic MoN were also studied theoretically. **Figure 5.11. b** shows the expected evolution of the Gibbs free energy of nitride formation and the corresponding *Fm-3m* lattice parameter with the volumetric degree of Mn substitution into the primitive *c*-MoN lattice.

As observed in **Figure 5.11. b**, increasingly negative ΔG_f was predicted for mixed MnMo nitrides with increasingly higher Mn content up to ca. 50 at%. Therefore, mixed MnMo nitrides are predicted to be more stable than the monometallic molybdenum nitride, hence favored in the bimetallic catalyst under the strongly nitrifying process conditions. Particularly for Mn doping contents in

excess of ca. 20 at%, the lattice parameter for the bimetallic nitride is predicted to reduce rather linearly with Mn content up to 60 at%.

Next, the thermodynamic properties of the corresponding oxo-nitride phases were investigated by isomorphically replacing N atoms by O atoms, at various substitution degrees, in the optimized mono- and bimetallic (Mo:Mn= 1:1 at) nitride structures. The results are summarized in **Figure 5.12**, which shows the predicted evolution of the Gibbs free energy of formation for the corresponding metal oxynitride structures as a function of the nitrogen lattice substitution degree by oxygen (at%) and the environmental oxygen chemical potential, referred to μ^0_O at 0 K and P_{O2}= 1 atm.

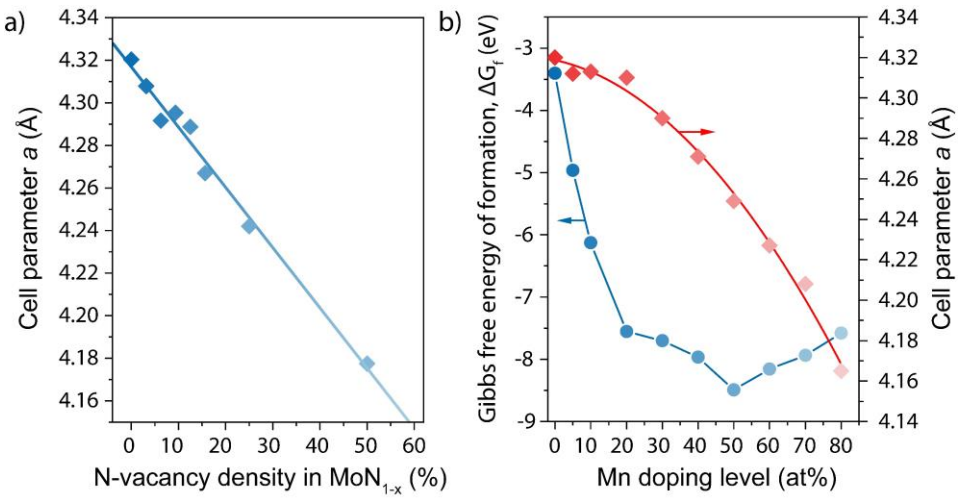

Figure 5.11: *a) Evolution of the lattice parameter (a) for Fm-3m MoN_{1-x} nitride as a function of the volumetric density of ordered N-vacancies; and b) Evolution of the Gibbs free energy of formation and the lattice parameter (a) for Fm-3m MoMnN mixed-metal nitride as a function of the volumetric degree of Mo isomorphic substitution for Mn, as derived from periodic DFT calculations (PAW-RPBE-D3). Calculations have considered a nitrogen chemical potential μ_N corresponding to a P_{N2}= 1.5 bar and T= 723 K, representative for the reaction conditions.*

As observed in **Figure 5.12**, first-principles thermochemistry predicts a significantly higher stability for mixed metal oxynitride compounds than for the monometallic molybdenum-based analogues, i.e., ΔG_f becomes negative at notably lower oxygen chemical potentials. In turn, for a given oxygen chemical potential, the free energy of formation of oxynitride compounds is significantly more negative for the mixed-metal composition. While the reaction conditions are overall not oxidative, hence estimating a relevant oxygen chemical potential is not feasible, oxygen is abundantly present in the oxidic catalyst precursors which undergo nitridation under the NH_3/syngas atmosphere. These theoretical results indicate that the retention of lattice oxygen under nitrifying conditions is considerably more favored, from the thermodynamic standpoint, in the case of the mixed metal Mn-Mo catalyst than for the monometallic Mo counterpart.

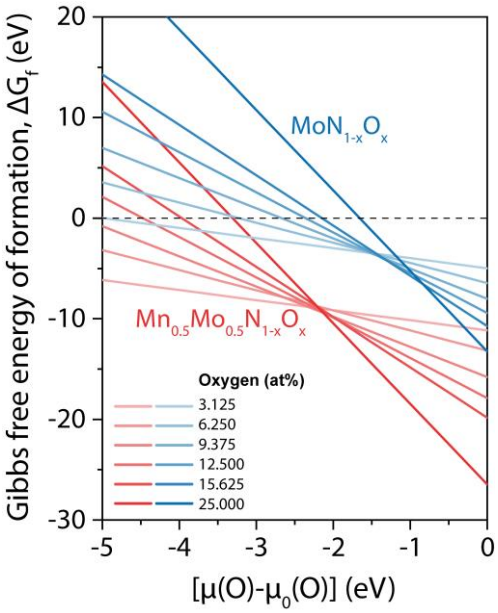

Figure 5.12: *a) Evolution of the Gibbs free energy of formation for monometallic and mixed-metal Fm-3m oxynitride materials as a function of the degree of lattice nitrogen substitution by oxygen (at%) and the environmental oxygen chemical potential, relative to that determined at 0 K and P_{O2}= 1 atm reference conditions. Calculations have considered a nitrogen chemical potential μ_N corresponding to a P_{N2}= 1.5 bar and T= 723 K, representative for the reaction conditions.*

In addition, the experimental XRD pattern registered for the fully developed MnMo catalyst (see **Figure 5.8** above) shows markedly asymmetric and broad diffractions, hinting at the presence of a comparatively high density of structural defects. Therefore, additional calculations were performed to investigate the energetics of the formation of different types of point structural defects in the crystal structure of mono- (Mo) and bimetallic (MnMo) oxynitride materials. Considering the bulk composition of the experimental catalyst (Mn: Mo= 1.1: 1 at.) and the particular stability predicted by DFT for the equimolar mixed-metal nitride (**Figure 5.11**, above) a $Mn_{0.5}Mo_{0.5}N(O)$ theoretical model compound has been considered hereafter to represent the bimetallic catalyst.

As summarized in **Figure 5.13**, the formation of N-vacancies is predicted to be exergonic, particularly for vacancy densities in excess of 5 %, for both monometallic and bimetallic nitride compounds. Nitrogen vacancy formation is particularly favorable for *c*-MoN, in line with the known stability of MoN_{1-x} phases, e.g. γ-Mo_2N. In contrast, the formation of N interstitials (not shown in the figure) was found to be associated to a very high free energy penalty (>3 eV). Also, the creation of cationic vacancies was found to be thermodynamically disfavored (**Figure 5.13. b)**. In the case of bimetallic $Mn_{0.5}Mo_{0.5}N$, the free energy penalty for the creation of Mn_{vac} remained relatively constant at 0.4 eV, whereas it scaled notably for Mo_{vac} upon increasing the volumetric density of vacancies. This suggests that the nitride structure undergoes destabilization to a lower extent upon departure of comparatively smaller Mn atoms than bulkier Mo atoms.

Next, the energetics for Schottky pair defects, which integrate anionic and cationic vacancies was studied for the mixed-metal material. NN1 Schottky defects were considered, i.e., those involving a pair of vacancies at the next nearest neighbor lattice positions. A single unit cell model was considered in this case, and therefore at a constant and relatively high defect concentration of 12.5 %. Besides, one would expect more favorable energetics at lower defect densities.

As shown in **Figure 5.13. c**, the formation of NN1 Schottky defects was found to be endergonic in $Mn_{0.5}Mo_{0.5}N$, with $\Delta G_{f,\,def}$>1 eV regardless of whether

Mn or Mo are considered for the cationic vacancy. Interestingly, partial substitution of O into the nitride lattice led to a significant stabilization of specifically Mn-N NN1 Schottky defects, to the point that defect formation became exergonic for a 50 % nitrogen replacement by oxygen. Therefore, it is concluded from these results that, while the formation N-vacancies is thermodynamically feasible, at significant defect densities, the formation of cationic vacancies in the metal nitride compounds requires the stabilization provided by the nearby formation of anionic vacancies, which provide a local charge compensation. Moreover, lattice oxygen in an oxynitride structure which, as shown above, is particularly favored after Mn doping, results in a remarkable stabilization of Schottky defects. This is in line with the markedly defective structure inferred for the bimetallic MnMo catalyst based on its XRD pattern.

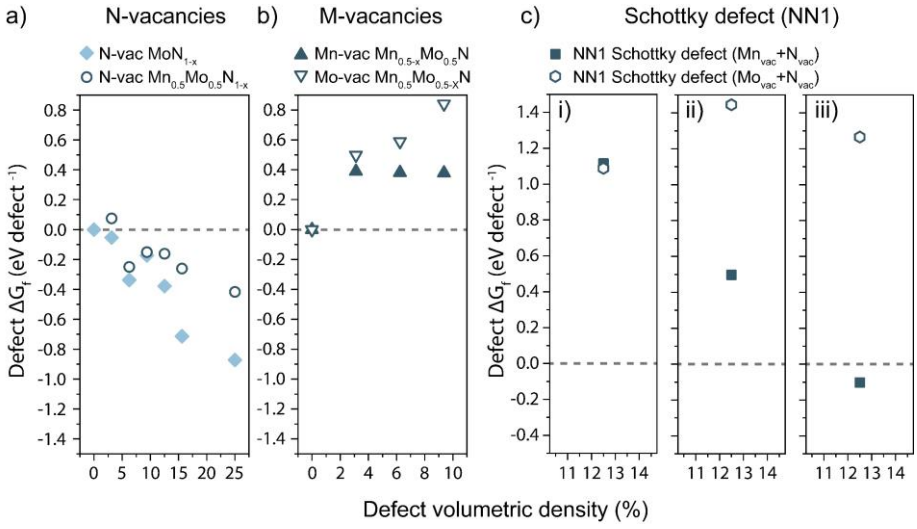

Figure 5.13: *Gibbs free energy of formation for a) nitrogen (anionic) vacancy, b) metal (cationic) vacancy and c) Schottky NN1 divacancy point defects, as predicted with DFT-based thermochemistry calculations for monometallic (MoN) and mixed-metal ($Mn_{0.5}Mo_{0.5}N$) Fm-3m nitrides as a function of defect volumetric concentration. Calculations have considered a nitrogen chemical potential μ_N corresponding to a P_{N2}= 1.5 bar and T= 723 K, representative for the reaction conditions. For NN1 Schottky defects, the influence of lattice substitution of i) 0 %, ii) 25 % and iii) 50 % of N atoms by O atoms, i.e., in a mixed-metal oxynitride, on the defect formation free energy has also been studied.*

5.6 EVOLUTION OF SHORT-RANGE STRUCTURE OF THE BIMETALLIC MANGANESE-MOLYBDENUM CATALYST UNDER REACTION CONDITIONS

The temperature- and time-resolved evolution of the short-range atomic structure of the mixed-metal MnMo catalyst precursor was additionally studied by means of Extended X-ray Absorption Fine Structure (EXAFS) Spectroscopy (**Figure 5.14**). The monometallic MoO_3 catalyst precursor was also investigated under the same settings, for comparison purposes. **Figure A.V.1** (see **Appendix A.V.** in **Appendices**) shows the k^3-weighted EXAFS spectra in the reciprocal k space at the corresponding Mo-k and Mn-k absorption edges, indicating the k-range delimit (red dashed lines) where the Hanning apodization window was applied for data reduction. Examination of the FT-EXAFS at the Mo-k edge indicated that the Mo-O bond distance within the first coordination shell in the monometallic MoO_3 catalyst increased when exposed to higher reaction temperatures (**Figure 5.14. c**). This elongation of the interatomic distance with the nearest neighbor atom was less evident in the bimetallic MnMo catalyst developed under process conditions below 723 K (**Figure 5.14. a**). Notably, when the temperature reached 873 K, the MoO_3 material displayed a second scattering contribution at approximately 2.5 Å (no phase correction), a feature which was absent in the bimetallic MnMo catalyst, that only exhibited a single coordination shell. Continuous Cauchy Wavelet Transform (CCWT) of the EXAFS spectra indicates that such a scattering contribution is due to heavier neighbor atoms than those contained in the first shell, similar to the Mo-Mo scattering of the bulk Mo_2N (**Figure 5.14. d**). The lack of this Mo-Mo scattering at higher radial distances in the bimetallic MnMo material suggests that Mn prevents the development of extended Mo_2N domains. Analysis of the FT-EXAFS at the Mn-k edge revealed that, additionally to a Mn-(N, O) scattering at around 1.5 Å (no phase correction), the MnMo catalyst developed a second coordination shell in the range of $2.1< R(Å)< 3.6$ (no phase correction), which increased in magnitude with rising temperatures (**Figure 5.14. b**). This additional scattering signal indicates the formation of localized regions enriched in Mn, likely a result of Mn segregation

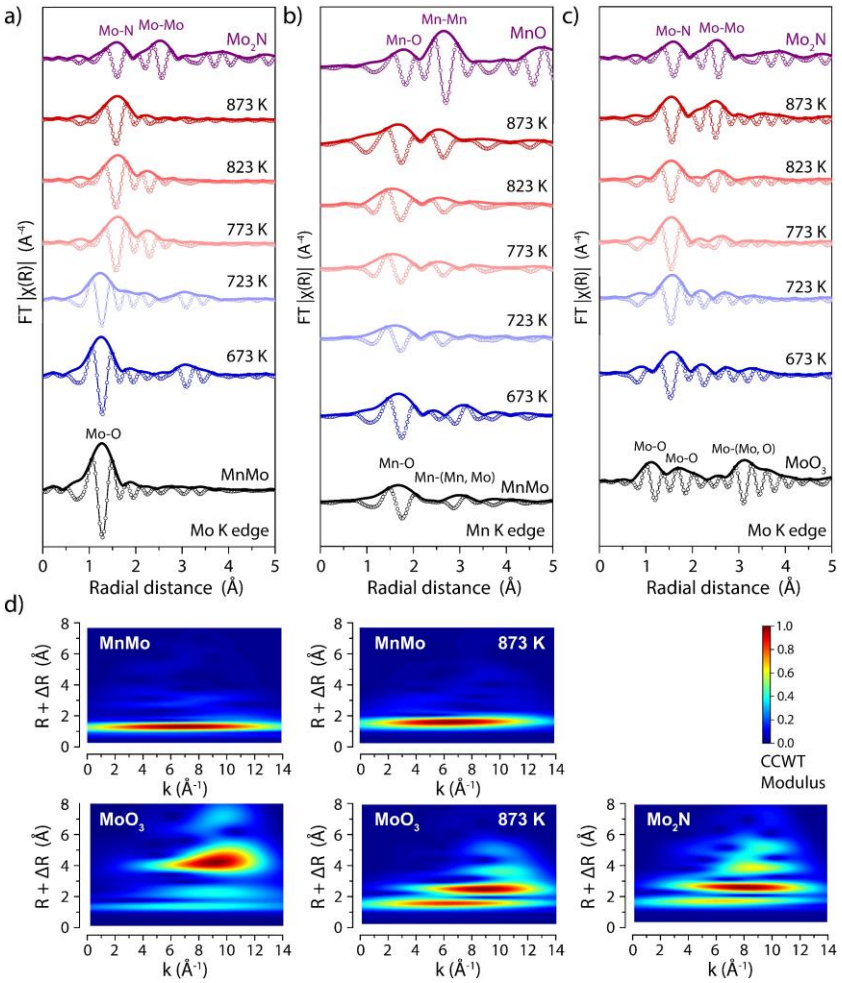

Figure 5.14: *Fourier Transform FT-χ(R) functions in the real space (no phase correction) collected at the a, c) Mo-k and b) Mn-k edges, after exposure of a, b) the bimetallic $(NH_4)_2H_2Mn_4Mo_4O_{18}\cdot 2H_2O$ and c) the monometallic MoO_3 precursor catalysts to reaction conditions ($3NH_3$:$1H_2$:1CO, P_{atm}) at increasing temperatures. The spectra of Mo_2N and MnO references are included for comparison purposes. d) Continuous Cauchy Wavelet Transforms (CCWT) of the k^3-weighted EXAFS functions for the MnMo (top) and MoO_3 (bottom) materials before and after exposure to reaction conditions ($3NH_3$:$1H_2$:1CO, P_{atm}) at 873 K. The CCWT contour map of the Mo_2N reference is provided for the purpose of comparison. The CCWT maps were calculated with a Cauchy order n= 200, and a Hanning apodization window was applied in the range $1<k(Å^{-1})<11$ to extract the Fourier transform signals in the R-space (no phase correction).*

occurring during the reaction conditions, as revealed by STEM/EDS (*vide infra*, **Figure 5.16** and associated discussion).

Based on the first-principle thermochemistry insights and X-ray diffraction results discussed above, various energetically plausible structural models (optimized using periodic DFT at the PAW-RPBE-D3 theory level) were considered to disentangle the complex structure of the MnMo catalyst via EXAFS fitting, see **section A.V** in **Appendices**. A collection of cubic mixed Mn-Mo nitrides was considered as the basis for the first coordination shell analysis. In these models, Mn partially and isomorphically replaces Mo in the MoN structure ($F\bar{4}3m$). The set of structural models included a stoichiometric $Mn_{0.5}Mo_{0.5}N$ nitride, but it additionally considered the presence of a variety of structural defects, i.e., N (anionic) as well as Mn/Mo (cationic) vacancies, Schottky and anti-site point defects (**Figures A.V. 2** & **A.V. 3**, see **Appendices**). Firstly, fitting the experimental Mo-K and Mn-K EXAFS spectra with those scattering paths extracted from the simulated structures was attempted at scatterer radial distances R< 2.5 Å and R< 2.5 Å, i.e., corresponding to the first coordination shell around Mo and Mn absorber atoms, respectively. Some of the models were found not to provide a relevant description of the working catalyst's local structure, either by resulting in physically nonsensible values for the free parameters or by providing a suboptimal fit to the experimental data. Out of those structural models scrutinized, a bimetallic $Mn_{0.5}Mo_{0.5}N$ nitride with Schottky-type defects (N and Mn vacancies, at a density of 1 defect/unit cell) delivered the best correspondence to the experimental spectrum when examining the first metal coordination sphere both at the Mn-k and Mo-k edges (**Figures A.V. 4** & **A.V. 5, Tables A.V. 2** & **A.V. 4** in **Appendix A.V.**).The analysis was then extended to radial (2^{nd} shell) coordination distances in the range of 1.0< R(Å)< 3.6, at which scattering events are apparent at the Mn-k EXAFS spectrum. In this case, considering solely those scattering paths simulated for the Schottky defective MnMo mixed metal nitride did not deliver a satisfactory fit to the experimental data. Hence, the incorporation of additional scattering paths was attempted. Based on first principles thermochemistry predictions of the higher oxophylicity induced by Mn doping and STEM/EDS results showing Mn-enriched nanosized domains in the material (*vide*

infra, **Figure 5.16)**, alternative coordination environments for Mn atoms in Mn-enriched cubic-symmetry clusters were considered, e.g., MnO, MnN as well as MnN_xO_y oxynitride compounds. Particularly the inclusion of the second scattering paths extracted from a Mn-Mo mixed metal oxynitride cluster (originated from the concurrent isomorphic substitution of three nitrogen atoms with one oxygen atom and the replacement of one manganese atom by one molybdenum atom in each unit cell of a cubic MnN) improved the overall fit. However, high EXAFS Debye-Waller factors σ^2>0.01 Å^2 and an increased number of variable parameters were required to attain a satisfactory fit with proposed models, hinting at a significant structural disorder in the developed MnMo catalyst.

All taken together, EXAFS analysis points to the development of a mixed-metal oxynitride as the working catalyst, in agreement with XRD results. Additionally, the analysis reinforces the notion of a material showing local defects and compositional heterogeneities, possibly in the form of Mn-enriched domains with lower local nitridation degrees, which defer a finer structural elucidation.

5.7 DEPTH-SENSITIVE NEAR-SURFACE TRACKING OF CATALYST NITRIDATION UNDER PROCESS CONDITIONS

Complementing the bulk-averaged structural information provided by XRD and XAS, near-surface compositions were studied by means of X-ray photoemission spectroscopy (XPS). In agreement with bulk compositional analyses, XPS revealed notably higher near-surface nitrogen uptakes for the monometallic Mn and Mo catalysts after extended exposure to reaction conditions, i.e., a $(N/Mn+Mo)_{surf}$ atomic ratio about twice as high than that for the MnMo bimetallic catalyst (**Table 5.1**). Analysis of the N1s photoemission core-level showed near-surface nitrogen species with BEs of 397.0± 0.3 eV and 399.2± 0.2 eV. These binding energies are in agreement with those expected for the corresponding metal nitrides, and partially hydrogenated nitrogen species in oxide environments, e.g. $MO_x(NH_2)_y$, respectively.[34]

Remarkably, the relative contribution from the latter was notably higher in the case of the MnMo catalyst, suggesting a higher availability of oxygen on the

surface. Inspection of the C1s region showed carbon species with BEs of 284.6± 0.0 eV, associated to graphitic and/or adventitious carbon species. Next, contributions with BEs of 286.1± 0.3 eV and 288.5± 0.8 eV were also discerned. The former signifies the presence of adsorbates with C-N bonding,[35] while the latter may be associated to surface carbonate species,[36] respectively. No signs for carbidic carbon species (BE~282.7 eV) were observed, ruling out any significant carbidization of the material. Taken together, the results from bulk and near-surface compositional analyses point to a significant incorporation of interstitial N atoms, but not C, into the catalyst structure under reaction conditions. Moreover, a concerted effect of Mn and Mo is suggested, which limits the maximum nitridation extent and preserves a more oxidized (near) surface composition for the working catalyst.

Table 5.1: Near-surface nitrogen-to-metal atomic ratios, as determined by XPS, for the MnMo mixed-metal and monometallic reference catalysts after 10 h of a $3NH_3$: 1CO: $1H_2$ feed exposure at 723 K.

Catalyst	**$N/(Mo+Mn)_{surf}$**
MnMo	0.7
Mo	1.2
Mn	1.5

The kinetics of the nitridation process under reaction conditions was studied by means of depth profiling SR-XPS, via the modulation of the incident photon energy in the range of 400-750 eV. **Figure 5.15** summarizes the Mo speciation determined from the analysis of the Mo3d core-level, following exposure to process conditions for different times on-stream. Four different Mo species could be discriminated, which have been ascribed to Mo^{6+} (232.2± 0.2 eV), Mo^{5+} (230.8± 0.2 eV), and Mo^{4+} (229.5± 0.1 eV) in oxide compounds, and Mo^{4+} in nitride compounds, e.g. Mo_2N ($Mo3d_{5/2}$, 228.8± 0.1 eV),[34] respectively, in order of increasing reduction degree. Nitridation was found to proceed swiftly under reaction conditions. As illustrated in **Figure 5.11. b**, already

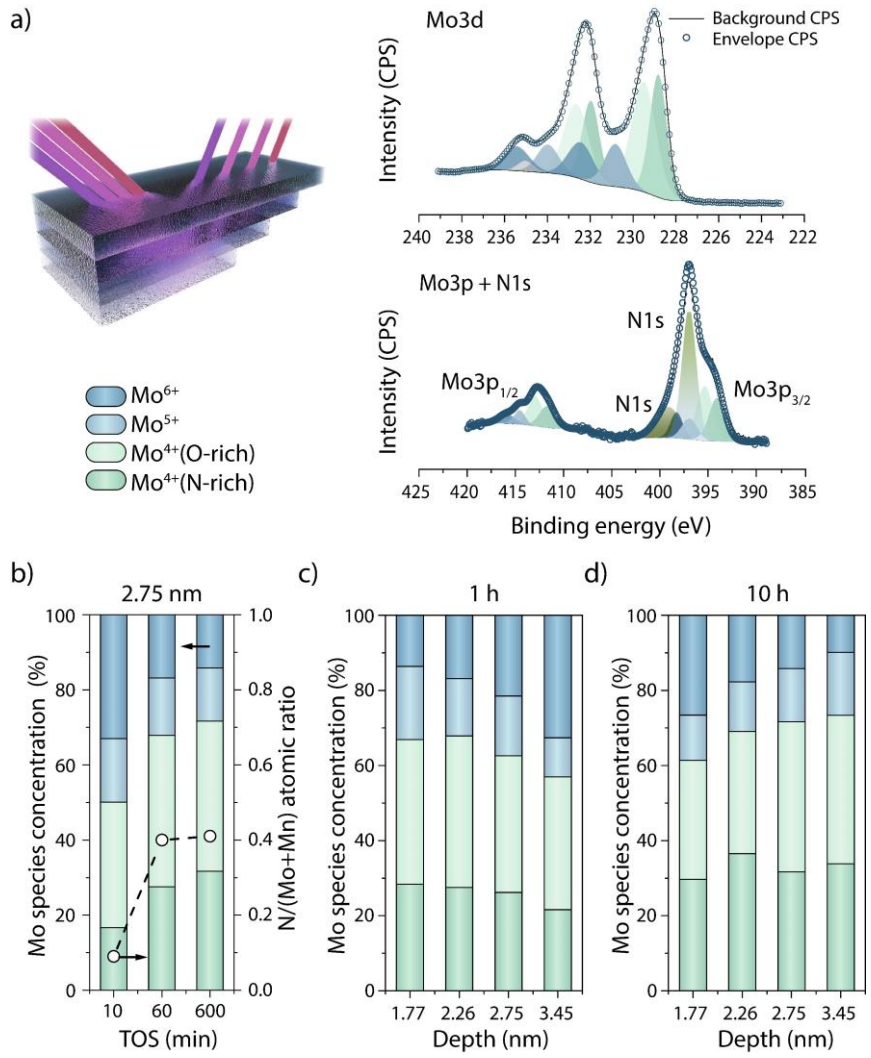

Figure 5.15: *a) Illustration of SR-XPS near-surface depth compositional profiling on powder solids upon energy modulation of the irradiating X-ray beam and exemplary deconvolution analysis of Mo3d and Mo3p+N1s core level spectral regions for the MnMo catalyst following exposure to reaction conditions at 723 K for 600 min. b) Evolution of the near-surface relative abundance of molybdenum species and the N/Mo atomic ratio on the MnMo catalysts with the time-on-stream under reaction conditions at 723 K. Data correspond to an analysis depth of 2.75 nm (incident energy 600 eV)). Evolution of molybdenum speciation with the photoemission analysis depth for the MnMo catalyst following exposure to reaction conditions at 723 K for c) 1 h and d) 10 h on stream.*

after 10 min on-stream, about 50 % of the surface Mo atoms had been reduced to lower valent Mo^{4+}.

Further reduction and nitridation were evident after 60 min. Beyond this time-on-stream, changes in surface Mo speciation were only minor up to 600 min on-stream, also coinciding with the plateauing in the N uptake by the solid. Depth profiling analysis on the catalyst exposed to reaction conditions for 60 min evidenced a Mo speciation gradient, i.e., a raising reduction degree towards the outer surface, as expected for a surface-to-bulk advancement of the nitridation front.

After 600 min, slightly higher overall near-surface Mo reduction extents were determined. However, in this case, the speciation radial gradient had inverted. Progressively higher contributions from lower valent Mo were detected with increasing analysis depth, while the concentration of $Mo^{5+/6+}$ species reached 38.6 % closest to the topmost surface. These findings suggest that a certain re-oxidation may take place on the catalyst´s outer surface, likely driven by the side-production of water, upon prolonged exposure to reaction conditions, i.e., once the driving force for nitridation has dampened.

5.8 NANOSTRUCTURE AND METAL NANOSPATIAL DISTRIBUTION

High-resolution STEM showed clearly that the comparatively large crystals of the oxidic catalyst precursor had transformed into individual, small (<20 nm) crystallites of the actual oxynitride catalyst. The latter remained aggregated into larger structures which preserved the shape of the starting crystals in the oxidic precursor, suggesting a pseudomorphic transformation into the working catalyst species. Cross-sectional EDS compositional maps showed a spatially very uniform distribution of Mo and Mn at both the nano- and mesoscales following 10 min exposure to reaction conditions, i.e., reaction times at which the *in situ* catalyst genesis is not yet complete, see **Figure A.V.7** in **Appendices**. After 600 min operation, i.e., for the fully developed working catalyst, the Mo distribution remained very uniform. However, nanosized speckles, locally

enriched in Mn, could be observed across the material (**Figure 5.16**). Noticeably, the N/(Mo+Mn) atomic ratio was lower at these patches, indicating that certain Mn segregation had taken place following the extensive nitrification of the catalyst.

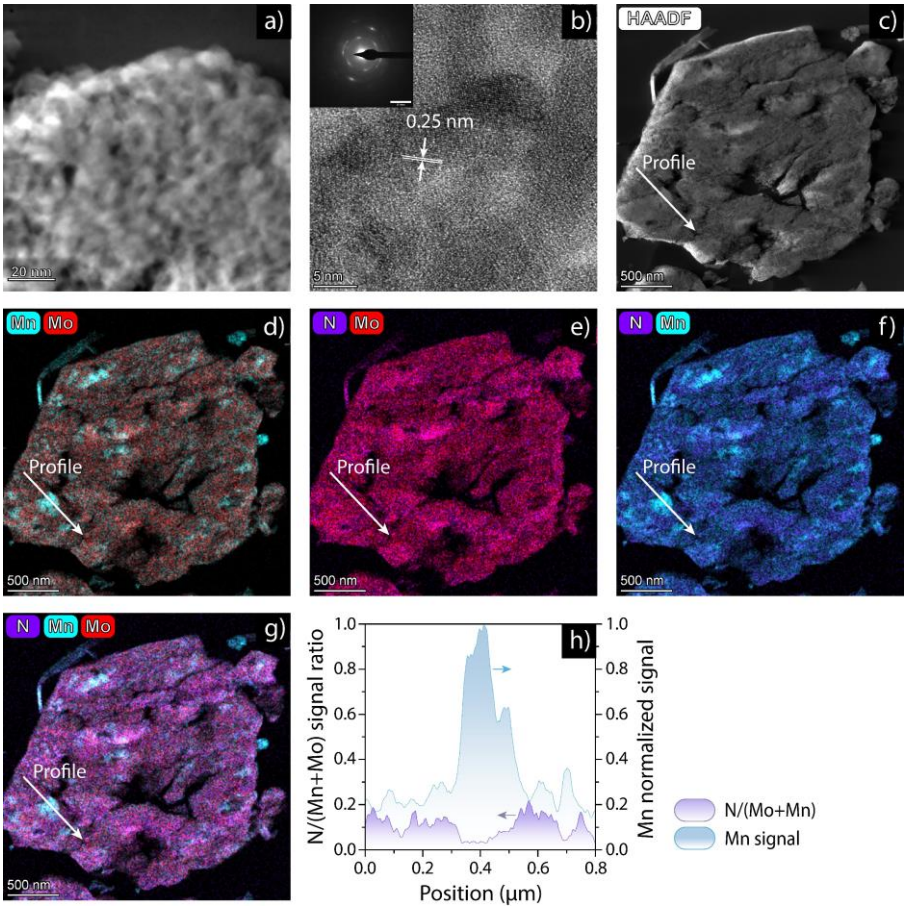

Figure 5.16: *a, b) Representative high-resolution scanning transmission electron microscopy (HR-STEM) for the MnMo catalyst after exposure to reaction conditions for 600 min. The insets show the corresponding Fast Fourier Transform pattern. c) Representative high-angle annular dark-field (HAADF) STEM micrograph of a catalyst particle cross-section. Panels d-g) show the corresponding EDS elemental maps for d) Mn, Mo e) N, Mo f) N, Mn and g) N, Mn, Mo. h) N/(Mn+Mo) signal ratio and Mn normalized signal of the EDS profile corresponding to the d-g panels. Reaction conditions: T=723 K, P=P_{atm}, gas feed molar composition: 3 NH_3:1 CO:1 H_2.*

This observation ties in well with the inhibition of N uptake observed for the bimetallic catalyst with respect to the monometallic references, as well as with the formal oxidation undergone by Mn upon the *in situ* development of the catalytically active material, indicating that Mn contributes to preserving locally more oxidic (less nitrified) domains on the working catalyst.

5.9 DFT INSIGHTS INTO SURFACE CHEMISTRY AND MIXED METAL PROMOTIONAL EFFECTS

The experimental results discussed in the preceding sections depict a working MnMo catalyst, which is nanocrystalline and it exhibits a rather defective cubic mixed-metal oxynitride structure. To gain insights into the possible working mode for the promotional effects observed upon Mn doping, we developed a surface model for the catalyst.

As discussed earlier, a cubic $Mn_{0.5}Mo_{0.5}N$ compound with *Fm-3m* structure has been considered based on the bulk catalyst composition and the crystallographic results above. In order to determine the surface facet which is preferentially exposed under reaction conditions, periodic DFT calculations were performed to estimate the surface energy of various surface terminations. The results are summarized in **Figure 5.17**.

The 100 surface was found to show the lowest surface energy and it thus dominated the Wulff construction for the mixed-metal nitride crystals (**Figure 5.17.a)**. Therefore, similarly to the case of the γ-Mo_2N monometallic catalyst modelled in **Chapter 3**, the (100) surface is considered to be predominantly exposed on the catalyst surface and thus it was selected for further calculations of surface phenomena. As a reference for the monometallic Mo catalyst, the γ-Mo_2N (100) surface was considered, similarly to those DFT calculations presented in **Chapter 4** and in line with additional *ex situ* XRD characterization results discussed earlier in the present chapter. Given the central mechanistic role revealed in **Chapter 4** for surface O^* adspecies for dissociative HCN activation, emphasis was given to the oxygen adsorption phenomena. Oxygen adatoms were

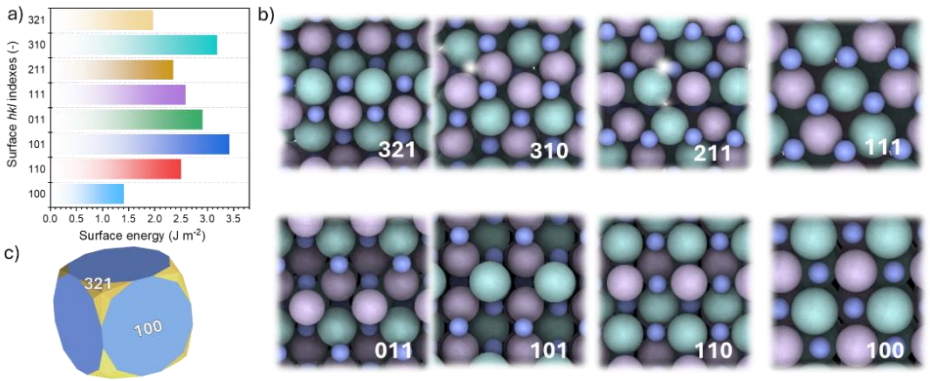

Figure 5.17: *a) DFT-predicted surface energy for different surface terminations of the $Mn_{0.5}Mo_{0.5}N$ nitride (Fm-3m). b) Zenithal views over the optimized structured for different surface terminations. c) Wulff construction derived from the different surface energetics. Assuming a truncated octahedron crystal morphology. For the polar 111 surface, nitrogen termination was found to be significantly more stable than the metal-terminated counterpart, hence it was the only 111 termination considered for the Wulff construction. For the latter, surface energy calculations were performed considering a nitrogen chemical potential μ_N corresponding to a P_{N2}= 1.5 bar and T= 723 K, representative for the reaction conditions.*

found to prefer *hollow sites* on both surfaces, originated by the formation of N-vacancies on the metal nitride surface.

On the mixed-metal nitride, a hollow site on a Mo atom was significantly preferred (by 76 kJ mol^{-1}) to the situation where there is a Mn atom at the immediate sub-surface layer. A higher $E_{ads, O}$ energy of -343 kJ mol^{-1} was computed on the bimetallic catalyst, relative to -330 kJ mol^{-1} in the case of the Mo_2N surface. Moreover, the difference in binding energy for O^* and CO^* was also higher for the mixed-metal nitride, i.e., -211 *vs* -173 kJ mol^{-1} for the monometallic nitride. These results suggest a higher relative coverage of oxygen adspecies on the former catalyst under working conditions. Considering the kinetic significance of O^* (or $^*OH$) adspecies for HCN activation, it appears sensible to posit that the higher oxophilicity of the mixed-metal oxynitride catalyst may underly the

promotional effect exerted by Mn doping in the synthesis of acetonitrile and higher nitriles.

5.10 CONCLUSIONS

The main conclusions derived from the results presented in this chapter are outlined below:

i. A series of crystalline ammonium mixed-metal molybdate compounds provide a structurally uniform set of catalyst precursors to address bimetallic promotional effects in Mo-based catalysts for acetonitrile synthesis, owing to the intrinsic atomic-level metal mixing provided by their regular structure at M:Mo atomic ratios of ca. 1.0, where M is a divalent first-row transition metal.

ii. Doping a Mo catalyst with Mn (at a Mn:Mo atomic ratio of ca. 1:1) affords a particularly selective and stable catalyst for acetonitrile synthesis from NH_3/syngas mixtures at 723 K, achieving an acetonitrile selectivity of 56 C% within the organic products and an acetonitrile formation rate of $50 \cdot 10^{-3}$ mmol g_{cat}^{-1} min^{-1}, in the pseudo-steady state, whereas Mn doping does not modify the nitrile ASF chain-growth probability.

iii. *Ex situ* bulk structural characterization by HRXRD, complemented by first-principles thermochemistry calculations, revealed that the long-range structural order of the working catalyst can be indexed to a highly defective cubic *Fm-3m* mixed-metal (oxynitride).

iv. *Ex situ* XANES analyses reveal that Mn doping retards Mo reduction upon exposure to relevant reaction conditions, additionally preventing the development of extended MoN_{1-x} nitride domains.

v. Analysis of *ex situ* EXAFS results, assisted by DFT-optimized structural models, points to the development of a mixed-metal oxynitride as the working catalyst, while it additionally reinforces the notion of a material showing abundant structural defects, including Schottky-type defects such as vicinal N and Mn vacancies, and compositional heterogeneities,

possibly in the form of Mn-enriched domains with lower local nitridation degrees, in line with observations provided by HAADF-STEM and EDS nanospectroscopy.

vi. Periodic DFT calculations predict stronger binding of O* species, particularly relative to molecular CO, on the surface of the mixed-metal oxynitride catalyst. This observation, coupled with the pivotal role of surface oxygen inferred in **Chapter 4**, suggests that the higher oxygen surface coverage on the more oxophilic mixed-metal oxynitride catalyst could be responsible for the promotional effect induced by Mn doping.

5.11 REFERENCES

(1) Olah, G. A.; Prakash, G. K. S.; Goeppert, A. Anthropogenic Chemical Carbon Cycle for a Sustainable Future. *J. Am. Chem. Soc.* **2011**, *133* (33), 12881–12898. https://doi.org/10.1021/ja202642y.

(2) Chen, J. G.; Crooks, R. M.; Seefeldt, L. C.; Bren, K. L.; Bullock, R. M.; Darensbourg, M. Y.; Holland, P. L.; Hoffman, B.; Janik, M. J.; Jones, A. K.; Kanatzidis, M. G.; King, P.; Lancaster, K. M.; Lymar, S. v.; Pfromm, P.; Schneider, W. F.; Schrock, R. R. Beyond Fossil Fuel–Driven Nitrogen Transformations. *Science (1979)* **2018**, *360* (6391). https://doi.org/10.1126/science.aar6611.

(3) Martin, A.; Kalevaru, V. N. Heterogeneously Catalyzed Ammoxidation: A Valuable Tool for One-Step Synthesis of Nitriles. *ChemCatChem*. **2010**, *2* (12), 1504–1522. https://doi.org/10.1002/cctc.201000173.

(4) Hubert, A. J.; Puentes, E. Hydrocyanation. In *Catalysis in C1 Chemistry; Keim, W.; Ed.;Springer Netherlands:Dordrecht* **1983**, 4, 219–244. https://doi.org/10.1007/978-94-009-7040-3_8.

(5) Chen, G.; Liang, T.; Yoo, P.; Fadaeerayeni, S.; Sarnello, E.; Li, T.; Liao, P.; Xiang, Y. Catalytic Light Alkanes Conversion through Anaerobic Ammodehydrogenation. *ACS Catal.* **2021**, *11* (13), 7987–7995. https://doi.org/10.1021/acscatal.1c02136.

(6) Foit, S. R.; Vinke, I. C.; de Haart, L. G. J.; Eichel, R.-A. Power-to-Syngas: An Enabling Technology for the Transition of the Energy System? *Angewandte Chemie International Edition* **2017**, *56* (20), 5402–5411. https://doi.org/10.1002/anie.201607552.

(7) Zhao, R.; Xie, H.; Chang, L.; Zhang, X.; Zhu, X.; Tong, X.; Wang, T.; Luo, Y.; Wei, P.; Wang, Z.; Sun, X. Recent Progress in the Electrochemical Ammonia Synthesis under Ambient Conditions. *EnergyChem.* **2019**, *1* (2), 100011. https://doi.org/10.1016/j.enchem.2019.100011.

(8) Nozaki, K.; Cerrito, E. Production of Methylamine. US3,410,904, **1968**.

(9) Corbin, D. R.; Schwarz, S.; Sonnichsen, G. C. Methylamines Synthesis: A Review. *Catal. Today* **1997**, *37* (2), 71–102. https://doi.org/10.1016/S0920-5861(97)00003-5.

(10) Walter, R. Catalytic Hydrogenation of Carbon Monoxide with Addition of Ammonia or Methylamine. US 2,821,537A, **1952**.

(11) Kliger, G. A.; Glebov, L. S.; Popova, T. P.; Marchevskaya, E. v.; Beryezkin, V. G.; Loktev, S. M. Carbon Number Distribution and the Chain-Growth Mechanism of Products in the Modified Fischer-Tropsch Synthesis on a Reduced Promoted Fused Magnetite Catalyst. *J. Catal.* **1988**, *111* (2), 418–420. https://doi.org/10.1016/0021-9517(88)90100-5.

(12) Kölbel, H.; Trapper, J. Aliphatic Amines from Carbon Monoxide, Steam, and Ammonia. *Angewandte Chemie International Edition in English* **1966**, *5* (9), 843–844. https://doi.org/10.1002/anie.196608433.

(13) Sango, T.; Fischer, N.; Henkel, R.; Roessner, F.; Steen, E. van; Claeys, M. Formation of Nitrogen Containing Compounds from Ammonia Co-Fed to the Fischer–Tropsch Synthesis. *Appl. Catal. A Gen.* **2015**, *502*, 150–156. https://doi.org/10.1016/j.apcata.2015.06.006.

(14) Fischer, N.; Henkel, R.; Kotzé, H.; Fürst, M.; Olivier, J.; Neethling, J.; Claeys, M. Acetonitrile via CO Hydrogenation in the Presence of NH_3. *Catal. Commun.* **2016**, *87*, 14–17. https://doi.org/10.1016/j.catcom.2016.08.019.

(15) Olive, G.; Olive, S. Process for Preparing Acetonitrile. US 4,179,462, 1979.

(16) Hamada, H.; Kuwahara, Y.; Matsuno, Y.; Wakabayashi, K. Synthesis of Acetonitrile from Syngas and Ammonia over Silica-Supported Molybdenum Catalysts Modified by Silver. *Journal of The Japan Petroleum Institute* **1987**, *30* (3), 188–194. https://doi.org/10.1627/jpi1958.30.188.

(17) Kim, K. N.; Lane, A. M. The Selective Synthesis of Acetonitrile from Carbon Monoxide, Hydrogen, and Ammonia over Mo/SiO_2. *J. Catal.* **1992**, *137* (1), 127–138. https://doi.org/10.1016/0021-9517(92)90144-7.

(18) Hummel, A. A.; Badani, M. V.; Hummel, K. E.; Delgass, W. N. Acetonitrile Synthesis from CO, H_2, and NH_3 over Iron Catalysts. *J. Catal*. **1993**, *139* (2), 392–405. https://doi.org/10.1006/jcat.1993.1035.

(19) Anderson, R. B.; Shultz, J. F.; Seligman, B.; Hall, W. K.; Storch, H. H. Studies of the Fischer—Tropsch Synthesis. VII. Nitrides of Iron as Catalysts [1]. *J. Am. Chem. Soc*. **1950**, *72* (8), 3502–3508. https://doi.org/10.1021/ja01164a051.

(20) Shultz, J. F.; Hall, W. K.; Seligman, B.; Anderson, R. B. Studies of the Fischer-Tropsch Synthesis. XIV. Hägg Iron Carbide as Catalysts [1]. *J. Am. Chem. Soc.* **1955**, *77* (1), 213–221. https://doi.org/10.1021/ja01606a079.

(21) Thornburg, N. E.; Thompson, A. B.; Notestein, J. M. Periodic Trends in Highly Dispersed Groups IV and V Supported Metal Oxide Catalysts for Alkene Epoxidation with H_2O_2. *ACS Catal.* **2015**, *5* (9), 5077–5088. https://doi.org/10.1021/acscatal.5b01105.

(22) Schaidle, J. A.; Thompson, L. T. Fischer–Tropsch Synthesis over Early Transition Metal Carbides and Nitrides: CO Activation and Chain Growth. *J. Catal.* **2015**, *329*, 325–334. https://doi.org/10.1016/j.jcat.2015.05.020.

(23) Schulz, H. Selforganization in Fischer–Tropsch Synthesis with Iron- and Cobalt Catalysts. *Catal. Today* **2014**, *228*, 113–122. https://doi.org/10.1016/j.cattod.2013.11.060.

(24) S. T. Oyama; M. Boudart. Ammonia Synthesis on Surface Layers of Molybdenum Nitride. *Journal of the Research Institute for Catalysis Hokkaido University* **1980**, *28*, 305–320.

(25) Ted Oyama, S. Crystal Structure and Chemical Reactivity of Transition Metal Carbides and Nitrides. *J Solid State Chem.* **1992**, *96* (2), 442–445. https://doi.org/10.1016/S0022-4596(05)80279-8.

(26) Garg, A.; Milina, M.; Ball, M.; Zanchet, D.; Hunt, S. T.; Dumesic, J. A.; Román-Leshkov, Y. Transition-Metal Nitride Core@Noble-Metal Shell Nanoparticles as Highly CO Tolerant Catalysts. *Angewandte Chemie International Edition* **2017**, *56* (30), 8828–8833. https://doi.org/10.1002/anie.201704632.

(27) Volpe, L.; Boudart, M. Ammonia Synthesis on Molybdenum Nitride. *J. Phys. Chem.* **1986**, *90* (20), 4874–4877. https://doi.org/10.1021/j100411a031.

(28) Zheng, W.; Cotter, T. P.; Kaghazchi, P.; Jacob, T.; Frank, B.; Schlichte, K.; Zhang, W.; Su, D. S.; Schüth, F.; Schlögl, R. Experimental and Theoretical Investigation of Molybdenum Carbide and Nitride as Catalysts for Ammonia Decomposition. *J. Am. Chem. Sc.* **2013**, *135* (9), 3458–3464. https://doi.org/10.1021/ja309734u.

(29) Fan, X.; Zhang, H.; Li, J.; Zhao, Z.; Xu, C.; Liu, J.; Duan, A.; Jiang, G.; Wei, Y. Ni-Mo Nitride Catalysts: Synthesis and Application in the Ammoxidation of Propane. *Chinese Journal of Catalysis* **2014**, *35* (3), 286–293. https://doi.org/10.1016/S1872-2067(14)60015-2.

(30) Hunter, S. M.; Gregory, D. H.; Hargreaves, J. S. J.; Richard, M.; Duprez, D.; Bion, N. A Study of $^{15}N/^{14}N$ Isotopic Exchange over Cobalt Molybdenum Nitrides. *ACS Catal.* **2013**, *3* (8), 1719–1725. https://doi.org/10.1021/cs400336z.

(31) Michalsky, R.; Avram, A. M.; Peterson, B. A.; Pfromm, P. H.; Peterson, A. A. Chemical Looping of Metal Nitride Catalysts: Low-Pressure Ammonia Synthesis for Energy Storage. *Chem. Sci.* **2015**, *6* (7), 3965–3974. https://doi.org/10.1039/C5SC00789E.

(32) Tatsumi, T.; Kunitomi, S.; Yoshiwara, J.; Muramatsu, A.; Tominaga, H. Synthesis of Acetonitrile and Related Compounds from CO-H_2-NH_3 over Mo/SiO_2. *Catal. Letters* **1989**, *3* (3), 223–226. https://doi.org/10.1007/BF00766397.

(33) Wei, S.-H.; Ferreira, L. G.; Bernard, J. E.; Zunger, A. Electronic Properties of Random Alloys: Special Quasirandom Structures. *Phys. Rev. B* **1990**, *42* (15), 9622–9649. https://doi.org/10.1103/PhysRevB.42.9622.

(34) Leung, Y. L.; Wong, P. C.; Mitchell, K. A. R.; Smith, K. J. X-Ray Photoelectron Spectroscopy Studies of the Reduction of MoO_3 Thin Films by NH_3. *Appl Surf Sci* **1998**, *136* (1–2), 147–158. https://doi.org/10.1016/S0169-4332(98)00341-9.

(35) Xingbin, Y.; Tao, X.; Gang, C; Shengrong, Y; Huiwen, L.; Qunji, X. Preparation and Characterization of Electrochemically Deposited Carbon Nitride Films on Silicon Substrate. *J. Phys. D Appl. Phys.* **2004**, *37* (6).

(36) Gengenbach, T. R.; Major, G. H.; Linford, M. R.; Easton, C. D. Practical Guides for X-Ray Photoelectron Spectroscopy (XPS): Interpreting the Carbon 1s Spectrum. *Journal of Vacuum Science & Technology A* **2021**, *39* (1), 013204. https://doi.org/10.1116/6.0000682.

CHAPTER 6.

SYNTHESIS OF N-COMPOUNDS FROM NH_3/METHANOL MIXTURES ON NICKEL-GALLIUM CATALYSTS: ALLOYS VS INTERMETALLIC COMPOUNDS

6.1 INTRODUCTION

For millennia, humanity has recognized the transformative power of integrating, through co-melting, two metals together. Among the earliest examples of alchemic metallurgy is the discovery of bronze, an alloy comprising 88 % Cu and 12 % Sn, which is heralded for its remarkable hardness and superior utility in crafting tools and weaponry, and which marked a watershed moment in material innovation.

The integration of alloys into catalytic processes represents a relatively recent frontier in material science and engineering, particularly when juxtaposed with their longstanding applications in the mechanical domain. As described in greater detail in the **Introduction chapter** to this thesis, metal alloying engenders transformative alterations in both the morphology of active sites and their electronic structure. The geometric influence of alloying emanates from its capacity to finely sculpt surface active sites which are not to be found in either of the two metals in their neat form. This may be the result of crystal lattice expansions, the stabilization of new crystallographic structures or through the spacing of specific surface motifs by atoms of an alien metal (ensemble effects). As an industrially relevant example for the latter, diluted Pd-Ag alloys have emerged as technically relevant catalysts for acetylene semi-hydrogenation in the presence of ethylene, leveraging the presence of low-carbophilicity Ag atoms to break apart surface domains of Pd and thereby mitigate alkene over-hydrogenation.[1]

The utilization of intermetallic compounds in catalysis confers even greater degrees of control compared to their alloy counterparts, owing to their distinctive crystal structures and long-range atomic ordering. Unlike alloys, which typically exhibit random distributions of atoms within a solid solution, intermetallics present well-defined stoichiometry and crystallographic arrangements. Moreover, the ordered atomic arrangement in intermetallics often confers enhanced stability and resistance to structural degradation, e.g., under catalysis conditions, providing, *a priori*, a more predictable playground to establish structure-

performance relations. Furthermore, intermetallic compounds possess the capability to adopt unique, e.g. low-symmetry crystal structures, a characteristic seldom observed in conventional alloys or neat metals, and which may provide extra degrees of freedom to engender catalytically active surface sites with unconventional geometric and/or electronic properties. An ancient example is the γ-brass phase, which is prevalent in numerous transition metal phase diagrams. The ideal γ-brass phase crystallizes in a body-centered cubic space group *I-43m*. However, numerous cubic γ-brass type phases have additionally been reported with cubic space groups *P-43m*, and *F-43m.*[2]

The last two decades have witnessed a surging interest in the design of (single-atom) alloy and intermetallic catalysts.[3–5] However, as important as designing and precisely establishing the structure of the static bimetallic (pre)catalyst is to assess potential structural (bulk and/or surface) modifications, which it may undergo when exposed to relevant catalysis conditions. This is particularly relevant under reaction conditions bearing high chemical potentials of light elements (C, O, N) which may diffuse into the subsurface of metal structures, profoundly affecting the (near-surface) structure and catalytic performance.[6]

In this chapter, a series of Ni-based SiO_2-supported catalysts has been developed. Gallium has been added as a second (post-transition) metal in the Ga:Ni compositional range spanning from 0:1 to 0.6:0.4 (atomic). Following reductive catalyst activation, undoped Ni nanocrystals as well as catalysts incorporating Ga at contents lower than 40 at% showed the *fcc* structure characteristic for nanosized nickel. However, a systematic enlargement of the crystal unit cell with increasing Ga contents was demonstrated, indicative for the incorporation of Ga into a NiGa alloy. In marked contrast, Ga contents in excess to 40 at% led to the formation of NiGa intermetallic structures. Particularly, a catalyst with a Ga:Ni atomic ratio of 0.6:0.4 presents, after reductive activation, a GaNi intermetallic nanostructure. Hence, the set of supported catalysts provided a suitable basis to rationalize the distinct catalytic behavior of neat Ni, and NiGa alloy and intermetallic compounds as catalysts for the synthesis of N-compounds through the conversion of mixtures of methanol and ammonia. While NiGa alloys

presented high selectivities to nitriles, evidencing activity for both C-N and C-C coupling from the C_1 and N_1 reactants,[7–9] the NiGa intermetallic compound showed high selectivities to methylamines and O-compounds.[10,11]

Moreover, multi-modal, temperature and time-resolved *in situ* and *operando* spectroscopic studies have been carried out using high-resolution X-ray diffraction (HRXRD), X-ray adsorption spectroscopy (XAS) and X-ray photoemission spectroscopy (XPS) to gain complementary insights into the dynamic evolution of the crystal and near-surface structure of the bimetallic catalysts during activation treatments as well as while at work, at relevant catalysis conditions.

6.2 RESULTS AND DISCUSSION

6.2.1 Bulk properties of Ni-Ga pre-catalyst series

Following their synthesis as detailed in **Chapter 3**, the series of $Ga_xNi_{(1-x)}/SiO_2$ catalysts (x= 0.02 to 0.6), were analyzed by X-ray diffraction (XRD). As shown in **Figure 6.1. a**, XRD-patterns showed diffraction signals characteristics for cubic NiO, consistent with ICSD 9866**.** While the monometallic Ni/SiO_2 catalyst showed well defined diffractions, increasingly higher Ga contents led to progressively wider diffraction peaks, suggesting a progressive decrease in the volume-average crystalline domain size. Moreover, a systematic shift to lower 2θ values was observed, indicative of enlarged lattice parameters. These results support the formation of Ni-Ga mixed oxides, although the presence of additional, amorphous gallium species, undetectable by XRD, cannot be ruled out.

The reducibility of the catalysts was studied by hydrogen temperature-programmed (H_2-TPR), and the corresponding reduction profiles are shown in **Figure 6.1. b**. The monometallic Ni/SiO_2 catalyst presented three mean hydrogen consumption peaks in the temperature range of 473-723 K. In all cases, this signal is considered to correspond to the reduction of Ni^{2+} species to zerovalent nickel (Ni^0). The first peak, with the lowest reduction temperature, at 497 K, can be attributed to highly dispersed (particularly small crystallites) of nickel (II)

(hydr)oxide. The most prominent band, peaking at 603 K,[12,13] is ascribed to the largest population of NiO nanocrystals. Finally, the shoulder at 720 K can be attributed to Ni (hydro)oxide species interacting strongly with the silica support, or Ni silicate metal-support compounds, which are hard to reduce.[14] For the series of bimetallic catalysts, increasingly higher Ga contents resulted in a progressive broadening of the reduction signals and their shift to higher temperatures, indicating that interaction with gallium retards the reduction of Ni(II) species.[14] In view of the set of H_2-TPR profiles, temperatures of 973-1023 K have been applied for the reductive activation of the series of catalysts, in order to ensure a consistent, full reduction of nickel species to Ni^0 prior to catalysis testing.

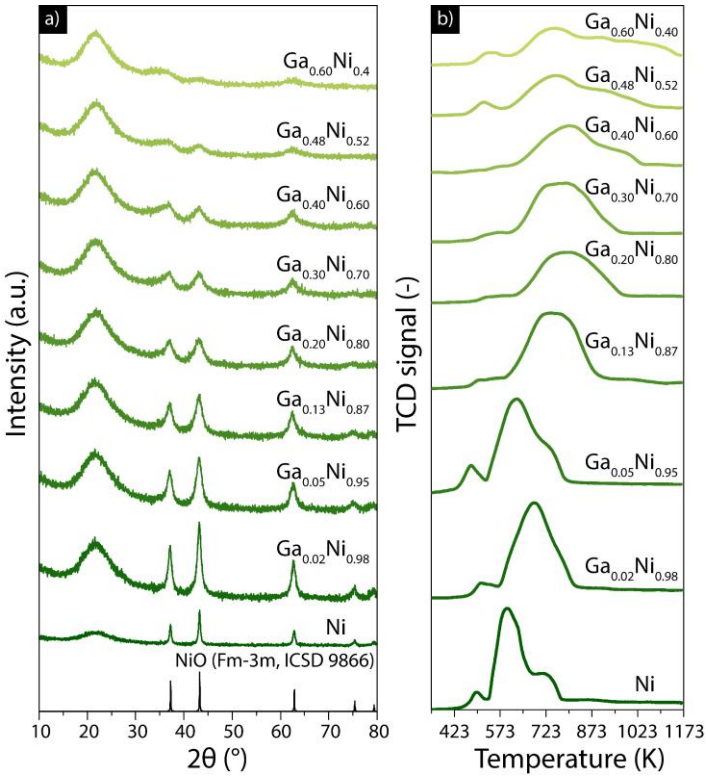

Figure 6.1: *a) X-ray diffractograms for the series of oxidic precursors for $Ga_xNi_{(1-x)}/SiO_2$ catalysts (x= 0.02 to 0.6) in their as-calcined state. b) Hydrogen temperature-programmed reduction (H_2-TPR) profiles for selected $Ga_xNi_{(1-x)}/SiO_2$ catalyst precursors.*

Laboratory-based X-ray diffraction was also applied to characterize the crystal structure of the series of catalysts following their reductive activation in H_2 and surface passivation (see **section 3.1.5** in **Chapter 3** for experimental details). The X-ray diffractograms for $Ga_xNi_{(1-x)}/SiO_2$ catalysts with x= 0-0.3 showed exclusively peaks corresponding to the face centered cubic (*fcc*) crystal phase (*Fm-3m*) characteristic for metallic Ni **(Figure 6.2 a)**. Rietveld refinement revealed a lattice cell parameter (a= 3.5241(1) Å) for Ni/SiO_2, well in line with that reported in the literature for metallic nickel (ICSD 260169). As shown in **Figure 6.2. b**, the experimental *a* parameter increased rather linearly with the incorporation of Ga, as expected for a systematic enlargement of the unit cell size in the α-Ni_xGa_y (*Fm-3m*) solid solution, up to Ga contents of ca. 15 at%. However, for Ga contents in excess of 20 at%, the experimental *a* parameter underwent a steep increment compared to the systematic trend expected for the α-Ni_xGa_y solid solution, which may indicate the formation of the α'-Ni_3Ga (*Pm-3m*) intermetallic. This is qualitatively consistent with the literature, wherein α-Ni_xGa_y (*Fm-3m*) solid solutions have been reported to be stabilized only for Ga contents up to 24.3 at%.[15]

As observed in **Figure 6.2. c**, catalysts with Ga-richer compositions, i.e., with $x \geq 0.4$, showed diffractions corresponding to the crystal structure of NiGa intermetallics. Hence, the XRD results served to delimit compositional ranges for the stabilization of either NiGa *Fm-3m* (*fcc)* alloys or NiGa intermetallic compounds.[15]

Figures 6.2. d-e show a Ni-Ga phase diagram reported in the literature, together with illustrations of the most representative alloy and intermetallic crystal structures within the compositional range spanning from 0 to 60 at% Ga. Several studies have shown agreement as to the phase equilibria between α, α´and β phases, however, phase equilibria specifically involving β, γ, δ, and ε phases are still the matter of debate.[15] For the set of catalysts included in **Figures 6.2. c,** different intermetallic crystal structures have been identified as a function of the bimetallic composition.

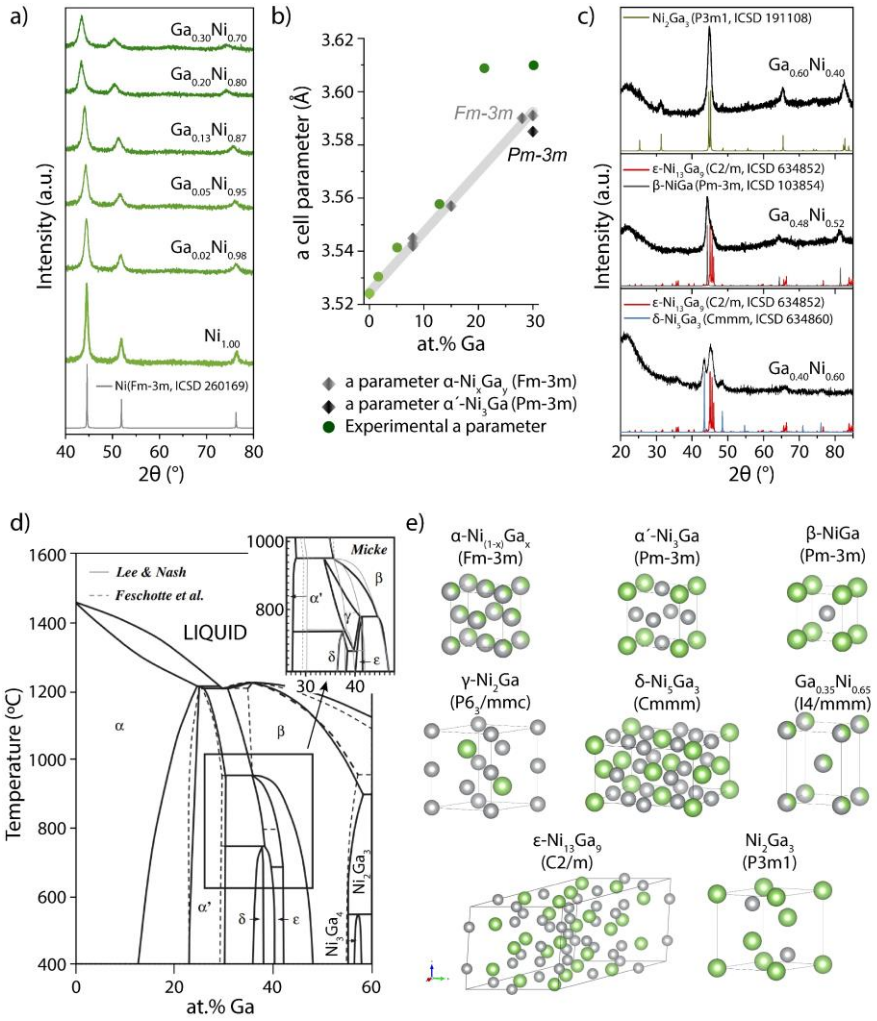

***Figure 6.2**. a) X-ray diffraction patterns and b) evolution of the a cell parameter with composition for the series of $Ga_xNi_{(1-x)}/SiO_2$ catalysts (x=0-0.3) following reduction in hydrogen at 1023 K. In panel b, gray and black diamonds represent the a parameter reported in the literature for α-Ni_xGa_y (Fm-3m) solid solutions and α´-Ni_3Ga intermetallics, respectively, while green circles correspond to the experimental a parameter determined in this study using Rietveld refinement. The gray line is a guide to the eye corresponding to the systematic lattice expansion for α-Ni_xGa_y (Fm-3m) alloy upon Ga incorporation. c) X-ray diffraction patterns for $Ga_xNi_{(1-x)}/SiO_2$ catalysts (x=0.4-0.6) showing diffractions indexable to intermetallic compounds. d) Ni-Ga phase diagram.[15] e) representation of the crystal structure described for the most relevant NiGa solid solution alloys and intermetallics. Ni and Ga atoms shown in gray and green color, respectively.*

$Ga_{0.40}Ni_{0.60}/SiO_2$ and $Ga_{0.48}Ni_{0.52}/SiO_2$ catalysts showed contributions from two intermetallic phases. Both catalysts presented the monoclinic ε-$Ni_{13}Ga_9$ phase (*C2/m*). Additionally, $Ga_{0.48}Ni_{0.52}/SiO_2$ showed β-NiGa (*Pm-3m*), while $Ga_{0.4}Ni_{0.6}/SiO_2$ showed the orthorhombic δ-Ni_5Ga_3 (*Cmmm*), respectively, in qualitative agreement with the stability of the different crystalline phases established by the phase diagram as a function of the relative Ga:Ni contents for bulk bimetallics. Finally, $Ga_{0.6}Ni_{0.4}/SiO_2$, with a greater Ga content, showed the presence of Ni_2Ga_3 (*P3m1*) as the sole intermetallic compound.

6.2.2 Catalytic performance in the conversion of NH_3/methanol mixtures

The performance of the series of GaNi catalysts was assessed for the conversion of mixtures of ammonia and methanol into N-compounds. The N:C molar ratio in the feed stream was fixed to 2.0 (hereafter denoted as N/C=2) while reaction temperatures were screened in the range spanning from 573 to 823 K. **Figures 6.3. a-d** summarize selected performances indicators, such as the methanol conversion, selectivity to CO, as well as formation rates for nitrile (C_1-C_5) and methylamine N-compounds, attained at a constant gas-catalyst *space velocity* of 5.22± 0.06 $mmol_{feed}\ mmol_{Metal}^{-1}\ h^{-1}$.

The monometallic Ni/SiO_2 catalyst attained methanol conversion levels increasing from 13.3 % to 96.4 % with increasing temperature. This catalyst delivered high selectivity to CO, between 88.1 and 96.2 % (C-basis) in the entire range of reaction temperatures and methanol conversion levels studied. Moreover, it showed very modest nitrile formation rates $< 2 \cdot 10^{-3}\ mmol_{Nitriles}\ mmol_{M}^{-1}\ min^{-1}$ in the entire operational window screened, underscoring its inefficiency to synthesize N-compounds from NH_3/methanol mixtures.

Addition of 2 at% Ga led to a noticeable decrease in methanol conversion, e.g., from 85.5 % to 57.7 % at 673 K. At this and lower reaction temperatures, a systematic decrease in methanol conversion was observed upon the incorporation of increasingly higher Ga contents.

The highest rate of nitrile formation was attained at a reaction temperature of 773 K, which was therefore selected as the standard testing temperature for nitrile synthesis. At 773 K, both activity and selectivity evolved in a less systematic manner with bimetallic composition. The addition of 2 at% Ga led to a the most marked drop in methanol conversion, from 97.3 % to 31.0 %. However, the general tendency of a decreasing methanol conversion with increasing Ga content was not preserved at this temperature. Bimetallic catalysts with Ga contents in the range from 5-20 at% outlaid the overall trend, leading to greater methanol conversion levels than catalysts with either lower or higher Ga contents. This enhanced methanol conversion values were parallelled by an increased CO selectivity and, as a result, a significant decrease in the rate of production of nitriles, e.g. from a maximum value of $23 \cdot 10^{-2}$ $mmol_{Nitriles}$ $mmol_{Metal}^{-1}$ min^{-1} for $Ga_{0.05}Ni_{0.95}/SiO_2$ down to $2 \cdot 10^{-2}$ $mmol_{Nitriles}$ $mmol_{Metal}^{-1}$ min^{-1} for $Ga_{0.20}Ni_{0.80}/SiO_2$, see **Figure 6.3. a-c**. For the latter catalyst, activity and product distribution at 773 K closely resembled those of the monometallic Ni/SiO_2 catalyst. These results suggest that metal segregation may have occurred under reaction conditions (at 773 K) for NiGa alloy nanocrystals with comparatively high Ga contents, approaching the solid solubility limit described earlier for the α-Ni_xGa_y (*Fm-3m*) alloy phase (**Figure 6.2. c**, *vide supra*).

As shown in **Figure 6.3. c**, the maximum nitrile formation rate was attained with $23 \cdot 10^{-2}$ $mmol_{Nitriles}$ $mmol_{Metal}^{-1}$ min^{-1} at 773 K. In contrast, as observed in **Figure 6.3. d,** the formation rate of methylamines scaled with Ga content and it was maximum for $Ga_{0.60}Ni_{0.40}/SiO_2$, within the series of bimetallic catalysts, also at a reaction temperature of 773 K.

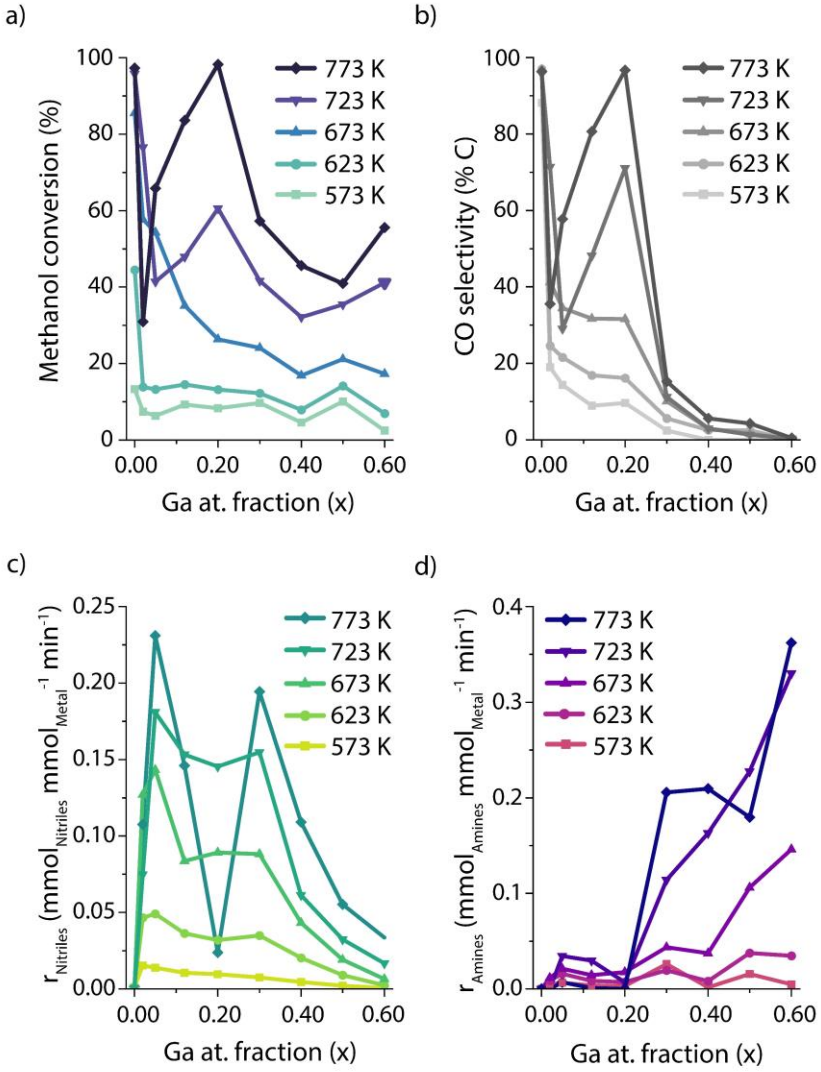

Figure 6.3: *Evolution of a) methanol conversion, b) CO selectivity, c) nitriles formation rate, d) methylamines formation rate with the Ga atomic fraction (x) in the bimetallic Ga_xNi_{1-x}/SiO_2 catalysts and the reaction temperature. Gas-catalyst space velocity= 5.22± 0.06 $mmol_{Feed}$ $mmol_{Metal}^{-1}$ h^{-1}, P=2± 0.5 bar.*

$$CH_3OH_{(g)} \rightarrow CO_{(g)} + 2H_{2(g)};\ \Delta H^{\circ}_{298} = 94.6\ kJ\ mol^{-1} \qquad \textbf{Eq. 6.1}$$

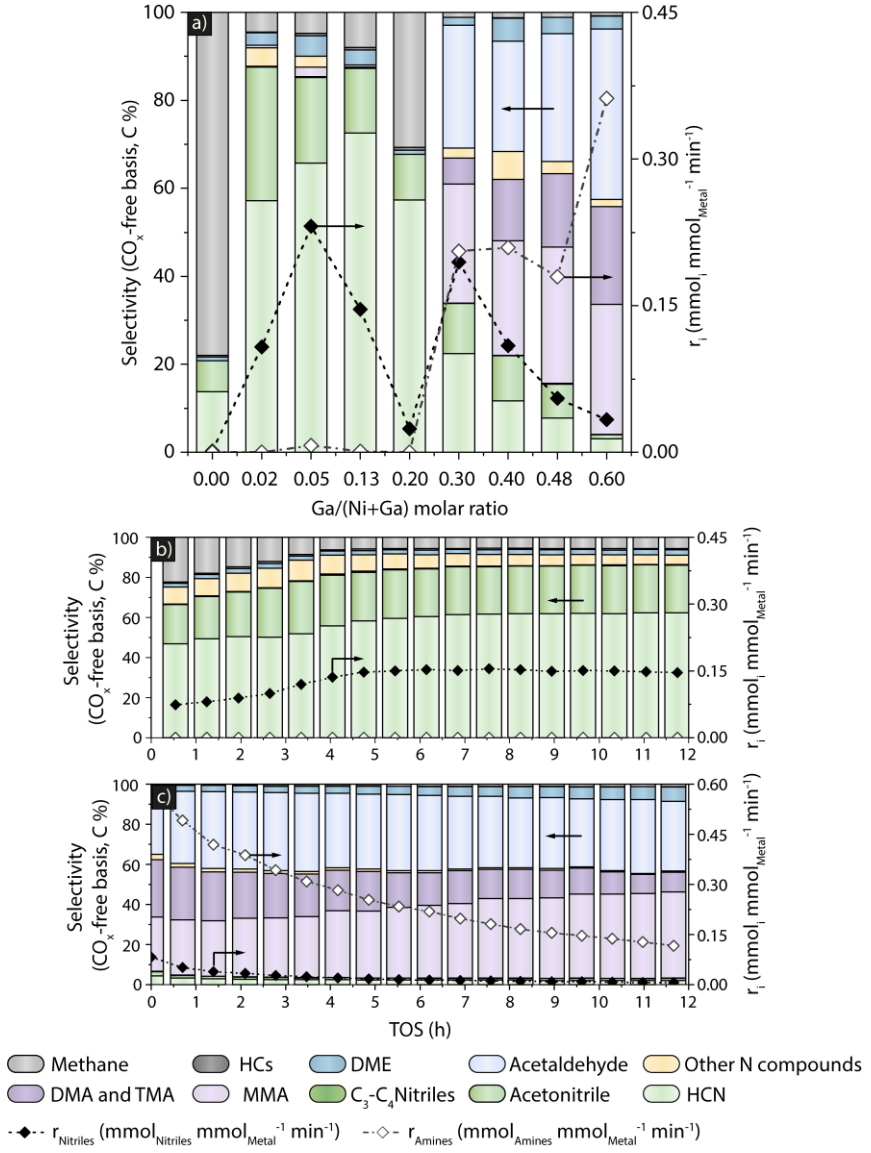

***Figure 6.4**. a) Selectivity within the organic products, i.e., on a CO_x-free basis, (bars), and formation rate of nitriles and methylamines (scatter-dotted lines) obtained with the series of $Ga_xNi_{(1-x)}/SiO_2$ catalysts in the conversion of a NH_3/methanol mixture (N/C=2) to N-compounds (TOS=12-16 h). b,c) Evolution of product formation rate (scatter-dotted lines) and selectivity pattern (bars) with time-on-stream for selected b) nitrile-selective catalyst ($Ga_{0.05}Ni_{0.95}/SiO_2$)* and c) amine-selective catalyst (*$Ga_{0.60}Ni_{0.40}/SiO_2$). Reaction conditions: T= 773 K, P=2±0.5 bar, NH_3:CH_3OH molar ratio of 2, GHSV= 5.2 $mmol_{feed}$ $mmol_M^{-1}$ h^{-1}.*

Figure 6.4. a summarizes the selectivity patterns to organic products obtained with the series of Ni-based catalysts at 773 K. These selectivity patterns correspond to methanol conversion levels of 50± 15 % with the exception of few catalysts which, as discussed above, showed too high methanol conversion rates, chiefly to CO, hence likely via dehydrogenation pathways (see **equation 6.1**).[16] This is the case of the monometallic Ni/SiO_2 catalyst, and those bimetallic catalysts with Ga contents close to the maximum Ga solid-state solubility in the cubic α-Ni_xGa_y (*Fm-3m*) alloy phase.

As illustrated in **Figure 6.4. a**. two compositional regimes could be discerned for the bimetallic GaNi catalysts, clearly differentiated by the corresponding product selectivity patterns. Catalysts with Ga contents ≤20% produced primarily nitriles within the organic products. In stark contrast, catalysts with Ga contents ≥30 % favored the formation of methylamine N-compounds.

Catalysts with Ga contents in the range of 2-12 at% attained the highest selectivity to nitriles, i.e., higher than 80 C% (CO_x-free basis). Acid cyanide was the prevalent nitrile in all cases, whereas the selectivity to acetonitrile was maximum for $Ga_{0.02}Ni_{0.98}/SiO_2$ (30.3 C%). Moreover, the carbon chain length distribution for C_2-C_5 nitriles was found to obey an Anderson-Schulz-Flory (ASF) distribution at all tested temperatures. This is exemplified in **Figures 6.5. a-b** for the $Ga_{0.05}Ni_{0.95}/SiO_2$ catalyst, which afforded the highest nitrile formation rate. The ASF chain growth parameter (α) showed a volcano dependence with temperature, peaking at α=0.33 at a reaction temperature of 673 K.

These results provide solid evidence for a chain-propagation mechanism proceeding on the surface of the bimetallic catalysts, by C-C coupling from C_1 monomeric species. Given that methanol can undergo dehydrogenation on nickel-based catalysts (**Equation 6.1)**, it may serve as an *in situ* source of syngas (CO/H_2). In turn, CO can be further activated into C_1 adspecies which engage into chain-growth and reaction to HCN, as it has been discussed previously in **Chapter 4**. Light (C_1-C_4) hydrocarbons were also produced, albeit at limited selectivities, i.e., ≤4.5 C% at 673 K, supporting the occurrence of a Fischer-Tropsch-like reaction mechanism from C_1 monomers. In view of the remarkably low selectivity

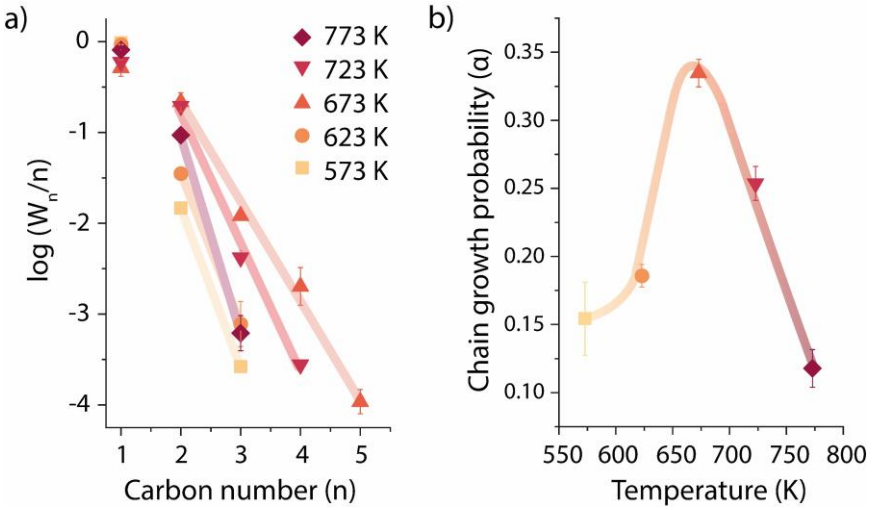

Figure 6.5: *a) Linearized Anderson-Schulz-Flory (ASF) product distribution for nitriles (HCN formally considered as a C_1 nitrile) as obtained with the $Ga_{0.05}Ni_{0.95}/SiO_2$ catalyst at various reaction temperatures. Lines correspond to linear regressions. b) Evolution of the average ASF chain growth probability parameter (α) for C_2-C_5 nitrile products, from tests with $Ga_xNi_{(1-x)}/SiO_2$ alloy-type catalysts with x=0.02-0.12 as a function of the reaction temperature. Line is a guide to the eye. Gas-catalyst space velocity= 5.22±0.06 $mmol_{Feed}mmol_{Metal}^{-1}h^{-1}$, P=2±0.5 bar.*

to CO_2, lower than 3.4 %, the occurrence of methanol steam reforming, e.g. with endogenous water (**Equation 6.2**), was inferred to be negligible in the range of reaction temperatures examined. Additional minor side-products included O-compounds, such as dimethyl ether (DME), with selectivities of 0.14-8.13 C%, and acetaldehyde (<0.80 C%).

$$CH_3OH_{(g)} + H_2O_{(g)} \rightarrow CO_{2_{(g)}} + 3H_{2_{(g)}};\ \Delta H^{\circ}{}_{298} = 53.3\ kJ\ mol^{-1} \qquad \textbf{Eq. 6.2}$$

In a second group of bimetallic catalysts, materials with Ga contents ≥30% favored the formation of methylamines as the prevailing N-compounds. Moreover, acetaldehyde became a relevant oxo-product, reaching selectivities of 25.0-38.8 C%. These results strongly suggest a change in the predominant reaction

mechanism. Given that methylamines are the products of methanol amination,[7,17,18] an alternative reaction path wherein methoxy species are derivatized through amination appears to be sensible.

The two compositional regimes within the bimetallic catalysts exhibited also noticeably different behaviors in terms of carbon build-up on the catalyst surface. **Figure 6.6** shows the evolution of the overall carbon balance, at different reaction temperatures, and the carbon, nitrogen and hydrogen content determined on the solid catalysts after the reaction test, as a function of the Ga content.

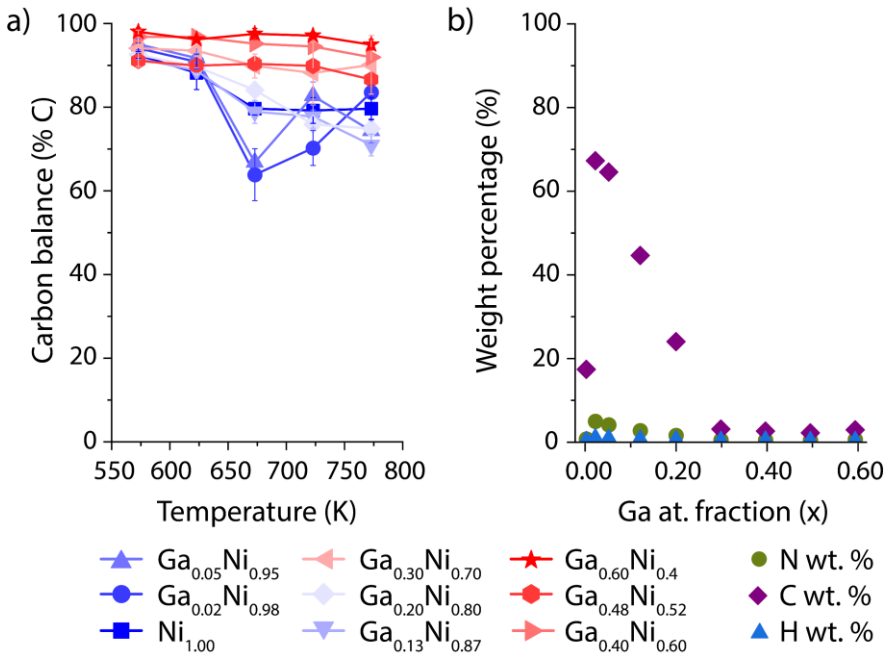

Figure 6.6: *a) Evolution of the overall carbon balance obtained with the series of $Ga_xNi_{(1-x)}/SiO_2$ catalysts in the conversion of NH_3/methanol mixtures to N-compounds with the reaction temperature. b) Evolution of the carbon, nitrogen and hydrogen weight loadings, as determined by elemental analysis, in the catalyst following exposure to catalysis conditions as a function of the Ga atomic fraction (x) in the bimetallic Ga_xNi_{1-x}/SiO_2 catalysts. In panel b, the standard deviation determined from several elemental analysis realizations is smaller than the dots on the figure.*

As observed, the monometallic Ni/SiO_2 catalyst, as well as catalysts with lower Ga contents ≤20 %, led to evidently non-closing carbon balances (<80 %) at relevant reaction temperatures ≥673 K. For these catalysts, significant carbon contents, in the range of 20-70 wt% were determined by elemental analysis following the catalytic test. Jointly, these results provide evidence for a significant carbon deposition on the catalyst surface. Next to carbon, also nitrogen was detected on the spent catalysts, with a maximum content of 4.7 wt%, indicating also a certain N uptake. In stark contrast, stable carbon balances (≥90 %) were obtained for catalysts with Ga contents ≥30 % at all reaction temperatures, suggesting that carbon build-up is minimal in this case. This observation agreed well with the results of elemental analysis on the spent catalysts, which showed decreasing C and N contents with increasing Ga content in the bimetallics, to plateau at 2.7± 0.4 C wt% and 0.56± 0.06 N wt% for Ga contents ≥30 at% (**Figure 6.6. b**).

Catalyst $Ga_{0.05}Ni_{0.95}/SiO_2$, representative of the first, Ga-poor, compositional regime, attained the highest nitrile formation rate of $23 \cdot 10^{-2}$ $mmol_{Nitriles}$ $mmol_{Metal}^{-1}$ min^{-1}. In turn, catalyst $Ni_{0.40}Ga_{0.60}/SiO_2$, representative of the second, Ga-rich compositional regime, achieved the highest methylamine formation rate of $36 \cdot 10^{-2}$ $mmol_{Amines}$ $mmol_{Metal}^{-1}$ min^{-1}. Therefore, these two catalysts were selected as representative for the nitrile-selective and methylamine-selective performances, respectively, and their stability under reaction conditions was assessed through specific isothermal tests at 773 K. The corresponding results, over a total testing period of 12 h on-stream, are shown in **Figure 6.4. b,c**, respectively.

Particularly in the case of $Ga_{0.05}Ni_{0.95}/SiO_2$, heating the pre-reduced catalyst under the reactive NH_3/methanol atmosphere from RT to 773 K, using a heating rate of 3 K min^{-1}, unexpectedly led to a remarkably unselective behavior, resemblant of that of the monometallic Ni/SiO_2 catalyst (results not shown). This behavior departed notably from that observed at the same reaction temperature, after having tested the catalyst for different times at lower temperatures when screening increasing reaction temperatures with a single catalyst load. Therefore,

an additional *in situ* activation step was performed, under the reactive atmosphere, at 673 K for 3 h, prior to increasing the temperature to 773 K for the stability test. The application of this activation procedure recovered the nitrile-selective performance at 773 K. Directly heating $Ga_{0.60}Ni_{0.30}/SiO_2$ to 773 K did not cause any significant deviation with respect to the performance registered for the catalyst in the temperature screening test, suggesting a higher stability of the active catalyst species and ruling out the need for activation treatments in addition to the standard, *in situ* catalyst reduction. However, the pretreatment at 673 K under the reactive atmosphere was also applied in this case, for the sake of establishing a consistent comparison between both catalysts.

As shown in **Figure 6.4. b**, $Ga_{0.05}Ni_{0.95}/SiO_2$ afforded an initial nitrile formation rate of $74 \cdot 10^{-3}$ $mmol_{Nitriles}$ $mmol_{Metal}^{-1}$ min^{-1}, corresponding to a selectivity to nitriles within the organic products of 66.7 C%. An induction period was observed over ca. five hours on-stream, during which both nitrile formation rate and CO_x-free selectivity surged to level off at $15 \cdot 10^{-2}$ $mmol_{Nitriles}$ $mmol_{Metal}^{-1}$ min^{-1} and 85.7 C%, respectively, at a methanol conversion of 53.2 %. Acid cyanide was the predominant nitrile, with a selectivity within the organic products of 61.5 C%, followed by acetonitrile (23.9 C%). In the pseudo-steady state, the total CO_x selectivity amounted to 43.5 C%, being CO the predominant carbon oxide side-product (40.0 C%). Following the initial transient period, all performance parameters remained remarkably stable up to the total test duration of 12 h. These results underscore that, in spite of the significant carbon deposition taking place on the surface of this catalyst (*vide infra*, **section 6.2.3**), those active centers involved in both C-N and C-C coupling elementary reactions remain particularly stable within the examined operation times.

A different behavior was observed for the amine-selective $Ga_{0.60}Ni_{0.40}/SiO_2$ catalyst (**Figure 6.4. c**). In this case, an initial methanol conversion of 88.2 % declined continuously over the test duration, down to 18.9 % after 12 hours on-stream. No pseudo-steady state was reached during the reaction time studied. As a result of catalyst deactivation, the overall methylamine formation rate dropped from 0.58 to 0.13 $mmol_{Amines}$ $mmol_{Metal}^{-1}$ min^{-1}. While the overall selectivity to

methylamines remained essentially constant at 53.7± 1.2 %, the relative abundance of different methylamines within the products changed in parallel to the activity decline. The amine distribution evolved from MMA: DMA: TMA of 69.4: 18.8: 11.9 to 90: 6.9: 2.3, evidencing the deactivation of secondary amine methylation paths. The selectivity to nitriles remained remarkably low over the entire test time and decreased from 6.63 C% at the start of the reaction to 3.2 C% after 12 h TOS. As an additional difference with the performance observed for $Ga_{0.05}Ni_{0.95}/SiO_2$, O-compounds accounted for a significant fraction of the products and particularly the selectivity to acetaldehyde remained within 31.9-39.0 % over the examined reaction time. This suggests that the intermetallic NiGa nanocrystals promote hydrocarbonylation pathways from methanol and the endogenously generated syngas under the process conditions.

Taken together, the above results emphasize the distinctly different catalytic performance exhibited by low- and high-Ga content bimetallic NiGa nanocrystals, exemplified by the $Ga_{0.05}Ni_{0.95}/SiO_2$ and $Ga_{0.60}Ni_{0.40}/SiO_2$ catalysts, respectively. In their activated state, the former exhibits an *fcc* NiGa alloy structure, whereas the later consists of the Ni_2Ga_3 intermetallic compound. Therefore, these two catalysts provide an excellent test set to assess catalytic differences between disordered (alloy) and ordered (intermetallic) Ni-Ga solid solutions. However, next to determining the structure of the catalyst in its activated form, i.e., prior to exposure to process conditions, it is important to track any structural modifications which may occur during the catalytic action before any specific performance can be unequivocally associated to a specific (bi)metallic nanostructure. The following sections summarize the results of various physicochemical characterization methods applied on the monometallic Ni/SiO_2, as well as the two selected bimetallic $Ga_{0.05}Ni_{0.95}/SiO_2$ and $Ga_{0.60}Ni_{0.40}/SiO_2$ catalysts, following activation and catalytic usage, as well as under *operando* conditions, i.e., with a simultaneous and time-resolved diagnostics of catalyst nanostructure and performance under relevant process conditions.

6.2.3 Catalyst nanostructure and near-surface structure prior to and after catalysis

The metal nanoparticle size and metal nanospatial distribution were assessed by means of (scanning-) transmission electron spectroscopy on cross-sectional catalyst specimens. As shown in **Figure 6.7**, in their reduced state, $Ga_{0.05}Ni_{0.95}/SiO_2$ and $Ga_{0.60}Ni_{0.40}/SiO_2$ catalysts showed monomodal metal nanoparticle size distributions centered at 18± 10 nm and 15± 10 nm, respectively. Energy dispersive X-ray spectroscopy (EDS) cross-sectional compositional maps confirmed uniform nanospatial metal distributions in both cases, with no indications for any noticeable metal segregation across nanoparticles (**Figure 6.7. c-f** and **i-l**).

Compositional and nanostructural changes, brought about by the exposure of the two catalysts to process conditions, were also assessed by studying the *spent* catalysts, i.e., following the 12 hour-long catalytic tests described in **section 6.2.2**.

In line with results discussed above (**section 6.2.2**), elemental analysis revealed a significant carbon (and nitrogen) uptake by $Ga_{0.05}Ni_{0.95}/SiO_2$. After catalysis, carbon and nitrogen contents were 70.2 wt% and 4.9 wt%, respectively. Hydrogen content was only 0.8 wt%, indicating that elemental carbon, rather than coke, is deposited on the catalyst surface. Conversely, $Ga_{0.60}Ni_{0.40}/SiO_2$ showed very limited carbon build-up, as evident from 2.5 C wt. %, 0.5 N wt. % and 0.2 H wt. % contents determined in the spent catalyst.

Further insights into the structure of the carbon deposits were gained with Raman spectroscopy. Raman experiments were performed *ex situ*, while the spent catalysts were handled under exclusion of air. No Raman bands were observed in the case of the spent $Ga_{0.60}Ni_{0.40}/SiO_2$ (not shown), in line with the very limited amount of carbon quantified with elemental analysis on this catalyst. In contrast, intense Raman bands associated to (partially) graphitic carbon species were detected in the case of $Ga_{0.05}Ni_{0.95}/SiO_2$, see **Figure 6.8 a**.[19] The so-called G band peaked at 1588.3 cm^{-1}. This Raman shift is slightly blue-shifted with respect to what is characteristic for graphene and bulk graphite (typically peaking

at 1580 cm^{-1}). This band shift suggests the presence of defects, such as non-sixfold rings in sp^2-hybridized clusters or local sp^3-ordering.[19] The occurrence of imperfections within the graphitic structures is indeed reinforced by the detection of a prominent so-called D-band, at 1352.5 cm^{-1}, which is associated with structural defects in graphitic nanostructures, as well as by the broad spectral band registered between 2400 and 3100 cm^{-1}, and thus the absence of a defined second-order 2D peak characteristic of fully crystalline graphite structures.[20] The I_D/I_G band ratio was determined to be 0.85, which is in line with values determined earlier for N-doped graphitic carbon such as carbon nanotubes (CNT) or graphene.[21] Therefore, taking the Raman spectroscopy and elemental analysis results together, it is inferred that nitrogen-doped graphitic nanostructures are developed and accumulate on the catalyst surface during its exposure to process conditions. As illustrated in **Figures 6.8. b,c**, high-resolution transmission electron microscopy revealed the presence of carbon nanofibers on the spent $Ga_{0.05}Ni_{0.95}/SiO_2$ catalyst. Metal nanocrystals were detected at the tip of the carbon filaments, indicating a tip-growth mechanism.[22] Furthermore**,** detailed inspection of the metal nanocrystals revealed a variety of nanoparticle morphologies, which had not been detected prior to catalysis, and therefore developed as a result of the exposure of the catalyst to reaction conditions. The particle shapes ranged from barely faceted spherical/ovoidal aspects to markedly faceted cubes/parallelepipeds and tetrahedra. The analysis of the nanoparticle size distributions was performed with shape specificity. Nanoparticles with sizes ≤5 nm were assumed to be spherical/ovoidal, due to resolution limits. As summarized in **Figure 6.8. f**, spherical nanoparticles presented the largest size and widest size distribution (22± 20 nm). Narrower size distributions, centered at 8± 2 nm and 12± 4 nm were determined for cubic and tetrahedral nanoparticle shapes, respectively. EDS compositional maps, included in **Figures 6.8 h-l**, further proved that Ga was primarily detected in nanocrystals with markedly faceted shapes, i.e., cubic and tetrahedra, whereas nanoparticles with rounder shapes were found to be substantially depleted in Ga.

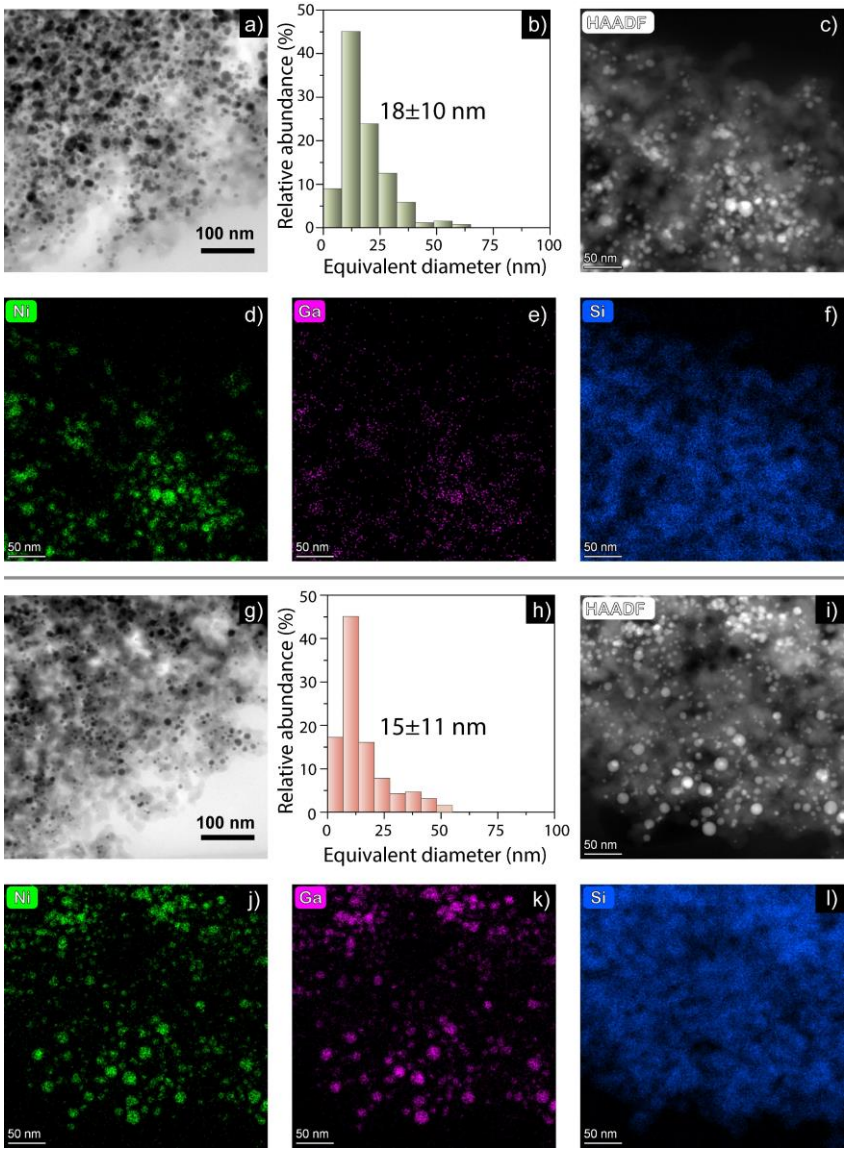

Figure 6.7**:** *a, g) Cross-sectional bright-field transmission electron micrographs and b, h), the respective metal nanoparticle size distributions. c, i) High-angle annular dark-field scanning-transmission electron microscopy (HAADF-STEM) micrographs and d-f, j-l) energy dispersive X-ray spectroscopy (EDS) compositional maps collected using Kα-emission lines for Ni, Ga and Si, respectively, for a-f) $Ga_{0.05}Ni_{0.95}/SiO_2$ and g-l) $Ga_{0.6}Ni_{0.40}/SiO_2$ catalysts following reduction activation. For size distributions, the equivalent nanoparticle diameter d was determined as $d = (4A/\pi)^{1/2}$, wherein A is the projected particle area.*

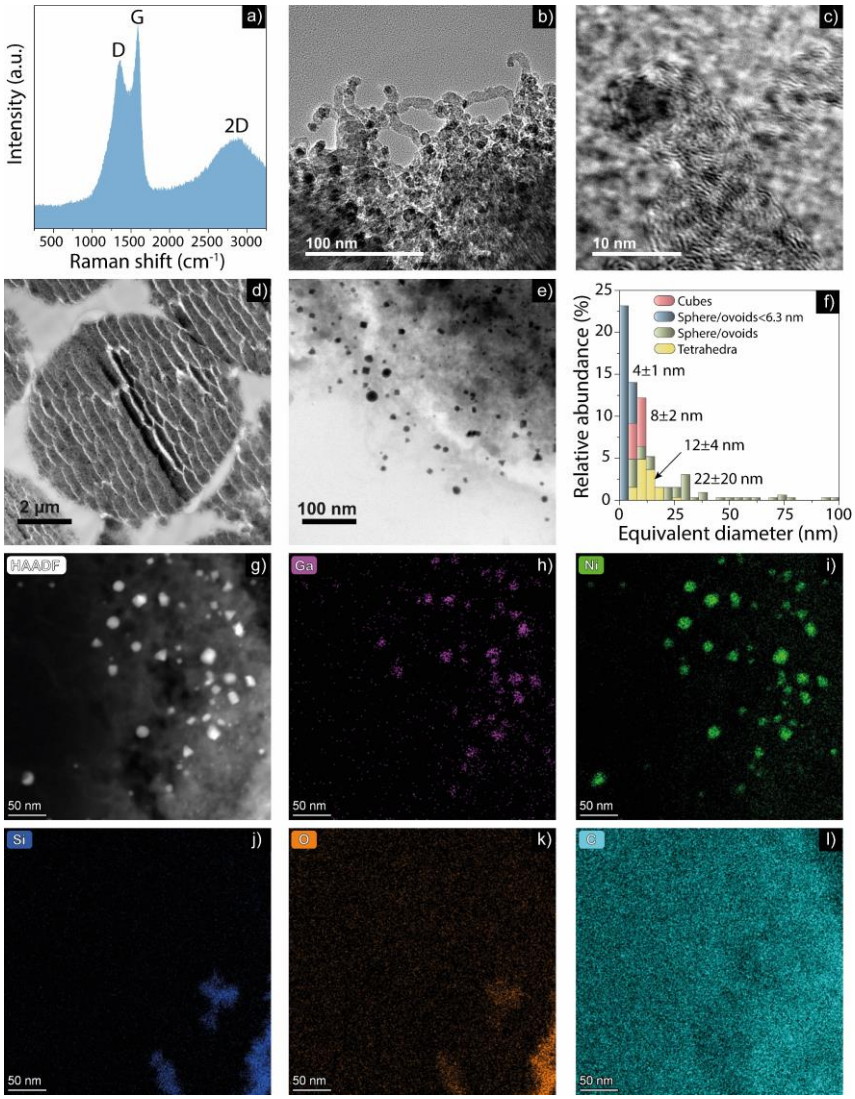

Figure 6.8: *a) Raman spectrum, b-c) (high-resolution) transmission electron micrographs, d,e) cross-sectional TEM micrographs, f) shape-specific metal nanoparticle size distributions, g) HAADF-STEM and h-l) cross-sectional EDS compositional maps for $Ga_{0.05}Ni_{0.95}/SiO_2$ catalyst following exposure to catalysis for 12 h. Reaction conditions: NH_3/methanol (N/C=2), T=773 K, P=2 bar, TOS=12 h. For particle size distributions, the equivalent diameter d was determined as $d = (4A/\pi)^{1/2}$ for spherical/ovoidal particles, $d = (A)^{1/2}$ for cubic-shaped particles, and $d(height) = \left(\sqrt{3}A\right)^{1/2}$ for tetrahedral particles, wherein A is the projected particle area.*

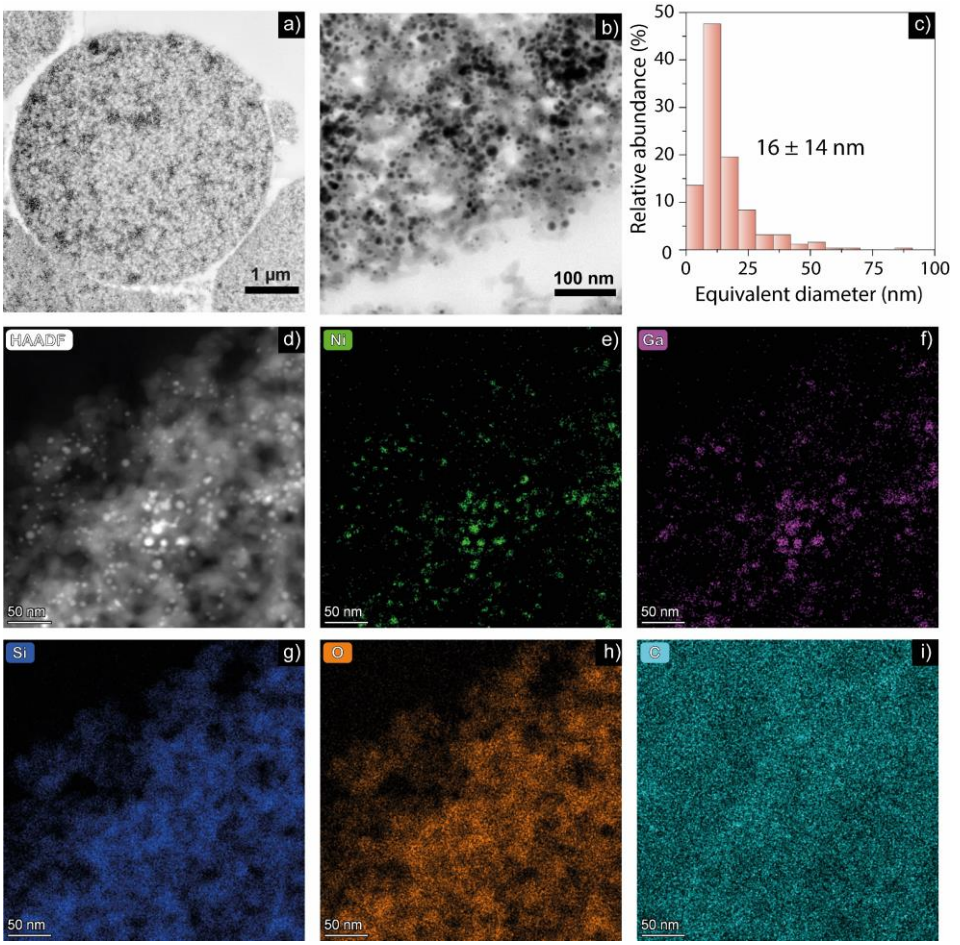

Figure 6.9: *a,b) Cross-sectional TEM micrographs, c) metal nanoparticle size distribution, d) HAADF-STEM and e-i) cross-sectional EDS compositional maps for $Ga_{0.60}Ni_{0.40}/SiO_2$ catalyst following exposure to catalysis for 12 h. Reaction conditions: NH_3/methanol (N/C=2), T=773 K, P=2 bar, TOS=12 h. For the size distribution, the equivalent nanoparticle diameter (d) was determined as $d = (4A/\pi)^{1/2}$, wherein A is the projected particle area.*

On the one hand, these results point to Ga redistribution during catalysis, given that no compositional differences had been observed across nanoparticles on the same catalyst prior to catalysis. On the other hand, these findings suggest that Ga stabilizes specific crystal facets in the bimetallic nanoparticles, driving nanocrystal reconstruction into well-defined shapes.

Similarly, the $Ga_{0.60}Ni_{0.40}/SiO_2$ catalyst was analyzed after reaction. The results are included in **Figure 6.9**. The metal nanoparticle size distribution was notably consistent with that observed prior to catalysis (16± 14 nm), signifying stability against metal sintering under reaction conditions. **Figures 6.9. d-i** present representative HAADF-STEM micrographs and EDS compositional maps. Unlike the case of the alloy catalyst, no signs of metal segregation were discerned in this case, additionally supporting the stability of the intermetallic nanocrystals against metal redistribution.

X-ray photoemission spectroscopy was applied to assess the near-surface composition and metal oxidation states on the two bimetallic catalysts. **Figure 6.10** shows the corresponding spectra at the Ni2p and Ga2p core-levels recorded for $Ga_{0.05}Ni_{0.95}/SiO_2$, which showed marked changes between as-reduced and spent states. The oxidic catalyst precursor showed a near-surface Ga/(Ga+Ni) molar ratio of 0.14, i.e., notably enriched in Ga compared to the bulk catalyst composition, Ga/(Ga+Ni)= 0.05, as determined by ICP-OES. Ni2p and Ga2p spectra corroborated the presence of Ni(II) and Ga(III) species. Following catalyst reduction at 1023 K, the near-surface Ga/(Ni+Ga) molar ratio was determined to be 0.08, in better correspondence with the bulk bimetallic composition, indicative for metal mobilization, from the oxidic precursor, and mixing. The $Ni2p_{3/2}$ BE of 852.6 eV indicated nickel reduction to its zerovalent state. The $Ga2p_{3/2}$ core-level spectrum presented two contributions at 1118.6 eV and 1116.2 eV, which can be ascribed to Ga(III) and Ga(0) in a NiGa alloy, respectively.

The corresponding XPS spectrum recorded *ex situ*, following the catalysis test, corresponded to a near-surface Ga/(Ga+Ni) molar ratio of 0.17, indicating that exposure to reaction conditions re-exposes part of the Ga on the catalyst outer surface. Analysis of the core electron binding energies revealed that the near-surface Ni remained metallic ($Ni2p_{3/2}$ BE of 852.7 eV). Remarkably, it additionally showed that exposure to reaction conditions contributed to the complete reduction of surface Ga species, for which a single spectral contribution at $Ga2p_{3/2}$ BE of 1116.3 eV was detected.

Extending the analysis to the C1s and N1s spectral regions (not shown) revealed near surface C/Ni and N/Ni molar ratios after catalysis of 139 and 8, respectively. These values exceed royally those expected for metal carbide or nitride compounds, proving that the C1s and N1s XPS spectrum was dominated by the N-doped carbon filaments, which deposited on the catalyst surface during catalysis.[23,24]

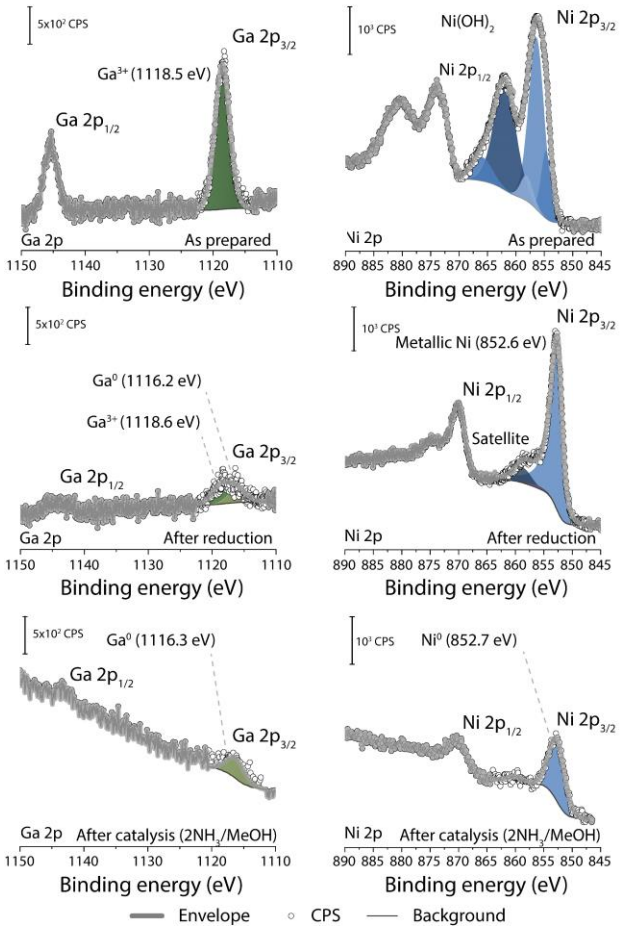

Figure 6.10: *Ni2p and Ga2p core-level spectral regions of the X-ray photoemission spectra for $Ga_{0.05}Ni_{0.95}/SiO_2$ at different stages: top) oxidic catalyst precursor, middle) following in situ reduction and bottom) after exposure to reaction conditions for the synthesis of N-compounds by conversion of a NH_3/methanol feed stream. Reaction conditions: NH_3/methanol (N/C=2), T=773 K, P=2 bar, TOS=12 h.*

6.2.4 *In situ* and *operando* HRXRD and XAS studies

Temperature and time-resolved insights into the dynamic evolution of the crystalline structure of the bimetallic nanocrystals were gained by means of high-resolution X-ray diffraction using synchrotron radiation. The alloy-based $Ga_{0.05}Ni_{0.95}/SiO_2$ and intermetallic-based $Ni_{0.40}Ga_{0.6}/SiO_2$ catalysts were again selected as representative for the two distinct solid solution structures and catalytic performance. The monometallic Ni/SiO_2 was also studied for reference purposes. In addition, the bulk average oxidation state and local coordination configuration of Ni and Ga atoms were studied by XAS. In this case, spectra were collected at 323 K, i.e., after *in situ* cooling the sample when previously treated at higher temperatures, in order to avoid excessive contributions from thermal disorder to the XAS spectra.

6.2.4.1 Structure of the Ni-based catalysts after in situ reduction

Figure 6.11 shows the temperature-resolved evolution of the XRD pattern for the three studied catalysts during their reduction under flow of 20 vol% H_2/He up to a temperature of 1023 K. Both Ni/SiO_2 and $Ga_{0.05}Ni_{0.95}/SiO_2$ samples evolved from a NiO cubic crystal structure to a metallic *fcc* Ni (*Fm-3m*) structure, which prevailed at temperatures above 640 K, consistent with the H_2-TPR profiles (see **section 6.2.1**). A lattice thermal expansion led to a displacement of the diffraction peaks to lower 2θ values compared to the reference *Fm-3m* diffractograms. Rietveld refinement in the range of 23-33° 2θ revealed cell parameters after catalyst reduction of 3.5261(1) Å and 3.5406(1) Å for Ni/SiO_2 and $Ga_{0.05}Ni_{0.95}/SiO_2$, respectively, consistent with the lattice expansion expected upon Ga incorporation into the metallic Ni lattice. For the *in situ* reduced catalysts, the diffraction peak intensities showed a mismatch with respect to those in diffractograms included in crystallographic databases for bulk metals. This effect has been observed in previous laboratory XRD analysis on supported metal catalysts, and it thus appears to be intrinsic to the supported catalyst samples, presumably due to anisotropic preferential crystallite growth in the confined space of the mesopores of the SiO_2 carrier.

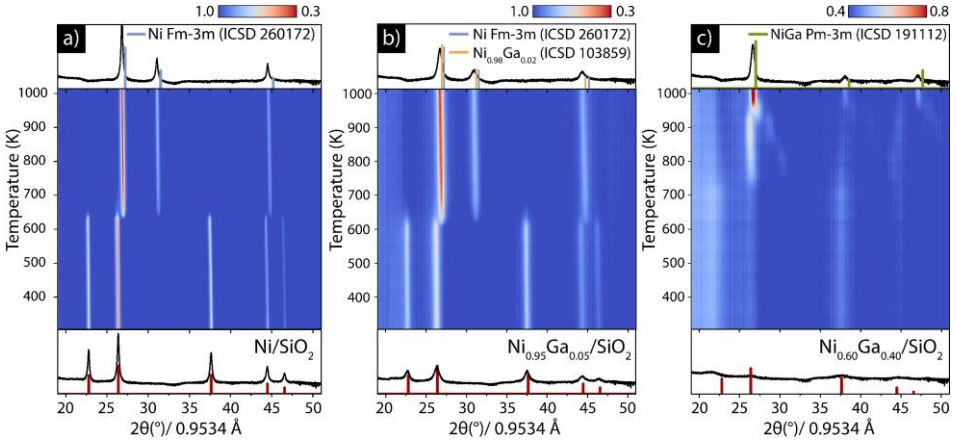

Figure 6.11: *In situ temperature-resolved high-resolution X-ray diffraction patterns (λ=0.9534 nm) recorded for a) Ni/SiO_2, b) $Ga_{0.05}Ni_{0.95}/SiO_2$ and c) $Ni_{0.4}Ga_{0.6}/SiO_2$ under exposure to 20* vol% *H_2/He reduction gas mixture. Initial and final diffractograms are shown at the bottom and top sides of the contour plot, respectively.*

Distinctly, for $Ga_{0.6}Ni_{0.4}/SiO_2$ diffraction lines indexable to the β-phase NiGa intermetallic compound (*Pm-3m)* emerged at temperatures above 923 K (**Figure 6.11 c**). However, following *in situ* cooling to 323 K, the diffractogram showed remarkably wider signals, which could be indexable to different intermetallics, i.e., NiGa (*Pm-3m)*, Ni_2Ga_3 (*P3-m1*) and/or $Ni_{13}Ga_9$ (*C2/m*), see **section 6.2.4.4** below. This is in contrast with the previous results, shown in **Figure 6.2 c** and discussed earlier in **section 6.2.1**, wherein better defined diffractions for Ni_2Ga_3 (*P3-m1*) has been observed following reduction, free convection cooling and *ex situ*, lab-based XRD analysis. The reasons behind this discrepancy remain unclear. However, it is posited that different cooling rates after *in situ* catalyst reduction, i.e., uncontrolled in the case of free convection cooling preceding *ex situ* XRD experiments in the lab (**Figure 6.2 c**), and fixed at a cooling rate of -10 K min^{-1} when applying the hot air blower in those *in situ* HRXRD experiments performed in a capillary flow cell with synchrotron radiation (**Figure 6.11 c**), could have affected recrystallization processes, at play during sample cooling.

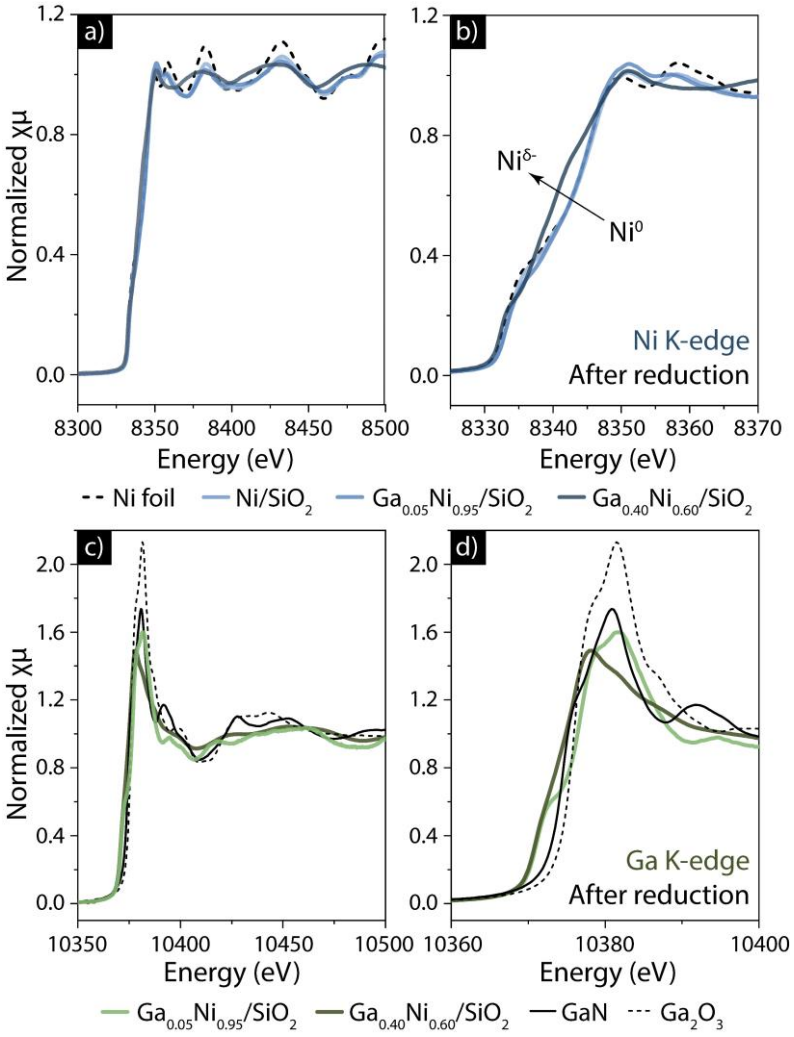

Figure 6.12: *Normalized XANES spectra for selected GaNi/SiO_2 catalysts and the monometallic Ni/SiO_2 catalyst, following in situ reduction under flow of 20 vol% H_2/He, recorded at the a,b) Ni-k and c,d) Ga-k absorption edges. Spectra for reference materials, i.e., metallic Ni foil, GaN and Ga_2O_3 have also been included for comparison. Panels b and d show blown-up views at the absorption edge.*

Analysis of the XANES region of the XAS spectra, recorded at the Ni-k and Ga-k absorption edges, provided information on the average metal oxidation states for the *in situ* reduced catalysts.

As shown in **Figure 6.12** the energy position of the Ni-k edge for the three studied catalysts was in agreement with the standard metallic Ni foil, indicating full reduction of nickel to zerovalent state. A second edge feature appeared shifted to lower energies in the case of $Ga_{0.4}Ni_{0.6}/SiO_2$ (**Figure 6.12. a,b**) unlike for counterpart catalysts with lower or no Ga content. Similar features have been observed previously and ascribed to an electron transfer from Ga to Ni in NiGa alloys ($Ga^{\delta+}Ni^{\delta-}$). This interpretation is supported by the apparency of this effect for the catalyst with the intermetallic nanostructure and the highest Ga content.[11,25] The XANES spectra recorded at the Ga-k absorption edge were analyzed in comparison to those in reference Ga compounds, i.e., Ga_2O_3 and GaN (**Figure 6.12. c,d**). Metallic Ga(0) was not included as reference given that it is liquid at ambient conditions. Upon catalyst reduction, the first edge feature shifted for both bimetallic catalysts to lower energies compared to GaN and Ga_2O_3 references, indicating gallium reduction, in line with XPS results (*vide supra*). A second edge contribution was observed in both cases at higher energies for the incident photons, in line with earlier results for GaNi bimetallics.[11,26] The white line shape was noticeably different for both catalysts, supporting significant differences in the direct coordination environment for Ga atoms in alloy ($Ga_{0.05}Ni_{0.95}/SiO_2$) and intermetallic ($Ga_{0.6}Ni_{0.4}/SiO_2$) solid solutions.

6.2.4.2 In situ and operando XRD/XAS studies on Ni/SiO_2

First, the structural dynamics of the monometallic Ni/SiO_2 catalyst was investigated by HRXRD during its exposure to catalysis conditions. As described in **section 3.2.7.4** (**Chapter 3**), mass spectrometry was applied to track catalytic performance simultaneously to the collection of XRD data. The results are gathered in **Figure 6.13**. As discussed previously for the *in situ* catalyst reduction step, the Ni *fcc* structure expanded upon increasing temperature causing a shift of all diffraction signals to lower 2θ angles. At temperatures above 450 K, diffractions corresponding to *fcc* Ni progressively lost intensity, and a different crystal system emerged. The new diffraction pattern resembled that of a cubic system, however, with split high-index diffractions, e.g., [200], [220] and [311], at high 2θ angles. To the best of our knowledge, this structure has not been observed

previously in literature. If the phase transition does not imply the reconstruction of the crystal, the original and the final unit cells may be related, e.g., through second-order transitions involving a symmetry change via lattice displacements.[27] This type of transitions give rise to a new, though closely related crystal system which, therefore, shows also a closely related diffraction pattern. In particular, the transformation of a cubic system into a crystal system with lower symmetry shall generate splits in the diffraction peaks. The simplest possible transition is the enlargement of the unit cell through one crystallographic direction, i.e., a≠b, leading to a tetragonal system.[27] This is consistent with the results observed experimentally in the present *operando* HRXRD experiment. Besides, indexing the emerging X-ray diffraction pattern suggested Bravais lattices corresponding to a tetragonal system. Tetragonal nitride compounds have been reported earlier for copper, e.g., $Cu_2N_{0.67}$ and $Cu_{3.6}N_{1.2}$ (*I4/mmm, ICSD* 167848 and *P4/mmm*, ICSD 167843).[28,29] Therefore, hypothetical nickel carbide/nitride compounds with *I4/mmm* and *P4/mmm* space groups were refined. Rietveld refinements revealed a good agreement of the hypothetical *I4/mmm* tetragonal structure with the experimental data. While unconventional high-pressure (ca. 12 GPa) synthesis conditions have been reported to realize the development of *I4/mmm* Cu_2N from Cu_3N (*Pm-3m*) precursors,[30] it is speculated that unconventional reaction conditions studied herein, for pore-confined metal nanocrystals, may be capable to drive such transformation at temperatures around 473-573 K. Nevertheless, the temperature-resolved HRXRD experimental results showed this particular structure to be transient and not connected to any significant catalytic activity for the formation of N-compounds, hence likely catalytically irrelevant.

At temperatures above 533 K, diffractions corresponding to a hexagonal *P6$_3$22* symmetry group, characteristic for Ni_3N, appeared. This was followed by the evolution of a trigonal *R-3c* phase, characteristic of the metastable Ni_3C, at slightly higher temperatures (573 K). The latter compound shows a (*R-3c*) symmetry due to the ordered super-lattice generated by formally incorporating carbon atoms into 1/3 of the octahedral interstitial sites of the *hcp* allotrope of metallic nickel. A drastic increment in the *a* cell parameter, corresponding to an expansion $a\text{-}a_0$~0.08 Å, relative to the a_0 parameter for Ni *fcc* at 328 K, was also

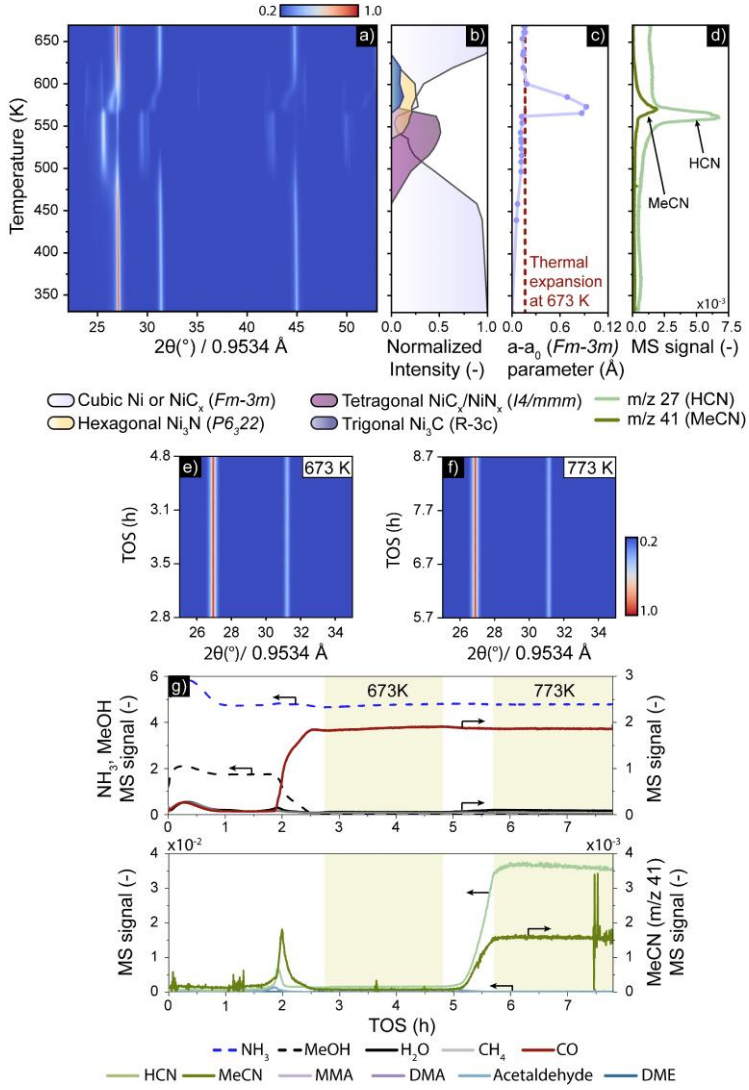

Figure 6.13: *a) Temperature-resolved high-resolution X-ray diffraction patterns (λ=0.9534 Å), b) evolution of the XRD diffraction peak intensities, normalized to the initial fcc metallic Ni, c) evolution of the a cell expansion parameter, relative to that detected for fcc Ni at RT, and d) evolution of the intensity of selected m/z mass spectrometry signals during an operando HRXRD experiment with Ni/SiO_2, under exposure of the NH_3/methanol reaction flow from RT to 673 K. e) Time-resolved high-resolution X-ray diffraction patterns during isothermal reaction stages at 673 K and f) 773 K. g) Evolution of the intensity of selected m/z mass spectrometry signals during the entire operando HRXRD experiment with Ni/SiO_2, including heating ramps and isothermal stages.*

observed at temperatures between 565-590 K, **Figure 6.13, c**. This effect has been ascribed to the incorporation of carbon and/or nitrogen atoms into octahedral interstitial positions of the *fcc* metal system, forming *fcc* carbides/nitrides.[31–33] Moreover, these phase transformations were paralleled by an increase of the m/z 27 and m/z 41 mass spectrometry signals at the outlet stream, which are ascribed to HCN and acetonitrile compounds. Maximum acetonitrile production was registered after the maximum HCN production, and coincided with the highest lattice displacement for the cubic nickel carbide/nitride structure, suggesting the involvement of the latter as an active catalyst for C-C chain propagation.

At temperatures above 590 K, the expanded cubic lattice underwent decomposition into Ni *fcc*, an structural effect which was accompanied by the loss of activity towards nitrile formation. The resulting Ni *fcc* structure remained unchanged during the isothermal treatment at 673 K, with a constant displacement a-a_0 of 0.016 Å, ascribed entirely to thermal expansion, see **Figure 6.13 e**.

As shown in **Figure 6.13. g**, MS signals associated to nitriles increased with increasing the reaction temperature from 673 to 773 K to then remain stable at a constant temperature of 773 K. At the latter temperature, the Ni lattice expansion detected by HRXRD became slightly higher than that corresponding to solely to thermal expansion under the hydrogen atmosphere applied during reductive activation, i.e., a-a_0= 0.026 vs 0.022 Å. This lattice expansion suggests the insertion of interstitial atoms (C, N) within the metal structure in its most nitrile-productive state.

Finally, cooling the catalyst to room temperature resulted in significant structural transformations. Very broad diffraction signals were detected for the *spent* catalyst at RT, which precluded proper structural refinement and phase quantification. Diffractions, which we ascribe to the hexagonal closed packed (*hcp*) Ni allotrope emerged, suggesting the exsolution of interstitial atoms. However, given the close structural similarity with *hcp*-Ni_3C, the presence of the latter interstitial compound cannot be discarded.[34] On the one hand, these results are in line with the stabilization of *hcp* allotropes in 3d transition metal nanocrystals upon decomposition of the structurally related metal carbide precursors.[35,36] On

the other hand, the results underscore the need for *operando* studies, as the structure of the catalyst after *in situ* cooling down to RT departs significantly from that detected under catalysis conditions.

6.2.4.3 In situ and operando XRD/XAS studies on $Ga_{0.05}Ni_{0.95}/SiO_2$

6.2.4.3.1 Operando XRD studies on $Ga_{0.05}Ni_{0.95}/SiO_2$

The structural dynamics of the $Ga_{0.05}Ni_{0.95}/SiO_2$ bimetallic catalyst was also investigated with *operando* HRXRD. The results are summarized in **Figure 6.14. a**. Following *in situ* catalyst reduction, an *a* cell parameter of 3.5418(1) Å was determined through Rietveld refinement for the *fcc* bimetallic GaNi nanocrystals, which corresponded to a lattice expansion parameter $a\text{-}a_0$ of 0.015 Å at 673 K relative to RT. This is approximately a twofold greater lattice expansion compared to that detected in the monometallic Ni/SiO_2 catalyst.

As shown in **Figure 6.14. b**, under flow of the reactive NH_3/methanol mixture, the expansion of the *fcc* metal lattice set in at ca. 475 K. This was paralleled by the detection of nitrile products at the microreactor's outlet (**Figure 6.14. c**). The widest crystal lattice was detected at ca. 613 K, corresponding to an expansion parameter $a\text{-}a_0$= 0.194 Å, in correspondence with the maximum concentration of HCN at the outlet gases.

Above 623 K, as well as during the isothermal stage at 673 K, the *a* cell parameter for the lattice-expanded *fcc* GaNi alloy stabilized at $a\text{-}a_0$=0.094 Å and remained constant for the entire dwell time at 637 K. Moreover, a second Ni_3C (*R-3c*) phase progressively developed with time (**Figure 6.15.a**)**. Figure 6.15. a** shows the Rietveld refinement results for the XRD patterns recorded right after reaching the reaction temperature of 673 K, as well as after the 2 hours isothermal stage at this temperature. As discussed earlier in **section 6.2.2**, this isothermal dwell step at 673 K corresponds to a catalyst activation pretreatment under the reactive atmosphere. The development of the additional phase was evident and a good agreement was found with Ni_3C (*R-3c, a*=*b*= 4.582, c= 13.03, α=β= 90, γ= 120). As shown in **Figure 6.15. d** the m/z=41 MS signal, associated to acetonitrile, experienced an increase during the 2 hour duration of this treatment,

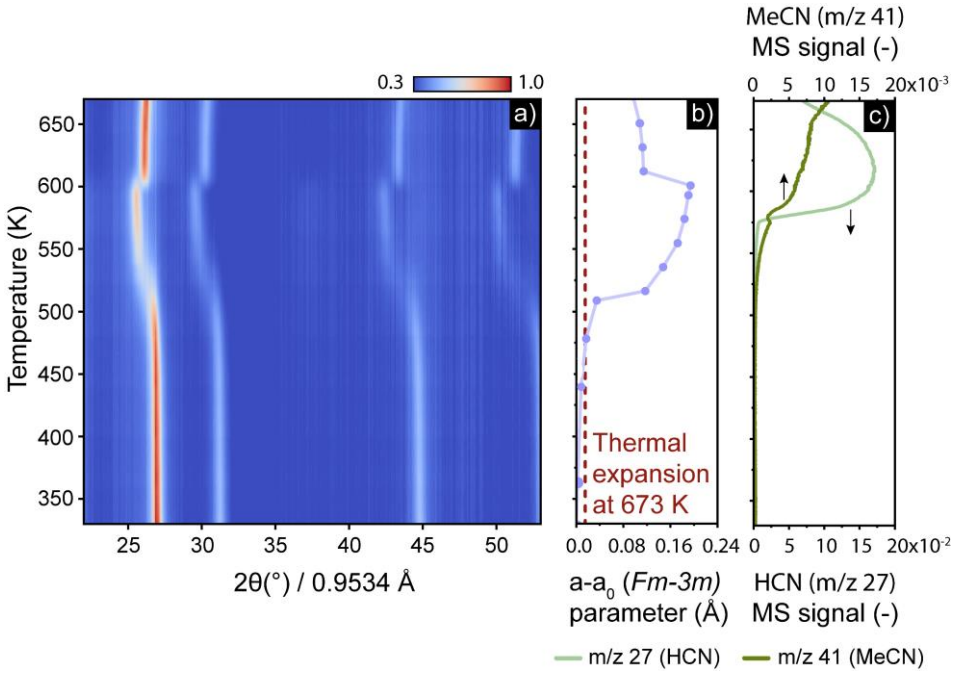

Figure 6.14: *a) Temperature-resolved high-resolution X-ray diffraction patterns (λ=0.9534 Å), b) evolution of the a cell expansion parameter, relative to that detected for fcc Ni at RT, and c) evolution of the intensity of selected m/z mass spectrometry signals at the outlet gases during an operando HRXRD experiment with* $Ga_{0.05}Ni_{0.95}/SiO_2$, *under exposure of the* NH_3*/methanol reaction flow from RT to 673 K.*

while that used to track HCN decreased, suggesting the engagement of the latter in C-C coupling steps.

Increasing the temperature further to 773 K led to a displacement of all diffraction signals to higher 2θ values, hinting at a lattice contraction compared to its more expanded structure at 673 K. This observation is suggestive of the ex-solution of interstitial carbon and its ejection onto the crystallites' surface, in agreement with the microscopy observation of the deposition of abundant graphitic carbon on the catalyst surface.

Rietveld refinement evidenced that new *fcc* NiGa lattice showed a lower cell expansion coefficient of $a\text{-}a_0$=0.034 Å, relative to its RT state, which further

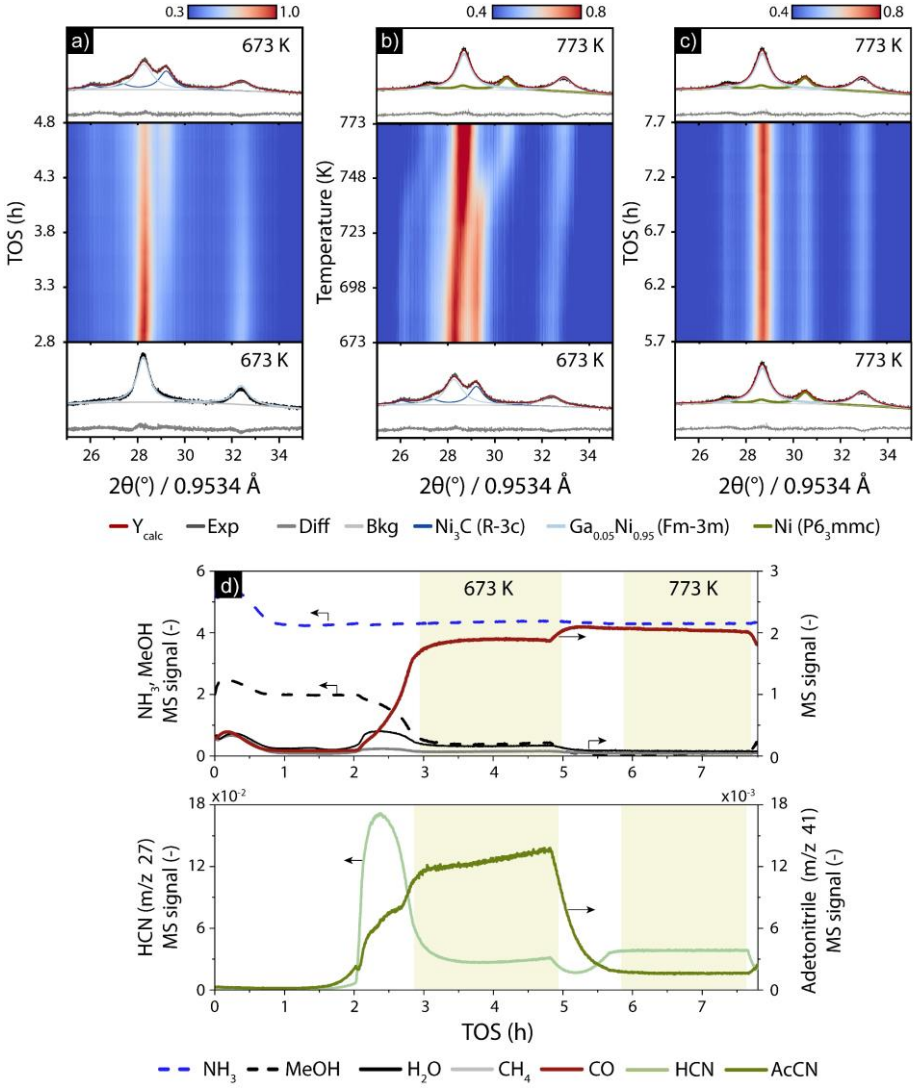

Figure 6.15: *a) Operando time-resolved X-ray diffraction patterns (λ=0.9534 nm) collected a) during an isothermal stage at 673 K, b) during the heating from 673 K to 773 K and, c) during an isothermal stage at 773 K during the exposure of the $Ga_{0.05}Ni_{0.95}/SiO_2$ catalyst to flow of the NH_3/methanol (N/C=2) reaction mixture. P=P_{atm}. g) Time-and temperature-resolved evolution of selected m/z mass spectrometry signals at the outlet gases during the entire operando HRXRD experiment.*

decreased with exposure time at 773 K, down to 0.029 Å. The latter lattice expansion was only slightly larger than that ascribed to thermal effects at this temperature (a-a_0 =0.020 Å). Moreover, the resulting a cell parameter (a=3.5704(2) Å) resembled the largest a cell parameter observed for the monometallic Ni/SiO_2 catalyst (a= 3.6137(4) Å) at a temperature of ca. 573 K, at which it showed some activity towards nitrile formation.

Simultaneously, the temperature rise produced a displacement of the diffraction signals associated to the hexagonal Ni_3C phase to lower angles, of 0.8° 2θ for the main [111] peak. Upon exsolution of interstitial carbon from Ni_3C, the stabilization of the *hcp* Ni (*P6$_3$mmc*) allotrope may be expected. Rietveld refinement revealed a strained Ni *hcp* structure with cell parameters a=b= 2.5285(6), c= 4.136(2), compared to a=b=2.622, c=4.321 reported in literature for this metallic Ni phase in bulk form and at RT. Earlier studies on the formation of *hcp* Ni by the thermal treatment of *fcc* Ni revealed a similar XRD pattern (λ= 1.54 Å) at temperatures ranging from 723 to 873 K. However, the resulting diffraction signals were not attributed to any particular crystalline phase.[37] Z. J. Huba and E. E. Carpenter also observed an analogous XRD pattern (λ= 1.54 Å) at 773 K, during the thermal decomposition of a nickel succinate precursor. These authors ascribed the evolving diffraction signals to *hcp* Ni, wherein the main diffraction peak was registered at ~47° 2θ compared to 45.07° in the literature reference pattern for *hcp* Ni, at RT.[38] The online MS spectra of the outlet gas stream showed a decrease in the acetonitrile concentration at 773 K, consistent with the catalysis tests discussed in **section 6.2.2** (*vide supra*), which showed a notably lower nitrile chain propagation at 773 K compared to 673 K.

After the 2-hour dwell at 773 K, the temperature at the catalyst bed was reduced back to RT. Rietveld refinement analysis of the final XRD at room temperature fitted well with a combination of *hcp* and *fcc* phases. Regarding the former, the results from structural refinement, using restricted cell parameters, was coherent with the *hcp* Ni structure reported in the literature (ICSD 76668), reinforcing the identification of this Ni allotrope from the *operando* XRD patterns recorded at 773 K. Regarding the *fcc* structure at RT, it showed a cell parameter

of 3.6823(3) Å with a lattice expansion parameter a-a_0 of 0.141 Å, suggesting the stabilization of interstitial light elements within the structure.

Additionally, **Appendix VI** shows the results of the Periodic DFT calculations performed at the PAW-RPBE-D3 level of theory, to assess the thermodynamic implications on the Ga doping of the metal carbides/nitrides with the cubic Ni (*Fm-3m*) and the *Ni_3C (R-3c)* crystal structures.

All taken together, the *operando* HRXRD results suggest that, once exposed to reaction conditions, the bimetallic nanocrystals take carbon/nitrogen up, stabilizing a slightly expanded *fcc* metal structure and the hexagonal *Ni_3C* carbide at temperatures of 673 K. A significant part of the interstitial carbon/nitrogen is expelled out of the structure at a higher temperature of 773 K, leading to a mixture of *hcp* and *fcc* metallic crystallites with lower interstitial carbon/nitrogen content. The mixed catalyst microstructure is in correspondence to the variability of metal nanocrystal shapes ascertained with electron microscopy for this catalyst, following its exposure to process conditions for 12 h, see **section 6.2.2**, vide supra.

Simultaneous monitoring of the catalytic performance showed that C-N coupling, as evidenced by the detection of HCN, occurs in combination with a comparatively wide range of expanded metal structures. However, the stabilization of the metal carbide appears to be key to attain C-C coupling activity to C_{2+} nitriles. Relative to the monometallic Ni/SiO_2 catalyst, Ga doping contributes to the stabilization of metal carbide/nitride phases in the catalysis relevant operational window.

6.2.4.3.2 *In situ* XAS studies on $Ga_{0.05}Ni_{0.95}/SiO_2$

The electronic properties and local coordination configuration of Ni and Ga atoms in the $Ga_{0.05}Ni_{0.95}/SiO_2$ catalyst was additionally assessed with *in situ* XAS. The spectra were recorded at RT, both following *in situ* catalyst reduction and exposure to catalysis conditions at 773 K (**Figure 6.16**).

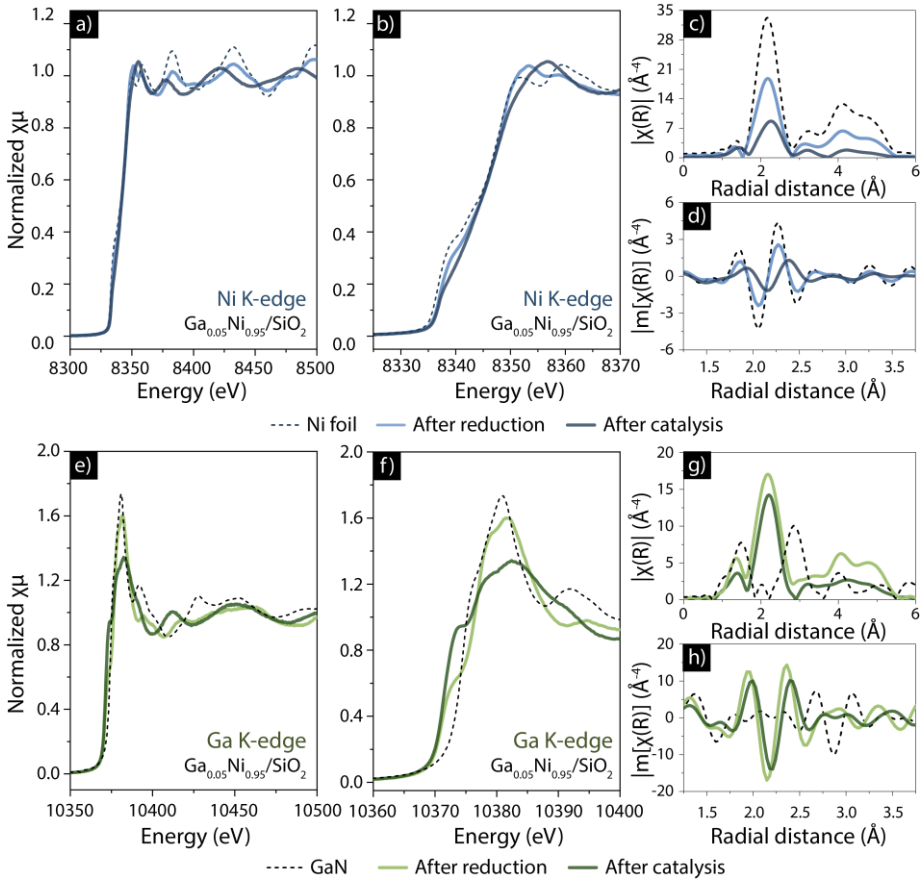

Figure 6.16: *a-b, e-f) Normalized XANES spectra, c, g) Fourier-Transform of the k^3-weighted EXAFS function (phase uncorrected) and d, h) Imaginary part of the Fourier-Transform of the k^3-weighted EXAFS function at Ni-k (a-d) and Ga-k (e-h) absorption edges, respectively, for $Ga_{0.05}Ni_{0.95}/SiO_2$ after in situ reduction and following subsequent exposure to catalysis conditions at 773 K. Spectra collected in all cases at room temperature, following the corresponding treatment in the capillary XAS/XRD cell.*

The spectra recorded at the Ni-k absorption edge presented a first edge contribution which resembled that in the Ni foil reference. A second edge feature shifted to higher energies, particularly after catalysis, resembling the absorption spectrum observed by X. D. Han and coworkers for nickel carbides.[39]

Regarding the spectra at the Ga-k edge (see **Figure 6.16. e,f**), the edge energy was lower (by 3 eV) compared to that in GaN, indicating the presence of metallic Ga. This shift was more marked after exposure to reaction conditions, indicating that the extent of Ga reduction increases following exposure to reaction conditions, in line with XPS results discussed in **section 6.2.3**.

Figure 6.16. c-d and **g-h** show the k^3-weighted EXAFS function (no phase correction), at the Ni-k and Ga-k absorption edges, respectively. The amplitude of the FT-EXAFS function at both edges damped after catalysis, suggesting a reduction in the average coordination number for both metals. This may be associated to the segregation of small metal clusters out of the larger nanocrystals under reaction conditions, or an increase in the density of structural defects in the latter.

6.2.4.3.3 Structural dynamics of $Ga_{0.05}Ni_{0.95}$ /SiO_2 upon selected reactant removal

In a different set of *operando* XRD experiments, the response of the catalyst microstructure to the removal of either the C_1 (methanol) or N_1 (ammonia) reactants from the gas feed stream was studied.

The first experiment involved the removal of NH_3 from the feed and it was performed using synchrotron radiation (λ= 0.9534 Å), under the same settings as the *operando* HRXRD experiments discussed in the preceding section. Following *in situ* reduction, the NH_3/methanol feed stream was admitted into the capillary cell, and the reaction was performed at 673 K. As observed earlier, those diffractions associated to the *fcc* NiGa metal nanocrystals shifted to lower 2θ angles, indicating the lattice expansion by incorporation of interstitial C/N. After one hour under process conditions, the hexagonal Ni_3C emerged, to attain the mixed phase microstructure characteristic of this catalyst under reaction

conditions. Simultaneously, online mass spectrometry showed evidence for the formation of nitrile products. Next, the flow of NH_3 was ceased, whereas that of methanol remained unchanged. The removal of the nitrogen chemical potential from the surrounding gas atmosphere rapidly led to a structural reorganization. Diffractions corresponding to the *fcc* GaNi alloy shifted to higher angles, indicating a unit cell contraction, while those ascribed to the Ni_3C phase vanished completely after one hour in the absence of ammonia. Concomitantly, mass spectrometry detected increased concentrations of carbon monoxide, dimethyl ether and acetaldehyde in the reaction products.

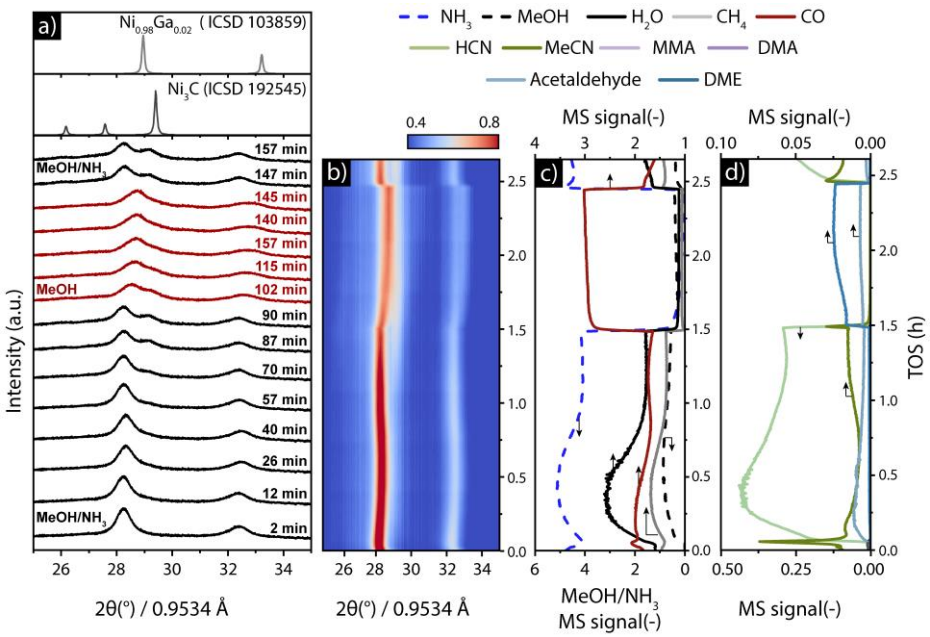

Figure 6.17: *a) Operando, time-resolved evolution of the X-ray diffraction patterns (λ= 0.9534 Å) during the exposure of the $Ga_{0.05}Ni_{0.95}/SiO_2$ catalyst to reaction conditions for the conversion of a NH_3/methanol (N/C=2) feed stream at P=1 bar, and T= 673 K. Black traces represent the catalyst under the flow of the complete NH_3/methanol feed stream, while red traces correspond to reaction conditions wherein the ammonia flow was temporarily halted. Simulated XRD patterns for Ni_3C and $Ni_{0.98}Ga_{0.02}$ alloy are shown as reference on top. b) Contour plot collection of operando XRD patterns and (c,d) time evolution of selected mass spectrometry traces for outlet gases.*

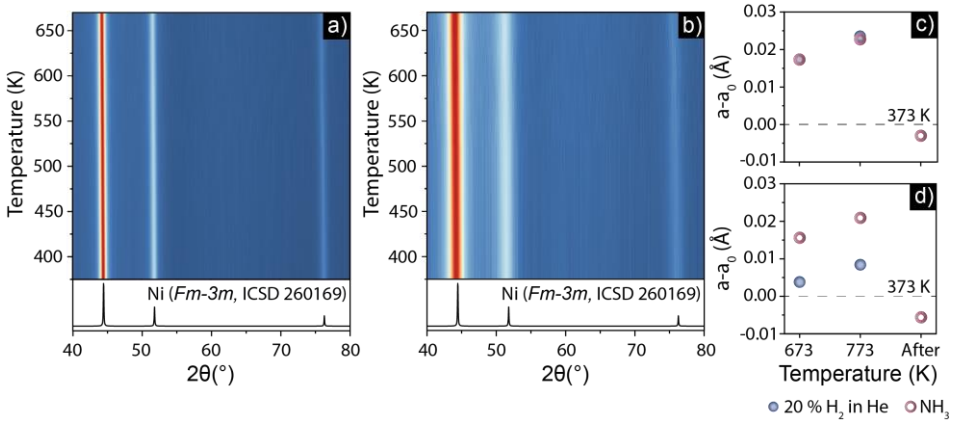

Figure 6.18: *Operando, temperature-resolved evolution of the X-ray diffraction pattern (λ=1.54 Å) for a) Ni/SiO_2 and b) $Ga_{0.05}Ni_{0.95}/SiO_2$ under flow of NH_3. P=1 bar. c,d) Evolution of the cell parameter a with temperature for c) Ni/SiO_2, and d) $Ga_{0.05}Ni_{0.95}/SiO_2$ under reaction conditions, relative to the a_0 reference cell parameter determined at 373 K after in situ catalyst reduction, i.e., a_0=3.5281(3)Å and a_0=3.5451(3)Å for Ni/SiO_2, and d) $Ga_{0.05}Ni_{0.95}/SiO_2$, respectively.*

Interestingly, resuming the flow of NH_3 in the feed, restored a XRD diffractogram closely resembling the one prior to NH_3 removal, underscoring that the system shows substantial and (partially) reversible structural dynamism in response to changes in the direct gas chemical environment.

The second experiment involved the removal of methanol from the feed stream, and it was performed in a laboratory XRD instrument (λ= 1.54 Å) mounting a high-temperature cell (as described in **section 3.2.5.2** of **Chapter 3**), due to the lack of additional synchrotron beamtime. The Ni/SiO_2 catalyst was also examined for reference purposes. The results are summarized in **Figure 6.18**. The a_0 cell parameter, taken as a reference for lattice expansions/contractions, was considered as that determined at the onset of the catalysis experiment, at 373 K. The *fcc* GaNi alloy structure was the only crystal structure detected during the entire reaction for both monometallic and bimetallic catalysts. The crystal structure of the monometallic nickel catalyst underwent a diffraction peak shift to lower 2θ angles, ascribed to thermal expansion effects (**Figure 6.18. b**), while a slightly higher lattice expansion than the thermal contribution was observed in the case

of the bimetallic $Ga_{0.05}Ni_{0.95}/SiO_2$ (**Figure 6.18. d**). However, this unit cell expansion was minor compared to that underwent in contact with the complete NH_3/methanol (N/C=2) feed stream. Moreover, unlike under the flow of both ammonia and methanol, no further crystal structure developments were observed, neither at 673 K nor at 773 K, even for more extended times on-stream.

Considered together, the above results suggest that simultaneous contact with both NH_3 and CH_3OH reactants is a requisite for the stabilization of the expanded GaNi alloy and metal carbide crystal structures developed during reaction. Besides, the presence of Ga contributes to the stabilization of metal carbides/nitrides structures at reaction temperatures, which appear to be responsible for nitrile synthesis.

6.2.4.4 In situ and operando XRD/XAS studies on $Ga_{0.60}Ni_{0.40}/SiO_2$

6.2.4.4.1 Operando XRD studies on $Ga_{0.60}Ni_{0.40}/SiO_2$

Finally, the structural dynamics of the $Ga_{0.60}Ni_{0.40}/SiO_2$ bimetallic catalyst was investigated with *operando* HRXRD. The results are summarized in **Figure 6.19**. Following *in situ* reduction, this catalyst showed an XRD pattern with notably lower signal-to-noise ratio compared to the previously studied neat Ni and low-Ga content GaNi bimetallic catalysts. Indeed, only a single and comparatively broad diffraction was registered with sufficient accuracy, peaking at 2θ=27°. The limited quality of the diffractogram hinted at a high density of structural defects and/or a lower crystalline domain size for metal species in this catalyst. This has limited the degree of certainty with which crystalline phases could be identified. After reduction, i.e., prior to exposure to the reactive gas mixture, the diffractogram could be assigned to a mixture of different intermetallic compounds, namely NiGa (*Pm-3m*), $Ni_{13}Ga_9$ (*C2/m*) and Ni_2Ga_3 (*P3m1*). Unlike for previously studied catalysts, exposure to reaction conditions did not result in very significant modifications of the diffraction pattern, excluding a severe structural reorganization in this case. The main diffraction peak became narrower upon increasing the reaction temperature, possibly as a result of one specific intermetallic structure becoming dominant, an increase in the average crystalline

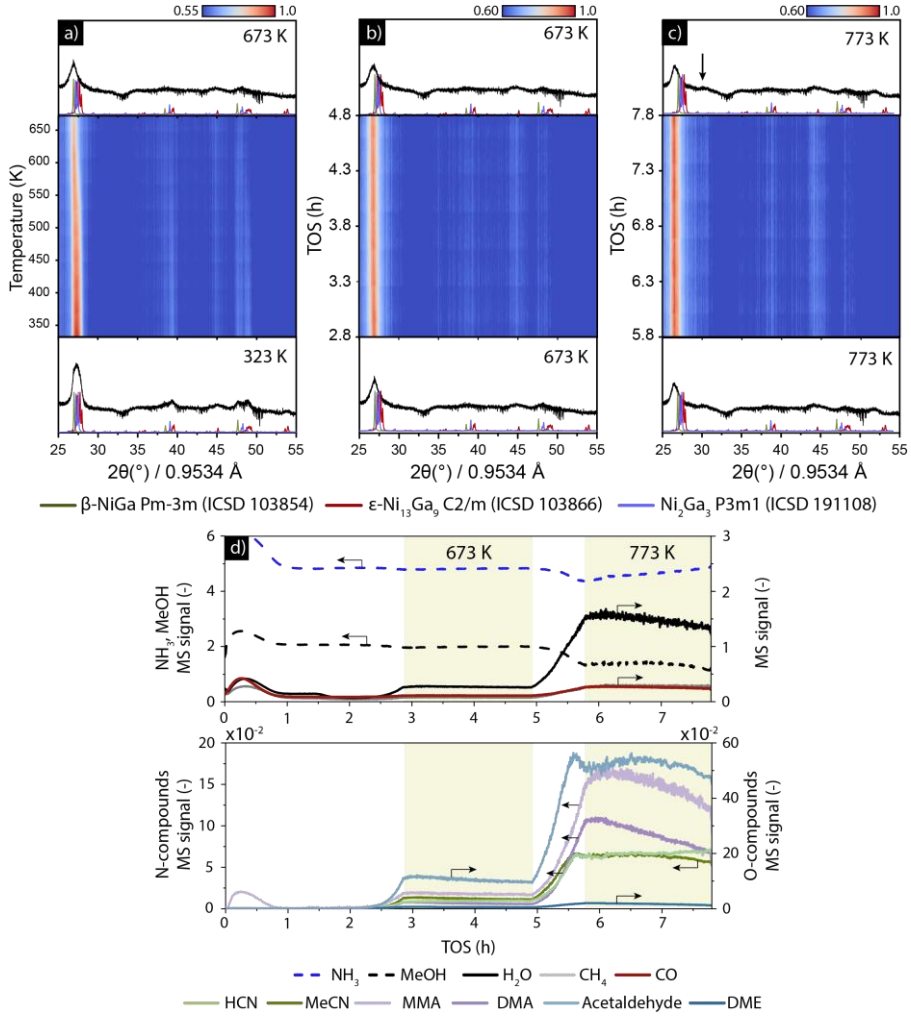

Figure 6.19: *Operando temperature-resolved X-ray diffraction patterns (λ=0.9534 Å) recorded for the bimetallic $Ga_{0.60}Ni_{0.40}/SiO_2$ catalyst a) during the heating ramp from 323 K to 673 K, b) during the 2-hour isothermal step at 673 K, and c) during the 2-hour isothermal step at 773 K, under flow of the reaction NH_3/methanol feed stream (N/C=2), at P=1 bar. On panel c, the arrow indicates an incipient diffraction signal which developed slowly with time-on-stream. d) Time- and temperature-resolved evolution of selected mass spectrometry traces for outlet gases. The plot on the top shows m/z signals used to follow the production of NH_3, MeOH, H_2O and CH_4 and CO, while the plot at the bottom shows the m/z signals used to follow the production of nitriles (C_1 and C_2), mono, di- and tri-methylamine (MMA, DMA, TMA, respectively), acetaldehyde and dimethyl ether (DME).*

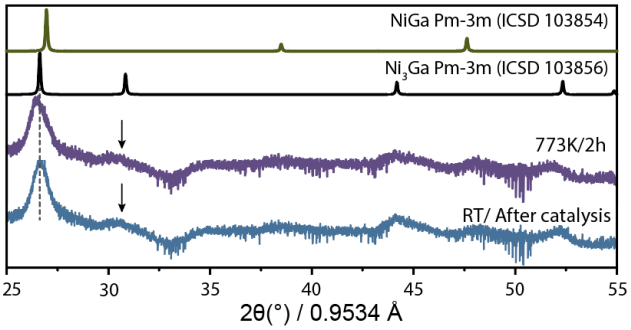

Figure 6.20: *X-ray diffraction patterns (λ=0.9534 Å) recorded for the bimetallic $Ga_{0.60}Ni_{0.4}/SiO_2$ catalyst after 2 h on-stream under reaction conditions at 773 K and after subsequent cooling to RT (NH_3/methanol feed (N/C=2), P=1 bar). The arrow indicates an incipient diffraction signal which developed slowly with time-on-stream at 773 K. Simulated diffraction patterns for NiGa and Ni_3Ga intermetallic compounds have been added for reference.*

domain size or a combination of both effects. Besides, the diffraction peak shifted to lower 2θ angles and progressively decreased in intensity on increasing the reaction temperature above 450 K, which further complicated a reliable identification of the intermetallic compound prevailing under working conditions. At 773 K, an additional, remarkably broad diffraction signal emerged incipiently at 31° 2θ and it slowly grew with time on-stream, indicating the development of an additional compound. While this signal is too broad to attempt its indexing, it could be tentatively ascribed to Ni_3Ga (*Pm-3m*).

Analysis of the temperature and time-resolved mass spectrometry profile for the outlet gases showed that high amounts of water were produced at the highest reaction temperature, 773 K, while significantly lower CO concentrations were inferred compared to those catalysts with lower and no Ga content. Next to m/z signals ascribed to nitrile products, methylamines and O-compounds, such as acetaldehyde and dimethyl ether (DME), were additionally detected at 673 K and their concentration surged at a higher reaction temperature of 773 K. With the exception of HCN, the concentration of N-organic compounds decreased progressively with time. These online analytics results are in good qualitative agreement with the selectivity pattern and deactivation behavior ascertained for

this catalyst in isothermal catalytic tests (see **Figure 6.4. c**) above and the associated discussion), providing validation to the *operando* HRXRD experimental results.

After completion of the *operando* HRXRD experiment, cooling down the catalyst to RT did not bring about any substantial modification of its diffraction pattern, indicative for the stability of the GaNi intermetallic compound/s developed under catalysis conditions (**Figure 6.20**). These results are in good correspondence with those retrieved using HAADF/STEM and EDS nanospectroscopy, which discarded any substantial metal segregation following prolonged exposure of the catalyst to process conditions and cooling to RT.

6.2.4.4.2 In situ XAS studies on $Ga_{0.60}Ni_{0.40}/SiO_2$

The electronic properties and local coordination configuration of Ni and Ga atoms in the $Ga_{0.60}Ni_{0.40}/SiO_2$ catalyst was additionally assessed with *in situ* XAS. The spectra were recorded at RT, both following *in situ* catalyst reduction and exposure to catalysis conditions at 773 K (**Figure 6.21**). The Ni-k XANES spectra departed significantly from that for the metallic Ni foil reference. The white line shape resembled that described earlier for Ni_3Ga in the literature,[40] (**Figure 6.21. a**), indicating the occurrence of significant charge transfer from Ga to Ni. Similarly, the Ga-k XANES spectrum after reduction showed a lower energy first edge feature compared to the GaN reference, signifying the (partial) reduction of Ga.

Exposure of the catalyst to reaction conditions up to 773 K led to modifications in the shape of the white line at both absorption edges, confirming that the catalyst undergoes chemical changes under process conditions. Analysis of the corresponding FT-EXAFS spectra revealed in increment in the amplitude at a radial distance of 2.15 Å (phase-uncorrected) at the Ni-k spectrum, suggesting an increment in the average Ni-Ni(Ga) coordination number. Conversely, the FT-EXAFS amplitude at a radial distance of 2.1 Å (phase-uncorrected) decreased in the Ga-k spectrum, in favor of an enhancement of the amplitude at a shorter radial distance of ca. 1.3 Å, indicative for partial oxidation of metallic Ga under reaction

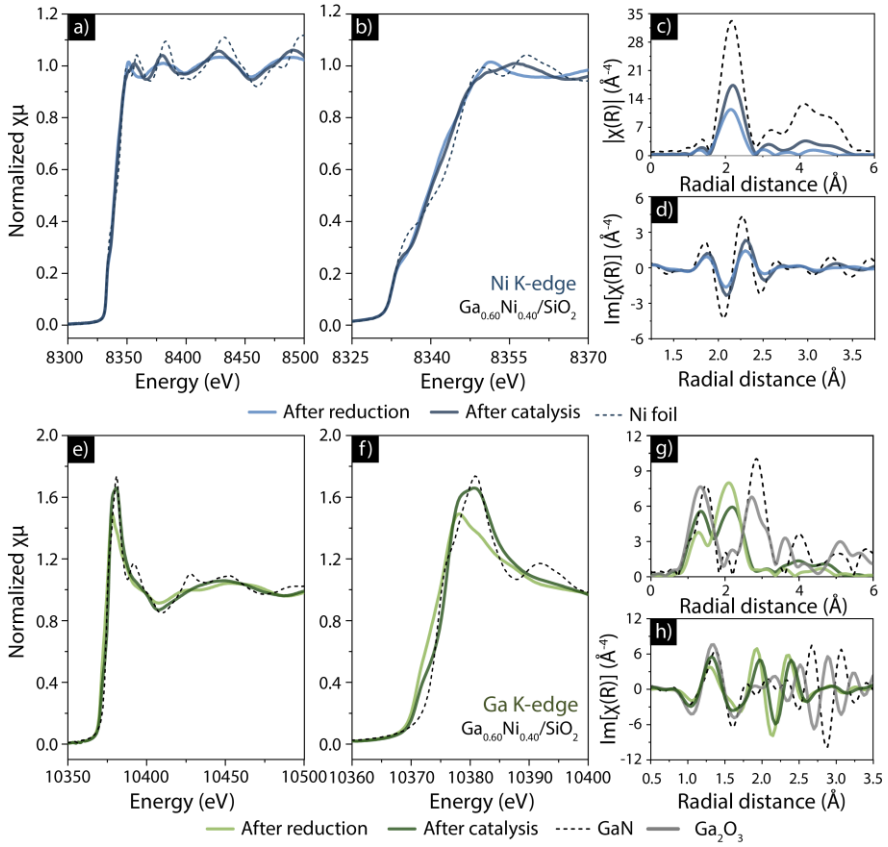

Figure 6.21 *a-b, e-f) Normalized XANES spectra, c, g) Fourier-Transform of the k^3-weighted EXAFS function (phase uncorrected) and d, h) Imaginary part of the Fourier-Transform of the k^3-weighted EXAFS function at Ni-k and Ga-k absorption edges, respectively, for $Ga_{0.60}Ni_{0.40}/SiO_2$ at different stages (after in situ reduction and after exposure to catalysis conditions at 773 K. Spectra collected in all cases at room temperature following the corresponding treatment in the capillary XAS/XRD cell.*

conditions, which results in a greater contribution from Ga-O first-shell scattering (**Figure 6.21. g**). Gallium reoxidation may be promoted by the high concentration of water detected at the gases evolving form the catalyst packed bed under reaction conditions, particularly at 773 K, as shown earlier in **Figure 6.19. d**.

The reoxidation of a fraction of the metallic Ga most likely resulted in amorphous or very small (hydro)xide crystallites, which therefore remained

undetectable by XRD. Given that Ga re-oxidation implies its segregation out of the intermetallic compound, it is a plausible explanation for the progressive deactivation observed for this catalyst at 773 K (vi*de supra*, **Figure 6.4**).

In addition, a slight displacement to higher radial distances was observed for the M-M scattering signals in the EXAFS spectra at both the Ni-k and Ga-k edges (**Figure 6.21. d, h**). This observation suggests that, also for this catalyst, light elements such as carbon and/or nitrogen may partially incorporate into interstitial positions of the GaNi intermetallic compound/s during exposure to the high carbon and nitrogen chemical potentials experienced under process conditions.

6.3 CONCLUSIONS

The following conclusions can be drawn from the results presented in this chapter:

i. A series of the series of $Ga_xNi_{(1-x)}/SiO_2$ catalysts (x= 0.02 to 0.6) allows assessing bimetallic effects in the synthesis of N-compounds by direct conversion of mixture of ammonia (N_1) and methanol (C_1) precursors.

ii. Stable Ga-Ni *fcc* alloys form after reduction of the oxidic catalyst precursors at 1023 K for bimetallic catalysts with Ga at % ranging ≤20%, while the formation of intermetallics is observed for Ga contents ≥40% in the supported metal phase.

iii. Ga-Ni alloys and intermetallic compounds lead to distinctly different product selectivity patterns under same. The former produce meanly aliphatic nitriles according to an Anderson-Schulz-Flory chain-length distribution, signifying activity for both C-N and C-C coupling reactions. In stark contrast, intermetallic compounds show higher selectivity to methylamines formation, indicative for a higher activity towards ammonia methylation, but limited C-C coupling.

iv. The highest overall nitrile formation rate of $23 \cdot 10^{-2}$ $mmol_{Nitriles}$ $mmol_{Metal}^{-1} min^{-1}$ is attained at 773 K with a $Ga_{0.05}Ni_{0.95}/SiO_2$ catalyst, while acetonitrile selectivity is maximum for $Ga_{0.02}Ni_{0.98}/SiO_2$ (30.3 C%).

v. Selecting $Ga_{0.05}Ni_{0.95}/SiO_2$ and $Ga_{0.60}Ni_{0.40}/SiO_2$ catalysts as representative alloy and intermetallic compound catalysts, respectively, *in situ*/*operando* HRXRD/XAS studies provide insights into the structural dynamics of the bimetallic species under relevant process conditions.

vi. For the alloy-based $Ga_{0.05}Ni_{0.95}/SiO_2$ catalyst, the stabilization of both a lattice-expanded *fcc* alloy (likely by uptake of interstitial carbon/nitrogen) as well as a *R-3c* Ni carbide is observed under catalysis conditions at 673 K. The development of the $(Ga_xNi_{1-x})_3C$ ($x \leq 0.05$, *R-3c*) structure coincides with the increase in acetonitrile concentration in the outlet gases, suggesting the involvement of this metal carbide in C-C coupling reactions. The metal carbide phase becomes destabilized at 773 K in favor of *hcp* Ni and *fcc* Ni structures, presumably with lower contents in interstitial carbon(nitrogen) as suggested by limited lattice expansions beyond thermal effects, resulting in lower nitrile chain-growth probability and acetonitrile production rate.

vii. The co-feeding of both NH_3 and CH_3OH reactants is proven to be essential for the stabilization of the expanded GaNi alloy and metal carbide crystal structures developed under reaction conditions, while Ga doping additionally contributes to stabilization thereof under reaction conditions.

viii. For the intermetallic-based $Ga_{0.6}Ni_{0.4}/SiO_2$ catalyst, likely a mixture of intermetallic compounds is observed with *operando* HRXRD in the working catalysts, exhibiting lower structural dynamics than their alloy counterpart. However, *in situ* XAS proves partial reoxidation of Ga at 773 K, probably into amorphous, XRD-silent GaO_x species, which may be related to the progressive decay in methylamines formation rate observed with time-on-stream at 773 K.

ix. The results emphasize marked differences in the intrinsic catalytic performance of GaNi disordered alloy and ordered intermetallic

compounds, respectively. Moreover, by illuminating severe structural reorganization during exposure to catalysis conditions, but also during *in situ* catalyst cooling to near-RT, the study underscores the need for *operando* methods to reliably identify the working catalyst (nano)structures.

6.4 REFERENCES

(1) Delgado, J. A.; Benkirane, O.; de Lachaux, S.; Claver, C.; Ferré, J.; Curulla-Ferré, D.; Godard, C. Controlled One-pot Synthesis of PdAg Nanoparticles and Their Application in the Semi-hydrogenation of Acetylene in Ethylene-rich Mixtures. *ChemNanoMat.* **2022**, *8* (5). https://doi.org/10.1002/cnma.202200058.

(2) Misra, S.; Pahari, D.; Giri, S.; Wang, F.; Puravankara, S.; Jana, P. P. The γ-Brass Type Cu–Rich Complex Intermetallic Phase $Cu_{41}Sn_{11}$: Structure and Electrochemical Study. *Solid State Sci.* **2021**, *119*, 106682. https://doi.org/10.1016/j.solidstatesciences.2021.106682.

(3) Nakaya, Y.; Furukawa, S. Catalysis of Alloys: Classification, Principles, and Design for a Variety of Materials and Reactions. *Chem. Rev.* **2023**, *123* (9), 5859–5947. https://doi.org/10.1021/acs.chemrev.2c00356.

(4) Armbrüster, M. Intermetallic Compounds in Catalysis – a Versatile Class of Materials Meets Interesting Challenges. *Sci. Technol. Adv. Mater.* **2020**, *21* (1), 303–322. https://doi.org/10.1080/14686996.2020.1758544.

(5) Hannagan, R. T.; Giannakakis, G.; Flytzani-Stephanopoulos, M.; Sykes, E. C. H. Single-Atom Alloy Catalysis. *Chem. Rev.* **2020**, *120* (21), 12044–12088. https://doi.org/10.1021/acs.chemrev.0c00078.

(6) Armbrüster, M.; Behrens, M.; Cinquini, F.; Föttinger, K.; Grin, Y.; Haghofer, A.; Klötzer, B.; Knop-Gericke, A.; Lorenz, H.; Ota, A.; Penner, S.; Prinz, J.; Rameshan, C.; Révay, Z.; Rosenthal, D.; Rupprechter, G.; Sautet, P.; Schlögl, R.; Shao, L.; Szentmiklósi, L.; Teschner, D.; Torres, D.; Wagner, R.; Widmer, R.; Wowsnick, G. How to Control the Selectivity of Palladium-based Catalysts in Hydrogenation Reactions: The Role of Subsurface Chemistry. *ChemCatChem.* **2012**, *4* (8), 1048–1063. https://doi.org/10.1002/cctc.201200100.

(7) Corbin, D. R.; Schwarz, S.; Sonnichsen, G. C. Methylamines Synthesis: A Review. *Catal. Today* **1997**, *37* (2), 71–102. https://doi.org/10.1016/S0920-5861(97)00003-5.

(8) Kim, K. N.; Lane, A. M. The Selective Synthesis of Acetonitrile from Carbon Monoxide, Hydrogen, and Ammonia over Mo/SiO_2. *J. Catal.* **1992**, *137* (1), 127–138. https://doi.org/10.1016/0021-9517(92)90144-7.

(9) Hadjigeorghiou, G. A.; Richardson, J. T. Fischer-Tropsch Selectivity of Ni/Al_2O_3 Catalysts. *Appl. Catal.* **1986**, *21* (1), 11–35. https://doi.org/10.1016/S0166-9834(00)81325-1.

(10) Studt, F.; Sharafutdinov, I.; Abild-Pedersen, F.; Elkjær, C. F.; Hummelshøj, J. S.; Dahl, S.; Chorkendorff, I.; Nørskov, J. K. Discovery of a Ni-Ga Catalyst for Carbon Dioxide Reduction to Methanol. *Nat. Chem.* **2014**, *6* (4), 320–324. https://doi.org/10.1038/nchem.1873.

(11) Zimmerli, N. K.; Rochlitz, L.; Checchia, S.; Müller, C. R.; Copéret, C.; Abdala, P. M. Structure and Role of a Ga-Promoter in Ni-Based Catalysts for the Selective Hydrogenation of CO_2 to Methanol. *JACS Au* **2024**, *4* (1), 237–252. https://doi.org/10.1021/jacsau.3c00677.

(12) Ermakova, M. A.; Ermakov, D. Yu.; Cherepanova, S. V.; Plyasova, L. M. Synthesis of Ultradispersed Nickel Particles by Reduction of High-Loaded $NiO{-}SiO_2$ Systems Prepared by Heterophase Sol−Gel Method. *J. Phys. Chem. B* **2002**, *106* (46), 11922–11928. https://doi.org/10.1021/jp021231q.

(13) Le, T. A.; Kang, J. K.; Park, E. D. Active Ni/SiO2 Catalysts with High Ni Content for Benzene Hydrogenation and CO Methanation. *Appl. Catal. A Gen.* **2019**, *581*, 67–73. https://doi.org/10.1016/j.apcata.2019.05.020.

(14) Wang, L.; Li, F.; Chen, Y.; Chen, J. Selective Hydrogenation of Acetylene on SiO_2-Supported Ni-Ga Alloy and Intermetallic Compound. *Journal of Energy Chemistry* **2019**, *29*, 40–49. https://doi.org/10.1016/j.jechem.2018.02.001.

(15) Ducher, R.; Kainuma, R.; Ishida, K. Phase Equilibria in the Ni-Rich Portion of the Ni–Ga Binary System. *Intermetallics (Barking)* **2007**, *15* (2), 148–153. https://doi.org/10.1016/j.intermet.2006.04.004.

(16) Takezawa, N.; Iwasa, N. Steam Reforming and Dehydrogenation of Methanol: Difference in the Catalytic Functions of Copper and Group VIII Metals. *Catal. Today* **1997**, *36* (1), 45–56. https://doi.org/10.1016/S0920-5861(96)00195-2.

(17) Gründling, CH.; Eder-Mirth, G.; Lercher, J. A. Surface Species in the Direct Amination of Methanol over Brønsted Acidic Mordenite Catalysts. *Research on Chemical Intermediates* **1997**, *23* (1), 25–40. https://doi.org/10.1163/156856797X00367.

(18) Segawa, K.; Ilao, M. C. Methanol Amination over Small-Pore Zeolite Catalysts. *Studies in Surface Science and Catalysis, El Sevier* **1997**, 1219–1226. https://doi.org/10.1016/S0167-2991(97)80760-4.

(19) Kovács, Gy. J.; Veres, M.; Koós, M.; Radnóczi, G. Raman Spectroscopic Study of Magnetron Sputtered Carbon–Nickel and Carbon Nitride–Nickel Composite Films: The Effect of Nickel on the Atomic Structure of the C/CN_x Matrix. *Thin Solid Films* **2008**, *516* (21), 7910–7915. https://doi.org/10.1016/j.tsf.2008.04.081.

(20) Ferrari, A. C. Raman Spectroscopy of Graphene and Graphite: Disorder, Electron–Phonon Coupling, Doping and Nonadiabatic Effects. *Solid. State. Commun.* **2007**, *143* (1–2), 47–57. https://doi.org/10.1016/j.ssc.2007.03.052.

(21) Li, H.-F.; Wu, F.; Wang, C.; Zhang, P.-X.; Hu, H.-Y.; Xie, N.; Pan, M.; Zeng, Z.; Deng, S.; Wu, M.; Vinodgopal, K.; Dai, G.-P. One-Step Chemical Vapor Deposition Synthesis of 3D N-Doped Carbon Nanotube/N-Doped Graphene Hybrid Material on Nickel Foam. *Nanomaterials* **2018**, *8* (9), 700. https://doi.org/10.3390/nano8090700.

(22) Tessonnier, J.; Su, D. S. Recent Progress on the Growth Mechanism of Carbon Nanotubes: A Review. *ChemSusChem.* **2011**, *4* (7), 824–847. https://doi.org/10.1002/cssc.201100175.

(23) Yang, F.; Chi, C.; Wang, C.; Wang, Y.; Li, Y. High Graphite N Content in Nitrogen-Doped Graphene as an Efficient Metal-Free Catalyst for Reduction of Nitroarenes in Water. *Green Chemistry* **2016**, *18* (15), 4254–4262. https://doi.org/10.1039/C6GC00222F.

(24) Wang, Y.; Shao, Y.; Matson, D. W.; Li, J.; Lin, Y. Nitrogen-Doped Graphene and Its Application in Electrochemical Biosensing. *ACS Nano* **2010**, *4* (4), 1790–1798. https://doi.org/10.1021/nn100315s.

(25) Li, C.; Chen, Y.; Zhang, S.; Zhou, J.; Wang, F.; He, S.; Wei, M.; Evans, D. G.; Duan, X. Nickel–Gallium Intermetallic Nanocrystal Catalysts in the Semihydrogenation of Phenylacetylene. *ChemCatChem.* **2014**, *6* (3), 824–831. https://doi.org/10.1002/cctc.201300813.

(26) Chang, Y. K.; Lin, K. P.; Pong, W. F.; Tsai, M.-H.; Hseih, H. H.; Pieh, J. Y.; Tseng, P. K.; Lee, J. F.; Hsu, L. S. Charge Transfer and Hybridization Effects in Ni_3Al and Ni_3Ga Studies by X-Ray-Absorption Spectroscopy and Theoretical Calculations. *J Appl Phys* **2000**, *87* (3), 1312–1317. https://doi.org/10.1063/1.372015.

(27) K. Cockcroft, J. *Powder Diffraction on the WEB*.

(28) Naberezhnov, A. A.; Sovestnov, A. E.; Fokin, A. V. Crystal Structure of Indium and Lead under Confined Geometry Conditions. *Technical Physics* **2011**, *56* (5), 637–641. https://doi.org/10.1134/S1063784211050240.

(29) Balamurugan, B.; Kruis, F. E.; Shivaprasad, S. M.; Dmitrieva, O.; Zähres, H. Size-Induced Stability and Structural Transition in Monodispersed Indium Nanoparticles. *Appl. Phys. Lett.* **2005**, *86* (8). https://doi.org/10.1063/1.1868879.

(30) Zhao, J. G.; You, S. J.; Yang, L. X.; Jin, C. Q. Structural Phase Transition of Cu_3N under High Pressure. *Solid State Commun.* **2010**, *150* (33–34), 1521–1524. https://doi.org/10.1016/j.ssc.2010.06.012.

(31) Singleton, M.; Nash, P. The C-Ni (Carbon-Nickel) System. *Bulletin of Alloy Phase Diagrams* **1989**, *10* (2), 121–126. https://doi.org/10.1007/BF02881419.

(32) Kodentsov, A. A.; van Dal, M. J. H.; Cserháti, C.; Daróczi, L.; van Loo, F. J. J. Permeation of Nitrogen in Solid Nickel and Deformation Phenomena Accompanying Internal Nitridation. *Acta Mater.* **1999**, *47* (11), 3169–3180. https://doi.org/10.1016/S1359-6454(99)00194-9.

(33) David, M.; Prillieux, A.; Monceau, D.; Connétable, D. First-Principles Study of the Insertion and Diffusion of Interstitial Atoms (H, C, N and O) in Nickel. *J. Alloys Compd.* **2020**, *822*, 153555. https://doi.org/10.1016/j.jallcom.2019.153555.

(34) He, L. Hexagonal Close-Packed Nickel or Ni_3C? *J. Magn. Magn. Mater.* **2010**, *322* (14), 1991–1993. https://doi.org/10.1016/j.jmmm.2010.01.020.

(35) Matsuda, J.; Yamamoto, T.; Takahashi, S.; Nakanishi, H.; Sasaki, K.; Matsumura, S. *In Situ* TEM Investigation of Structural Changes in Ni Nanoparticle Catalysts under Gas Atmospheres: Implications for Catalyst Degradation. *ACS Appl. Nano Mater.* **2021**, *4* (2), 2175–2182. https://doi.org/10.1021/acsanm.1c00006.

(36) Sadeqzadeh, M.; Karaca, H.; Safonova, O. V.; Fongarland, P.; Chambrey, S.; Roussel, P.; Griboval-Constant, A.; Lacroix, M.; Curulla-Ferré, D.; Luck, F.; Khodakov, A. Y. Identification of the Active Species in the Working Alumina-Supported Cobalt Catalyst under Various Conditions of Fischer–Tropsch Synthesis. *Catal. Today* **2011**, *164* (1), 62–67. https://doi.org/10.1016/j.cattod.2010.12.035.

(37) Neiva, E. G. C.; Oliveira, M. M.; Marcolino, L. H.; Zarbin, A. J. G. Nickel Nanoparticles with Hcp Structure: Preparation, Deposition as Thin Films and Application as Electrochemical Sensor. *J. Colloid Interface Sci.* **2016**, *468*, 34–41. https://doi.org/10.1016/j.jcis.2016.01.036.

(38) Huba, Z. J.; Carpenter, E. E. Monitoring the Formation of Carbide Crystal Phases during the Thermal Decomposition of 3d Transition Metal Dicarboxylate Complexes. *Dalton Trans.* **2014**, *43* (32), 12236–12242. https://doi.org/10.1039/C4DT01207K.

(39) Kang, J.; Zhang, D.; Guo, G.; Yu, H.; Wang, L.; Huang, W.; Wang, R.; Guo, L.; Han, X. Au Catalyzed Carbon Diffusion in Ni: A Case of Lattice Compatibility Stabilized Metastable Intermediates. *Adv. Funct. Mater.* **2018**, *28* (21). https://doi.org/10.1002/adfm.201706434.

(40) Hejral, U.; Timoshenko, J.; Kordus, D.; Lopez Luna, M.; Divins, N. J.; Widrinna, S.; Zegkinoglou, I.; Pielsticker, L.; Mistry, H.; Boscoboinik, J. A.; Kuehl, S.; Roldan Cuenya, B. Tracking the Phase Changes in Micelle-Based NiGa Nanocatalysts for Methanol Synthesis under Activation and Working Conditions. *J. Catal.* **2022**, *405*, 183–198. https://doi.org/10.1016/j.jcat.2021.11.024.

CHAPTER 7.

GENERAL CONCLUSIONS

The results presented in this thesis provide fundamental insights into bimetallic effects in solid catalysts for the integration of C-N and C-C coupling reactivities from alternative, potentially renewable, C_1 and N_1 feedstocks. These catalysts are designed for processes that enable a direct production of C_{2+} N-compounds, particularly aliphatic nitriles. *Ex situ* and *in situ* and *operando* diffraction and spectroscopy methods provide temperature- and time-resolved information into chemical and structural changes, which catalyst precursors undergo at their near-surface as well as within their bulk, when exposed to particularly invasive reaction atmospheres combining syngas (H_2+CO) or methanol, as C_1 reactants, with ammonia as a nitrogen source. The rationalization of the structure of the truly working catalysts, which develop only under relevant process conditions, serves to rationalize the superior performance, in terms of selectivity and/or stability, brought about by the combination of two metals in solid state solutions or mixed-metal interstitial compounds.

More specifically, major conclusions drawn from the studies presented in this thesis are:

i. A MoO_3 catalyst precursor undergoes (near surface) nitridation under reaction conditions for the direct synthesis of acetonitrile from syngas and ammonia mixtures, rendering molybdenum nitride the actual working catalyst.

ii. The combination of catalytic testing with periodic Density Functional Theory simulations on a model γ-Mo_2N(100) surface suggest that C-N coupling elementary steps are likely kinetically irrelevant in the conversion path towards acetonitrile and higher aliphatic nitriles, owing to a low energy barrier (33 kJ mol^{-1}) for the coupling of CH and N adspecies.

iii. HCN is a key, stable reaction intermediate towards higher nitriles, the dehydrogenative activation of which is facilitated by H-abstraction on surface oxygen (or hydroxyl) species. This conversion step, necessary for further C-C coupling, is predicted to face a notably higher activation

energy of 132 kJ mol^{-1} and thus it is likely determinant for the overall rate of acetonitrile synthesis.

iv. Crystalline ammonium mixed-metal molybdate compounds provide excellent precursors to address bimetallic promotional effects in Mo-based catalysts for acetonitrile synthesis, owing to the intrinsic atomic-level metal mixing provided by their regular structure at M:Mo atomic ratios of ca. 1.0, where M is a divalent first-row transition metal.

v. Doping a Mo catalyst with Mn (at a Mn:Mo atomic ratio of 1.1:1) affords a particularly selective and stable catalyst for acetonitrile synthesis from NH_3/syngas mixtures, achieving an acetonitrile formation rate of $50 \cdot 10^{-3}$ mmol g_{cat}^{-1} min^{-1}, in the pseudo-steady state.

vi. *Ex situ* and *operando* physicochemical methods reveal that a defective MnMo mixed-metal oxynitride, with a *Fm-3m,* best represents the working catalyst.

vii. The combination of first-principles thermochemistry and *ex situ* EXAFS studies supports the notion of a MnMo working catalyst showing local defects such as nitrogen vacancies and Schottky pair defects and a greater amount of lattice oxygen compared to a monometallic Mo catalyst counterpart, particularly at Mn-enriched domains with lower local nitridation degrees.

viii. The higher oxophilicity offered by the mixed-metal MnMo catalyst, alongside the key role of surface oxygen for the kinetically relevant step of HCN dissociative activation are suggested to underlie the bimetallic promotional effect observed for the synthesis of acetonitrile and higher nitriles.

ix. Bimetallic promotional effects are also exploitable in the reaction of methanol and ammonia (N/C=2) for the production of N-compounds. Unlike supported neat Ni nanocrystals, which show a particularly unselective performance, GaNi bimetallic nanocrystals show a notably

more selective behavior for the synthesis of nitrogenated organic compounds.

x. Bimetallic $Ga_xNi_{(1-x)}/SiO_2$ catalysts with comparatively low Ga contents (x=0.02 to 0.12), i.e., below the Ga solubility limit in *fcc* Ni, appear in the form of *fcc* GaNi alloys following reduction catalyst activation. These catalysts were shown to be most selective to nitrile production (C_1-C_5) and the nitrile production rate was maximum at 773 K (P_{atm}). Moreover, an *in situ* activation of *fcc* GaNi alloy nanocrystals at 673 K, under the NH_3/methanol reaction atmosphere was required to preserve a nitrile-selective performance at 773 K.

xi. Bimetallic $Ga_xNi_{(1-x)}/SiO_2$ catalysts with comparatively higher Ga contents (x>0.40), appear in the form of ordered intermetallic compounds following reduction catalyst activation. Unlike random alloys, intermetallics showed high selectivity to methylamines and O-compounds (DME, acetaldehyde) among the organic products. The amine production rate was maximum at 773 K (P_{atm}).

xii. *In situ* and *operando* high-resolution X-ray diffraction and X-ray absorption spectroscopy revealed a high structural dynamics of GaNi alloy solid solutions under process conditions, wherein Ga contributes to the stabilization of metal interstitial metal compounds at reaction conditions, the latter comprising lattice-expanded *fcc* Ni(C,N) and specially Ni_3C, which appear to be responsible for C-C coupling, as required for nitrile synthesis.

xiii. In contrast, GaNi intermetallic nanocrystals, as exemplified in the $Ga_{0.6}Ni_{0.4}/SiO_2$ catalyst, showed a greater structural stability under reaction conditions, with limited reorganization of their bulk structure. However, partial reoxidation of Ga species was detected following reaction at 773 K, possibly driven by water side product, implying Ga ex-solution from the intermetallic/s lattice. The latter is tentatively associated to the marked deactivation undergone by the catalyst with testing time at 773 K.

xiv. Interstitial carbide compounds, emerging *operando* out of GaNi random alloys, show combined activities towards C-Cn coupling and C-C chain-propagation via a Fischer-Tropsch like mechanism, leading to aliphatic nitrile products which obey a statistical Ander-Schulz-Flory chain-length distribution. Conversely, GaNi intermetallic compounds appear to steer reaction mechanisms based on methanol dehydration and amination pathways, lacking the ability to propagate the C-C chain.

xv. Tracking the structure of metal nanocrystals under *operando* conditions is essential to establish reliable connections between catalyst nanostructure and catalytic performance, as emphasized by the fact that cooling to RT after catalysis, even *in situ*, under exclusion of air and humidity, led to significant metal segregation and recrystallization from the actual working state.

APPENDICES

Appendix I: List of figures and tables

List of figures

Chapter 1	*p.*
Figure 1.1. *Major industrial routes for the manufacture of methylamines (methylamine, MMA, dimethylamine, DMA, and trimethylamine, TMA) and short-chain (C_{1-3}) nitriles.*	*4*
Figure 1.2: *a) Evolution of global CO_2 emissions in the period 1978-2022. b) CO_2 emissions, breakdown per sector, for recent years, adapted from the International Energy Agency (IEA) report. c) Global methane emissions by sector, in 2022, adapted from International Energy Agency (IEA) report (2022). d) Major reactions and typical H_2/CO ratios in the syngas product mixture for different processes for methane-to-syngas conversion. SMR: steam methane reforming, POX: partial methane oxidation, ATR: autothermal reforming, DMR: dry methane reforming. e) Breakdown of major methanol industrial uses (2022).*	*8*
Figure 1.3: *Scheme of some syngas conversion routes into valuable ammonia, O-containing compounds and hydrocarbons/olefins chemicals.*	*9*
Figure 1.4: *Different color shades associated to industrial hydrogen depending on the source and carbon footprint attached to the production technologies.*	*17*
Figure. 1.5: *Illustration depicting the integration of renewable energy sources into a sustainable process for ammonia synthesis. The scheme outlines the sequential stages involving electricity application from renewables, encompassing nitrogen purification from air, nitrogen electroreduction, and the Haber-Bosch process. The hydrogen reactant for the latter is generated through water electrolysis with renewable power (green hydrogen).*	*21*
Figure 1.6: *Illustration of the integration of C_1 and N_1 sources, via catalytic C-N coupling, for the synthesis of N-compound commodity chemicals.*	*23*

Figure 1.7: *a) Scheme for HCN formation via either direct coupling of NH_3 and CH_4 or the participation of NO as reaction intermediate, as postulated for the oxidative synthesis of HCN in the Andressow process (* marks adsorbed species). Secondary reactions that may be undesirably exacerbated be enhanced by an imbalanced availability of activated oxygen species are denoted with dashed lines. b) Scheme for HCN formation over metal catalyst under the non-oxidative conditions of the Degussa process, based on mechanistic proposals put forth in the scientific literature.* 25

Figure 1.8: *Timeline and selected milestones for investigations on catalytic reactions between carbon monoxide and ammonia from 1920 to date, showcasing the varying product distributions —amines, amides, and nitriles—reported as a function of the catalyst and reaction conditions applied.* 33

Figure 1.9: *Summary of different mechanistic proposals put forth in the earlier scientific literature for the synthesis of N-compounds from mixtures containing carbon monoxide and ammonia. a) Via alkyl-metal bond amination for the production of amines. b) Via an isocyanide intermediate for the synthesis of acid cyanide and acetonitrile. c) Via a formate intermediate for the synthesis of amines and nitriles. Species marked with * are meant to be adsorbed on the catalyst's surface.* 36

Figure 1.10: *a) Qualitative representation of the Sabatier principle in catalysis. b) Correlation of DFT-calculated surface adsorption energy for oxygen- and carbon-based adspecies and experimental bulk formation energy for different metal compounds.* c) *Evolution of the annual number of scientific publications with title containing the words metal, alloy or intermetallic in combination with the word catalyst in the period from 1950 to 2020.* 46

Figure 1.11: *a) Schematic representation of substitutional solid solutions (top-left), interstitial compounds (top-right) eutectic alloys (bottom-left) and intermetallic compounds (bottom-right). b) Schematic representation of the evolution of the lattice parameter with the fractional composition in a substitutional solid solution with complete solubility of pure compounds. c) Compositional-lattice parameter curves and phase diagrams of conventional binary alloys with complete solubility (left), partial solubility (e.g., A possesses higher valence than B, middle) and with high electrochemical A-B interaction leading to a different and more stable phase (right).* 50

Figure 1.12: *a) Van Arkel triangles of N-poor and N-rich ternary nitrides showing the dependency with the metallic, ionic and covalent bond character. The hexagons are represented when more than two data points are available. b) Formation enthalpy for carbides and nitrides of first row transition metals. c) Comparison of the crystal structures for the hexagonal hcp-Ni (top) and the rhombohedral Ni_3C carbide interstitial solid solution forming a superlattice. d) Phase diagram for molybdenum nitrides determined by H. Jehn. et al.* 53

Figure 1.13: *Illustrative AB crystal lattice with major point defects discussed in this section, including anion and cation vacancies, substitutional, Schottky, Frenkel and (self-) interstitials defects.* 56

Figure 1.14: *Periodic table highlighting the common active metals (red) and the second metal providing electronic, structural, steric, and order effects in intermetallic compounds. Blue dashed means metals that are less common utilized.* 61

Chapter 3 *p.*

Figure 3.1: *a) Interplanar distances between periodically arranged lattice planes of atoms in a crystal structure. b) Geometric correlation between the interplanar distance (d) and the diffraction angle (θ) of Bragg´s law.* 97

Figure 3.2: *a) Schematic representation of the L and M levels and the generated K_α radiation and K_β radiation by electron relaxation after K level ionization. b) X-ray spectrum scheme of a metallic anode showing the continuously radiation or "Bremsstrahlung" and characteristic radiation. Blue inset provides a magnified view of the K_α radiation.* 99

Figure 3.3: *Temperature program applied for in situ, laboratory powder XRD analysis during catalyst reduction (top) and exposure to NH_3 atmosphere (bottom). Scatter data points mark specific times along the experiment when the temperature was held steady to record XRD patterns.* 101

Figure 3.4: *Schematics of the operation principle of X-ray photoelectron spectroscopy (XPS).* 103

Figure 3.5: *a, right) Ejection of a photoelectron to the continuum by the electron absorption in the K edge of an X-ray photon. a, left) Consequently, the production of X-ray fluorescence (K_α and K_β) and Auger emission by the relaxation of an electron to the core-hole. b) K-* 108

edge XAS spectrum of Ni foil. Inset represents the interference effect produced by the back-scattered photoelectron with its shelf when interacting with adjacent neighbors at distances R_1 and R_2.

Figure 3.6: *Capillary cell configuration of the In-situ/Operando High-resolution XRD and X-ray absorption experiments pressure under ammonia/methanol feed at atmospheric. The products were analyzed downstream by a MS spectrometer.* *113*

Figure 3.7: *P&ID diagram of the reactor setup applied for catalytic conversion tests, with a close-up view in the packed-bed reactor.* *125*

Figure 3.8: *Representative Scion 456 gas chromatogram for a test of the catalytic synthesis of acetonitrile from syngas/NH_3 mixtures. a) TCD channel, b) FID channel. Major compounds have been labelled on the figure. Light hydrocarbons are represented as C_2, $C_2^{=}$, C_3, $C_3^{=}$, C_4 corresponding to ethane, ethylene, propane, propene and racemic C_4 hydrocarbons, respectively.* *127*

Figure 3.9: *Representative Agilent 8860 System gas chromatograms along a) the TCD channel and b,c) the FID channel for tests of the catalytic synthesis of acetonitrile from b) syngas/NH_3 mixtures and c) methanol/NH_3 mixtures. Major compounds have been labelled on the figure. Light hydrocarbons are represented as C_2, $C_2^{=}$, C_3, $C_3^{=}$, C_4, corresponding respectively to ethane, ethylene, propane, propene and racemic C_4 hydrocarbon. MMA, DMA and TMA represent the methylamines that comprise mono-, di-, and tri-methylamine, respectively. Additionally, DME represents dimethyl ether.* *128*

Chapter 4 *p.*

Figure 4.1: *a) Dependence of CO conversion (X_{CO}) and product selectivity with WHSV and b) evolution of CO conversion, acetonitrile formation rate (r_{MeCN}) and product selectivity (within organic products, CO_2-free basis) with time on stream (TOS) for the direct synthesis of acetonitrile from a NH_3/syngas mixture. Reaction conditions: T=723 K, P=3 bar, gas feed molar composition NH_3: CO: H_2=2: 1: 1. c) Temperature-resolved X-ray diffraction patterns recorded during the exposure of the MoO_3 catalyst precursor to the NH_3/syngas reactive atmosphere in the temperature range of 523-873 K and P= 1 bar. d, e) X-ray photoemission spectra, in the Mo3d and Mo3p + N1s core level spectral regions, for d) the pristine MoO_3 catalyst precursor and, e) the* *141*

Mo-based catalyst after exposure to reaction conditions for 10 hours-on-stream.

Figure 4.2: *Linearized Anderson-Schulz-Flory plot and the corresponding chain-growth probability (α) for nitrile products obtained in the direct conversion of a NH_3/syngas mixture on the Mo nitride catalyst. Reaction conditions: T=723 K, P=3 bar, gas feed molar composition $2NH_3$: 1CO: $1H_2$, WHSV= 7.1 h^{-1}. W_n stands for the weight fraction of nitrile products with n carbon atoms within the products. The dotted line corresponds to the linear regression of the data set.* 142

Figure 4.3: *Ex situ XRD of MoO_3 exposed to reaction conditions for the direct conversion of a NH_3/syngas (T=723 K, gas feed molar composition $2NH_3$:1CO:$1H_2$) for different times on stream (10, 60 and 600 min, respectively). On the top side of the plot, simulated diffraction patterns for MoO_2 (ICSD 80830) and γ-Mo_2N (ICSD 251625) are shown for reference purposes.* 143

Figure 4.4: *X-ray photoemission spectra in the Mo3d and Mo3p + N1s core level spectral regions for a γ-Mo_2N standard.* 144

Figure 4.5: *Transmission electron micrographs and the corresponding particle size distributions for a,c) the pristine MoO_3 catalyst precursor and b,d) following exposure to reaction conditions for the conversion of a NH_3/syngas mixture to acetonitrile ($2NH_3$:1CO:$1H_2$ feed stream, T=723 K) for 10 h. Given the anisotropic shape of the particles, individual particle sizes (d) were assessed as $d = (4A/\pi)^{1/2}$, wherein d is the equivalent particle diameter and A is the projected particle area.* 146

Figure 4.6: *a) Representative high-resolution transmission electron microscopy (HR-TEM) and, b) high-angle annular dark-field scanning-transmission electron microscopy (HAADF-STEM) micrographs for the molybdenum catalyst following 10 h of exposure to reaction conditions for the synthesis of acetonitrile from syngas/NH_3 mixtures. Feed composition: $3NH_3$: 1CO: $1H_2$ (vol), reaction temperature= 723 K. c-e) EDS compositional maps collected for the area imaged in (b). f) Spatial evolution of the Mo signal and the N/O signal ratio along the linescan EDS compositional profile recorded across a representative particle (see segment marked on panels b-d). Distance expressed from left to right along the profile segment.* 147

Figure 4.7: *Top view of the γ-Mo_2N(100) surface showing a p(1x1) unit cell and adsorption sites, 1) Atop (Mo^{III}), 2) Top (Mo^{II}), 3) Bridged, 4) Hollow. Mo atoms are depicted gray and N atoms in blue.* 148

Figure 4.8: *Potential energy diagram for CO dissociation pathways on the Mo_2N (100) surface, via direct dissociation (red trace) and via hydrogen-assisted CO hydrogenation pathway to HCO (blue trace) and H_2CO formation (black trace) followed by dissociation into HC, O and H species and H_2C and O species, respectively. Zenithal views over the optimized transition states (TS) along the different reaction pathways are included on the right-hand side. Mo, N, C, O and H atoms are shown in gray, blue, yellow, red and cyan, respectively.* 151

Figure 4.9: *Potential energy diagram for the hydrogenation of CH_2 adspecies to methane (red trace) and coupling of HC species to N adatoms to produce HCN (black trace) on the Mo_2N (100) surface. Zenithal views over the optimized transition states are inserted as insets on the diagram. Mo, N, C, O and H atoms are shown in gray, blue, yellow, red and cyan, respectively.* 152

Figure 4.10: *Potential energy diagram for NH_3 dissociation, i.e., direct (red trace) vs O-assisted (black trace) on the Mo_2N(100) surface. Zenithal views over the optimized transition states (TS) along the different reaction pathways are included on the right-hand side. Mo, N, C, O and H atoms are shown in gray, blue, yellow, red and cyan, respectively.* 153

Figure 4.11: *Potential energy diagram for acetonitrile formation from HCN decomposition into -CN and -OH adspecies on the O pre-covered Mo_2N(100) surface, followed by C-C coupling with CH_3 species. Zenithal views over the optimized transition states are inserted as insets on the diagram. Mo, N, C, O and H atoms are shown in gray, blue, yellow, red and cyan, respectively.* 157

Figure 4.12: *Experimental Arrhenius plot for acetonitrile formation (formation rates determined at pseudo-steady state for X_{CO}<15 %) obtained for the studied unsupported Mo catalyst in the direct conversion of NH_3/syngas mixtures. Reaction conditions: P_{atm}, gas feed molar composition NH_3: CO: H_2=2: 1: 1. The dotted line corresponds to the linear regression of the dataset.* 158

Chapter 5 *p.*

Figure 5.1: *a-i) Representative field-emission scanning electron microscopy (FE-SEM) micrographs for the series of (a) MnMo, (b) CoMo, (c) NiMo, (d) CuMo and (e) ZnMo bimetallic ammonium molybdate catalyst precursors. b-j) Rietveld refinement results and full structure solution for b) MnMo, d) CoMo, f) NiMo, h) CuMo and j) ZnMo from experimental XRD profiles (experimental data: blue scatter cross, calculated pattern: green line, residual profile: bottom blue line). Schematic representations for the corresponding crystal structures are also included.* *168*

Figure 5.2: *Acetonitrile (MeCN) formation rates (black scatter), selectivity (blue bars, upwards), and percentual drop in acetonitrile (MeCN) production rate experiencde over the course of 3 h on-stream (red bars, downwards) for the series of bimetallic MMo catalysts applied in the direct conversion of NH_3/syngas mixtures. Reaction conditions: T= 723 K, P=3 bar, gas feed molar composition: 2 NH_3:1 CO:1 H_2, X_{CO}<18 %.* *169*

Figure 5.3: *a) Evolution of CO conversion (X_{CO}), acetonitrile formation rate (r_{MeCN}) and product selectivity (CO_2-free basis) with time on stream (TOS) for the MnMo bimetallic catalyst (space velocity= 7.1 h^{-1}); b) Dependence of CO conversion and product selectivity with WHSV for the MnMo bimetallic catalysts in the direct conversion of NH_3/syngas mixtures. Reaction conditions: T=723 K, P=3 bar, gas feed molar composition NH_3: CO: H_2= 2: 1: 1; c) Experimental Arrhenius plot for MeCN formation (formation rates determined at pseudo-steady-state for X_{CO}< 15 %). d) Log-plot for the C-N bond formation rate dependence with the partial pressure of NH_3, CO and H_2 reactants in the feed, respectively, over the bimetallic MnMo catalyst. Reaction conditions: T=723 K, P=1.2-2.5 bar, X_{CO}< 15 %. The corresponding apparent reaction orders α(NH_3), β(CO) and γ(H_2) are indicated on the figure.* *171*

Figure 5.4: *a) Evolution of CO conversion (X_{CO}), acetonitrile formation rate (r_{MeCN}) and product selectivity (CO_2-free basis) with time on stream (TOS) for the Mn monometallic catalyst (space velocity= 7.1 h^{-1}); and b) dependence of CO conversion and product selectivity with WHSV for the Mn monometallic catalysts in the direct conversion of NH_3/syngas mixtures. Reaction conditions: T= 723 K, P= 3 bar, gas feed molar composition NH_3: CO: H_2= 2: 1: 1).* *172*

Figure 5.5: *Linearized Anderson-Schulz-Flory plots and the corresponding chain-growth probability for nitrile products for the direct conversion of NH_3/syngas mixtures on the bimetallic MnMo as well as the corresponding monometallic reference catalysts. Reaction conditions: T=723 K, P=3 bar, gas feed molar composition 2 NH_3 :1 CO: 1 H_2, WHSV= 7.1 h^{-1}.* 173

Figure 5.6: *Acetonitrile and HCN mass spectrometry signals recorded during the earliest stages of the reaction of conversion of NH_3/syngas mixtures on the MnMo bimetallic catalyst. Reaction conditions: T= 723 K, P= 1.5 bar, molar gas feed composition 2 NH_3: 1 CO: 1 H_2, GHSV=7.5 h^{-1}.* 174

Figure 5.7: *Temperature-resolved powder X-ray diffractograms for the a) MnMo precursors during exposure to flow of the reactive NH_3/syngas atmosphere from room temperature to 873 K. Diffraction patterns for selected reference compounds have also been included.* 176

Figure 5.8: *Selected temperature-resolved powder high-resolution X-ray diffraction patterns for the MnMo catalyst after its exposure to reaction conditions in the direct conversion of NH_3/syngas mixtures for 10, 60 and 600 min. Reaction conditions: T= 723 K, P_{atm}, molar gas feed composition 3NH_3: 1CO: 1H_2. XRD measurement conditions: Debye-Scherrer geometry at 30 keV photon energy, λ= 0.4125 Å. Samples were sealed under inert atmosphere in a glass capillary (OD= 0.5 mm, wall thickness= 0.01 mm). The experimental pattern recorded for bulk γ-Mo_2N (Fm-3m) is included as reference*. 177

Figure 5.9: *Evolution of the average oxidation state (OS) for a, e) Mo and b) Mn, as derived from the analysis of the energy shift for Mo-k and Mn-k X-ray absorption edge energies with respect to the corresponding metallic foil (E^0_{sample}-E^0_{foil}), as a result of the exposure of the a, b) $(NH_4)_2H_2Mn_4Mo_4O_{18}{\cdot}2H_2O$ and e) MoO_3 precursor to reaction conditions at increasing temperatures. Green square data points correspond to the series of standard pure compounds with known Mo and Mn oxidate states while circles and triangle symbols represent the temperature-resolved data for the MnMo and Mo catalyst, respectively. The dashed line corresponds to the linear regression for those data points determined for the standard compounds. Detail of the temperature-resolved changes in the pre-edge XANES spectra features for the bimetallic MnMo catalyst at the c) Mo-k and d) Mn-k absorption edge energies, respectively. f) Comparison of the evolution of the OS_{Mo} with temperature for the bimetallic MnMo catalyst and a* 178

monometallic Mo counterpart. Reaction conditions: P= P_{atm}, gas feed molar composition: 3 NH_3: 1 H_2: 1 CO.

Figure 5.10: *Temperature-resolved bulk nitrogen and carbon contents, as determined by elemental analysis, for the MnMo catalyst exposed to reaction conditions for the direct conversion of NH_3/syngas mixtures. Reaction conditions: P_{atm}, gas feed molar composition: 3NH_3: 1CO: 1H_2. Data correspond to an exposure time of 10 min at each temperature. For selected operation temperatures, data are provided also after longer times-on-stream (TOS). For comparison data are also provided for the corresponding monometallic catalysts after 600 min on-stream at 723 K.* 180

Figure 5.11: *a) Evolution of the lattice parameter (a) for Fm-3m MoN_{1-x} nitride as a function of the volumetric density of ordered N-vacancies; and b) Evolution of the Gibbs free energy of formation and the lattice parameter (a) for Fm-3m MoMnN mixed-metal nitride as a function of the volumetric degree of Mo isomorphic substitution for Mn, as derived from periodic DFT calculations (PAW-RPBE-D3). Calculations have considered a nitrogen chemical potential μ_N corresponding to a P_{N2}= 1.5 bar and T= 723 K, representative for the reaction conditions.* 182

Figure 5.12: *a) Evolution of the Gibbs free energy of formation for monometallic and mixed-metal Fm-3m oxynitride materials as a function of the degree of lattice nitrogen substitution by oxygen (at%) and the environmental oxygen chemical potential, relative to that determined at 0 K and P_{O2}= 1 atm reference conditions. Calculations have considered a nitrogen chemical potential μ_N corresponding to a P_{N2}= 1.5 bar and T= 723 K, representative for the reaction conditions.* 183

Figure 5.13: *Gibbs free energy of formation for a) nitrogen (anionic) vacancy, b) metal (cationic) vacancy and c) Schottky NN1 divacancy point defects, as predicted with DFT-based thermochemistry calculations for monometallic (MoN) and mixed-metal ($Mn_{0.5}Mo_{0.5}N$) Fm-3m nitrides as a function of defect volumetric concentration. Calculations have considered a nitrogen chemical potential μ_N corresponding to a P_{N2}= 1.5 bar and T= 723 K, representative for the reaction conditions. For NN1 Schottky defects, the influence of lattice substitution of N atoms by O atoms, i.e., in a mixed-metal oxynitride, on the defect formation free energy has also been studied.* 185

Figure 5.14: *Fourier Transform FT-χ(R) functions in the real space (no phase correction) collected at the a, c) Mo-k and b) Mn-k edges, after exposure of a, b) the bimetallic $(NH_4)_2H_2Mn_4Mo_4O_{18}\cdot 2H_2O$ and c) the* 187

monometallic MoO_3 precursor catalysts to reaction conditions ($3NH_3$:$1H_2$:1CO, P_{atm}) at increasing temperatures. The spectra of Mo_2N and MnO references are included for comparison purposes. d) Continuous Cauchy Wavelet Transforms (CCWT) of the k^3-weighted EXAFS functions for the MnMo (top) and MoO_3 (bottom) materials before and after exposure to reaction conditions ($3NH_3$:$1H_2$:1CO, P_{atm}) at 873 K. The CCWT contour map of the Mo_2N reference is provided for the purpose of comparison. The CCWT maps were calculated with a Cauchy order n= 200, and a Hanning apodization window was applied in the range $1<k(Å^{-1})<11$ to extract the Fourier transform signals in the R-space (no phase correction).

Figure 5.15: *a) Illustration of SR-XPS near-surface depth compositional profiling on powder solids upon energy modulation of the irradiating X-ray beam and exemplary deconvolution analysis of Mo3d and Mo3p+N1s core level spectral regions for the MnMo catalyst following exposure to reaction conditions at 723 K for 600 min. b) Evolution of the near-surface relative abundance of molybdenum species and the N/Mo atomic ratio on the MnMo catalysts with the time-on-stream under reaction conditions at 723 K. Data correspond to an analysis depth of 2.75 nm (incident energy 600 eV)). Evolution of molybdenum speciation with the photoemission analysis depth for the MnMo catalyst following exposure to reaction conditions at 723 K for c) 1h and d) 10h on stream.* 191

Figure 5.16: *a, b) Representative high-resolution scanning transmission electron microscopy (HR-STEM) for the MnMo catalyst after exposure to reaction conditions for 600 min. The insets show the corresponding Fast Fourier Transform pattern. c) Representative high-angle annular dark-field (HAADF) STEM micrograph of a catalyst particle cross-section. Panels e-g) show the corresponding EDS elemental maps for d) Mn, Mo e) N, Mo f) N, Mn and g) N, Mn, Mo. g) N/(Mn+Mo) signal ratio and Mn normalized signal of the EDS profile corresponding to the e-g panels. Reaction conditions: T=723 K, $P=P_{atm}$, gas feed molar composition: 3 NH_3:1 CO:1 H_2.* 193

Figure 5.17: *a) DFT-predicted surface energy for different surface terminations of the $Mn_{0.5}Mo_{0.5}N$ nitride (Fm-3m). b) Zenithal views over the optimized structured for different surface terminations. c) Wulff construction derived from the different surface energetics. Assuming a truncated octahedron crystal morphology. For the polar 111 surface, nitrogen termination was found to be significantly more stable than the metal-terminated counterpart, hence it was the only 111 termination* 195

considered for the Wulff construction. For the latter, surface energy calculations were performed considering a nitrogen chemical potential μ_N corresponding to a P_{N2}= 1.5 bar and T= 723 K, representative for the reaction conditions.

Chapter 6

p.

Figure 6.1: *a) X-ray diffractograms for the series of oxidic precursors for $Ga_xNi_{(1-x)}/SiO_2$ catalysts (x= 0.02 to 0.6) in their as-calcined state. b) Hydrogen temperature-programmed reduction (H_2-TPR) profiles for selected $Ga_xNi_{(1-x)}/SiO_2$ catalyst precursors.* 206

Figure 6.2*. a) X-ray diffraction patterns and b) evolution of the a cell parameter with composition for the series of $Ga_xNi_{(1-x)}/SiO_2$ catalysts (x=0-0.3) following reduction in hydrogen at 1023 K. In panel b, gray and black diamonds represent the a parameter reported in the literature for α-Ni_xGa_y (Fm-3m) solid solutions and α´-Ni_3Ga intermetallics, respectively, while green circles correspond to the experimental a parameter determined in this study using Rietveld refinement. The gray line is a guide to the eye corresponding to the systematic lattice expansion for α-Ni_xGa_y (Fm-3m) alloy upon Ga incorporation. c) X-ray diffraction patterns for $Ga_xNi_{(1-x)}/SiO_2$ catalysts (x=0.4-0.6) showing diffractions indexable to intermetallic compounds. d) Ni-Ga phase diagram. e) representation of the crystal structure described for the most relevant NiGa solid solution alloys and intermetallics. Ni and Ga atoms shown in gray and green color, respectively.* 208

Figure 6.3: *Evolution of a) methanol conversion, b) CO selectivity, c) nitriles formation rate, d) methylamines formation rate with the Ga atomic fraction (x) in the bimetallic Ga_xNi_{1-x}/SiO_2 catalysts and the reaction temperature. Gas-catalyst space velocity= 5.22±0.06 $mmol_{Feed}mmol_{Metal}^{-1}h^{-1}$, P=2±0.5 bar.* 211

Figure 6.4*. a) Selectivity within the organic products, i.e., on a CO_x-free basis, (bars), and formation rate of nitriles and methylamines (scatter-dotted lines) obtained with the series of $Ga_xNi_{(1-x)}/SiO_2$ catalysts in the conversion of a NH_3/methanol mixture (N/C=2) to N-compounds. b,c) Evolution of product formation rate (scatter-dotted lines) and selectivity pattern (bars) with time-on-stream for selected b) nitrile-selective catalyst ($Ga_{0.05}Ni_{0.95}/SiO_2$)* and c) amine-selective 212

catalyst ($Ga_{0.60}Ni_{0.40}/SiO_2$). Reaction conditions: T= 773 K, P=2±0.5 bar, NH_3:CH_3OH molar ratio of 2, GHSV= 5.2 $mmol_{feed}mmol_M^{-1}h^{-1}$.

Figure 6.5: *a) Linearized Anderson-Schulz-Flory (ASF) product distribution for nitriles (HCN formally considered as a C_1 nitrile) as obtained with the $Ga_{0.05}Ni_{0.95}/SiO_2$ catalyst at various reaction temperatures. Lines correspond to linear regressions. b) Evolution of the average ASF chain growth probability parameter (α) for C_2-C_5 nitrile products, from tests with $Ga_xNi_{(1-x)}/SiO_2$ alloy-type catalysts with x=0.02-0.12 as a function of the reaction temperature. Line is a guide to the eye. Gas-catalyst space velocity= 5.22±0.06 $mmol_{Feed}mmol_{Metal}^{-1}h^{-1}$, P=2±0.5 bar.* 214

Figure 6.6: *a) Evolution of the overall carbon balance obtained with the series of $Ga_xNi_{(1-x)}/SiO_2$ catalysts in the conversion of NH_3/methanol mixtures to N-compounds with the reaction temperature. b) Evolution of the carbon, nitrogen and hydrogen weight loadings, as determined by elemental analysis, in the catalyst following exposure to catalysis conditions as a function of the Ga atomic fraction (x) in the bimetallic Ga_xNi_{1-x}/SiO_2 catalysts. In panel b, the standard deviation determined from several elemental analysis realizations is smaller than the dots on the figure.* 215

Figure 6.7**:** *a, g) Cross-sectional bright-field transmission electron micrographs and b, h), the respective metal nanoparticle size distributions. c, i) High-angle annular dark-field scanning-transmission electron microscopy (HAADF-STEM) micrographs and a-f, g-l) energy dispersive X-ray spectroscopy (EDS) compositional maps collected using Kα-emission lines for Ni, Ga and Si, respectively, for a-f) $Ga_{0.05}Ni_{0.95}/SiO_2$ and g-l) $Ga_{0.6}Ni_{0.40}/SiO_2$ catalysts following reduction activation. For size distributions, the equivalent nanoparticle diameter d was determined as $d = (4A/\pi)^{1/2}$, wherein A is the projected particle area.* 221

Figure 6.8: *a) Raman spectrum, b-c) (high-resolution) transmission electron micrographs, d,e) cross-sectional TEM micrographs, f) shape-specific metal nanoparticle size distributions, g) HAADF-STEM and h-l) cross-sectional EDS compositional maps for $Ga_{0.05}Ni_{0.95}/SiO_2$ catalyst following exposure to catalysis for 12 h. Reaction conditions: NH_3/methanol (N/C=2), T=773 K, P=2 bar, TOS=12 h. For particle size distributions, the equivalent diameter d was determined as $d = (4A/\pi)^{1/2}$ for spherical/ovoidal particles, $d = (A)^{1/2}$ for cubic-shaped* 222

particles, and $d(height) = \left(\sqrt{3}A\right)^{1/2}$ for tetrahedral particles, wherein A is the projected particle area.

Figure 6.9: *a,b) Cross-sectional TEM micrographs, c) metal nanoparticle size distribution, d) HAADF-STEM and e-i) cross-sectional EDS compositional maps for $Ga_{0.60}Ni_{0.40}/SiO_2$ catalyst following exposure to catalysis for 12 h. Reaction conditions: NH_3/methanol (N/C=2), T=773 K, P=2 bar, TOS=12 h. For the size distribution, the equivalent nanoparticle diameter (d) was determined as $d = (4A/\pi)^{1/2}$, wherein A is the projected particle area.* 223

Figure 6.10: *Ni2p and Ga2p core-level spectral regions of the X-ray photoemission spectra for $Ga_{0.05}Ni_{0.95}/SiO_2$ at different stages: top) oxidic catalyst precursor, middle) following in situ reduction and bottom) after exposure to reaction conditions for the synthesis of N-compounds by conversion of a NH_3/methanol feed stream. Reaction conditions: NH_3/methanol (N/C=2), T=773 K, P=2 bar, TOS=12 h.* 225

Figure 6.11: *In situ temperature-resolved high-resolution X-ray diffraction patterns (λ=0.9534 nm) recorded for a) Ni/SiO_2, b) $Ga_{0.05}Ni_{0.95}/SiO_2$ and c) $Ni_{0.4}Ga_{0.6}/SiO_2$ under exposure to 20% H_2/He reduction gas mixture. Initial and final diffractograms are shown at the bottom and top sides of the contour plot, respectively.* 227

Figure 6.12: *Normalized XANES spectra for selected $GaNi/SiO_2$ catalysts and the monometallic Ni/SiO_2 catalyst, following in situ reduction under flow of 20%H_2/He, recorded at the a,b) Ni-k and c,d) Ga-k absorption edges. Spectra for reference materials, i.e., metallic Ni foil, GaN and Ga_2O_3 have also been included for comparison. Panels b and d show blown-up views at the absorption edge.* 228

Figure 6.13: *a) Temperature-resolved high-resolution X-ray diffraction patterns (λ=0.9534 Å), b) evolution of the XRD diffraction peak intensities, normalized to the initial fcc metallic Ni, c) evolution of the a cell expansion parameter, relative to that detected for fcc Ni at RT, and d) evolution of the intensity of selected m/z mass spectrometry signals during an operando HRXRD experiment with Ni/SiO_2, under exposure of the NH_3/methanol reaction flow from RT to 673 K. e) Time-resolved high-resolution X-ray diffraction patterns during isothermal reaction stages at 673 K and f) 773 K. g) Evolution of the intensity of selected m/z mass spectrometry signals during the entire operando HRXRD experiment with Ni/SiO_2, including heating ramps and isothermal stages.* 231

Figure 6.14: *a) Temperature-resolved high-resolution X-ray diffraction patterns (λ=0.9534 Å), b) evolution of the a cell expansion parameter, relative to that detected for fcc Ni at RT, and c) evolution of the intensity of selected m/z mass spectrometry signals at the outlet gases during an operando HRXRD experiment with $Ga_{0.05}Ni_{0.95}/SiO_2$, under exposure of the NH_3/methanol reaction flow from RT to 673 K.* 234

Figure 6.15: *a) Operando time-resolved X-ray diffraction patterns (λ=0.9534 nm) collected a) during an isothermal stage at 673 K, b) during the heating from 673 K to 773 K and, c) during an isothermal stage at 773 K during the exposure of the $Ga_{0.05}Ni_{0.95}/SiO_2$ catalyst to flow of the NH_3/methanol (N/C=2) reaction mixture. P=P_{atm}. g) Time- and temperature-resolved evolution of selected m/z mass spectrometry signals at the outlet gases during the entire operando HRXRD experiment.* 235

Figure 6.16: *a-b, e-f) Normalized XANES spectra, c, g) Fourier-Transform of the k^3-weighted EXAFS function (phase uncorrected) and d, h) Imaginary part of the Fourier-Transform of the k^3-weighted EXAFS function at Ni-k (a-d) and Ga-k (e-h) absorption edges, respectively, for $Ga_{0.05}Ni_{0.95}/SiO_2$ after in situ reduction and following subsequent exposure to catalysis conditions at 773 K. Spectra collected in all cases at room temperature, following the corresponding treatment in the capillary XAS/XRD cell.* 238

Figure 6.17: *a) Operando, time-resolved evolution of the X-ray diffraction patterns (λ= 0.9534 Å) during the exposure of the $Ga_{0.05}Ni_{0.95}/SiO_2$ catalyst to reaction conditions for the conversion of a NH_3/methanol (N/C=2) feed stream at P=1 bar, and T= 673 K. Black traces represent the catalyst under the flow of the complete NH_3/methanol feed stream, while red traces correspond to reaction conditions wherein the ammonia flow was temporarily halted. Simulated XRD patterns for Ni_3C and $Ni_{0.98}Ga_{0.02}$ alloy are shown as reference on top. b) Contour plot collection of operando XRD patterns and (c,d) time evolution of selected mass spectrometry traces for outlet gases.* 240

Figure 6.18: *Operando, temperature-resolved evolution of the X-ray diffraction pattern (λ=1.54 Å) for a) Ni/SiO_2 and b) $Ga_{0.05}Ni_{0.95}/SiO_2$ under flow of NH_3. P=1 bar. c,d) Evolution of the cell parameter a with temperature for c) Ni/SiO_2, and d) $Ga_{0.05}Ni_{0.95}/SiO_2$ under reaction conditions, relative to the a_0 reference cell parameter determined at* 241

373 K after in situ catalyst reduction, i.e., a_0=3.5281(3)Å and a_0=3.5451(3)Å for Ni/SiO_2, and d) $Ga_{0.05}Ni_{0.95}/SiO_2$, respectively.

Figure 6.19: *Operando temperature-resolved X-ray diffraction patterns (λ=0.9534 Å) recorded for the bimetallic $Ga_{0.60}Ni_{0.40}/SiO_2$ catalyst a) during the heating ramp from 323 K to 673 K, b) during the 2-hour isothermal step at 673 K, and c) during the 2-hour isothermal step at 773 K, under flow of the reaction NH_3/methanol feed stream (N/C=2), at P=1 bar. On panel c, the arrow indicates an incipient diffraction signal which developed slowly with time-on-stream. d) Time- and temperature-resolved evolution of selected mass spectrometry traces for outlet gases. The plot on the top shows m/z signals used to follow the production of NH_3, MeOH, H_2O and CH_4 and CO, while the plot at the bottom shows the m/z signals used to follow the production of nitriles (C_1 and C_2), mono-, di- and tri-methylamine (MMA, DMA, TMA, respectively), acetaldehyde and dimethyl ether (DME).* 243

Figure 6.20: *X-ray diffraction patterns (λ=0.9534 Å) recorded for the bimetallic $Ga_{0.60}Ni_{0.4}/SiO_2$ catalyst after 2 h on-stream under reaction conditions at 773 K and after subsequent cooling to RT (NH_3/methanol feed (N/C=2), P=1 bar). The arrow indicates an incipient diffraction signal which developed slowly with time-on-stream at 773 K. Simulated diffraction patterns for NiGa and Ni_3Ga intermetallic compounds have been added for reference.* 244

Figure 6.21 *a-b, e-f) Normalized XANES spectra, c, g) Fourier-Transform of the k^3-weighted EXAFS function (phase uncorrected) and d, h) Imaginary part of the Fourier-Transform of the k^3-weighted EXAFS function at Ni-k and Ga-k absorption edges, respectively, for $Ga_{0.60}Ni_{0.40}/SiO_2$ at different stages (after in situ reduction and after exposure to catalysis conditions at 773 K. Spectra collected in all cases at room temperature following the corresponding treatment in the capillary XAS/XRD cell.* 246

List of tables

Chapter 1 *p.*

Table 1.1: *Interstitial site position in a face-centered cubic (fcc) crystal system with tetrahedra and octahedra coordination and the geometrically calculated r_i/r_M ratio.* *54*

Chapter 3 *p.*

Table 3.1: *Details on analysis settings at the SCION 456 and Agilent 8860 System gas chromatographs applied for online analytics during catalysis tests.126* *129*

Chapter 4 *p.*

Table 4.1: *Individual adsorption and co-adsorption energies of CO and NHx species, on γ-Mo_2N(100) as determined by DFT calculations (GGA-PBE). All adsorption energies are expressed in kJ mol^{-1}.* *149*

Chapter 5 *p.*

Table 5.1: Near-surface nitrogen-to-metal atomic ratios, as determined by XPS, for the MnMo mixed-metal and monometallic reference catalysts after 10 h of a $3NH_3$: 1CO: $1H_2$ feed exposure at 723 K. *190*

Appendix II: List of symbol and acronyms

List of abbreviations

A	*Projected particle area of a particle in TEM*	***C_4***	*Racemic C_4 hydrocarbon*
AD	*Anaerobic digestion*	***CCU***	*Carbon capture and utilization*
AECs	*Alkaline electrolysis cells*	***CCWT***	*Continuous Cauchy Wavelet Transforms*
AEM	*Alkaline anion exchange membrane*	***CI-NEB***	*Climbing Image-Nudged Elastic Band*
A_i	*Interstitial defects*	***C_n***	*Compound or group of compounds with n carbon atoms in the carbon chain*
A_i	*Peak area of compound i in GC*	***CN***	*Coordination number*
ASF	*Anderson-Schulz-Flory*	***d***	*Equivalent particle diameter determined by TEM micrographs*
atm	*Atmospheric*	***DAC***	*Direct air capture*
ATR	*Autothermal reforming*	***DF***	*Dark field*
AWE	*Alkaline water electrolysis*	***fcc***	*Face-centered cubic*
bbc	*Body-centered cubic*	***FEGs***	*Field-Emission Electron Guns*
BE	*Binding energy*	***$f_{i/Ar}$***	*Molar-based response factor of a compound i relative to Ar*
BET	*Brunauer–Emmett–Teller*	***$f_{i/CH4}$***	*Weight-based response factor of a compound i relative to methane*
BF	*Bright field*	***FID***	*Flame ionization detector*
BJH	*Barrett-Joyner-Halenda*	***FT***	*Fischer-Tropsch*
BMA	*Blausäure aus Methan and Ammoniak*	***FT***	*Fourier Transform*
C_2,	*Ethane*	***FTICR***	*Fourier transform ion cyclotron resonance*
$C_2^{//}$	*Ethylene*	***FWHM***	*Full width at half maximum*
C_3,	*Propane*	***GC***	*Gas Chromatograph(y)*
$C_3^{//}$,	*Propene*		

GGA	*Generalized gradient approximation*	**MeCN**	*Acetonitrile*
GHG	*Greenhouse gas*	**MMA**	*Monomethylamine*
G_f	*Formation Gibbs free energies*	**MO_x**	*Metal oxide*
H_2-TPR	*Hydrogen temperature programmed reduction*	**MS**	*Mass spectroscopy*
HAADF	*High-angle annular dark-field*	**MTNs**	*transition metal nitrides*
hcp	*Hexagonal closed-packed*	**MTO**	*Methanol to Olefins*
HEA	*High-entropy alloys*	**M_w**	*Molecular weight*
HER	*Hydrogen evolution reaction*	**NRR**	*Nitrogen reduction reactions*
hkl	*Miller index*	**OD**	*Outer diameter*
HR-TEM	*High-resolution transmission Electron Microscopy (*	**OER**	*Oxygen evolution reaction*
HR-XRD	*High resolution X-ray diffraction*	**Oh**	*Octahedral*
Hydrocarbons	*HCs*	**OS_M**	*Oxidation states of a Metal M*
i	*Compound $_i$*	**P**	*Pressure*
ICP-OES	*Inductively Coupled Plasma Optical Emission*	**PAW**	*Projector-augmented wave*
ICSD	*Inorganic Crystal Structure Database*	**PCET**	*Proton-coupled electron transfer (*
ID	*Internal diameter*	**PEM**	*Proton exchange membrane*
IEA	*International Energy Agency*	**PEMECs**	*Polymer electrolyte membrane electrolysis cells*
k_b	*Boltzmann constant*	**POX**	*Partial oxidation*
KE	*Kinetic energy*	**PRSV**	*Peng-Robinson-Stryjek-Vera*
LiNR	*Lithium-mediated nitrogen reduction*	**PtX**	*Power-to-X*
M	*Metal*	**R**	*Radial distances to neighboring atoms in EXAFS*
m/z	*Mass-to-charge ratio*	**r_i**	*i-product formation rates*

-R	*Substituent of an organic compound*	T_h	*Tetrahedral*
RPBE	*Revised Perdew-Burke-Ernzerhof*	***TMA***	*Trimethylamine*
RT	*Room temperature*	***TMN***	*Transition metal nitrides*
r-WGSR	*Reverse water splitting reaction*	***TOS***	*Time on stream*
SAAs	*Single-atom alloys*	***TS***	*Transition states*
SDD	*Silicon Drift detector*	V_a	*vacancies*
SEI	*Solid-electrolyte interphase*	***VASP***	*Vienna Ab-initio Simulation Package*
SEM	*Scanning electron microscopy*	***WGSR***	*Water gas shift reaction*
S_i	*Product selectivities of a compound i*	***WHSV***	*Weight hour space velocity*
SMR	*Steam methane reforming*	$\widetilde{W}_i$	*Molar flow of compound*
SOE	*Solid oxide electrolyzers*	***XANES***	*X-ray Absorption Near Edge Structure (*
SOECs	*Solid oxide electrolysis cells*	***XAS***	*X-ray absorption*
SR-XPS	*Synchrotron-radiation X-ray photoelectron spectroscopy*	X_i	*Compound i conversion*
STEM	*Scanning-transmission electron microscopy*	***XPS***	*X-ray photoelectron spectroscopy*
T	*Temperature*	***XPS***	*X-ray photoelectron spectroscopy*
t	*time*	***XRD***	*X-ray diffraction*
TCD	*Thermal conductivity detector*	***XRPD***	*Ex situ powder X-ray diffraction*
TEM	*Transmission Electron Microscopy*	***ZPE***	*Zero-point energy of the gas-phase compound derived from DFT*

List of greek symbols and operator

θ	Diffraction angle	**α, β, γ, ε , δ**	Crystal structure phases
∆	Difference operator	**β**	Integral breadth in XRD
Ø	Granules diameter	**λ**	Wavelength
α	Anderson-Schulz-Flory chain growth probability	μ_i	chemical potential of the i compound in the gas phase
α, β, γ	Cell parameters in crystallography	σ^2	Debye-Waller factor in XAS
	Apparent reaction kinetic orders		

Appendix III: Supporting information for Chapter 3

Table A.III.1: *List of chromatographic response factors employed for the quantification of compounds detected in both TCD (relative to Ar) and FID (relative to methane) channels of the gas chromatographs employed for online analytics during catalyst testing.*

Compound TCD	$f_{(i/Ar)TCD}$
CO_2	0.96
NH_3	0.37
Ar	1
N_2	0.88
Methane	0.65
CO	0.91
Compound FID	$f_{(i/CH4)FID}$
HCs	1
HCN	0.35
AcCN	0.44
Propionitrile	0.62
Acrylonitrile	0.64
n-Butyronitrile	0.74
Iso-Butyronitrile	0.72
Valeronitrile	0.9
Methanol	0.31
Ethanol	0.46
Propanol	0.6
Iso-Propanol	0.53
Butanol	0.66
Iso-Butanol	0.68
Methylamine	0.31
Dimethylamine	0.39
Trimethylamine	0.46
DME	0.37
Acetaldehyde	0.48
Other N compounds	0.8

***Table A.III.2**: Relative abundances expected for different fragmentation ions for selected reaction product compounds following electron impact ionization. Abundances below 4 % have been excluded.*

m/z	25	27	30	31	37	41	43	54
Acetonitrile						100		
HCN		100						
Methylamine		8.7	100	66				
Propionitrile		15.2						85
Ethane		33.7	26.6					
Ethylene	8.4	62.5						
Propane		42.4				14	23.8	
Propene		40			13.4	100		

Appendix IV: Supporting information for Chapter 4

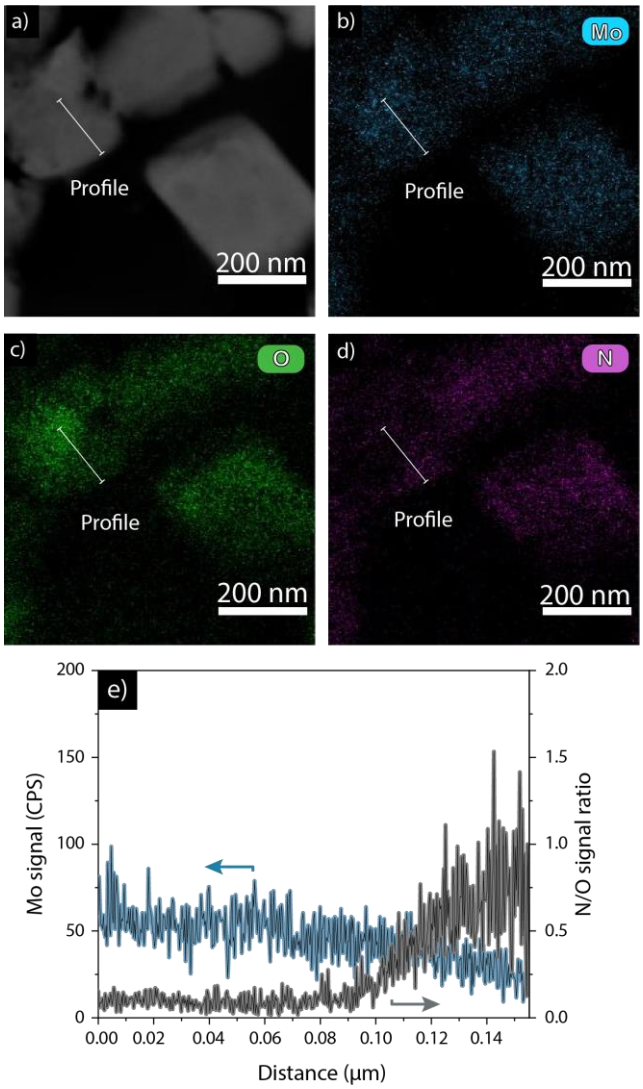

***Figure* A.IV.1:** *a) High-angle annular dark-field (HAADF) STEM micrograph, b-d) EDS compositional maps for Mo, N, and O, respectively and e) spatial evolution of the Mo signal and the N/O signal ratio along the linescan marked on panels b-d (distance expressed from left to right along the profile segment), of a representative particle cross-section of MoO_3 exposed to the reactive $3NH_3$: 1CO: $1H_2$ feed stream at 723 K for 10 h.*

Table A.IV.1: *X-ray photoemission band assignments in the Mo3d and Mo3p + N1s core level spectral regions for the pristine MoO_3 catalyst precursor, following exposure to reaction conditions for the direct conversion of NH_3/syngas to acetonitrile at T=723 K for 10 h, and a γ-Mo_2N standard obtained by ex situ high-temperature nitridation of MoO_3 (see* ***Chapter 3: Methods*** *for details).*

Material	**Core level**	**Species**	**Position (eV)**	**Conc. (%).**	**$N1s_{(M-N)}/Mo3d_{5/2}$ at. ratio**
MoO_3	Mo $3d_{5/2}$	Mo^{5+}	230.92		
		Mo^{6+}	232.72		
	Mo $3p_{3/2}$	Mo^{5+}	396.63		
		Mo^{6+}	398.2		
MoO_3 / 723 K/ $3NH_3$:1CO:$1H_2$ feed/ 10 h	Mo $3d_{5/2}$	Mo^{4+}(-N)	228.35	27.50	0.77
		Mo^{4+}(-O)	229.66	3.00	
		Mo^{5+}	230.85	9.81	
		Mo^{6+}	232.44	5.77	
	N1s	MoN_x	396.51	35.50	
		C_xH_y-N	398.68	18.43	
	Mo $3p_{3/2}$	Mo^{4+}(-N)	394.16		
		Mo^{4+}(-O)	395.53		
		Mo^{5+}	396.76		
		Mo^{6+}	398.33		
Mo_2N standard	Mo $3d_{5/2}$	Mo^0	227.79	10.45	0.55
		Mo^{4+}(-N)	228.21	35.79	
		Mo^{4+}(-O)	229.85	8.61	
		Mo^{6+}	232.08	4.55	
	N1s	MoN_x	397.36	32.66	
		C_xH_y-N	399.95	7.93	
	Mo $3p_{3/2}$	Mo^0	391.89		
		Mo^{4+}(-N)	393.99		
		Mo^{4+}(-O)	395.67		
		Mo^{6+}	397.50		

Appendix V: Supporting information for Chapter 5

Local structure determination for the working MnMo catalyst via EXAFS fitting to computationally optimized structural models

Information on the local structure of the MnMo catalyst developed under process conditions (873 K, $3NH_3$: $1H_2$: 1CO) was gained via EXAFS fitting at both the Mn-k and Mo-k edges. This analysis was conducted using various structural models computationally optimized through periodic DFT calculations at the PAW-RPBE theory level (**Figures A.V. 2- A.V. 3**). The extraction of the scattering paths and the fitting of the experimental spectra were performed in the Artemis application from Demeter software package (version 0.9.26) based on IFEFFIT. Results of the EXAFS fitting and the values of the free parameters for each model are reported in **Figures A.V. 4- A.V. 6**- and in **Tables A.V. 2- A.V. 4**, respectively. In each case, the average coordination number (CN) along each simulated $\chi_i(k)$ scattering path was fixed to the one in the DFT-optimized structural model. Only single scattering paths with a rank> 50 and R_{eff}< 2.5 Å were considered to fit the first coordination shell of the spectra collected at the Mo-k and Mn-k edges extracted in a 1.0< k($Å^{-1}$)< 11 and 1.0< k($Å^{-1}$)< 8 range, respectively. Analysis of the second coordination shell of Mn-rich domains was performed considering single scattering paths R_{eff}< 3.65 Å.

In order to reduce the number of fitting variables, a common Debye-Waller factor (σ^2) and adjustment of the bond length (ΔR) were assigned to the paths depending on the nature of the scattering atom, i.e., O, N, Mn or Mo. The fits were performed on a multiple k-weighted approach (k^1, k^2, k^3) to distribute the sensitivity of Xv^2 over the whole k-range evaluated. To assess the suitability with which the computational structural model is compatible with the experimental EXAFS data, the R-factor and Xv^2 were considered.

Out of the models scrutinized, the structure a.3 corresponding to a bimetallic $Mn_{0.5}Mo_{0.5}N$ nitride with NN1 Schottky-type defects (N and Mn vacancies, at a defect density of 1 defect/unit cell) provided the best correspondence to the experimental spectrum at the examined first metal coordination sphere, delivering minimum values of the statistical descriptors (R-

factor and Xv^2) both at the Mn-k and Mo-k edges (**Figures A.V. 4- A.V. 5** and **Tables A.V. 2- A.V. 3**). The models a.1 and a.5 describing a stoichiometric $Mn_{0.5}Mo_{0.5}N$ nitride and a bimetallic MnMo oxynitride, respectively, were found to acceptably represent the experimental data in the Mn-k edge, but not so faithfully at the Mo-k edge. Structural models a.2 and a.4, which consider anionic defects (one N vacancy per unit cell) and anti-site point defects (one N atom isomorphically replaced by Mn occupying anti-site position) resulted in negative Debye-Waller factors with non-physical sense, both at the Mn-k and Mo-k edges.

The analysis was then extended to radial (second shell) coordination distances in the range of 1.0<R(Å)<3.6, at which scattering events are apparent at the Mn-k EXAFS spectrum (**Figure A.V.6** and **Table A.V.3**). In this case, considering solely those scattering paths simulated for the Schottky defective Mn/Mo mixed metal nitride a.3 did not deliver a satisfactory fit to the experimental data. Hence, we attempted to incorporate additional scattering paths of structural models rich in Mn, such as MnN, MnN_xO_y oxynitrides and MnO, with unsatisfactory results. The inclusion of second scattering paths extracted from a Mn-Mo mixed metal oxynitride cluster allowed to reproduce specific spectral features observed in the experimental data. However, the high EXAFS Debye-Waller factors $\sigma^2 > 0.01$ Å^2, and the increased number of variable parameters required to attain a satisfactory fit, also hinted at a significant structural disorder in the developed MnMo catalyst. All taken together, EXAFS analysis reinforces the notion of a material showing local defects and compositional heterogeneities, possibly in the form of Mn-enriched domains with slightly lower local nitridation degrees (as observed with STEM-EDS), whose complexity hinders a more precise structural elucidation.

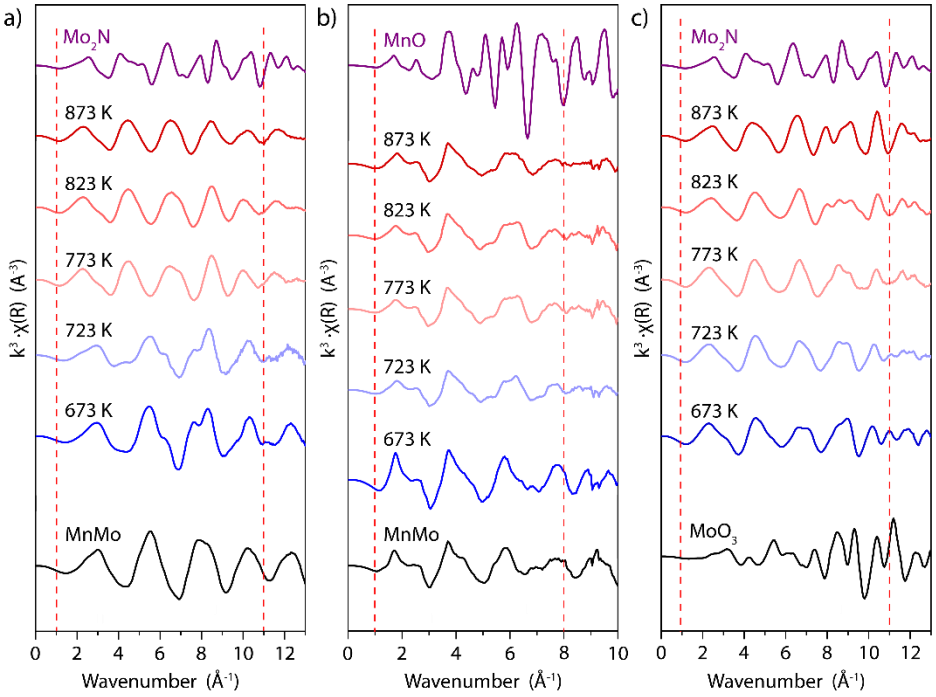

Figure A.V.1: *a, b) k^3-weighted EXAFS spectra in the reciprocal k space and the corresponding at the Mo-k and Mn-k edges, after exposure of the $(NH_4)_2H_2Mn_4Mo_4O_{18}{\cdot}2H_2O$ precursor to reaction conditions ($3NH_3$: $1H_2$: 1CO, P_{atm}) at increasing temperatures. c) k^3-weighted EXAFS spectra in the reciprocal k space and the corresponding collected at the Mo-k edge, after exposure of the monometallic MoO_3 catalyst to reaction conditions ($3NH_3$: $1H_2$: 1CO, P_{atm}) at increasing temperatures. The red dashed lines delimit the k-range where the Hanning apodization window was applied for the data reduction.*

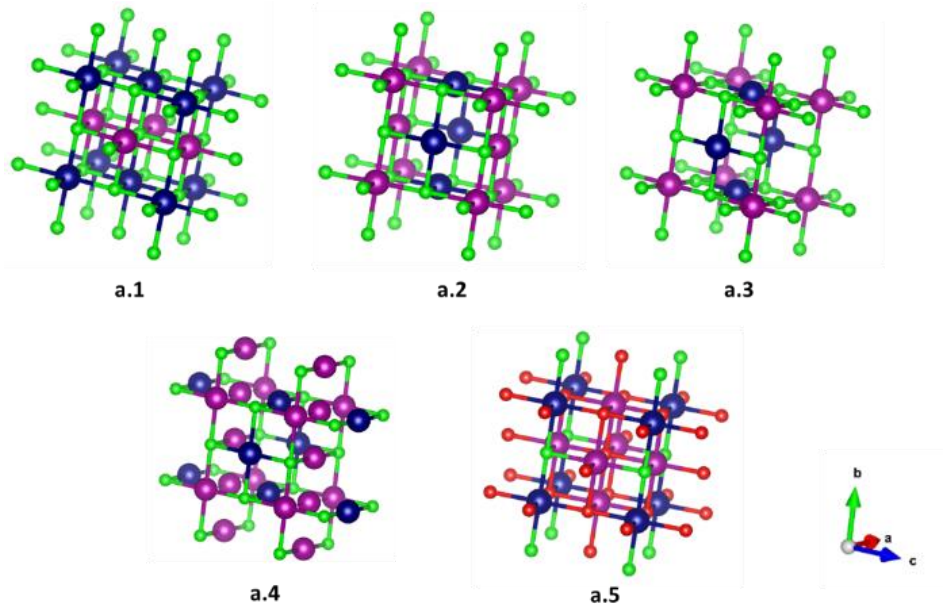

Figure A.V.2: *Illustrations of the DFT-optimized structural models (at the PAW-PBE theory level) used to disentangle the local structure of MnMo catalyst at the first coordination shell (1<R(Å)<2.5) via EXAFS fitting collected at the Mn and Mo-k edge. Model* ***a.1*** *corresponds to a stoichiometric* $Mn_{0.5}Mo_{0.5}N$ *nitride; models* ***a.2*** *&* ***a.3*** *consider the* $Mn_{0.5}Mo_{0.5}N$ *bearing anionic and cationic defects, e.i., one N vacancy per unit cell and NN1 Schottky-type defects (N and Mn vacancies, at a density of 1 defect/unit cell), respectively; model* ***a.4*** *illustrates the* $Mn_{0.5}Mo_{0.5}N$ *with anti-site point defects (one N atom isomorphically replaced by Mn occupying anti-site position); and model* ***a.5*** *represents a bimetallic MnMo oxynitride originated from the concurrent isomorphic substitution of three nitrogen atoms with one oxygen atom and the replacement of one manganese atom by one molybdenum atom in each unit cell of a cubic MnN. Mn atoms are shown in purple, Mo in dark blue, N in light green, and oxygen in red.*

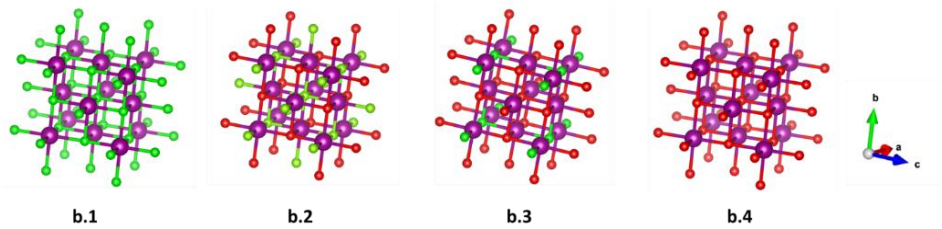

Figure A.V.3: *Illustrations of the DFT-optimized structural models (at the PAW-PBE theory level) used to disentangle the Mn-rich domains of the MnMo catalyst extended to the second coordination shell (1< R(Å)< 3.6) via EXAFS fitting at the Mn-k edge. Model* ***b.1*** *corresponds to a cubic MnN nitride; models* ***b.2*** *&* ***b.3*** *consider* MnN_xO_y *oxynitrides formed by including 2 and 3 oxygen atoms in substitutional positions of N per unit cell of the pristine cubic MnN nitride, respectively; model* ***b.4*** *illustrates a cubic MnO. Mn atoms are shown in purple, N in light green, and oxygen in red.*

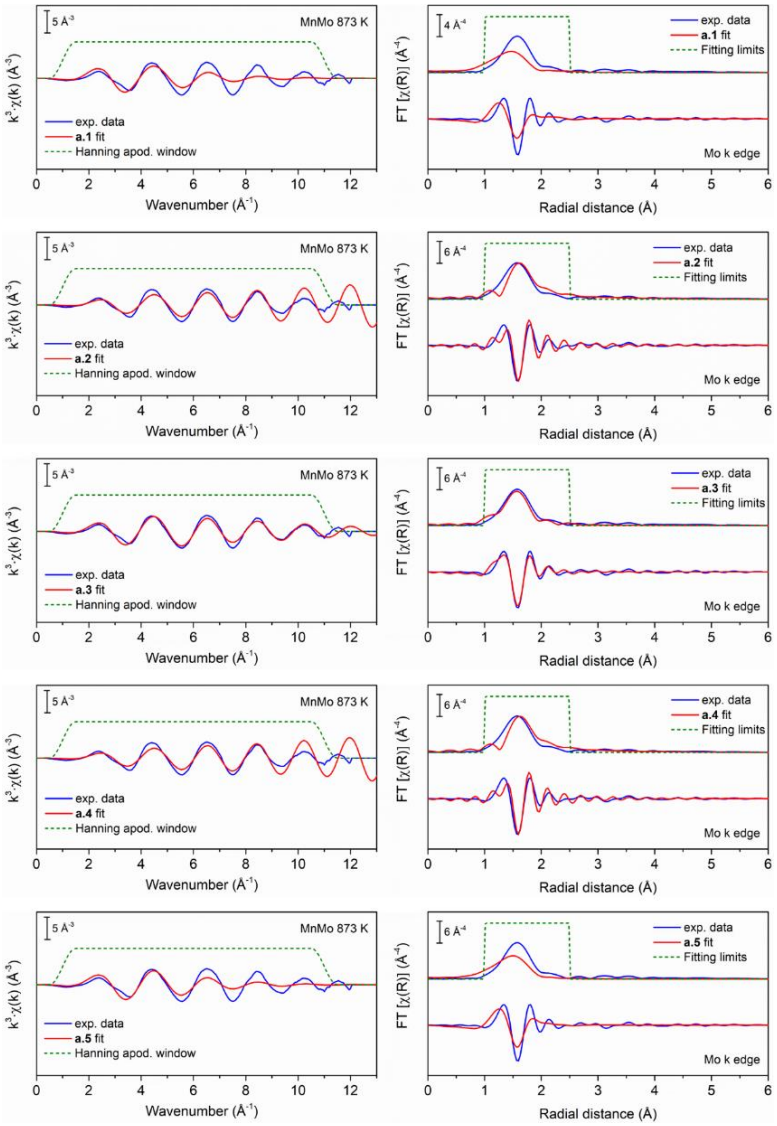

Figure A.V.4. First coordination shell analysis at the Mo-k edge: *Fitting of the k^3-weighted EXAFS data of the MnMo catalyst developed under process conditions (873 K, $3NH_3$:$1H_2$:1CO) to various DFT-optimized structural models (see models in Figure FE1). (left) k^3-weighted EXAFS function in the reciprocal k space. The green dashed lines delimit the k-range where the Hanning apodization window was applied for the data reduction. (right) Fourier Transform of the k^3-weighted EXAFS function (no phase correction). The experimental data were fitted in the range 1.0<R(Å)<2.5 (multiple k-weighted approach k^1,k^2,k^3). See* ***Table A.V. 2*** *for details on the scattering paths and fitting results.*

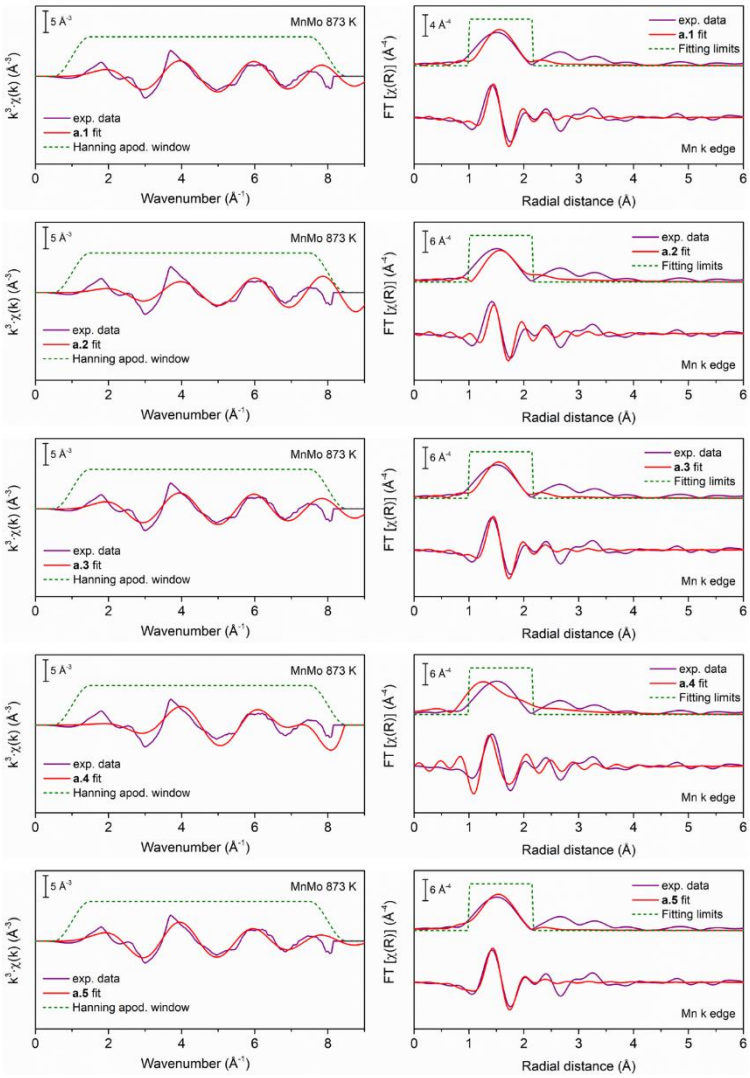

Figure A.V.5: First coordination shell analysis at the Mn-k edge: *Fitting of the k3-weighted EXAFS data of the MnMo catalyst developed under process conditions (873 K, $3NH_3$:$1H_2$:1CO) to various DFT-optimized structural models (see models in Figure FE1). (left) k^3-weighted EXAFS function in the reciprocal k space. The green dashed lines delimit the k-range where the Hanning apodization window was applied for the data reduction. (right) Fourier Transform of the k^3-weighted EXAFS function (no phase correction). The experimental data were fitted in the range 1.0<R(Å)<2.1 (multiple k-weighted approach k^1,k^2,k^3). See* ***Table A.V. 3*** *for details on the scattering paths and fitting results.*

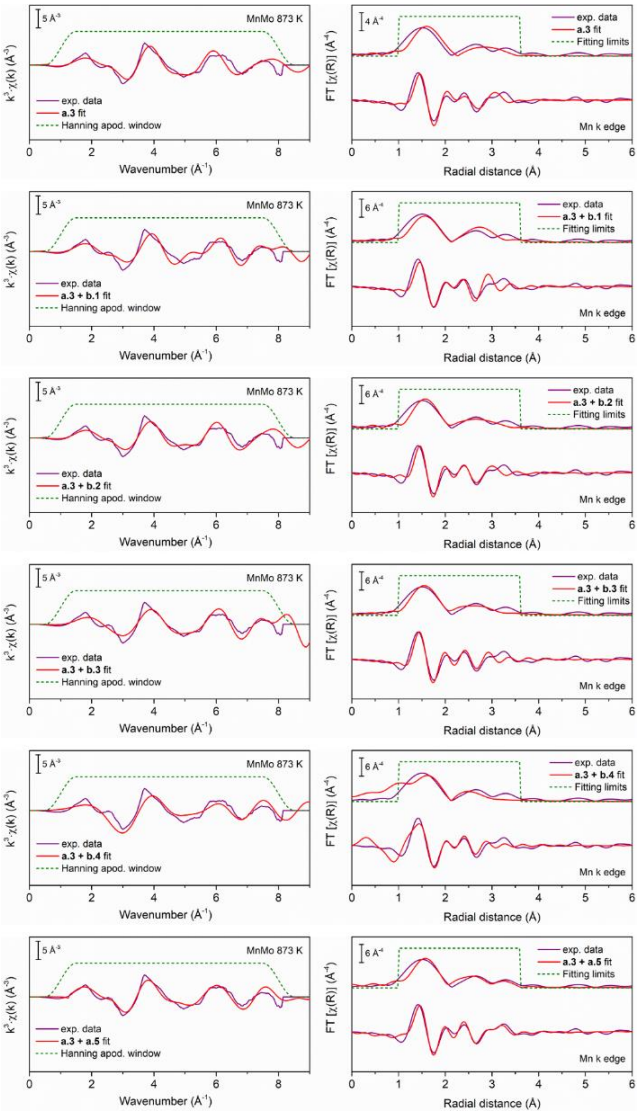

Figure A.V.6. Second coordination shell analysis at the Mn-k edge: *Fitting of the k^3-weighted EXAFS data of the MnMo catalyst developed under process conditions (873 K, $3NH_3$:$1H_2$:1CO) to various DFT-optimized structural models (see models in Figure FE2). (left) k^3-weighted EXAFS function in the reciprocal k space. The green dashed lines delimit the k-range where the Hanning apodization window was applied for the data reduction. (right) Fourier Transform of the k3 - weighted EXAFS function (no phase correction). The experimental data were fitted in the range 1.0<R(Å)<3.6 (multiple k-weighted approach k^1,k^2,k^3). See* ***Table A.V. 4*** *for details on the scattering paths and fitting results.*

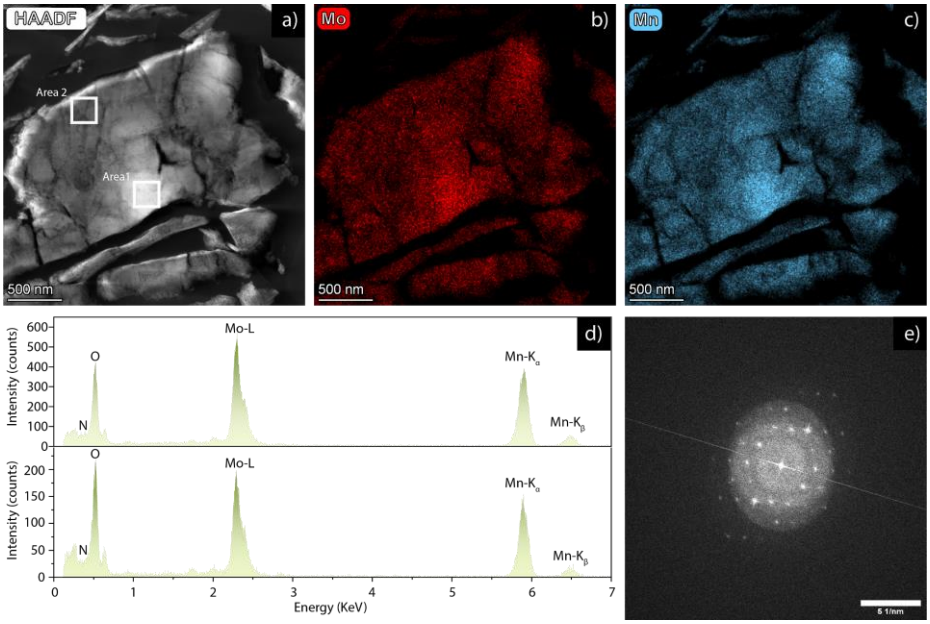

Figure A.V.7: *a) High-resolution bright-field scanning transmission electron micrograph (STEM) and the corresponding EDS compositional maps for b) Mo and c) Mn elements; d) EDS spectra collected at areas 1 and 2, as marked on panel a; and e) Fast Fourier Transform derived from the high-resolution scanning transmission electron microscopy (HRSTEM) imaging of the MnMo mixed-metal catalyst following exposure to under reactive conditions for 10 min. 3 NH_3:1 CO:1 H_2 feed, T=723 K, P=P_{atm}.*

***Table A.V.1**. Acetonitrile (MeCN) selectivity and formation rate, lumped nitrile (C_1-C_5) formation rate, CO conversion, CO_2 selectivity over the course of 9-11 h on-stream and percentual drop in acetonitrile (MeCN) production rate experience over the course of 3 h on-stream, attained with the series of bimetallic MMo catalysts applied in the direct conversion of NH_3/syngas mixtures. Reaction conditions: T= 723 K, P=3 bar, gas feed molar composition: 2 NH_3:1 CO:1 H_2, X_{CO}< 18 %.*

Metal-based catalyst	MeCN selectivity (C%, CO_2-free)	r_{MeCN} (mmol g_{cat}^{-1} min^{-1})	$r_{Nitriles}$ (mmol g_{cat}^{-1} min^{-1})	CO conv. (%)	CO_2 select. (%)	Drop of r_{MeCN} over first 3h TOS (%)
Mo	33.0	0.013	0.054	8.9	56.1	62.5
MnMo	63.0	0.049	0.100	17.2	48.4	13.0
CoMo	29.6	0.052	0.180	6.9	49.6	69.8
NiMo	19.7	0.157	0.351	7.9	41.4	52.2
CuMo	12.0	0.004	0.058	3.7	41.4	51.8
ZnMo	51.2	0.027	0.065	17.5	39.7	41.7

***Table A.V.2**. Results of the EXAFS fitting for the first coordination shell analysis at the Mo-k edge of the MnMo catalyst developed under process conditions (873 K, $3NH_3$:$1H_2$:1CO) to various DFT-optimized structural models depicted in Figure FE1. The experimental data (k-range: 1.0-11 $Å^{-1}$) were fitted in the R-range 1.0<R(Å)<2.5. ΔR gives the adjustment of the bond length and σ^2 represents the Debye-Waller factor. R-factor and reduced χv^2 represent the misfit between experimental data and theory and the goodness of the fit, respectively. Value parameters that worsen the quality of the fit or took values which are physically nonsensible are highlighted in red, as an eye guide to discard the model evaluated*

DFT model	Path	CN	Reff (Å)	ΔE_0 (eV)	ΔR (Å)	σ^2 ($Å^2$)	N_{ind}/ N_{var}	R factor	reduced χv^2 ($x10^3$)
a.1	*N*	3	2.127	-0.7 ±2.7	-0.08 (5)	0.015 (5)	9/3	0.241	132.2
	N	3	2.233						
a.2	*N*	1	2.145	2.2 ±0.1	-0.07 (2)	-0.004 (2)	9/3	0.142	100.7
	N	1	2.215						
a.3	*N*	2	2.145	0.2 ±1.0	-0.07 (2)	0.004 (1)	9/3	0.041	30.6
	N	2	2.215						
a.4	*N*	1	2.145	1.1 ±2.8	-0.06 (3)	-0.004 (2)	9/3	0.160	116.8
	N	1	2.215						
a.5	*N*	2	2.189	1.0 ±2.6	-0.09 (5)	0.018 (5)	9/3	0.193	103.3
	O	4	2.189						

***Table A.V.3**. Results of the EXAFS fitting for the first coordination shell analysis at the Mn-k edge of the MnMo catalyst developed under process conditions (873 K, 3NH3:1H2:1CO) to various DFT-optimized structural models depicted in Figure FE1. The experimental data (k-range: 1.0-8.0 $Å^{-1}$) were fitted in the R-range 1.0<R(Å)<2.1. ΔR gives the adjustment of the bond length and σ^2 represents the Debye-Waller factor. R-factor and reduced χv^2 represent the misfit between experimental data and theory and the goodness of the fit, respectively. Value parameters that worsen the quality of the fit or took values which are physically nonsensible are highlighted in red, as an eye guide to discard the model evaluated.*

DFT model	Path	CN	Reff (Å)	ΔE_0 (eV)	ΔR (Å)	σ^2 ($Å^2$)	N_{ind}/N_{var}	R factor	reduced χv^2 ($x10^3$)
a.1	*N*	2	2.127	-0.3 ±4.5	-0.06 (6)	0.002 (6)	5/3	0.112	11.6
	N	2	2.233						
a.2	*N*	1	2.145	-1.0 ±10	-0.1 (1)	-0.01 (1)	5/3	0.313	32.5
	N	1	2.215						
a.3	*N*	2	2.145	-1.2 ±3.8	-0.06 (6)	0.004 (6)	5/3	0.091	9.5
	N	2	2.215						
a.4	*Mo*	1	2.145	-13 ±25	-0.1 (2)	σ^2_{Mo}=-0.01 (2) σ^2_{Mn}=0.01 (2)	5/3	0.305	68.5
	Mn	2	2.145						
a.5	*N*	2	2.189	-0.3 ±2.5	-0.08 (4)	0.014 (3)	5/3	0.031	3.7
	O	4	2.189						

Table A.V. 4 *Results of the EXAFS fitting for the second coordination shell analysis at the Mn-k edge of the MnMo catalyst developed under process conditions (873 K, $3NH_3$:$1H_2$:1CO) to various DFT-optimized structural models depicted in Figure FE2. The experimental data (k-range: 1.0-8.0 $Å^{-1}$) were fitted in the R-range 1.0<R(Å)<3.6. ΔR gives the adjustment of the bond length and σ^2 represents the Debye-Waller factor. R-factor and reduced χv^2 represent the misfit between experimental data and theory and the goodness of the fit, respectively. Value parameters that worsen the quality of the fit or took values which are physically nonsensible are highlighted in red, as an eye guide to discard the model evaluated.*

DFT model	Path	CN	Reff (Å)	ΔE_0 (eV)	ΔR (Å)	σ^2 ($Å^2$)	N_{ind}/ N_{var}	R factor	Reduced χv^2 ($x10^3$)
a.3	*N*	2	2.145	1.6 ±1.7	ΔR_N= -0.02 (3) ΔR_{Mo}= -0.04 (9)	σ^2_N=0.006 (5) σ^2_{Mo}=0.03 (1)	11 /5	0.126	4.66
	N	2	2.215						
	Mo	2	3.033						
	Mo	4	3.083						
	Mo	2	3.133						
a.3 + b.1	**a.3**			1.1 ±1.8	ΔR_N= -0.03 (4) ΔR_{Mn}= -0.4 (1)	σ^2_N=0.006 (5) σ^2_{Mn}=0.06 (3)	11 /5	0.170	5.89
	N	2	2.145						
	N	2	2.215						
	b.1								
	Mn	12	2.901						
	N	8	3.553						
a.3 + b.2	**a.3**			1.3 ±2.2	ΔR_N= -0.03 (4) ΔR_{Mn}= -0.4 (2) ΔR_O= -0.1 (1)	σ^2_N=0.004 (5) σ^2_{Mn}=0.06 (3) σ^2_O=0.02 (2)	11 /7	0.137	7.26
	N	2	2.145						
	N	2	2.215						
	b.2								
	Mn	12	2.964						
	O	8	3.630						

a.3 + b.3	**a.3**			-0.3 ±3.6	ΔR_N= -0.05 (6) ΔR_{Mn}= -0.4 (3) ΔR_O= -0.3 (1)	σ^2_N=0.004 (6) σ^2_{Mn}=0.07 (6) σ^2_O=-0.03 (1)	11 /7	0.171	10.26
	N	2	2.145						
	N	2	2.215						
	b.3								
	Mn	12	3.020						
	O	8	3.648						
a.3 + b.4	**a.3**			-19 ±9	ΔR_N= -3.4 (2) ΔR_{Mn}= -0.3 (2) ΔR_O= 0.3 (1)	σ^2_N=0.06 (2) σ^2_{Mn}=0.03 (1) σ^2_O=0.01 (1)	11 /7	0.190	12.07
	N	2	2.145						
	N	2	2.215						
	b.4								
	O	6	2.224						
	Mn	12	3.145						
a.3 + a.5	**a.3**			6.0 ±2.1	ΔR_N= 0.3 (1) ΔR_O= -0.04 (4) ΔR_{Mo}= 0.2 (1) ΔR_{Mn}= 0.1 (1)	σ^2_N=0.05 (3) σ^2_O=0.009 (5) σ^2_{Mo}=0.02 (1) σ^2_{Mn}=0.03 (1)	11 /9	0.049	3.99
	N	2	2.145						
	N	2	2.215						
	a.5								
	N	2	2.189						
	O	4	2.189						
	Mo	4	3.096						
	Mn	8	3.096						

Appendix VI: Supporting information for Chapter 6: First-principles DFT and thermochemistry insights into Ni metal and mixed (Ni, Ga)-metal nitride/carbides

Ga doping into fcc Ni

The relative stability of NiGa alloys was studied by ab initio thermochemistry. **Figure A.VI.1** shows the evolution of the energy of formation (E_f) as a function of the degree of lattice substitution of Ga into the *fcc* Ni (Fm-3m) crystal lattice. As observed, E_f took negative values and decreased systematically on increasing Ga content up to 25 at%. At this Ga doping level, E_f was -1.27 eV. These results indicate the higher thermodynamic stability of NiGa alloys, relative to the neat *fcc* Ni phase, hence their favorable formation in line with the experimental XRD evidence. Further increasing the Ga doping level to 50% resulted in essentially no further decrease of the formation energy, indicating no additional stabilization.

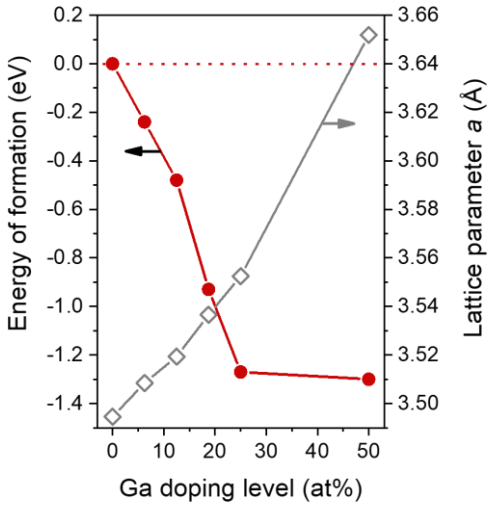

Figure A.VI.1: *Evolution of the energy of formation and the lattice cell parameter a for fcc Ni(Ga) (Fm-3m) as a function of the degree of lattice Ni replacement by Ga, as predicted by DFT calculations (PAW-PBE). The dotted line serves as a guide to the eye for E_f=0, corresponding to neat fcc Ni. Faced centered cubic Ni (Fm-3m) and orthorhombic Ga (Cmce) have been used as reference compounds.*

Experimentally, *fcc* NiGa alloys have been shown to be stable up to Ga contents of approximately 22.3 at%, beyond which content intermetallic compounds are preferably formed.[1] As also observed in **Figure A.VI.1**, addition of the bulkier Ga into the lattice is predicted to result in a systematic enlargement of the lattice parameter *a*, by a ca. 1.7 % at a Ga content of 25 at%.

Interstitial atoms in *fcc* NiGa alloys

Ab initio thermodynamics was also applied to assess the impact of Ga incorporation into *fcc* NiGa alloys on the energetics of interstitial dopants. Given that the catalysts are exposed to sources of both carbon (CH_3OH) and nitrogen (NH_3), the insertion of both C and N interstitials was studied. Both tetrahedral and octahedral interstitial positions defined by the *Fm-3m* lattice were probed. Tetrahedral interstitial occupation was found to be unstable and C/N migration the nearest octahedral interstitial was observed in all cases upon structural optimization.

Figure A.VI.2 shows the energy of interstitial defect formation upon C (red) or N (blue) uptake into octahedral interstitials as a function of the carbon and nitrogen chemical potential, respectively. Interstitial atom uptake is predicted to be endothermic over the entire range of chemical potential studied. However, the energy of defect formation becomes markedly affected by the incorporation of Ga into lattice positions. Already at a Ga content of 6.25 at%, particularly the incorporation of N becomes significantly less endothermic compared to the nest *fcc* Ni host. At a Ga content of 12.5 at%, the energy of interstitial dopant uptake is further reduced and the traces for E_{def} for C and N interstitial dopants essentially overlap, indicating a similar energetics regardless of the nature of the interstitial dopant. Moreover, at high carbon and nitrogen chemical potentials the uptake energy penalty becomes smaller than the background thermal energy under process conditions, suggesting the feasibility of interstitial atom incorporation. This trend towards more favorable interstitial defect formation is reverted when the Ga content is further increased to 25 at%. At this higher Ga content, the traces shift upwards and the corresponding E_{def} surpass those in the pristine *fcc* Ni lattice.

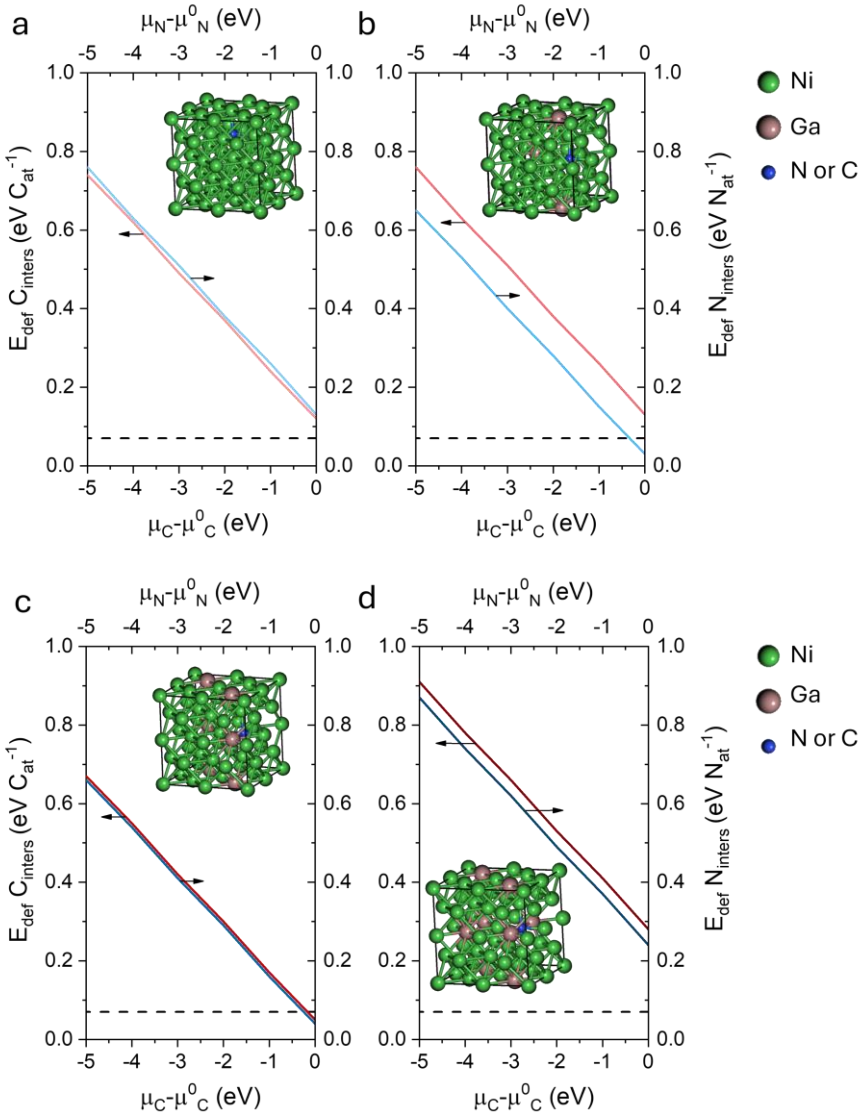

Figure A.VI.2: *Evolution of the energy of defect formation for the uptake carbon and nitrogen into octahedral interstitial positions for fcc metals (Fm-3m) a) neat Ni, and b-d) NiGa alloys with b) 6.25 at%, c) 12.5 at% and d) 25 at% Ga contents, as a function of the carbon and nitrogen chemical potentials, respectively, as predicted by DFT calculations (PAW-PBE). The dashed line serves as a guide to the eye for the background thermal energy at the reaction temperature of 773 K (0.07 eV). The insets showcase optimized 2x2x2 supercell models.*

The results indicate that the lattice expansion caused already by low Ga doping favors the dissolution of C and N atoms at interstitial positions in NiGa alloys compared to the neat *fcc* Ni. While interstitial incorporation benefits from the swelling of the metal lattice, carbon and nitrogen atoms are more stable at interstitial positions having only Ni atoms in their direct coordination environment. Both dopants show similar formation energies in the alloy at comparable carbon and nitrogen chemical potentials, making the uptake of both C and N energetically equally feasible under the applied reaction conditions. However, higher Ga doping of the metal lattice, close to the solubility limit of Ga in NiGa alloys, results in the establishment of direct Ga coordination with the interstitial solute, which is energetically disfavored, particularly for carbon, and it results in higher defect formation energies. These *ab initio* predictions tie in well with the experimental results, which showed the stabilization of lattice-expanded *fcc* NiGa alloys owing to C and/or N interstitial dopant uptake under process conditions.

Energetics of $(Ni_xGa_{1-x})_3(C_yN_{1-y})$ (nitro)carbide phases

Operando XRD results showed the development of a phase isostructural with Ni_3C (*R-3c*). The possible participation of nitrogen in the development of this phase as well as the role of Ga was studied with *ab initio* thermochemistry. **Figure A.VI.3 a** shows the evolution of the energy of formation and the unit cell volume with the degree of C substitution by N in the Ni_3C lattice. For all compounds investigated, the energy of formation was positive, indicating that the (nitro)carbide compounds were not thermodynamically favored over *fcc* Ni(Ga) and graphite reference compounds. Progressive nitrogen doping results in a systematic enlargement of the unit cell. Moreover, the replacement of C by N was found to lower the energy of the formation of $Ni_3(C_yN_{1-y})$ compounds up to y=0.5. $Ni_3(C_{0.5}N_{0.5})$ is predicted to be more stable than Ni_3C, while a surplus of lattice nitrogen beyond this composition becomes thermodynamically unfavorable compared to the reference nickel carbide.

For the preferred C:N molar ratio of 1, the effect of replacing lattice Ni by Ga on the relative thermodynamic stability of $(Ni_xGa_{1-x})_3(C_{0.5}N_{0.5})$ carbonitride

compounds was investigated next. As shown in **Figure A.VI.3 b**, Ga contents higher than ca. 5 at% make the energy change for lattice C replacement by N progressively more negative, hence thermodynamically favored over that in Ni_3C. Taken together, DFT calculations predict a higher stability of Ni(Ga) carbonitride compounds with trigonal *R-3c* structure and underscore that Ga doping into the lattice of bimetallic catalysts contributes further to the relative stability of these carbonitride compounds.

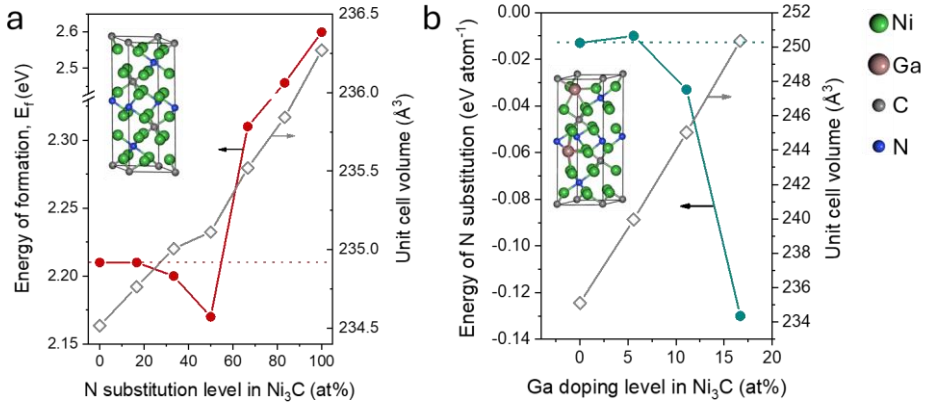

Figure A.VI.3: *a) Evolution of the energy of formation and the unit cell volume for Ni_3C (R-3c) as a function of the degree of lattice carbon substitution by nitrogen as predicted by DFT calculations (PAW-PBE) Evolution of the energy of substitution lattice carbon by nitrogen and unit cell volume for $(Ni_xGa_{1-x})_3(C_{0.5}N_{0.5})$ carbonitride compounds as a function of the degree of Ga doping into the Ni lattice positions as predicted by DFT calculations (PAW-PBE). The insets showcase optimized structural models for (a) $Ni_3(C_xN_{1-x})$ and (b) $(Ni_xGa_{1-x})_3(C_{0.5}N_{0.5})$ compounds, respectively.*

References

(1) Ducher, R.; Kainuma, R.; Ishida, K. Phase Equilibria in the Ni-Rich Portion of the Ni–Ga Binary System. *Intermetallics (Barking)* **2007**, *15* (2), 148–153. https://doi.org/10.1016/j.intermet.2006.04.004.

Appendix VII: ASPEN-HYSYS simulation: Thermodynamic analysis

In silico thermodynamic simulations have been performed to assess the thermodynamic bounds of the process of the conversion of C_1 sources, specifically syngas ($CO + H_2$), and N_1 sources, specifically ammonia. The analysis also serves to establish specific target reactions for kinetic inhibition to attain the maximum possible selectivity and yield to nitriles. Specifically, HCN and acetonitrile were considered. The thermodynamic data was calculated with Aspen-Hysys (V10) software, using a Gibbs reactor (**Figure A.VII.1**) and the Peng–Robinson–Stryjek–Vera (PRSV) equation of state in the fluid package.

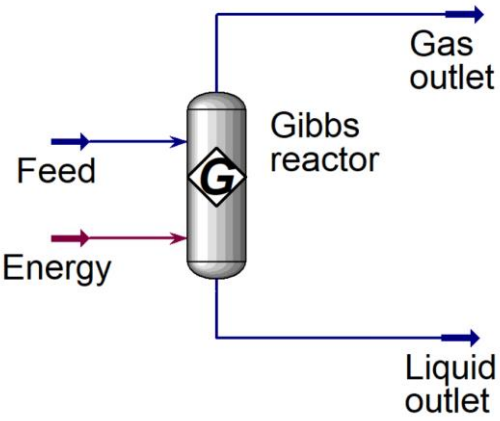

Figure A.VII.1: Diagram of the Gibbs reactor of the Aspen-Hysys software.

Syngas/Ammonia reaction

The CO conversion and product selectivity were calculated using a feed composition of 2 NH_3: 1CO: 1H_2 (v/v %), which emulates the feed considered of relevance for experimental testing in **Chapters 4** and **5** of this thesis. The Gibbs reactor was set to operate isothermally, and without pressure drop. Various temperatures in the range of 673-873 K and total pressures 1 to 10 bar were

screened. The following compounds were considered at the outlet stream, in thermodynamic equilibrium: methane, a possible product from the methanation reaction, carbon dioxide, a possible product from the water-gas shift reaction (WGSR), N_2 from ammonia decomposition, water, alongside acid cyanide, acetonitrile, and methylamine were included as specific N-compound products.

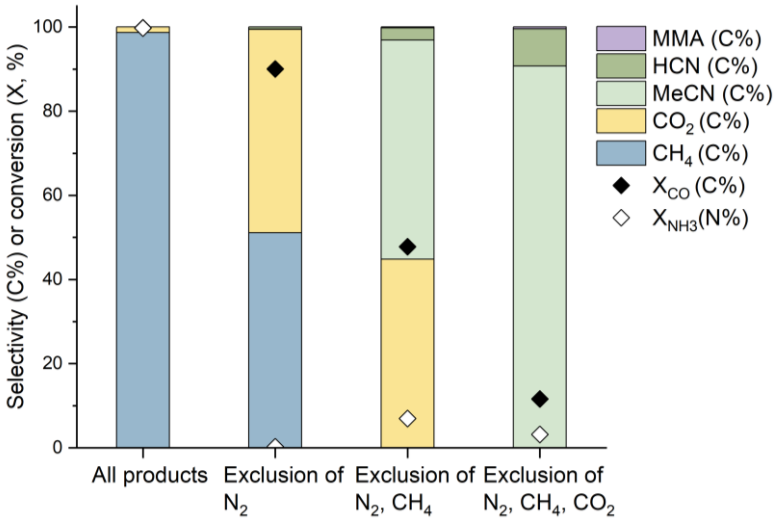

***Figure A.VII.2*:** Summary of the thermodynamic predictions obtained for the conversion of syngas/ammonia mixtures to N-compounds using Aspen-Hysys simulations. Feed compositions: $2NH_3$: $1CO$: $1H_2$ (v/v %), T=723 K and P=3 bar. "*Exclusion of*" refers to the components that are disregarded as products in each case of study. Only carbon-containing products have been considered to determine selectivity (expressed on a molar C basis). Note that the C:N molar ratio of 0.5 in the feed stream determines that CO is the limiting reactant for the synthesis of nitriles.

The most representative reaction conditions studied in syngas/ammonia reactions, as detailed in **Chapter 4-5**, were 723 K and 3 bar. **Figure A.VII.2** summarizes the results of the reactant conversion per reactor pass and the product selectivity distribution predicted under equilibrium conditions.

The study revealed that including N_2 and CH_4 within the products resulted in a predicted essentially complete conversion of NH_3 and CO to these

compounds, respectively, indicating that their higher stability makes them the thermodynamically favored products. These results underscore the necessity for kinetic inhibition of N* recombination to N_2 and CO methanation to attain the production of N-compounds. The exclusion of N_2 as a possible product led to negligible ammonia conversion. In terms of carbonaceous products, the predicted selectivity distribution of 51.1 % for CH_4 and 48.4 % for CO_2, which are thermodynamically more stable than any N-compound possible product.

As discussed in **Chapters 4-5**, methane selectivity can be maintained to low values (<10%) with the use of appropriate catalysts. Therefore, in a third simulation scenario, methane was disregarded as a product. As shown in **Figure A.VII.2**, the production of nitriles from ammonia/syngas mixtures is thermodynamically feasible under the specified conditions, excluding N_2 and methane as components. Ammonia and CO conversion at equilibrium were predicted to be 7.0 % and 47.8 %, respectively. Under these conditions, acetonitrile (MeCN) is favored, with a selectivity of 52.0 %, accompanied by CO_2 at 44.9 %. HCN and MMA are less favored, with selectivities of 2.9 % and 0.2%, respectively. These predictions align with the experimental results obtained in **Chapter 5**.

Additionally, in a final scenario, CO_2 was also disregarded as product, alongside N_2 and CH_4, to emulate the case where not only methanation but also the WGSR are kinetically inhibited. In this case, equilibrium ammonia and CO conversions remained at comparatively low levels of 3.2 and 11.6 %, respectively. Moreover, the equilibrium acetonitrile selectivity reached 90.7 % indicating that both methanation and WGSR would need to be inhibited kinetically to maximize the selectivity to C_{2+} nitriles.

These results indicate that the synthesis of nitriles from syngas/ammonia mixtures is thermodynamically feasible within the operational window studied in this thesis. Developing effective catalysts presents the challenge of inhibiting nitrogen recombination into N_2, which is thermodynamically preferred to C-N coupling, as well as methanation and WGS reactions, given that CH_4 and CO_2 are thermodynamically favored over C_{2+} products, including N-compounds.